

# Analysis of the Impact of External Optical Feedback on the Performance of High-Power and High-Brightness Laser Diodes

**By**


## Mohamad Anas Helal, MSc

Department of Electrical and Electronic Engineering


Thesis submitted to the University of Nottingham for the Degree of
Doctor of Philosophy
February 2017

# Abstract

The main motivation behind this work was to answer the following question: what is the impact of unintentional external optical feedback on laser performance. During the course of this PhD, however, two more questions were raised: how does the spectral external feedback (i.e. intentional feedback from a grating) enhances the spectral performance of the laser? And why does the beam quality of Distributed Bragg Reflector (DBR) tapered lasers degrade at >2.5 times the threshold current? To answer these two questions, new simulations were performed and more results were obtained.

The impact of external feedback can be positive or negative. High-brightness lasers are mostly characterised under stand-alone conditions. Nevertheless, high-brightness lasers are almost always operated in external cavity configurations. The external cavity will produce reflections, whether they are intentional reflections off mirrors or gratings, or unintentional reflections off the optics elements. In order to have an accurate prediction of how the high-brightness laser will perform in an external optical system, a modelling tool, which is capable of self-consistently modelling the laser cavity and the fields propagating in the external optical system, is needed.

In this work, an external cavity laser simulation tool was developed. This tool consists of an in-house 2.5D laser modelling tool, *Speclase*; a commercial coherent ray-tracing software, *OpticStudio*; and an interface software to bidirectionally couple the two different light modelling algorithms used by these tools: finite difference beam propagation (FD-BPM) method and coherent ray-tracing. The author was responsible for: developing the interface software – using Matlab - between *Speclase* and *OpticStudio*. Also, the author cooperated with Dr. Kaunga-Nyirenda to modify

*Speclase* so that the coupling between *Speclase* and *OpticStudio* modelled the physics correctly. This way the software was able to produce external cavity designs to study the impact of external feedback, intentional and unintentional.

The external cavity tool was used to investigate and analyse the impact of parasitic reflections on the performance of high-brightness diode lasers. It was also used to analyse how the Littrow cavity works, which is an example of how intentional feedback is used to improve laser performance. Finally, *Speclase* was used to investigate why the beam quality of high-brightness DBR tapered lasers degrade at higher power, i.e. at currents > 2.5 times the threshold current. This gave an insight on how the external optical feedback affects the degradation of beam quality. It also helped differentiate between the impact of external feedback coupled to the fundamental mode and to the higher-order vertical modes.

This work contributes to the knowledge of how external feedback alters the performance of high-brightness laser diodes. It shows that unintentional feedback can lead to the degradation of output power, power conversion efficiency and beam quality. It also shows the significance of modal discrimination and external cavity coupling coefficients and how they can be used to mitigate the unwanted impacts of external optical feedback.

The developed model also contributes to the optimisation of external cavity systems with intentional feedback to get optimum performance. It shows how spectral feedback coupled to the laser cavity can force the laser to favour a specific wavelength that is, by allowing the beam of that wavelength to couple into the RW section, while other wavelengths are spatially filtered out.

This work also answers a significant question of why the beam quality of DBR tapered lasers degrade at currents 2.5 times the threshold current, although the back-

facet reflectivity is patterned, allowing fields propagating outside the RW to escape the structure. The results show clearly how the patterned back facet reflectivity creates a diffraction of the back-propagating beam which allows the diffracted beam to exit the RW and couple into the taper section, exciting higher-order lateral modes.

# Acknowledgments

I would like to thank my PhD supervisors Professor Eric Larkins and Dr Steve Bull for their support and continuous encouragement throughout the course of this work. I am indebted to Dr Simeon Kaunga-Nyirenda for all the help and assistance in developing the external cavity simulation tool and for the fruitful technical discussions. Thanks are due to Dr Roderick MacKenzie who helped me in the development of the gain measurement code. I gratefully acknowledge both BRIDLE project and the School of Electrical and Electronic engineering for the funding that enabled me to complete this work. I also would like to express my gratitude to Dr Andrew Phillips who helped me while applying for the PhD funding. Last but not least, I carry the greatest appreciation and gratitude to my parents who supported me tremendously through the course of this PhD.

# Publications

## Conference abstracts:

- M. A. Helal, S. Bull, S. N. Kaunga-Nyirenda, J. J. Lim and E. C. Larkins, "Simulation of high-brightness diode lasers with optical feedback from modules and systems," 2013 High Power Diode Lasers and Systems Conference (HPD), Coventry, 2013, pp. 14-15.
- E. C. Larkins, S. Bull, S. N. Kaunga-Nyirenda, M. A. Helal, *et. al.* "Design Optimisation of High-Brightness Laser Diodes for External Cavity Operation in the BRIDLE Project," 2014 International Semiconductor Laser Conference, Palma de Mallorca, 2014, pp. 21-22.
- M. A. Helal, S. Bull, S. N. Kaunga-Nyirenda, J. J. Lim and E. C. Larkins, "Self-consistent simulation of high-brightness diode lasers with external optical feedback," 2015 IEEE High Power Diode Lasers and Systems Conference (HPD), Coventry, 2015, pp. 27-28.

## Book chapters:

- M. A. Helal, S. Kaunga-Nyirenda, S. Bull, E. Larkins, “High-Brightness Laser Diodes with External Feedback”, *Handbook of Optoelectronic Device Modelling and Simulation, Taylor & Francis Books (2017).* To be published.

## Conferences presentations:

- M.A. Helal, S.N. Kaunga-Nyirenda, S. Bull, and E.C. Larkins, “Self-Consistent Simulation of High-Brightness Laser Diodes with External Cavity Feedback”, Semiconductor and integrated optoelectronics (SIOE 15), Cardiff, Wales. 31$^{st}$ March-2$^{nd}$ April, 2015

- “Design and simulation of high-brightness diode lasers for operation in the presence of external feedback”, M.A. Helal, S. Bull, S.N. Kaunga-Nyirenda, D. Moss and E.C. Larkins, Novel In-Plane Semiconductor Lasers XV, Photonics West, San Francisco, 18 February 2016 (invited)
- “Beam quality degradation processes in high brightness tapered lasers”, M. Anas Helal, Stephen Bull, Simeon Kaunga-Nyirenda, Eric Larkins, Nonlinear Dynamics in Semiconductor Lasers, Weierstrass Institute, Berlin – 15 June 2016. (invited)
- “Beam Quality Degradation Mechanisms in Tapered Lasers”, M.A. Helal, S.N. Kaunga-Nyirenda, S. Bull and E.C. Larkins, European Semiconductor Laser Workshop, Darmstadt, Germany, 23 September 2016. (invited)

# Table of Contents

List of Common Symbols and Abbreviations ..... 1

Symbols ..... 1

Abbreviations ..... 5

1 Introduction ..... 8

1.1 Fundamentals of semiconductor laser diodes ..... 10

1.1.1 Homojunction and heterojunction lasers ..... 11

1.1.2 Lattice matching and energy bands ..... 13

1.1.3 Quantum-well (QW) lasers ..... 16

1.1.4 Population inversion ..... 21

1.1.5 Resonant cavity ..... 26

1.1.6 Non-radiative carrier recombinations ..... 29

1.1.7 Rate equations ..... 31

1.2 High-power semiconductor laser technology ..... 32

1.3 Important concepts in high-power laser diodes ..... 34

1.3.1 Efficiency and output power ..... 34

1.3.2 Near-field and far- field patterns ..... 37

1.3.3 Beam quality ..... 38

1.3.4 Astigmatism ..... 41

1.3.5 Catastrophic optical mirror damage (COMD) ..... 42

1.3.6 Absorption bleaching (optical pumping) ..... 43
1.4 Thesis structure ..... 44
1.5 References ..... 45
2 High-brightness laser diodes and external cavity systems ..... 49
2.1 Evolution of High-brightness laser diode sources ..... 51
2.1.1 Ridge waveguide lasers ..... 52
2.1.2 Broad area lasers ..... 53
2.1.3 Narrow-stripe broad area lasers ..... 55
2.1.4 α-DFB lasers ..... 55
2.1.5 Master oscillator power amplifier (MOPA) ..... 56
2.1.6 Tapered lasers ..... 58
2.2 Vertical cavity design for operation in external cavity ..... 60
2.3 High-power laser systems and beam combination techniques ..... 65
2.4 Role of intentional feedback in external cavity lasers and systems ..... 68
2.5 Impact of unintentional feedback on laser performance ..... 74
2.6 References ..... 78
3 Modelling of external cavity high-brightness laser diodes ..... 89
3.1 Laser diode simulation tool *"Speclase"* ..... 90
3.1.1 Electrical model ..... 91
3.1.2 Optical model ..... 93
3.1.3 Coupling between models ..... 97

3.1.4 *Speclase* output variables ..... 100
3.2 External cavity simulation tool ..... 102
3.2.1 Coupling of the laser diode simulation tool and coherent ray tracing tools ..... 103
3.3 Post simulation results processing ..... 115
3.3.1 Heat calculations ..... 116
3.4 References ..... 117
4 Analysis of beam quality degradation in high-brightness tapered lasers at high output power ..... 120
4.1 Beam quality degradation mechanisms in conventional tapered lasers ..... 121
4.2 Attempts to improve beam quality of tapered lasers ..... 124
4.3 References ..... 136
5 Investigation of the role of parasitic feedback on DBR tapered laser ..... 139
5.1 Description of the laser and simulation parameters ..... 141
5.2 Parasitic reflections with on-axis alignment ..... 143
5.3 Parasitic reflections with off-axis alignment, at $+ 0.5$ µm ..... 155
5.4 Parasitic reflections with off-axis alignment, at $- 0.25$ µm ..... 162
5.5 Analysis and discussion ..... 168
5.6 References ..... 174
6 Tapered laser diode operating in a Littrow cavity: Impact of asymmetric spectral feedback ..... 175
6.1 Description of the laser, external cavity and simulation parameters ..... 177
6.2 External cavity with asymmetric spectral feedback ..... 180

6.3 References ..... 186

7 Conclusions and future work ..... 188

7.1 Conclusions ..... 189

7.2 Suggestions for future work ..... 192

7.3 References ..... 192

Appendix I ..... I

Appendix II ..... VIII

# List of Common Symbols and Abbreviations

## Symbols

$\boldsymbol{E_{ph}}$ Photon energy

$\boldsymbol{h}$ Planck's constant

$\boldsymbol{v_{12}}$ Frequency of an emitted/absorbed photon with energy corresponding to the energy difference between E1 and E2

$\boldsymbol{B_{12}}$, $\boldsymbol{B_{21}}$ **and** $\boldsymbol{A_{21}}$**:** Einstein proportionality constants

$\boldsymbol{N}$ Electron density in energy states

$\boldsymbol{P}(\boldsymbol{E_{12}})$ Density of photon field

$\boldsymbol{n}$ Refractive index

$\boldsymbol{c}$ Speed of light in vacuum

$\boldsymbol{R_{stm}}$ Rate of stimulated emission

$\boldsymbol{R_{abs}}$ Rate of absorption

$\boldsymbol{\rho_{eh}}$ Electron-hole pair joint density of states

$\boldsymbol{f_1}$, $\boldsymbol{f_2}$ Probabilities of electrons being in either the valence or the conduction bands, respectively.

$\boldsymbol{F_p}$ , $\boldsymbol{F_n}$ Quasi Fermi levels for the electron and hole population respectively.

$\boldsymbol{k}$**:** Boltzmann constant.

$\boldsymbol{T}$**:** Temperature.

$\boldsymbol{E_g}$**:** Bandgap energy.

$\boldsymbol{L}$**:** Length of the laser cavity.

$\boldsymbol{v}$**:** Frequency of longitudinal modes in a laser cavity.

$\boldsymbol{\Gamma}$**:** Confinement factor.

$\boldsymbol{R}$**:** Laser facet power reflectivity.

$\boldsymbol{\alpha_i}$**:** Internal loss in laser cavity.

$\boldsymbol{\tau_{n0}}$ **,** $\boldsymbol{\tau_{p0}}$**:** Recombination lifetimes for electrons and holes, respectively.

$\boldsymbol{R_{SRH}}$**:** Shockley-Read-Hall **r**ecombination rate.

$\boldsymbol{n, p}$**:** Density of states for electrons and holes, respectively.

$\boldsymbol{n_i}$**:** Intrinsic carrier concentration.

$\boldsymbol{C_n}$**,** $\boldsymbol{C_p}$**:** Auger recombination coefficients for electrons and holes respectively.

$\boldsymbol{q}$**:** Electron charge

$\boldsymbol{V}$**:** Volume of the active region in which the carriers are injected

$\boldsymbol{R_{st}}$**:** Rate of stimulated emission in semiconductor lasers

$\boldsymbol{R(N)}$**:** Total electron-hole recombination rate including spontaneous emission, Shockley-Read-Hall and Auger recombination rates

$\boldsymbol{\tau_N}$**:** Carriers life-time

$\boldsymbol{S}$**:** Photon density

$\boldsymbol{\alpha_m}$**:** Mirror loss in laser cavity

$\boldsymbol{R_{sp}}$**:** Rate of spontaneous emission in semiconductor lasers

$\boldsymbol{v_g}$**:** Photons group velocity

$\boldsymbol{I_{stm}}$**:** Electric current contributing to stimulated emission

$\boldsymbol{\eta_i}$**:** Internal quantum efficiency

$\boldsymbol{I_{th}}$**:** Threshold current in semiconductor lasers

$\boldsymbol{\eta_d}$**:** Differential quantum efficiency

$\boldsymbol{\eta_{PCE}}$**:** Power conversion efficiency

$\boldsymbol{U_0}$**:** Turn on voltage of a semiconductor laser

$\boldsymbol{R_s}$**:** Series resistance in semiconductor lasers

$\boldsymbol{P_O}$**:** Optical output power

$\boldsymbol{P_e}$**:** Electrical input power

$\boldsymbol{Q}$**:** Beam propagation factor

$\boldsymbol{\omega_0}$**:** Angular frequency

$\boldsymbol{\theta_{div}}$**:** Divergence angle of a diffracted beam

$\boldsymbol{B}$**:** Laser output Brightness

$\boldsymbol{M^2}$**:** Beam quality measure

$\boldsymbol{P_{int}}$**:** Internal power in a high-power laser

$\boldsymbol{\psi(x,z)}$**:** Lateral **s**patial distribution of photon field of a laser

$\boldsymbol{\phi(y)}$**:** Vertical mode profile of a laser

$\boldsymbol{E(x,y,z)}$**:** 3D electric field distribution

$\boldsymbol{\beta, \beta_{eff}(x,z)}$**:** Propagation constant and effective propagation constant of an electromagnetic wave

$\boldsymbol{n_{eff}}$**:** Effective index

$\Delta\, \boldsymbol{n_{eff}}$**:** Change in effective index

$\boldsymbol{\alpha_{fca}}$**:** Free-carrier absorption incurred loss

$\boldsymbol{g}$**:** Gain of the active region within a laser

$\boldsymbol{\alpha_{scat}}$**:** Scattering loss

$\boldsymbol{g_{eff}(x,z)}$**:** Lateral spatial distribution of effective gain

$\boldsymbol{\sigma_{fc,n}, \sigma_{fc,p}}$**:** Free-carrier cross section for electrons and holes, respectively.

$\boldsymbol{S(x,y,L)}$**:** Photon density spatial distribution at the front facet

$\boldsymbol{R_0}$**:** Output facet power reflectivity

$\boldsymbol{\psi_f(x,L)}$**:** Lateral spatial distribution of optical field at the front facet

$\boldsymbol{N_{ph}(x,y,L)}$**:** Transverse photon density at the facet

$N_s$: Average photon density

$J_n, J_p$: Current density for electrons and holes, respectively.

$\psi(\theta_H), \psi(\theta_V)$: Horizontal and vertical far fields

$\eta_n(x)$: Lateral spatial distribution of coupling coefficient between external feedback and vertical mode n

$TE_n(y)$: Transverse electric field of vertical mode n

$E_{ext}(y; x)$: Vertical spatial distribution of external feedback

$\varphi_n(x)$: Lateral distribution of the phase of external electric field, belonging to vertical mode n, coupled into the cavity

$E_{n,\ ext,coupled}(x)$: Lateral distribution of external electric field, belonging to vertical mode n, coupled into the cavity

$\psi_b(x, L)$: Lateral distribution of back-propagating internally reflected optical field at the front facet

$\psi_{b,comp}(x, L)$: Lateral distribution of the composite back-propagating internally reflected optical field and externally coupled field

$H_{Joule}$: Joule heating rate

$J_{stm}(x, z)$: Stimulated current density

$H_{abs}$: The rate of generated heat due to absorption bleaching

$H_{FCA}$: The rate of generated heat due to free-carrier absorption

$H_{RW}$: Ridge waveguide filter response

$P_{forward}, P_{backward}$: Power of forward and backward travelling fields.

$I_{RW}\ I_{taper}$: Ridge waveguide and taper sections current

# Abbreviations

| | |
|---|---|
| **LIGO** | Laser Interferometer Gravitational-Wave Observatory |
| **SCH** | Separate Confinement Heterostructure |
| **GRINSCH** | Graded Index Separate Confinement Heterostructure |
| **DBR** | Distributed Bragg Reflector |
| **SRH** | Shockley-Read-Hall |
| **EHP** | Electro-Hole Pair |
| **MBE** | Molecular Beam Epitaxy |
| **MOCVD** | Metal Organic Chemical Vapour Deposition |
| **QW** | Quantum Well |
| **BA** | Broad Area |
| **RW** | Ridge Waveguide |
| **NF** | Near-Field |
| **FF** | Far-Field |
| **BPP** | Beam Product Parameter |
| **COMD** | Catastrophic Optical Mirror Damage |
| **LOC** | Large Optical Cavity |
| **SLM** | Selective Laser Melting |
| **PCE** | Power Conversion Efficiency |
| **SCOWL** | Slab-Coupled Optical Waveguide Laser |

| | |
|---|---|
| **NBA** | Narrow-Stripe Broad Area |
| **EDFA** | Erbium Dipped Fibre Amplifier |
| **MOPA** | Master Oscillator Power Amplifier |
| **AR** | Anti-Reflection |
| **HR** | High-Reflection |
| **SHB** | Spatial-Hole Burning |
| **MD** | Modal Discrimination |
| **ASE** | Amplified Spontaneous Emission |
| **ELoD2** | Extremely Low Vertical Divergence |
| **IBC** | Incoherent Beam Combination |
| **CBC** | Coherent Beam Convergence |
| **SBC** | Spectral Beam Convergence |
| **WBC** | Wavelength Beam Convergence |
| **FWHM** | Full-Width Half-Maximum |
| **VBG** | Volume Bragg Grating |
| **WA FDBPM** | Wide Angle Finite Difference Beam Propagation Method |
| **VLS** | Vertical Line Source |
| **HLS** | Horizontal Line Source |
| **TE** | Transverse Electric |
| **TA** | Tapered Amplifier |

| | |
|---|---|
| **ASLOC** | Asymmetric Large Optical Cavity |
| **VD** | Vertical Displacement |
| **SA** | Stand-Alone simulation (no external feedback) |
| **ECOA** | External-Cavity On-Axis |
| **ECOF** | External-Cavity Off-Axis |
| **EC** | External Cavity |
| **EOF** | External Optical Feedback |
| **FCA** | Free-Carrier Absorption |
| **SAC** | Slow-Axis Collimation |
| **FAC** | Fast-Axis Collimation |

Chapter 1

# 1 Introduction

When the first laser was invented in 1960, the ruby laser, it was a significant scientific breakthrough. However, in the very early days the invention was perceived as "A solution looking for a problem". Nevertheless, engineers and physicist started testing copies of the ruby laser and found that pulsed lasers were able to make holes in in thin metal sheets. A year later, after the ruby laser invention, Charles Campbell succeeded in the first retina attachment procedure, on a human patient, using millisecond laser pulses on November 1961 [1]. Lasers now are essential tools in scientific research in biology, chemistry, physics and engineering. The laser technology has enabled subwavelength spectroscopy making them essential tools in biology. Lasers also allow for the precise measurements of length. In 2015, the laser interferometer, in the Laser Interferometer Gravitational-Wave Observatory (LIGO), succeeded in detecting gravitational waves by observing strains of the order of $1 \times 10^{-21}$ [2]. Lasers have also found applications in other various fields: optical communications, spectroscopy, material cutting and welding, optical disk storage, printers, displays lighting, milling machines guiding, missiles guiding, fusion neutron generations, and medicine.

The basic concept of the laser , the idea that photons can stimulate the emission of identical photons with the same frequency, direction and phase, was first proposed by Albert Einstein in 1917 [3]. Later, this idea of stimulated emission saw first application in microwave frequencies. Charles Townes and James Gordon demonstrated the first maser in 1954[4]. The maser was a step towards moving to optical frequencies, to form what was called: the optical maser. In 1958, Townes and

# Chapter 1

Arthur Schawlow suggested the extension of maser techniques to the infrared and optical frequencies in their paper "Infrared and Optical Masers", published in *Physical Review* [5]. They suggested that at such frequencies, the generation of highly intense coherent radiation would allow for higher resolution spectroscopy than was possible with masers. Their proposal included the use of a resonant cavity with multiple oscillating modes, but the selection of a single mode was possible by making the end walls of the cavity highly reflective. They used an example of vaporised potassium, as active material, and potassium lamp as a pump source. At the same time, Theodore Maiman started investigating ruby as active material and white flash lamps as pumping source. In 1960, he succeeded in making the first ruby laser, consisting of a ruby rod, with the two sides polished and silvered, inside a coil of photographic flash lamp. Maiman published the description of his invention in the same year in *Nature* [6].

In the early sixties, there were other attempts at utilising the principle of stimulated emission to produce lasers but with different gain media. Bell labs succeeded in making the first continuous-wave gas laser, using helium-neon as active gain material in a meter-long high-reflective cavity, producing light at 1.15μm [7] and the pumping was accomplished through electrical discharge. In 1961, the first fibre laser, consisted of a neodymium-glass rod, was demonstrated [8]. Also, lasing in solid-state materials (other than ruby), such as Nd-YAG, was demonstrated in 1964 [9], which became a dominant solid-state laser material.

The lasing process in semiconductor material was being investigated within the same decade. In 1955, radiation by carrier injection in III-V semiconductor materials was observed [10]. The carrier injection was accomplished through contacts and the intensity was proportional the injected current. However, the emission spectra did not completely match the bandgap energy, and self-absorption could not explain

the discrepancy. The importance of direct bandgap was not clear at that time. Later, the first semiconductor laser was made using a GaAs p-n homojunction, pumped with short current pulses and cooled to liquid nitrogen temperature [11]. A new class of junctions was proposed later- the p-n hetero-junction structure was developed, which allowed the operation at room temperature, using continuous current and producing continuous wave output [12].

This chapter discusses fundamental principles of semiconductor lasers such as population inversion, the resonant cavity and radiative and non-radiative carrier recombinations. Next, it gives a brief introduction to high-power semiconductor lasers and the technologies that had to converge to achieve high output power. After that, the important the concepts and metrics used to characterise high-power lasers are discussed. Finally, the outline of the thesis is given.

## 1.1 Fundamentals of semiconductor laser diodes

One of the most popular basic structures of a semiconductor laser is comprised of a resonant cavity, enclosing a gain medium (p-n junction), sandwiched between two mirrors. The resonant cavity ensures that the photons are confined in all three dimensions and kept inside for long durations allowing them to multiply via stimulated emission and thereby generating a large population of photons inside the cavity. This optical cavity is called a Fabry-Perot cavity and is shown in figure 1.1.

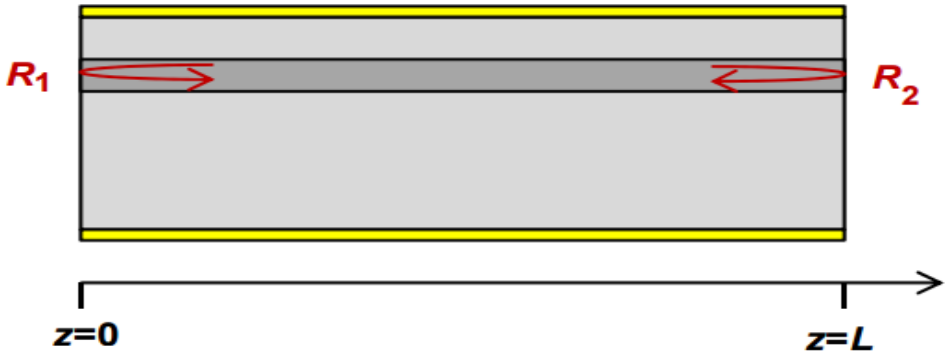



**Figure (1.1): Basic Fabry-Perot laser cavity.**

### 1.1.1 Homojunction and heterojunction lasers

Semiconductor lasers or junction lasers were invented in 1962 utilising a single type of materials, GaAs, doped properly to form a p-n junction[11]. These homojunction devices had high threshold current and their operation was only possible through pulsed current and at cryogenic temperatures as the developed heat would destroy them. The shortcomings of the homojunctions came from the fact that they did not have a way of confining either light or carriers, and when these devices were biased, the electrons would diffuse across the junction requiring high threshold current to achieve population inversion. Also, the lack of light confinement meant that the optical mode would overlap with the bulk material, incurring high optical losses, which required high current densities to overcome these losses. Later advances made the confinement of electrons better through the use of heterostructures. In heterostructures, different materials are grown which resulted in narrow regions that could confine the carriers. This sort of carrier confinement makes population inversion easier to establish using lower currents, and hence, could operate at room temperature. For example, the first p-n homojunction was made using an n-doped GaAs substrate, on which a p-doped GaAs is grown, as shown in figure 1.2 (left). However, growing

a different p-doped material on GaAs, like AlGaAs, on top of thin p-doped GaAs layer, would create a narrow region to confine carriers, shown in figure 1.2 (right). This sort of material compositions is found in diode lasers emitting in the near-infra-red.

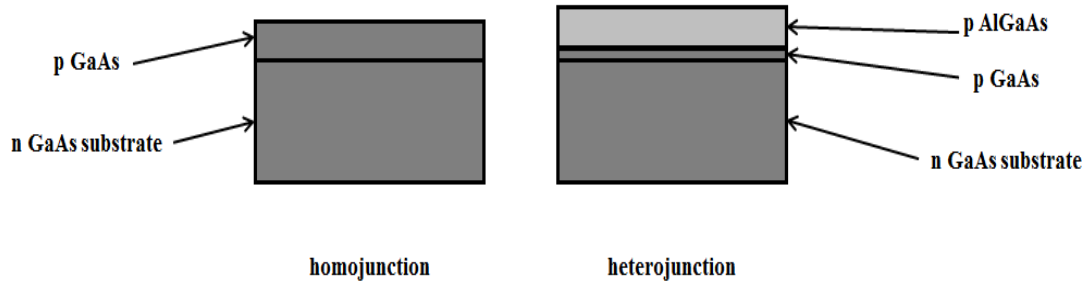



**Figure (1.2): Use of different semiconductor materials to create heterostructures. GaAs homojunction structure (left). AlGaAs heterojunction structure (right)**

A further improvement can be obtained by sandwiching the active GaAs material between two AlGaAs layers. This is called the double-heterostructure and the contrast in refractive index in GaAs-AlGaAs-GaAs boundaries creates waveguiding properties for more confinement of the optical wave. This structure is depctid in figure 1.3.

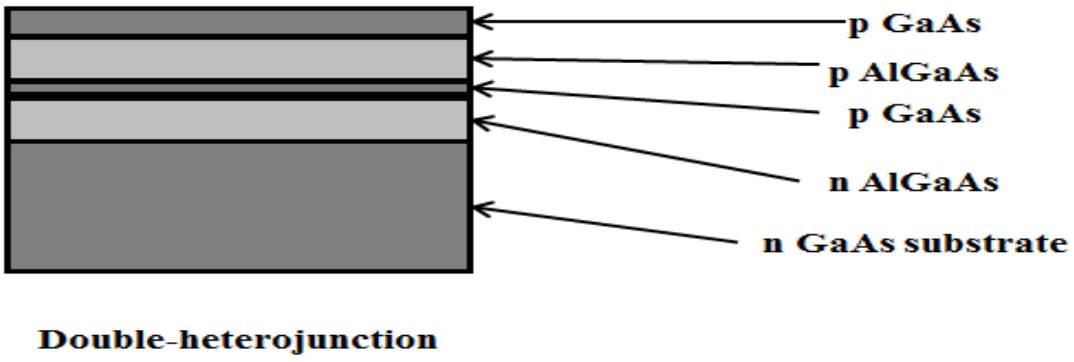



**Figure (1.3): Use of multiple layers to create confinement of carriers as well as waveguiding for the optical waves.**

A further step in heterostructure development was the use of separate regions, one for confining carriers and the other for optical waveguiding. The new structure is

called the separate confinement heterostructures (SCH). This was achieved changing the composition to create low refractive index regions to confine the optical wave in a wider waveguide region, while confining the carriers in a narrow active region layer. A further optimisation of SCH structures is to grade the composition of the optical waveguide to create what are called graded index separate confinement hetero structures (GRINSCH).

### 1.1.2 Lattice matching and energy bands

There are two major requirements relating to the materials used for semiconductor lasers. The use of a lattice-matched substrate is one of the key considerations. The other key requirement is for the semiconductor materials to have a direct bandgap. Lattice matching is important for the growth of semiconductor materials on other semiconductor materials. When there is a lattice growth mismatch, strain is introduced into the layers, which prevents the epitaxial growth of thicker layers without defects. As for direct bandgap, this is required so that energy and momentum are conserved as well as the transition probability in direct bandgap material is large, making light emission easily obtained. Figure 1.4 shows the bandgap of different semiconductor materials as a function of lattice constant. For example, InGaAsP can be lattice matched to InP to create a heterostructure laser. This lattice matching is achieved through modifying the composition of different materials within the compound. InGaAsP is used to make the standard material for telecom lasers.

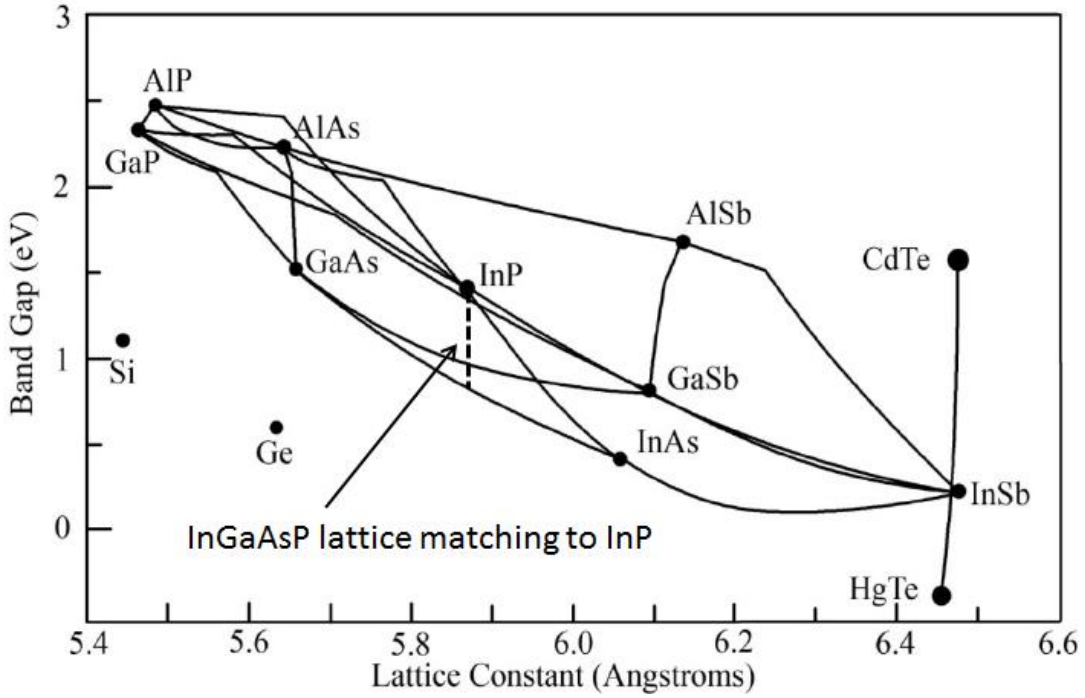



**Figure (1.4): bandgap energy of different III-V and II-VI materials as a function of lattice constant.**

In principle, the production of light in a laser is a result of the interaction of electromagnetic radiation with the excited atoms forming the gain medium. This is true for solid-state and gas lasers. One way of exciting atoms is achieved though optical pumping. However, in semiconductor lasers, the electrons transitions happen between two bands of energy states: the valence band and the conduction band. Therefore, lasing in semiconductor material is based on the interaction between electromagnetic radiation and the electric-dipoles formed between the electrons in the conduction band and the holes in the valence band. When materials of different semiconductor materials are joined, the bands of energy states are formed. Electrons, whether in conduction or valence bands, have energy and momentum associated with them, and it is useful plot the energy of these bands as a function of momentum. Figure

1.5 shows two plots of energy vs momentum, one for a direct bandgap while the other for an indirect bandgap.

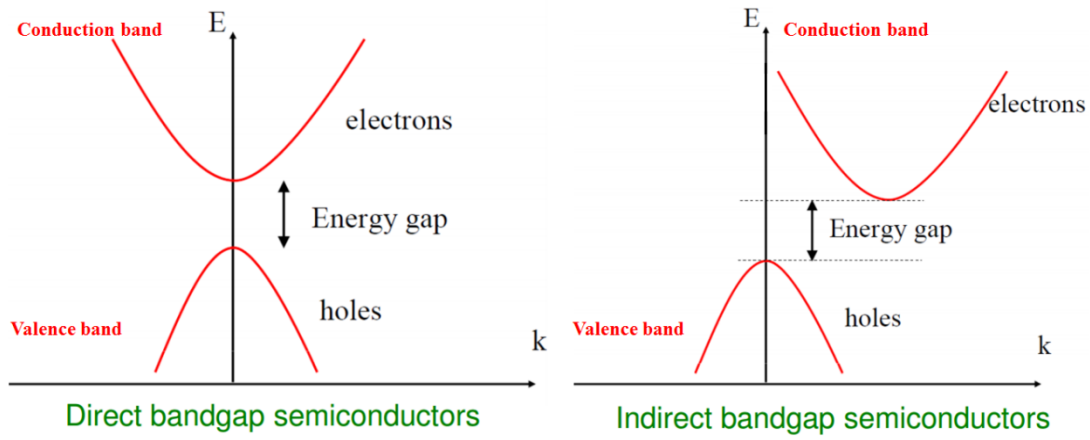



**Figure (1.5): Energy (E) bands as a function of momentum (k) for two types of material. Direct bandgap energy bands (left). Indirect bandgap energy bands (right).**

When the p-n junction is forward biased, a significant number of electrons and holes is present in the depletion region, and photons passing through this region will lead to the stimulation of identical photons. The radiated photons will have energy equal to the energy of the photons initiating the stimulated emission. The first few photons come as a result of spontaneous emission. When the conduction band is filled with electrons, electrons decaying to the valence band by spontaneous emission will give off energy in the form of photons. If the laser is designed properly and with the right conditions, these spontaneously emitted photons will start the stimulated emission process. With right choice of mirror reflectivities, the generated photons will reflect off the mirrors leading to more stimulated emission and thus amplification of light. Also, the right choice of the length of the resonant cavity plays an important role in cavity mode and phase selection.

### 1.1.3 Quantum-well (QW) lasers

The thickness of the active region in a double heterostructure (DH) plays an important role in its optical properties. If this thickness starts to get below ~100 nm, quantum effects must be considered, and this regime of operation is called the quantum confined regime. Quantum wells are thin layered structures capable of providing quantum confinement of carriers (electrons and holes). The structure of the quantum well is obtained by sandwiching a very thin layer of one semiconductor called the "well" between other semiconductor layers, called the "barriers". The energy bandgap for the barriers must be larger than that of the quantum well, this ensures proper confinement of the carriers within the quantum well. The total thickness of heterostructure is comparable to 40 atomic layers or less than 10 nm.

In the quantum well, electrons and holes are confined in two dimensions and their wave-like properties cannot be neglected. The allowed states in the quantum well structure correspond to standing waves in the direction perpendicular to the QW layers. And since only particular waves are standing waves, the energy states allowed for electrons/holes are quantised. Inside the quantum well, the electrons and holes can be considered to be particles but with effective masses different from the bulk effective masses.

#### 1.1.3.1 Strained quantum wells

The ability to grow very thin layers of semiconductors was only realised after the development of epitaxial growth techniques such as molecular beam epitaxy (MBE) and metal organic chemical vapour deposition (MOCVD) [13]. As mentioned in section 1.1.2, while growing structures containing different semiconductor materials, it is important to ensure that the lattice constant of the different materials is

the same. While the previous statement is true for growing structures with thick layers, the case is different for quantum wells (QW); a lattice constant mismatch between the layers can be tolerated up to a critical thickness. These structures are called strained QW. There are two types of strain: *compressive* strain, where the lattice constant of the barrier material is larger than that of the QW material, and *tensile* strain, where the lattice constant of the barrier material is smaller than that of the QW material [14]. The strain, both compressive and tensile, shifts the conduction band and the valence bands, leading to different bandgap energies and hence, different operating wavelengths. The use strained QWs in lasers provides a method to control the emission wavelength by adjusting the strain. These structures have made it possible to achieve wavelengths that previously could not be achieved with lattice matched materials. For example, the use of the InGaAs strained quantum wells provides an emission at wavelengths where the GaAs substrate is transparent [14], i.e. 980 nm. Additionally, this kind of structure can result in a further reduction in the threshold current density by changing the optical density of states of the QW gain material [15].

#### 1.1.3.2 Physics of quantum wells

The physics of the quantum well can be understood by solving Schrödinger's equation in one dimension. The one dimension Schrödinger's equation is given in equation (1.1) .

$$\frac{\hbar^2}{2m}\frac{d^2\,\emptyset_n}{dz^2} + V(z)\,\emptyset_n = E_n\,\emptyset_n \tag{1.1}$$

$V(z)$ is the potential energy seen by the particle in direction perpendicular to the layers, $m$ is the particle's effective mass, $E_n$ and $\emptyset_n$ are the energy eigenvalue and eigenfunction associated with the $n_{th}$ solution of the equation. If the walls of the quantum well are assumed to be infinite, as shown in figure 1.6 (left), then the

wavefunction, at the QW well walls, is zero and the solution of equation (1.1) is given by equations (1.2) and (1.3). The wavefunction solutions are shown graphically in figure 1.6 (right).

$$E_n = \frac{-\hbar^2}{2m}\left[\frac{n\,\pi}{L_z}\right]^2 \text{, n = 1, 2, 3, …} \tag{1.2}$$

$$\emptyset_n = A\ \sin\left(\frac{n\,\pi\,z}{L_z}\right) \tag{1.3}$$

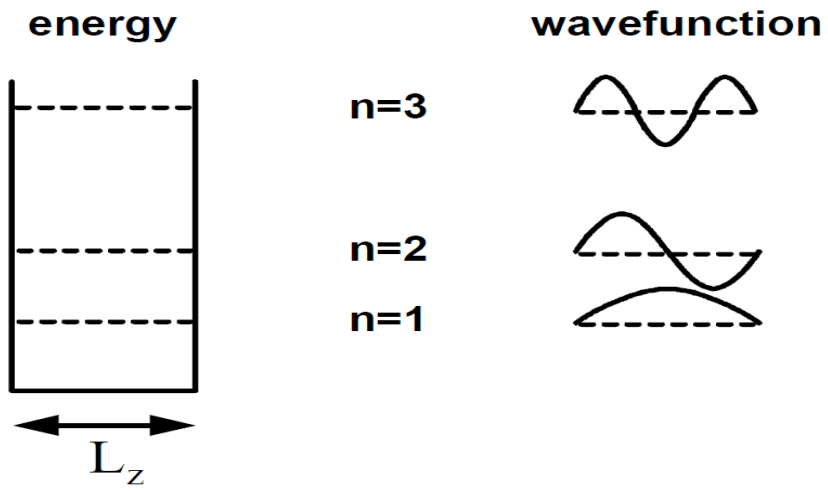



**Figure (1.6): Energy discretisation and associated wavefunctions in a quantum well with infinite barriers. Energy levels (left). Wavefunctions (right).**

From equation (1.2), the energy levels (confinement energies) are quadratically spaced, and the wavefunctions are sine waves. Another thing that can be noticed is that the energy levels spacing decreases with the width of the quantum well, i.e. the spacing becomes large for narrow quantum wells.

The solution of the problem for a quantum well with finite barriers is similar with some important differences. A quantum well with finite barriers is shown in figure 1.7 (right).

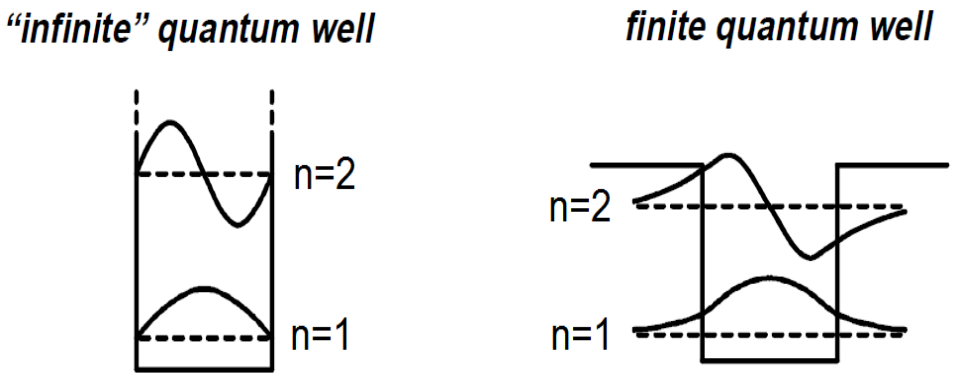



**Figure (1.7): Comparison of energy discretisation and associated wavefunctions in two quantum wells: an infinite quantum well (left) and a finite quantum well (right).**

The wavefunctions cannot be zero at the barriers, as the tunnelling penetration needs to be considered. Consequently, the wave functions within the well are sin waves but exponentially decaying outside the well. Also, the confinement energies for finite wells are lower than those of an infinite well, as shown in figure (1.7).

A structure with a one quantum well is called a single quantum well structure (SQW), and structure with more than quantum well is called a multi-quantum well (MQW) structure.

#### 1.1.3.3 Optical absorption in quantum wells

The absorption model within bulk semiconductor dictates that an electron is raised from the valence band to an empty state within the conduction band. This transition must conserve momentum, and because photons have no momentum, the momenta difference between the states in the valence and conduction bands must be zero, i.e. the transition is vertical in E-k space. In quantum wells, what governs the transition – in a direction perpendicular to the QW layers- is the selection rule, rather than the momentum conservation. This rule states that transition between energy states takes place between energy levels, belonging to the valence and conduction bands, of

the same quantum number only. This rule is derived from the fact that the optical absorption strength is proportional the overlap integral between the valence and conduction bands wavefunctions. Since the wavefunctions within the QW are sine waves, then the overlap integral will only have a value if it is between two energy levels with identical wavefunctions, i.e. of the same quantum number, which is depicted in figure 1.8.

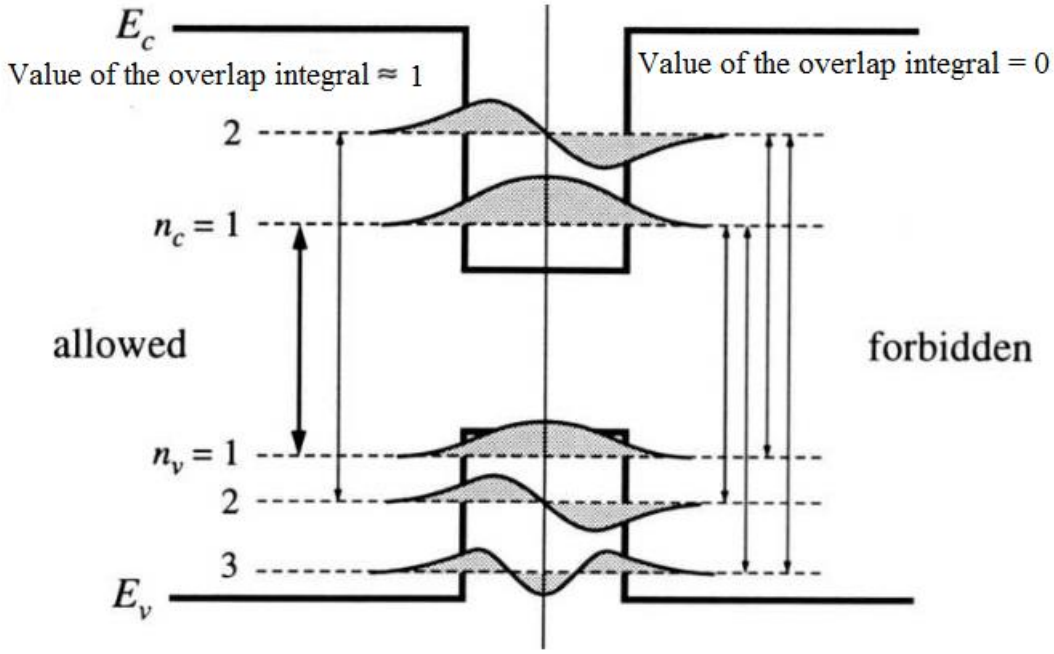



**Figure (1.8): Allowed and forbidden transitions in a finite quantum well [14].**

### 1.1.3.4 Optical confinement within quantum wells

The quantum well depicted in figure 1.8 represents the basic quantum well which has poor optical confinement; the well is too narrow to act as a waveguide. Therefore, in practice, a common modification to the structure in figure 1.8 is to use a thinner carrier-confining-active-region and a surrounding intermediate bandgap that offers a separate confinement for photons. In this case, the structure is referred to as

separate-confinement heterostructure single quantum well (SCH-SQW). This structure is depicted in figure 1.9 left. Another way of confining photons within a quantum well is to use a graded refractive index for the region surrounding the quantum well, creating what is called the graded refractive index separate confinement heterostructure (GRINSCH) which is depicted in figure 1.9 (right). In the SCH and GRINSCH laser structures, the refractive indices of the layers adjacent to the well are set at values higher than that of the outside layers, meaning the light is confined to the SCH and GRINSCH regions, as shown in figure 1.9 by depicting how the electric field (photons) is confined. These structures also enhance the carrier collection efficiency of the QW and further reduce the threshold current density.

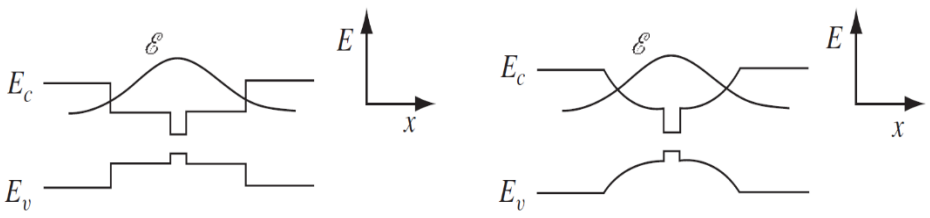



**Figure (1.9): Two examples of quantum well structures offering separate confinements of carriers and light. Standard SCH (left). Graded refractive index SCH (GRINSCH) (right). The electric field of the confined light is also depicted [14].**

### 1.1.4 Population inversion

When an electron falls from the conduction band to the valence band it must release energy, and when it moves from valence band to the conduction band it must absorb energy. There are two ways in which a photon is emitted. When an excited electron relaxes into the valence band by itself, a photon is emitted and this process is called spontaneous emission. However, the excited electron can be stimulated to relax to the valence band by means of a photon, with proper energy, passing through the

active material. When p-n junction is formed, and in thermal equilibrium, the majority of electrons are in the valence band, and any passing photon is far more likely to be absorbed, exciting an electron to the conduction band. This leads to a question: how can we make a substantial percentage of electrons in the conduction band? This is where term "population inversion" comes. For the probability of stimulated emission to be greater than absorption or spontaneous emission, a significant number of electrons need to exist in the conduction band. This can be done by injecting electrons to the conduction band though forward bias. Figure 1.10 shows the three processes of absorption, spontaneous emission and stimulated emission.

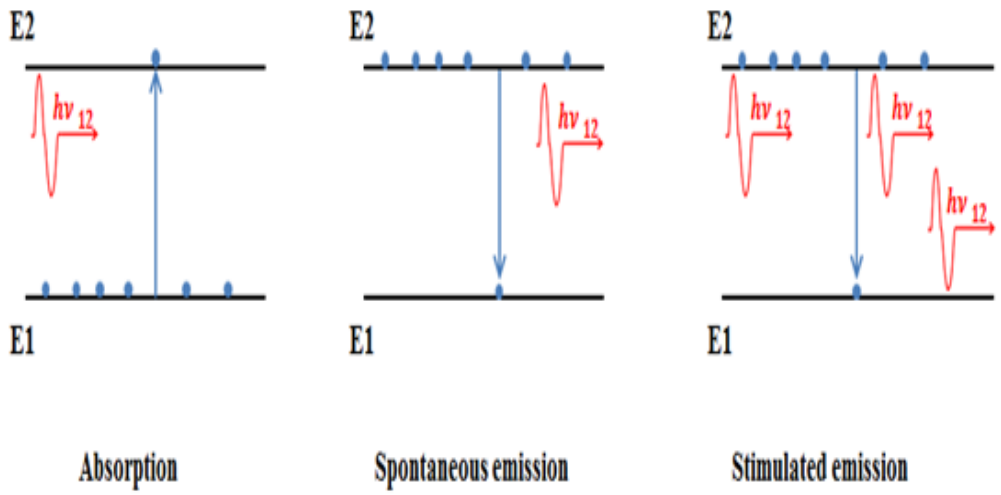



**Figure (1.10): Electron transition between two energy states and the resulting processes of absorption (left), spontaneous emission (middle) and stimulated emission (right).**

The energy of the photons passing through the material needs to be equal to or higher than the energy difference between the valence and conduction bands to cause either absorption or stimulated emission:

$$E_2 - E_1 = E_{ph} = h\upsilon_{12} \tag{1.4}$$

With quantum mechanics governing the transition of electrons and holes between energy levels as well as the large number of electrons and holes states with equal momentum, it is more accurate to describe the above processes in terms of probabilities. Considering two energy states, one in the conduction band denoted as $E_2$, and another in the valence band, denoted as $E_1$, the rate of stimulated emission is proportional to both the intensity of the photon field and the density of electrons in the energy state $E_2$. Similarly, the rate of absorption is also proportional to the intensity of the photon field but conversely, to the density of electrons in energy state $E_1$. Thus, if the electron density in both energy states are denoted $n_1$ and $n_2$ and the density of photons field is denoted as $P(E_{12})$, then the stimulated emission rate can be written as $B_{21}\, n_2 P(E_{12})$ and the rate of absorption can be written as $B_{12}\, n_1 P(E_{12})$ . As the spontaneous emission, like the simulated emission, is proportional to $n_2$ but independent of photon density, the spontaneous emission rate can be written as $A_{21}\, n_2$. At steady-state, the mentioned processes are related by the following expression [6]:

$$B_{12}\, n_1 P(E_{12}) \;=\; B_{21}\, n_2 P(E_{12}) \;+ A_{21}\, n_2 \tag{1.5}$$

Physically, this means that, the absorption rate at steady-state must be equal to the emission rate, including both the spontaneous and stimulated emission. The above expression was described by Einstein and the proportionality constants $A_{21}, B_{12}, B_{21}$ are called Einstein coefficients and are related to each other by the following expressions:

$$B_{12} \;=\; B_{21} \tag{1.6}$$

$$A_{21} \;= (8\pi\, n^3\, E_{21}/h^3 c^3) B_{21} \tag{1.7}$$

where n is the refractive index, h is Planck's constant and c is the speed of light. At equilibrium, the stimulated emission rate is negligible compared to the spontaneous

emission rate, even with the presence of photon field. The ratio of stimulated emission rate to the spontaneous emission rate is given by:

$$\frac{stimulated\ emission\ rate}{spontaneous\ emission\ rate} = \frac{B_{21}\, n_2 P(E_{12})}{A_{21}\, n_2} = \frac{B_{21}}{A_{21}}\, P(E_{12}), \qquad (1.8)$$

and hence, the ratio is less than unity. From the expression above, it is clear that in order to increase the stimulated emission over the spontaneous emission, the photon field energy density needs to be increased. This is achieved by the Fabry-Perot cavity (resonator) in which photons are reflecting off the facets and sweeping electrons from the upper energy level, leading to more stimulated photons that build up to a large photon density. Similarly, comparing the stimulated emission rate to the absorption rate we get:

$$\frac{stimulated\ emission\ rate}{absorption\ rate} = \frac{B_{21}\, n_2 P(E_{12})}{B_{12}\, n_1 P(E_{12})} = \frac{B_{21}\, n_2}{B_{12}\, n_1} \qquad (1.9)$$

This shows that, for the stimulated emission rate to be greater than the absorption rate, the electron population of the upper energy state needs to be increased. Knowing that in equilibrium $n_1 > n_2$, then for the stimulated emission rate to be enhanced the electron population in the two energy states needs to be inverted and maintained this way, i.e. $n_2 > n_1$, which can be achieved through electrical pumping. Thus, the condition $n_2 > n_1$ is called population inversion.

In semiconductors, the expressions for stimulated emission and absorption rates include the probability of electrons being in either the valence or the conduction bands, $f_1$ and $f_2$, respectively. They also deal with electron-hole pair (EHP) joint density of states, $\rho_{eh}(E_{12})$ rather than electron densities $n_1$ and $n_2$. The stimulated emission rate, in semiconductors, proportional to the EHP joint density of states, the

probability that the conduction band is filled, the probability that the valence band is empty and the photon density in the gain medium:

$$R_{stm} = B_{21}\,\rho_{eh}(E_{12})\,f_2(1-f_1)P(E_{12}) \tag{1.10}$$

The absorption rate, on the other hand, is proportional to the EHP joint density of states, the probability that the valence band is filled, the probability that the conduction band is empty and the photon density in the gain medium:

$$R_{abs} = B_{12}\,\rho_{eh}(E_{12})\,f_1(1-f_2)P(E_{12}) \tag{1.11}$$

Therefore, in order to achieve population inversion the following condition must be met:

$$R_{stm} > R_{abs} \tag{1.12}$$

Substituting (1.10) and (1.11) into (1.12) and cancelling equal terms on both sides:

$$f_2(1-f_1) > f_1(1-f_2) \tag{1.13}$$

Equation (1.13) can be further simplified by expanding the brackets and cancelling equal terms on both sides to give the following expression:

$$f_2 > f_1 \tag{1.14}$$

Equation (1.14) gives the condition for population inversion in terms of probabilities of states in the conduction and valence bands. These probability terms can be given by the following expressions:

$$f_1 = \frac{1}{1+\exp\left(\frac{E_1 - F_p}{k\,T}\right)} \tag{1.15}$$

$$f_2 = \frac{1}{1+\exp\left(\frac{E_2 - F_n}{k\,T}\right)} \tag{1.16}$$

where $F_n$ and $F_p$ are the quasi Fermi levels for the electron and hole population respectively. By substituting (1.15) and (1.16) into (1.14) and after rearrangement of terms, the population inversion expression (1.14) can be rewritten as:

$$F_n - F_p > E_2 - E_1 \tag{1.17}$$

The right hand side of (1.17) is equal to the energy bandgap of the material $E_g$ . Thus, (1.17) can be rewritten as:

$$F_n - F_p > E_g \tag{1.18}$$

Thus, population inversion occurs when separation of the quasi Fermi levels is greater than the band gap energy

### 1.1.5 Resonant cavity

According to equation (1.9), when population inversion is achieved, i.e. the density of electrons in the conduction band is greater than in the valence band, the rate of stimulated emission is greater than absorption rate. However, equation (1.8) shows that for the stimulated emission rate to be greater than the spontaneous emission rate, the photon field energy density has to be high. Moreover, in the early stages of lasing process, spontaneously emitted photons, as well as the photons that are stimulated as a result, propagate in all directions. One way of increasing the photon energy field and aligning the stimulated photons is through enclosing the p-n junction in a cavity with two mirrors. The use of mirrors ensures that a significant number of photons stay within the cavity, through multiple reflections off the mirrors, building a large photon field within the cavity reinforcing the stimulated emission process. In a way, the cavity and the mirrors act as resonator with optical feedback. The resonant cavity allows for the propagating waves to be in standing wave configuration. Photons of a certain

wavelength are allowed to traverse the cavity back and forth on if the length of the cavity (the distance L between the mirrors) is multiple integer of half the wavelength:

$$L = m\,\frac{\lambda}{2} \tag{1.19}$$

where $m$ is an integer number, $L$ is the length of the cavity and λ is the wavelength in the cavity. Figure 1.11 shows the standing waves that supported by the resonant cavity.

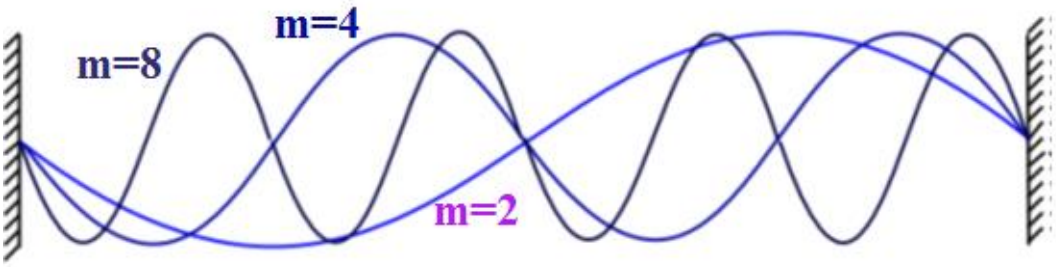



**Figure (1.11): Longitudinal modes supported by the resonant cavity**

There is infinite number of oscillatory standing waves that can exist in the cavity, which are called longitudinal modes. Each longitudinal mode has a unique frequency $\nu_m$ and the spectral separation of any two consecutive longitudinal modes is a constant given by[16]:

$$\Delta\nu = \nu_m - \nu_{m-1} = \frac{\nu}{2L} \tag{1.20}$$

which is called the spectral range of the cavity. The resonant cavity modes are narrower in frequency than the spontaneous emission bandwidth, and hence, lasing can happen at different frequencies leading to wide spectrum (multimode) output as shown in figure 1.12.

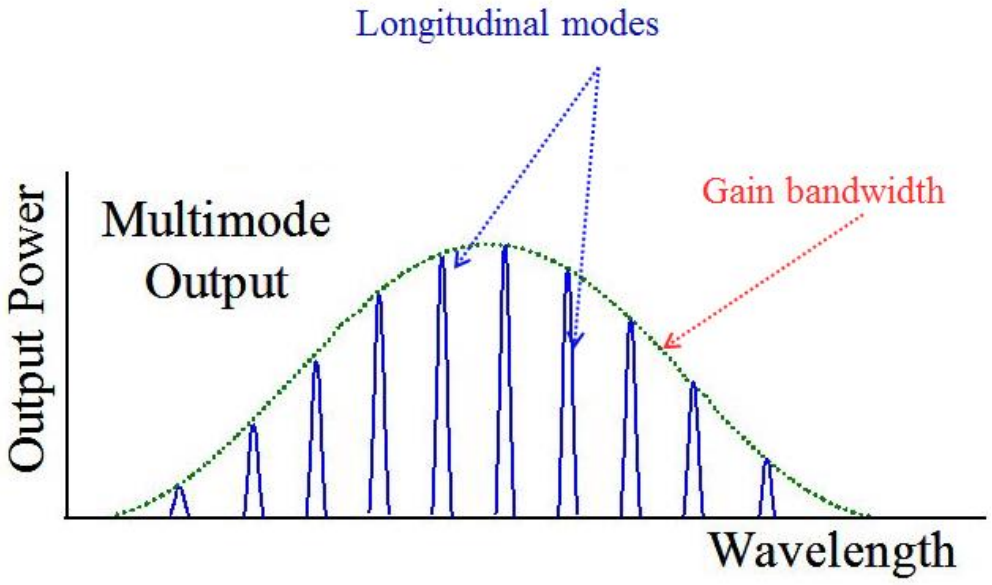



**Figure (1.12): Longitudinal modes and gain bandwidth**

One way of making the cavity select a single mode is to change its length so that the difference between any consecutive modes is larger than the bandgap energy. However, this approach has implications on the length of the gain medium and thereby the output power. Other ways of selecting a single mode is by incorporating a distributed Bragg reflector (DBR) in the active medium, which is wavelength selective and allows only one longitudinal mode to exist.

In addition to longitudinal modes, the cavity supports transverse modes. The number of vertical modes relies on the vertical structure of the cavity. The number and the shape of vertical modes can be engineered by modifying the refractive index profile of the multiple layers forming the junction. The number of lateral modes is determined by the lateral dimension of the cavity.

One mirror of the resonant cavity is usually coated with an antireflective coating to enable light to be radiated from only one end of the device. The other mirror is usually coated with a high reflectivity coating preventing photon loss out of the back

of the device. For a laser to lase at a given energy, the material gain *g(E)*, multiplied by the confinement factor must equal all the losses (i.e. internal cavity losses and the mirror losses). The gain is given by:

$$\Gamma g(E) = \alpha_i + \frac{1}{2L} \ln(\frac{1}{R_1 R_2}) \tag{1.21}$$

where $\alpha_i$ is the internal loss coefficient, $L$is the length of the cavity, $R_1$ & $R_2$ are the power reflectivities of the mirror facets and $\Gamma$ is the confinement factor. The confinement factor is a measure of the spatial localisation of the optical mode in the active region:

$$\Gamma(y) = \frac{\int_{-d/2}^{+d/2} E(y)^2 \, dy}{\int_{-\infty}^{+\infty} E(y)^2 \, dy} \tag{1.22}$$

where $y$ is the spatial dimension in the vertical direction, $d$ is the thickness of the active region and $E$ is the electric field.

### 1.1.6 Non-radiative carrier recombinations

Radiative recombination processes are not the only processes in semiconductors. There are also non-radiative recombination processes, which produce no light. The main non-radiative recombination processes in semiconductors at room temperature are the Shockley-Read-Hall (SRH) and Auger recombination processes. SRH describes the recombination of electrons (in the conduction band) and holes (in the valence band) through defect states within the band gap, as shown figure 1.13 (left).

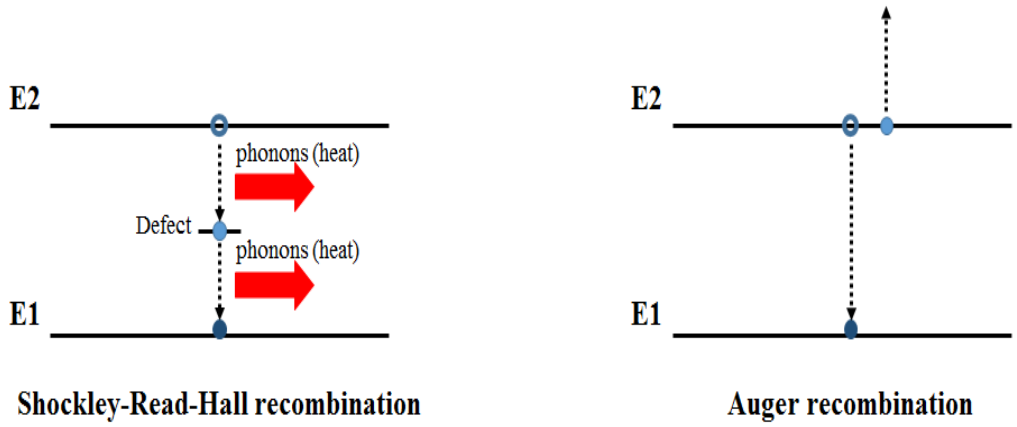



**Figure (1.13): Graphical representation of Shockley-Read-Hall recombination (left) and Auger recombination processes in semiconductors**

The released energy is given off to the lattice. The SRH recombination rate is given by the following expression [6]:

$$R_{SRH} = \frac{np - {n_i}^2}{\tau_{n0}(p + n_i) + \tau_{p0}(n + n_i)} \tag{1.23}$$

where the lifetimes $\tau_{n0}$ and $\tau_{p0}$ are the recombination lifetimes for electrons and holes, respectively.

Auger recombination is a three-body process involving either two electrons and a hole or two holes and an electron, in which one electron and one hole recombine and the released energy is given to the extra electron or hole, as shown in figure 1.13 (right). The recombination rate is phenomenologically described by[17]:

$$R_{Auger} = (\, C_p p + C_n n)(np - {n_i}^2) \tag{1.24}$$

where $C_n$ and $C_p$ are the Auger recombination coefficients for electrons and holes respectively.

### 1.1.7 Rate equations

The dynamics of energy level populations in the active medium are often modelled by differential equations. These equations are called rate equations and they describe the temporal evolution of the carrier and photon populations in the active region as a result of the various recombination processes (radiative and non-radiative).

The carrier rate equation describes the concentrations of carriers injected into the active region and is given by:

$$\frac{dN}{dt} = \frac{I}{qV} - R(N) - \left(\frac{1}{V}\right) R_{st} S \tag{1.25}$$

where $N$ is the electron-hole pair (EHP) density, $I$ is the electrical injection current, $q$ is the electron charge, $V$ is the volume of the active region, $R_{st}$ is the rate of the stimulated emission and $S$ is the number stimulated emission photons generated. The left-hand side of equation (1.25) describes the net EHP density in time. The rate at which the EHP density is increased due to the current injected $I$, is given by $\frac{I}{qV}$. The rate at which the EHP density is decreased due to EHP recombination, due to stimulated emission, is given by $R_{st}S$. The EHP density can decrease due to EHP recombination -spontaneous emission, Shockley-Read-Hall, and Auger- which is given by $R(N)$. $R(N)$ is given by the following expression:

$$R(N) = AN + BN^2 + CN^3 = \frac{N}{\tau_N} \tag{1.26}$$

where $AN$ accounts for Shockley-Read-Hall recombination rate, $BN^2$accounts for spontaneous emission recombination rate and $CN^3$ accounts for the Auger recombination rate.

The other rate equation describes generation of photons due to stimulated emission and spontaneous emission in time which is given by:

$$\frac{dS}{dt} = R_{st}S - (\alpha_i + \alpha_m)\, v_g S + R_{sp} \tag{1.27}$$

where $\alpha_i$ and $\alpha_m$ are the cavity internal and mirror loss, respectively. $v_g$ is the group velocity and $R_{sp}$ is the rate of coupling of spontaneously emitted photons in the lasing mode. The left-hand side of equation (1.27) represents the rate at which photons, in the active region, are generated. The rate of photon generation is increased by the rate at which stimulated photons are emitted ($R_{st}S$) and by the rate at which spontaneously emitted photons are coupled to the lasing mode. The rate at which the generated photons are lost, either due to internal losses ($\alpha_i v_g S$) or due to photons escaping the cavity ($\alpha_m v_g S$) , decreases the photon generation rate.

## 1.2 High-power semiconductor laser technology

Since the discovery of stimulated emission process in semiconductors, which led to the semiconductor diode laser, many applications were foreseen to utilize it, among which were fibre optics, optical data storage and free-space communications[13]. However, p-n junction lasers were far from being realised as sources for high-power laser applications. Different technologies had to be realised first. By the late 1970s, double hetero-junction structure lasers were developed, leading to a reduced threshold current allowing for continuous wave emission. After the advancement of crystal growth technologies, such as molecular beam epitaxy (MBE) and metal organic chemical vapour deposition (MOCVD), it was possible to grow uniform epitaxial layers with thicknesses compared to those of atomic layers. With uniform epitaxial layers, it was possible to build large laser diode structures capable of producing high-output power. The capability of growing thin epitaxy layers

lead to the realisation of quantum well (QW) active regions[18]. Quantum-well lasers, lasers with active layer thicknesses on the order of 10 nm, resulted in a number of advantages including a dramatic reduction in threshold current, a reduction in the free carrier loss, and a reduction in the temperature sensitivity of the threshold current. All of these effects increased the efficiency of the laser and the ability to make lasers with longer cavities and therefore lower thermal resistance. Furthermore, as the overlap of the optical mode with the active layer was much less, the power limitation caused by catastrophic optical damage of the laser was significantly improved. The net effect was the ability to demonstrate higher output power lasers.

While the total output power of a laser is a very significant attribute, nevertheless, it is not the only one. Other requirements, such as beam quality and power conversion efficiency are as significant. And with growing need for high-power lasers in various fields, the output power and beam quality requirements differ for each and every application. Despite the high output power given by large laser cavities, it comes with caveat: poor beam quality, due to multi-mode operation and other effects such as carrier and thermal lensing[19]. Therefore, it was required to obtain high output power as well good beam quality, which led to a redefinition of the high-power laser as high-brightness laser. Brightness is defined as the total output power density per emission area and per unit solid angle of the output beam. Many techniques have been devised to improve the quality of the output beam, including operating the laser in an external cavity configurations, such as asymmetric feedback broad-area (BA) lasers [20]. With ever increasing demand for higher power, and limitation to the total output power per single emitter, laser bars emerged where the individual beams are coherently combined. This beam combination method is capable of scaling the output power to multi kilo watts. In this case, the external cavity configuration is used to

phase lock the individual emitters in a bar, such as Talbot cavity laser [21]. External cavity configurations are also used for other purposes such as wavelength stabilization and modal filtration.

## 1.3 Important concepts in high-power laser diodes

The continuous development of high-power laser diodes has made them desirable to replace other high-power laser technologies such as solid-state lasers, fibre lasers and gas lasers. With their compact size, reliability, efficiency and low-cost, high-power laser diodes are becoming strong contenders in the high-power laser application market. Nevertheless, high-power laser diodes need to demonstrate high performance that is as equal to the other high-power laser technologies. Different high-power laser technologies have different performances, and usually different applications require different performances. In the domain of high-power lasers, there are fundamental parameters that characterise the performance of these devices defining different targets required for different applications. These parameters include output power, efficiency, beam quality and far-field divergence.

### 1.3.1 Efficiency and output power

The term efficiency has several meanings when it comes to lasers. There is the internal quantum efficiency, the differential efficiency and the power conversion efficiency.

The internal quantum efficiency is one of the most important parameters for a high-power laser. It influences the external efficiency and the optical output power.

The internal quantum efficiency is defined as the fraction of current above threshold that results in stimulated emission and is given by the following expression[14]:

$$\eta_i = \frac{I_{stm}}{(I - I_{th})} \tag{1.28}$$

where $I_{stm}$ is the stimulated current required to support the stimulated emission process, $I_{th}$ is the threshold current, and $I$ is the total current. All the currents are measured in [A] and hence, the internal quantum efficiency is unitless.

Mechanisms such as spatial hole burning and gain compression, due to increased photon density in the cavity, lead to carrier leakage which causes reduction in the internal efficiency. Other factors that affect the internal efficiency are the non-radiative processes such as Shockley-Read-Hall and Auger recombintaions.

The performance of the laser can also be characterised by the differential quantum efficiency. This efficiency is important in determining the electrical to optical modulation efficiency. It is defined as the ratio of the rate of photons emitted to the rate of carriers injected and it is given by the following expression:

$$\eta_d = \frac{dS}{dN} = (\frac{dP}{dI})\,(\frac{q}{hf}) \tag{1.29}$$

where $\frac{dS}{dN}$ is the ratio of the rate of emitted photons [$cm^{-3}$] to the rate of injected carriers [$cm^{-3}$].

It can also be defined as the slope efficiency, which is equal to the slope of the L-I characteristic as shown in figure 1.14, and thus it can be expressed as:

$$P = \eta_d \frac{hf}{q}(I - I_{th}) \tag{1.30}$$

where $h$ is planck's constant [J.s], $f$ is the light frequency [Hz], $q$ is the electron charge [C], $I$ and $I_{th}$ are the injected and threshold current, respectively [A].

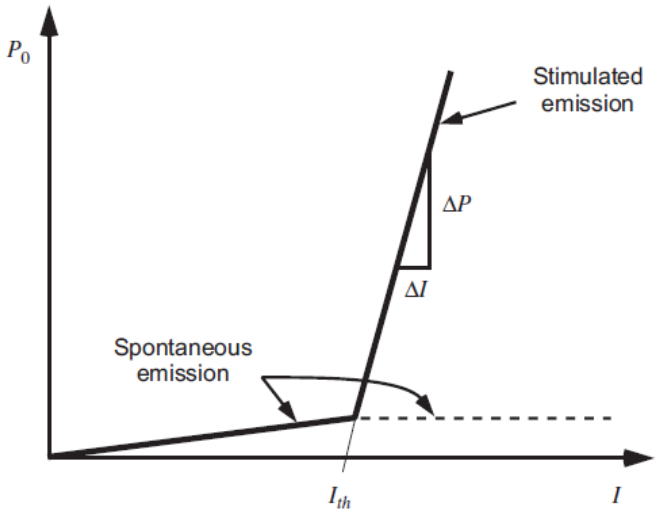



**Figure (1.14): L-I characteristic of a laser diode**

The differential efficiency is also related to the internal quantum efficiency:

$$\frac{1}{\eta_d} = \frac{\alpha_i}{\eta_i \ln(1/R)} L + \frac{1}{\eta_i} \tag{1.31}$$

Equation (1.31) shows that cavity length and mirror loss affect the differential efficiency.

The power conversion efficiency is important for high-power laser diodes. This is the type of efficiency that makes high-power laser diodes desirable compared to fibre and solid-state lasers. It shows how efficient the laser diode is in converting electrical power input into optical power output:

$$\eta_{PCE} = \frac{P_O}{P_e} = \frac{\eta_d \frac{hf}{q}(I - I_{th})}{U \,.\, I} = \frac{\eta_d \frac{hf}{q}(I - I_{th})}{(U_0 + I.R_s) \,.\, I} \tag{1.32}$$

where $U_0$ is the turn on voltage of the diode, $R_s$ is the series resistance of the vertical structure.

### 1.3.2 Near-field and far- field patterns

When a laser beam emanates from the laser aperture it undergoes diffraction. If a screen is put very close to the aperture and parallel to it, the image on that screen will resemble the aperture image. This image is a result of Fresnel diffraction which is called the near-field pattern. If the screen is moved far away from the laser aperture, the image projected on the screen will start to develop fringes and will cease to resemble the aperture image. At this point the pattern seen on the screen is a result of Fraunhofer diffraction and it is called the far-field pattern. Both patterns are related through the complex Fourier transform:

$$E(K_x, K_y) = \iint_{-\infty}^{+\infty} A(x, y) e^{i(K_X x + K_Y y)} dx dy \tag{1.33}$$

where $A(x, y)$ is the spatial field distribution of the output beam (near-field), $x$ and $y$ are the transverse spatial dimensions, $E(K_x, K_y)$ is the angular distribution of the output beam (far-field) and $K_x$ and $K_y$ are the transverse spatial frequencies. A derivation of equation (1.33) is detailed in Appendix I. As both patterns are related by a Fourier transform, then generally, a wider near-field pattern corresponds to a narrower far-field pattern. However, wavelength and spatial frequencies components play a significant role in the width of the far-field pattern.

Both, the near-field and far-field patterns are used to characterise the output beam of the laser, and high-power laser designers use both patterns to assess the suitability of these devices for different applications. Generally, a wider near-field is sought after, as wider near-fields give narrower far-fields, which makes it significantly easier to couple to external optics as well as making the system more tolerant to optics misalignments. Moreover, near- and far- fields serve as an indication of the output

beam quality. The existence of higher spatial frequency components in the near-field leads to degradation in the beam quality and to a wider far-field.

### 1.3.3 Beam quality

Metrics such as the beam parameter product $Q$ or beam propagation factor $M^2$ are common metrics used by manufacturers and industries to specify the beam quality of both individual laser diodes and direct diode laser systems. The beam parameter product (BPP) is the product of beam radius (measured at the beam waist) and the half-angle beam divergence:

$$Q = \omega_0 \times \theta_{div} \tag{1.34}$$

where $\omega_0$ is the beam radius measured in $mm$ and $\theta_{div}$ measured in $mrad$ and $Q$ is the BPP measured in $mm.mrad$. The higher the parameter product, the lower is the beam quality. The beam parameter product allows optical designers to determine the number of individual beams that can be imaged onto the end of a fibre with a fixed diameter (physical aperture) and maximum acceptance angle (numerical aperture). The power coupled into the fibre also depends on the power of the combined beam (and hence of the individual emitters). The brightness (units: $Wcm^{-2}sr^{-1}$) is defined as:

$$B = \frac{P}{\pi^2\, Q^2} = \frac{P}{\lambda^2 M^2} = \frac{P}{\lambda^2 M_x^2\, M_y^2} \tag{1.35}$$

where $P$ is the laser output power, $Q$ is the BPP, $\lambda$ is the wavelength and $M^2$ is the beam propagation factor. $M^2$ is another measure of beam quality as defined by ISO 11146. The beam quality metrics, $M^2$ and $Q$, are related by equation (1.35), as shown in table 1.1 for $\lambda$ = 975nm.

| $M^2$ | $Q$ $(mm.mrad)$ |
|---|---|
| 1.0 | 0.31 |
| 1.5 | 0.47 |
| 2.0 | 0.62 |
| 3.0 | 0.93 |
| 5.0 | 1.6 |
| 10. | 3.1 |
| 20. | 6.2 |
| 30. | 9.3 |

**Table (1.1): Correspondent values of $M^2$ and $Q$**

The brightness of a high-power laser is dependent on multiple parameters, among which are the divergence angle, output power, beam waist and wavelength. The brightness is one the most significant parameters of a high-power laser system that determines whether a specific laser system is suitable for a specific application or not. From equation (1.34) the brightness can be written as a function of the beam propagation factor:

$$B = \frac{P}{\pi^2 \, w_0^2 \, \theta_{div}^2} = \frac{P}{\lambda^2 M^2} \tag{1.36}$$

The beam propagation factor is then written as:

$$M^2 = \frac{w_0^2 \, \theta_{div}^2 \pi^2}{\lambda^2} = \frac{Q^2 \, \pi^2}{\lambda^2} \tag{1.37}$$

In practice, and especially in the case of high-power laser diodes, output beams are not diffraction limited. Given that a perfect diffraction-limited beam has a beam parameter product of $\frac{\lambda}{\pi}$, then $M^2$ is the ratio of beam parameter product for a realistic beam to the beam parameter product of a diffraction-limited beam. Therefore, for a diffraction-limited Gaussian beam, this ratio is equal to 1, in other words $M^2$ is a

measure of how the realistic beam departs from the diffraction-limited Gaussian beam of the same wavelength. Therefore, realistic laser beams are often said to be $M^2$ times diffraction-limited. Less than 1 values of $M^2$ are not physically possible. Values of $M^2$ for real laser beams are $\geq 1$ and indicate the degree to which the beam can be focused. For astigmatic beams, where the beam waists and divergence angles are different in each of the two directions orthogonal to the beam axis, the $M^2$ factors are also different in each direction. The general expression for calculating $M^2$ is given by:

$$M^2 = \frac{\pi}{2\lambda} w_0 \theta \tag{1.38}$$

Based on the way the beam waist $w_0$ is measured, two values of $M^2$ can be obtained. If the beam waist is measured at $1/e^2$ of the intensity of the beam then the resultant beam propagation factor is denoted as $M^2_{1/e^2}$, while if it is calculated using the second-moment then the factor is denoted as $M^2_{2ndmom}$. For Gaussian beams, the $M^2_{1/e^2}$ definition is sufficient, however for realistic beams, this definition is problematic as it does not take all the beam profile into account. It is useful to quote the beam quality with the two definitions, as they yield different values for realistic lasers. In chapter 4, it is argued that the use of $M^2_{2ndmom}$ gives a more accurate measure of the beam quality, as $M^2_{1/e^2}$ is insensitive to the significant changes in the near-field profile incurred at high-power or due to external feedback coupling to the laser. The beam width at second-moment can be calculated from the variance of the spatial intensity profile:

$$w_{0d} = 4\sigma \tag{1.39}$$

where $\sigma$ is the standard deviation calculated from the following variance expression:

$$\sigma^2 = \int_{-\infty}^{\infty} x^2 \ |\psi(x)|^2 \, dx \tag{1.40}$$

### 1.3.4 Astigmatism

The output beam of a coherent point source of light- if propagating in a uniform medium- is spherical, i.e. when the beam is projected on a screen we see a circular spot. At any point in space when this beam is back traced it will lead to the perfect point source. However, with a high-power laser, the output beam is far from spherical and when projected on a screen we see an elliptical spot. This comes from the fact that the output aperture dimensions are not identical. As described in chapter 2, high-power lasers have apertures that are few microns in the vertical direction and tens to few hundreds of microns in the lateral direction. As the laser beam goes through the output aperture it undergoes diffraction. And because the vertical and lateral dimensions are not identical, the output beam will have non-identical divergence angles in the lateral and vertical directions. The lateral divergence angle is typically ($8^\circ - 10^\circ$) while in the vertical direction it is ( $30^\circ - 70^\circ$), hence the elliptical beam shape. Therefore, this beam, when focused, will focus into foci belonging at different unique planes, corresponding to the vertical and lateral dimensions of the beam. Similarly, back tracing the beam into the laser will give two virtual line sources- this was taken into account when constructing the external cavity model in chapter 3. Astigmatism therefore can be defined as the difference, in unit length, between virtual point sources- or line sources of the vertical and lateral dimensions of the beam.

In high-power lasers, and due to non-liner effects at high-power, the astigmatism becomes a more complex problem. Effects such as carrier- and thermal- lensing cause

refractive index perturbations within the laser cavity, which contribute to the astigmatism [22]. What makes the problem of astigmatism even worse is that these nonlinear effects are current dependent and this results in amount of astigmatism changing with current, leading what is called wandering astigmatism [19].

Excessive astigmatism in high-power laser diodes affects the overall beam quality of these diodes, and hence, it affects the overall beam quality of the high-power laser system. To correct the astigmatism, different collimation optics (vertical and lateral) are needed. Laser systems consisting of laser emitters with large astigmatism must incorporate external lenses if the beam is to be accurately focused or collimated.

### 1.3.5 Catastrophic optical mirror damage (COMD)

Catastrophic optical mirror damage (COMD) is one of the most common power limitations of high power diode-lasers, leading to irreversible damage of the laser chip. COMD is a sudden facet degradation caused by increased facet temperature due to non-radiative surface recombination processes in the vicinity of the facet surface. The output power leading to COMD is proportional to the internal power density $P_{int}$ (often indicated as $P_{COMD}$, i.e. the internal power density which is reached at the moment of COMD failure). For a given output power, the internal power density is given by [23]:

$$P_{int} = P_{out} \cdot \frac{1 + R_f}{1 - R_f} \cdot \frac{1}{\frac{d}{\Gamma} . W} \tag{1.41}$$

where $R_f$ refers to the reflectivity of a front facet, d is the quantum well thickness [µm] and $\Gamma$ is the optical confinement factor, $P_{out}$ is the output power [W] and $W$ is the width of the facet [µm]. The term , $\frac{1+R_f}{1-R_f}$, represents the inverse of the transmission

coefficient. Also, the term $\frac{d}{\Gamma} . W$ represents the area of the mode. From the above equation, one can see that the facet heating, leading to its failure, depends on the modal cross-section (i.e. equivalent vertical spot-size ($^{d}/_{\Gamma}$) and lateral stripe width $W$) as well as on the reflectivity of the front facet. Reducing the optical mode intensity (and thereby increasing the COMD threshold) by increasing the modal cross section leads to a higher output power before catastrophic optical damage (COMD) occurs.

### 1.3.6 Absorption bleaching (optical pumping)

The absorption process is the opposite to the stimulated emission process; a passing photon is absorbed and as a result an electron is raised from the valence band to the conduction band (see section 1.1.3). Absorption bleaching can take place in unpumped regions where the population is normal, rather than inverted, and hence, this region provides attenuation (due to absorption) rather than amplification. Photons passing through this region are absorbed, raising electrons from the valence band to the conduction band. This absorption continues to take place until the stimulated emission and absorption are balanced, i.e. $R_{stm} = R_{abs}$. As the result, this region becomes transparent and the absorption is bleached, i.e. any other photons passing this region will not interact with the material. This effect is used in saturable absorbers[24].

Absorption bleaching (or optical pumping) in high-power tapered lasers is a well-known effect. It causes the regions adjacent to the ridge waveguide (absorbing regions) to become transparent which allows the back-propagating fields to pass to the rear facet and to couple into the taper section. This has been found to have a significant impact on output beam quality [22], [25], which will be discussed in more details in both chapter 4 and chapter 5.

## 1.4 Thesis structure

The next chapter explores the literature review of high-power and high-brightness laser diodes and systems. It starts by reviewing the evolution of the brightness for different laser structures and how they compare to each other. It emphasises the need to manufacture lasers with high output power and high beam quality. Next, different aspects of vertical cavity design such as modal discrimination and free-carrier absorption for vertical modes are explored. The aim of this section is to engineer large optical cavity (LOC) lasers to make them less sensitive to external optical feedback while maintaining easy coupling to the external optics. The last two sections of this chapter discuss intentional and unintentional optical feedback and how they affect the laser performance and reliability.

In chapter 3, the modelling tools used in this thesis are discussed. The laser simulation tool is explained and how the electrical and optical solvers are coupled. Next, the external modelling tool is described. Finally, chapter 3 explains in details how the coupling between the two tools is achieved, making them work self-consistently to predict the impact of external feedback on the laser performance.

In chapter 4, beam degradation mechanisms of high-brightness tapered lasers are investigated. It also shows how the $2^{nd}$ moment definition of beam propagation factor $M^2$ is more sensitive to filaments formed in the near-field. It ends with an explanation of why the beam in DBR tapered lasers degrades at high power.

Chapter 5 demonstrates the use of the external cavity laser modelling and how it was used to investigate the impact of external optical feedback on high-brightness DBR tapered laser performance. It shows how external optical feedback can couple laser cavity modes, leading to lower power conversion efficiency, lower output power

and degraded beam quality. This chapter also analyses and distinguishes between the impacts of feedback coupling to the fundamental mode from the coupling to higher order modes. It also shows what happens to the optical power coupled into the cavity and how this affects the laser performance.

In chapter 6, the external cavity laser modelling tool is used to understand and explain how Littrow cavities (used for spectral beam combination) work and how they serve to lock multiple lasers to different wavelengths as well as narrowing the spectral bandwidth of each laser.

Chapter 7 discusses the conclusions of this work and outlines the contributions to the knowledge about external cavity lasers and how to mitigate the detrimental impact of feedback on high-power and high-brightness lasers. This chapter also provides suggestions for future work and how the external cavity model can be enhanced.

Appendix I explains the similarities between the Fraunhofer diffraction expression and the Fourier transform and how it can be used to calculate the far-field distribution from the near field pattern.

Appendix II derives the Fourier optics expression used for the backpropagation of the lateral near-field to obtain the horizontal line source.

## 1.5 References

[1] J. Hecht, “Short history of laser development,” *Opt. Eng.*, vol. 49, no. 9, pp. 91002–91023, 2010.

[2] B. P. Abbott *et al.*, “Observation of gravitational waves from a binary black hole merger,” *Phys. Rev. Lett.*, vol. 116, no. 6, pp. 1–16, 2016.

[3] A. Einstein, “The Quantum Theory of Radiation,” *Phys. Zeitschrift*, vol. 18, pp. 121–128, 1917.

[4] J. P. Gordon, H. J. Zeiger, and C. H. Townes, “Molecular microwave oscillator and new hyperfine structure in the microwave spectrum of NH3,” *Phys. Rev.*, vol. 95, pp. 282–284, 1954.

[5] A. L. Schawlow and C. H. Townes, “Infrared and optical masers,” *Phys. Rev.*, vol. 112, no. 6, pp. 1940–1949, 1958.

[6] T. H. MAIMAN, “Stimulated Optical Radiation in Ruby,” *Nature*, vol. 187, no. 4736, pp. 493–494, Aug. 1960.

[7] A. Javan, W. R. Bennett, and D. R. Herriott, “Population inversion and continuous optical maser oscillation in a gas discharge containing a He-Ne mixture,” *Phys. Rev. Lett.*, vol. 6, no. 3, pp. 106–110, 1961.

[8] E. Snitzer, “Optical Maser Action of Nd+3 in a Barium Crown Glass,” *Phys. Rev. Lett.*, vol. 7, no. 12, pp. 444–446, Dec. 1961.

[9] J. E. Geusic, H. M. Marcos, and L. G. Van Uitert, “Laser oscillations in nd-doped yttrium aluminum, yttrium gallium and gadolinium garnets,” *Appl. Phys. Lett.*, vol. 4, no. 10, pp. 182–184, 1964.

[10] H. J. Bowlden, “Radiative transitions in semiconductors,” *Phys. Rev.*, vol. 106, no. 3, pp. 427–431, 1957.

[11] R. N. Hall, G. E. Fenner, J. D. Kingsley, T. J. Soltys, and R. O. Carlson, “Coherent light emission from GaAs junctions,” *Phys. Rev. Lett.*, vol. 9, no. 9, pp. 366–368, 1962.

[12] H. Kroemer, “A Proposed Class of Hetero-junction Injection Lasers,” *Proc. IEEE*, vol. 51, no. 12, pp. 1782–1783, 1963.

[13] D. F. Welch, “A brief history of high-power semiconductor lasers,” *IEEE J.*

*Sel. Top. Quantum Electron.*, vol. 6, no. 6, pp. 1470–1477, 2000.

[14] L. A. Coldren and S. W. Corzine, *Diode Lasers and Photonic Integrated Circuits*. Wiley, 1995.

[15] M. Fukuda, *Optical Semiconductor Devices*. JOHN WILEY & SONS, INC., 1999.

[16] E. Hecht, *Optics*, 4th ed. Pearson, 2014.

[17] S. K. B. B. G. Streetman, *Solid State Electroinc Devices*, 6th ed. Pearson, 2005.

[18] H. I. and G. D. Goodno, *High Power Laser Handbook*. McGraw-Hill Professional, 2011.

[19] J. J. Lim *et al.*, "Design and simulation of next-generation high-power, high-brightness laser diodes," *IEEE J. Sel. Top. Quantum Electron.*, vol. 15, no. 3, pp. 993–1008, 2009.

[20] L. Lang, J. J. Lim, S. Sujecki, and E. C. Larkins, "Improvement of the beam quality of a broad-area diode laser using asymmetric feedback from an external cavity," *Opt. Quantum Electron.*, vol. 40, no. 14–15 SPEC. ISS., pp. 1097–1102, 2008.

[21] J. R. Leger, "Lateral mode control of an AlGaAs laser array in a Talbot cavity," *Appl. Phys. Lett.*, vol. 55, no. 4, pp. 334–336, 1989.

[22] S. Sujecki, L. Borruel, J. Wykes, P. Moreno, B. Sumpf, P. Sewell, H. Wenzel, T. M. Benson, G. Erbert, I. Esquivias, and E. C. Larkins, "Nonlinear properties of tapered laser cavities," *IEEE Journal of Selected Topics in Quantum Electronics*, vol. 9, no. 3. pp. 823–834, 2003.

[23] D. Botez, "Design considerations and analytical approximations for high continuous-wave power, broad-waveguide diode lasers," *Appl. Phys. Lett.*, vol. 74, no. 21, pp. 3102–3104, 1999.

[24] B. E. A. Saleh and M. C. Teich, *Fundamentals of Photonics*, 6th ed. JOHN WILEY & SONS, INC., 1991.

[25] J. V. Moloney, R. A. Indik, and C. Z. Ning, “Full space-time simulation for high-brightness semiconductor lasers,” *IEEE Photonics Technol. Lett.*, vol. 9, no. 6, pp. 731–733, 1997.

Chapter 2

# 2 High-brightness laser diodes and external cavity systems

High-power laser diodes first gained interest as pump sources for solid-state lasers, fibre amplifiers in telecommunications, and fibre lasers. With their compactness, low-cost, reliability and high efficiency, high-power diode lasers started to see more applications as direct-diode high-power sources, replacing other traditional sources such as diode-pumped solid state sources and carbon dioxide ($CO_2$) gas lasers [1]. In recent years, new markets have been opened by increases in the brightness of the laser diode sources and by advances in the optical systems for beam shaping and combining. The first markets that saw the use of high-power laser diodes, operating in the range of a few Watts, were marking and thermal printing [2]. Other applications, in a different average power range (100 W -1000 W), were welding and sheet metal cutting. These are still the most lucrative industrial laser markets, but they are also the most demanding in terms of brightness. Laser additive manufacturing processes, such as selective laser melting (SLM), are also quickly becoming a reality, producing hard metallic structures with high density that cannot be achieved by traditional means [3]. With the requirement of more detailed and small-size structures, SLM systems are contributing to the development of new manufacturing paradigms. With above mentioned applications driving the high-power laser market, the performance requirements are also becoming more demanding. Performance requirements for next-generation high brightness laser diodes include narrow spectral linewidth (< 1 nm), high beam quality (Q < 1.5 mm.mrad), high power conversion

efficiency (> 60 %)and high output power (10 W – 20 W). Figure 2.1 shows the beam product parameter and laser power requirements for different applications. A laser with a power of 20 W, $M^2$ ~ 20-30 and Q~5-9 mm.mrad (e.g. a good broad-area laser diode [4]) is suitable for printing and material processing, but not for additive manufacturing, welding or cutting. Conversely, a laser with a power of 10 W and $M^2$ < 1.5 (e.g. a good tapered laser diode [5]) is suitable for sheet metal drilling, marking, additive manufacturing, welding and cutting of metal. The requirements of the driving markets material processing and additive manufacturing are modules/systems with output powers between 100 W and 10 kW and an overall beam quality of < 30 mm.mrad. Accordingly, the individual laser diodes, making up these laser modules, should have high brightness (e.g. P ≥ 10 W, Q < 2 mm-mrad or $M^2$ < 5) and high-power conversion efficiency (e.g. PCE ≥ 60%). The sources and their performance (power and beam quality) should be reliable and insensitive to reflections.

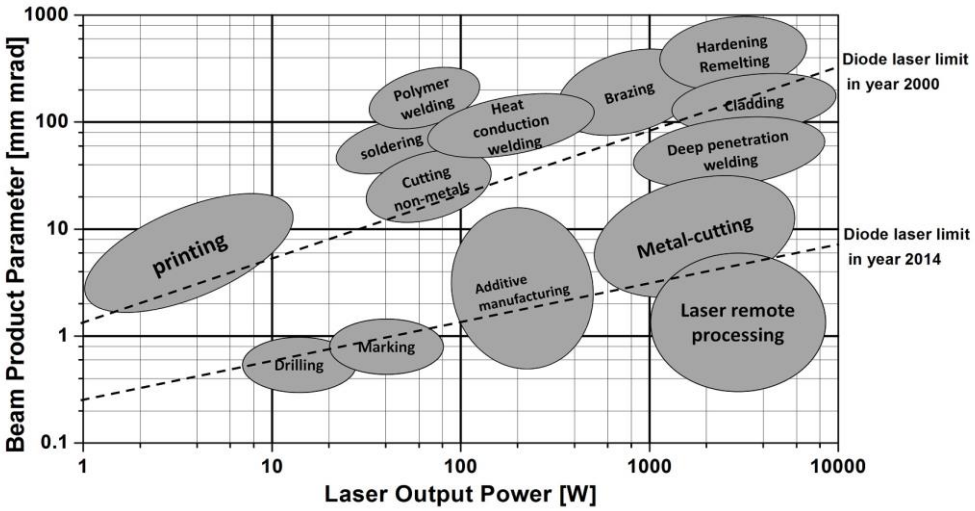



**Figure (2.1): Beam parameter product vs. laser power for different applications.**

With practical limitations to the maximum output power produced by an individual laser, direct diode laser systems for industrial applications combine the beams from many individual laser diodes (or diode arrays). The combined beams are

then coupled into an optical fibre for delivery to the target. The role of the optical system is to combine the individual beams without losing their brightness. High-power direct diode lasers rely on multiple beam combining methods, including incoherent beam combining, coherent beam combining and spectral beam combining (or wavelength beam combining). The first commercial kW-class direct diode laser system used an external cavity (Littrow cavity) to wavelength stabilise and spectrally combine the beams of a large number of broad area lasers to couple a 1 kW beam into a 200 μm fibre [6]. The brightness of the final system is ultimately limited by the brightness of the individual sources.

All beam combining techniques couple light back into the laser diodes – either deliberately, as in external wavelength stabilisation for spectral beam combining, or accidentally due to reflections off the optics. This optical feedback has been observed to affect both the beam quality and the degradation of the laser diodes [7]. Thus, as the power and performance requirements increase, the role of external optical feedback is becoming increasingly interesting.

This chapter reviews the various high-brightness laser diode structures, the employment of these structures in external systems and the types of feedback (intentional and unintentional) produced by these external systems. It also discusses the impact of unintentional feedback on laser diode performance and how vertical cavity design must take into account the external unintentional feedback.

## 2.1 Evolution of High-brightness laser diode sources

Different power, beam quality and efficiency requirements resulted in the high-power laser systems adopting different structures and diode geometries. State of the

art high-power lasers, for driving markets such as metal cutting and additive manufacturing, need large output power (100 W – 1000 W), high power conversion efficiency (PCE > 60%) and excellent beam quality (Q < 10 mm.mrad). A variety of laser diode structures, have been developed, which offer different performance characteristics. These include ridge waveguide (RW) lasers, slab-coupled optical waveguide lasers (SCOWL), broad-area (BA) lasers, narrow broad-area lasers (NBA) and tapered lasers.

### 2.1.1 Ridge waveguide lasers

Ridge waveguide lasers, with typical stripe widths of ≤ 4 μm, offer single mode operation, diffraction-limited beam quality and output powers in the range of few hundreds of milliwatts. Figure 2.2 shows the geometry of the ridge waveguide laser.

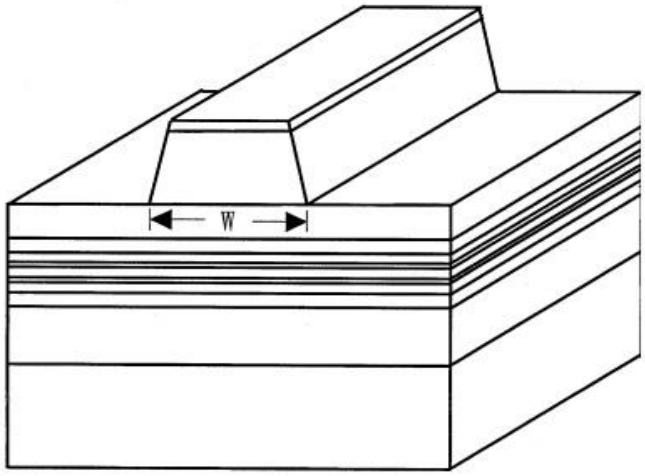



**Figure (2.2): Schematic of a typical ridge waveguide laser**

Ridge waveguide lasers have gained attention mainly as pump sources for telecommunications fibre amplifiers, e.g. the erbium doped fibre amplifier (EDFA)[8]–[10]. There have been many attempts to increase the laser chip power beyond the 100s of milliwatt range while maintaining excellent beam quality.

However, physical limitations, like high facet load (high power density at the facet) leading to COMD, have resulted in ridge waveguide lasers only managing to achieve reliable output powers of 1-1.6 W[11], [12].

Different techniques were proposed to increase the output power of ridge waveguide lasers, while maintaining single mode operation. The use of trenches next to the ridge, while increasing the ridge width, ensured that only complex fundamental mode existed, however, only powers of up to 2 W were achieved[13]. Flared ridge waveguide lasers have achieved a maximum power of 3 W and kink free power of 2.2 W[14]. Slab-coupled optical waveguide laser (SCOWL) diodes [15] use a shallower ridge waveguide etch to allow the beam profile to expand laterally in the "slab" below. They have been used as high-brightness sources for power scaling by spectral beam combining[16]. SCOWLs have good beam quality and low astigmatism, but their limitations are similar to those of the flared ridge waveguide laser and comparatively low power (2.8 W) [17]limits their single-emitter brightness.

### 2.1.2 Broad area lasers

A laser diode needs a large gain volume (energy reservoir) to achieve higher output powers. This can be most easily achieved by increasing the emitter width, which has the added benefit of lowering the power density at the facet – thereby increasing the catastrophic optical mirror damage (COMD) threshold. Broad area (BA) laser diodes are the simplest to fabricate, and are known to provide high power with high power conversion efficiency. Typical widths of the gain region in broad-area lasers can be as wide as 200μm. With this large gain medium, BA laser diodes have achieved powers of 29W, reliable operation at 20W and PCE (55%) at 20°C[18]. Figure 2.3 shows the schematic of a BA laser diode.

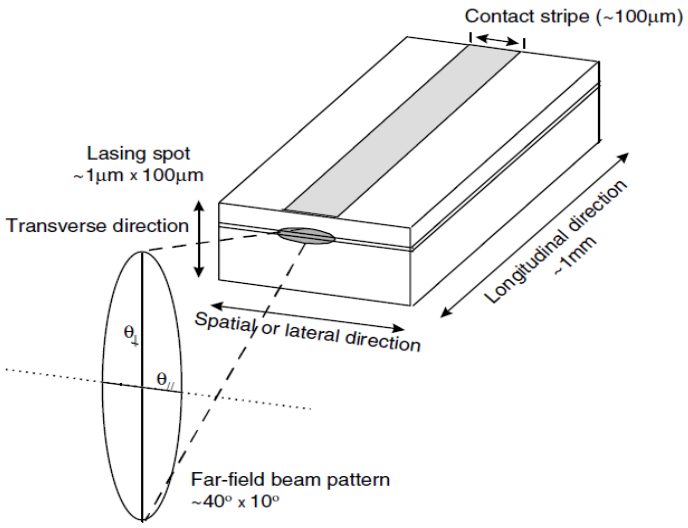



**Figure (2.3): Schematic of a typical broad-area laser [19]**

BA lasers have simultaneously achieved high power *and* high PCE at 300 K (14.5 W, PCE > 60%)[18], [20]. Their main limitation is their poor slow axis beam quality. With increased width, BA lasers should have a wide near-field but narrow far-field; i.e. narrow divergence. However, the increased width makes BA lasers support multiple lateral modes. Moreover, BA lasers suffer from near-field filaments, due to changes in carrier density affecting both the gain and refractive index seen by the propagating lateral field[21]. This all results in spatial-hole burning leading to self-focusing of the propagating beam within the laser. The self-focusing phenomenon eventually leads to the near-field to be broken into multi-lobes, limiting the ability for the output beam to be focused[22]. This has a significant impact on the beam quality; the typical beam quality of a BA laser is $M^2 \sim$ 20-30[23]. This poor beam quality limits the brightness of the BA lasers. Several techniques have been proposed to overcome the shortcomings of BA lasers. These include the use of external optical feedback (intentional feedback) to reinforce a specific lateral mode, by lowering its threshold. (This will be discussed in the external cavity systems section).

### 2.1.3 Narrow-stripe broad area lasers

J.J. Lim, *et al.* used laser simulations to investigate the dependence of the beam quality of broad area lasers on cavity length and width as a function of power[24]. Lim's work showed that the brightness of gain-guided broad area lasers improved with reduced cavity width and increased cavity length. It also showed that the modal discrimination of higher-order modes decreases with increasing current, thereby compromising the single-mode operation and lowering the beam quality. The simulations suggested that single mode operation can be achieved with an output power of 1.16 W and beam quality $M^2$=1.62 using a 16 μm wide and 2 mm long gain guided NBA laser. Lim's work established a new basis for the development of narrow-stripe broad area (NBA) laser diodes. Since then, NBA laser diodes have received increasing attention [24]–[26]. For example, by reducing the emitter width from 95 μm to 32 μm, NBA lasers produced output power of 7.5 W (contained in the fundamental mode), beam quality of $Q_{slow\ axis}$ = 1.8 mm-mrad and high efficiency (PCE = 57%)[26]. Despite their impressive performance, narrow broad area laser diodes still fall short of the desired performance for the most demanding applications

### 2.1.4 α-DFB lasers

α-DFB lasers are angled-grating lasers which allow for increased aperture sizes while maintaining good beam quality. A schematic representation of the device is shown in figure 2.4.

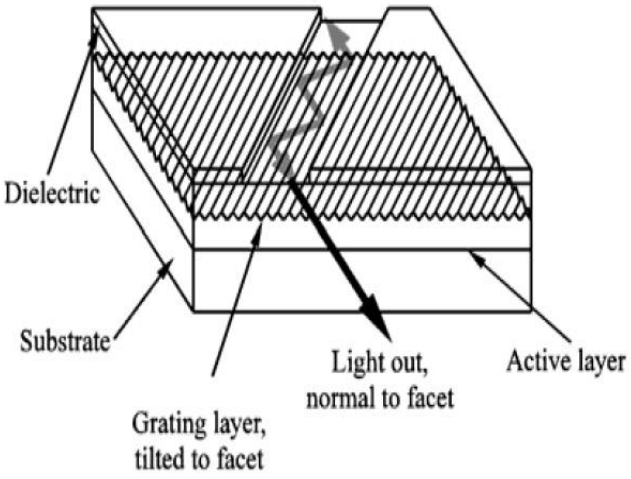



**Figure (2.4): Schematic diagram of a typical α-DFB laser.**

The α-DFB laser can be considered as a combination of DFB and Fabry-Perot (FP) lasers exhibiting DFB characteristics due to the evenly distributed grating and also FP cavity behaviour because the facets are required for resonance. Only modes which are almost normal to the facet will be coupled back into the cavity and hence produce an output beam with a very low divergence. For example, 1W diffraction limited output power has been achieved with a lateral divergence of only 0.2°[28]. Nevertheless, α-DFB lasers cannot achieve excellent beam quality at high power, and the excellent beam quality yielded by these lasers is limited to low powers. For example, the best beam quality reported was $M^2 = 3.2$ but at an output power of only 3 W[29]. Moreover, these lasers suffer from low electrical to optical conversion efficiency, kinky light-current characteristics at higher power [Wenzel et. al] and a complicated manufacturing process.

### 2.1.5 Master oscillator power amplifier (MOPA)

Semiconductor optical amplifiers have also been used to produce high brightness beams. Broad-area lasers which normally produce a multimode output as

oscillators have been used as optical amplifiers. Such broad-area stripes behave well as amplifiers, when antireflection coatings are applied at both ends and injected with a high-power, high-quality input beam. The input beam to these amplifiers must fully illuminate the broad input facet (width to height aspect ratio of ~ 400). The introduction of tapered stripe amplifiers with narrow input apertures relaxes the requirement of such high aspect ratio input beams and thus permits the use of diode lasers as the input source. The tapered amplifier is designed in such a way as to allow the input beam to diffract freely from the narrow input aperture to fill the gain region uniformly and propagate towards the large output facet. This uniformly diverging beam causes the output beam to be stable at higher output levels and reduces its susceptibility to self-focusing effects. Master oscillator power amplifiers (MOPAs) have been produced by monolithically integrating both laser diodes and tapered stripe amplifiers on the same device, as shown in figure 2.5. MOPAs have demonstrated high output powers, up to 7.4 W, while maintaining single longitudinal mode operation.

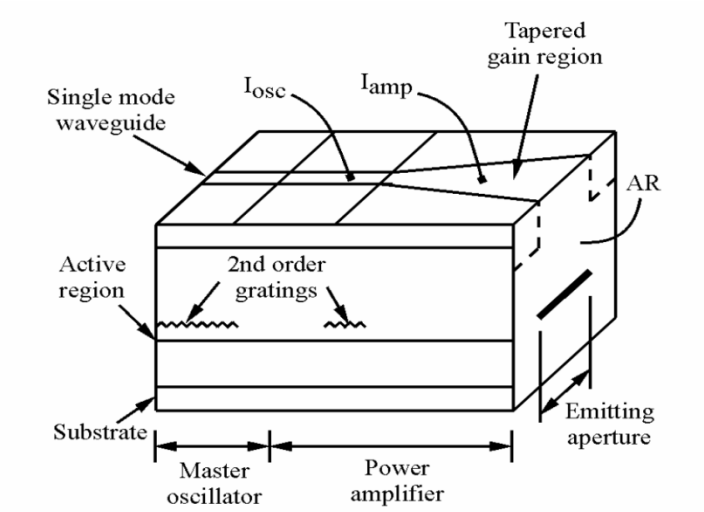



**Figure (2.5): Schematic of a typical MOPA laser.**

Although the MOPA has shown promise in producing single longitudinal and lateral mode operation, these structures are complex, non-compact and non-efficient[30].

### 2.1.6 Tapered lasers

Tapered lasers have a superior performance, compared to broad-area and ridge waveguide lasers, due to multiple factors inherent in their lateral design. Furthermore, the complexity of manufacturing tapered lasers is relatively low, compared with some other laser structures. Figure 2.4 shows the schematic diagram of a typical tapered laser diode.

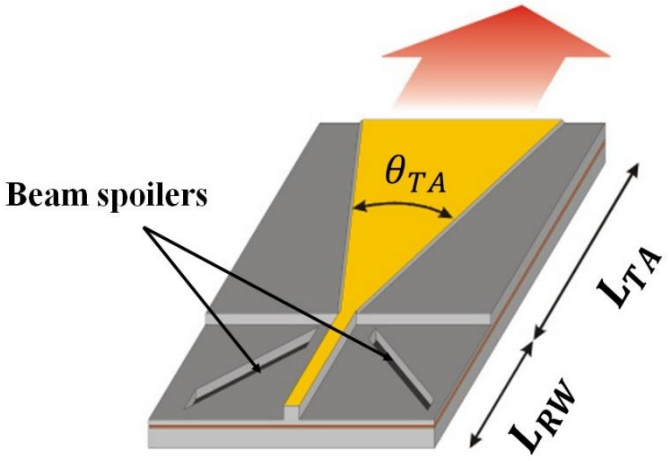



**Figure (2.6): Schematic diagram of a typical tapered laser. $L_{RW}$ is the length of the RW section while $L_{TA}$ is the length of the taper section. $\theta_{TA}$ is the taper angle.**

The RW section acts as a lateral spatial mode filter, filtering out higher-order lateral modes. The tapered gain section acts as an amplifier of the lateral mode, excited in the RW. Thus, tapered lasers are able to produce a high output power (12W) with high beam quality ($M^2 < 1.2$) and exceptional brightness (B = 1.1 $GWcm^{-2}sr^{-1}$)[31]–[33]. However, this comes at the expense of lower power conversion efficiency (43% - 55%) – as compared to PCE values achieved by BA lasers (65% - 80%) [34], [35]-

and power dependent “wandering” astigmatism[5], [36]. Nonetheless, considering all of the above factors, the tapered laser remains a very strong candidate for high-brightness direct diode laser systems.

The lateral design of the tapered laser allows designers to optimise the device performance. Firstly, the width and the length of the RW section have a direct impact on the modal filtering performance. Secondly, the length and the angle of the taper section ensures that the single lateral mode excited in the RW section is allowed to expand gradually while being amplified, thereby, minimising spatial hole-burning and filamentation. In particular, the taper angle must match the diffraction angle from the RW aperture, to enhance the higher-order modes filtering. Proper optimisation of these factors leads to brightness levels that cannot be achieved by most other laser diode structures.

Tapered lasers are still sensitive to filamentations, but there are other parameters that can be optimised to minimise the filamentation, such as the front facet reflectivity. The front facet reflectivity determines the intensity of the internally reflected fields. With high front facet reflectivity, reflected fields that are filtered by the RW propagate in the regions adjacent to the RW. This leads to optical pumping of these regions leaving them transparent, which leads to reduced filtering performance of the RW section[37]. When these reflected fields couple into the taper section they to excitation of higher order lateral modes, which eventually leads to the formation of filaments. Thus, optimising the front facet reflectivity can help to minimise the filamentation.

Versatility of the tapered lasers also comes in the form of split contacts for the RW and taper section. This capability makes the tapered lasers attractive for

applications that require high modulation efficiency ($^{dP}/_{dI}\ W/A$), such as wireless optical communications. By modulating the RW current and fixing the taper current, higher modulation efficiencies can be achieved[38]. Split contacts are also good for optimising the RW filtering performance (this is discussed in chapter 4).

There have been different attempts to enhance the modal filtering performance of tapered lasers, and hence, the beam quality, such as using a DBR and beam spoilers[39]. It was shown that using an AR coating ($R_b = 0.01\%$) on the back facet while using a DBR at the back side of the RW, has a significant impact on both the laser spectrum and RW filtering performance. This will be explored further in chapter 4. The main issue affecting the beam quality in tapered lasers is the back-propagating field in the absorbing regions, adjacent to the RW. These fields bleach the absorption in these regions, making them transparent. This gives the fields reflected from the HR back facet the ability to propagate forward and couple back into the taper section and excite higher-order lateral modes. With an AR coating on the back facet, these back-propagating fields are allowed to leave the structure. Also, the use of beam spoilers can block the back-propagating fields from entering the RW section. Nevertheless, at high bias (> 2.5 times the threshold current [5]), even the beam quality of DBR tapered lasers degrades, which is further investigated and analysed in chapter 4. The main challenges remaining for tapered lasers are to control the beam quality degradation at high power and to understand the role of optical feedback, internal or external.

## 2.2 Vertical cavity design for operation in external cavity

The vertical cavity design of a laser diode for efficient, high-power operation in an external cavity is more complicated than that of an isolated high-power laser diode.

Firstly, a wide vertical mode profile (vertical near-field pattern) is needed for efficient external cavity coupling and reduced alignment tolerance. This also increases the tolerance to "smile" (a bend in the horizontal axis of a laser bar which introduces pointing errors in the slow-axis) across a laser array and thereby, allowing the use of simpler, less costly optics. Secondly, the excitation and lasing of higher order vertical cavity modes by external optical feedback must be suppressed. Thirdly, a narrow vertical far-field divergence is needed to minimise the impact of optical aberrations, thereby improving the cost and performance of the optical system. Finally, the need for high power conversion efficiency means that Joule heating and free-carrier absorption must be taken into account during the vertical cavity design[40].

High brightness laser diodes typically use large optical cavity (LOC) waveguides to produce a wide vertical near field pattern and a narrow far-field divergence pattern. The LOC cavity reduces the power density at the facet, increasing the mirror damage threshold, and reducing the vertical confinement factor. The reduced confinement factor leads to less overlap of the optical mode with the active region and hence, reduced variation of the optical index (carrier-induced lensing) due to spatial-hole burning (SHB). The confinement factor is the ratio of modal power contained in the active area to that contained in the structure. The definition of the vertical confinement factor is:

$$\Gamma(y) = \frac{\int_{-d/2}^{+d/2} E(y)^2 \, dy}{\int_{-\infty}^{+\infty} E(y)^2 \; dy} \tag{2.1}$$

The LOC waveguide also facilitates external cavity feedback (e.g. for wavelength stabilisation and/or lateral mode filtering), but also makes the device more sensitive to parasitic reflections.

Further increases in waveguide thickness raise the Joule heating and free carrier absorption losses, but do not significantly increase the near field width or reduce the far-field divergence. Wider near field patterns can be achieved (with thinner, more efficient waveguides) using other methods. These include: low-index quantum barriers to reduce the index contrast between the active region and the waveguide[41]; or high-index optical traps to draw the field profile out into the waveguide [42].

LOC waveguides support multiple vertical modes, but, in the absence of external feedback, lasing is limited to the mode that reaches threshold first. When operated in a system with external feedback, however, back coupling to higher-order modes can cause these modes to lase. Even if the higher order modes do not lase, the additional stimulated emission and free-carrier absorption can reduce the laser's efficiency and increase self-heating. External feedback also affects the reliability of high-power laser diodes[43]. Thus, the impact of feedback is becoming increasingly important as diode laser systems grow in power and complexity.

The suppression of higher order vertical modes becomes more challenging when the laser is operated in an external cavity, where the optical feedback also excites the higher-order vertical modes. Firstly, as little power as possible must couple into the higher order vertical modes. Secondly, the higher-order vertical modes must be prevented from reaching threshold. This can be achieved by engineering the laser cavity to make the confinement factors of higher-order modes much lower than that of the fundamental mode, so that their modal gain is lower. Accordingly, we define a new figure of merit for modal discrimination (MD):

$$MD = \Gamma(1) / \Gamma(n) \tag{2.2}$$

where $\Gamma$ is the optical confinement factor and n refers to the higher-order mode with the largest confinement factor. $MD_n$ can also be used to describe the modal discrimination of a particular mode $n$. (*Note:* Propagation loss is neglected in MD, as it depends on the doping profile and operating bias – which are usually optimised *after* the initial cavity design.)

Power from the external cavity can be coupled into the higher-order modes, even if they do not reach threshold. The modal gain of the higher-order modes can also be reduced by increasing their propagation loss - either by free-carrier absorption or by substrate leakage. Damping of the higher-order vertical modes also reduces the total amplified spontaneous emission (ASE) from these parasitic modes. ASE and gain of light coupled into these modes do not contribute to the fundamental mode. Instead, they act as current leakage paths, contributing to self-heating and reducing the power conversion efficiency.

LOC laser structures based on both the low index quantum barrier and the high-index optical trap approaches were optimised (optically and electrically) for operation with external optical feedback[40].

The tapered laser in this thesis is based the ELoD2 vertical cavity with low-index quantum barriers[44]. This structure supports eight vertical modes, as shown in figure 2.8. Their confinement factors and modal discrimination values are given in Table 2.1.

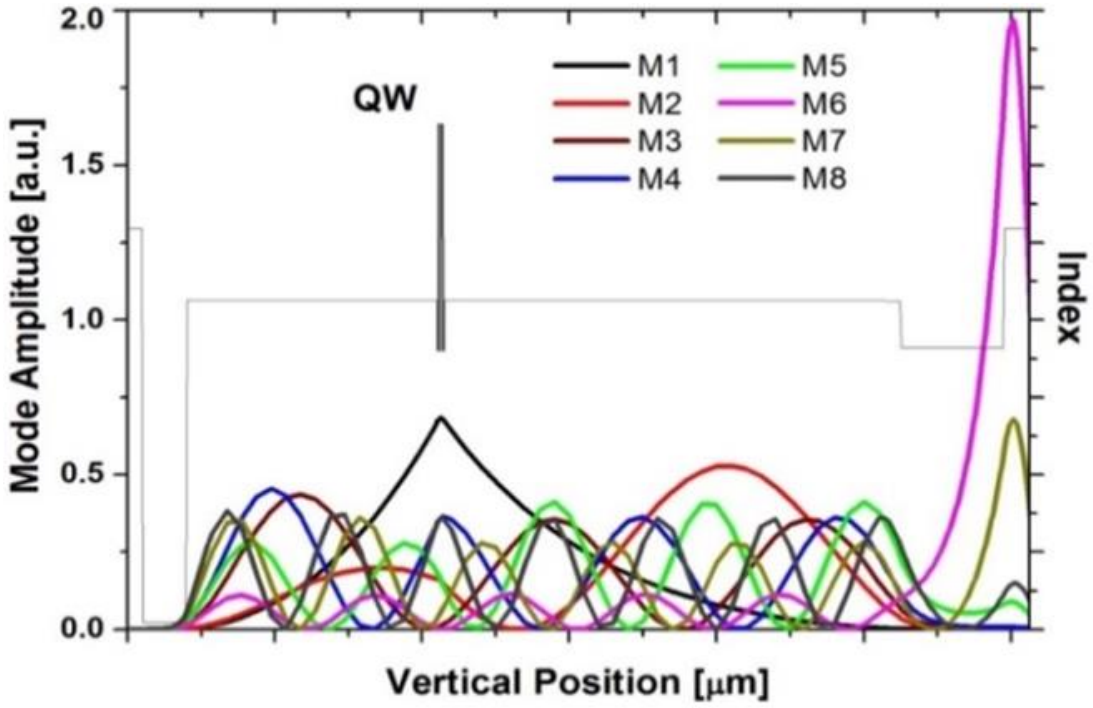



**Figure (2.8): Vertical mode profiles in the ELoD2 LOC laser structure.**

| Mode Number | Confinement Factor (Γ) | Modal Discrimination (MD) |
|---|---|---|
| 1 | 0.0163 | 1 |
| 2 | 0.00376 | 4.33 |
| 3 | 0.000282 | 57.72 |
| 4 | 0.00856 | 1.90 |
| 5 | 0.00390 | 4.17 |
| 6 | 1.090E-05 | 1491.39 |
| 7 | 0.00130 | 12.58 |
| 8 | 0.00424 | 1.92 |

**Table (2.1): Confinement factors and modal discrimination values of all vertical modes in ELoD2 LOC laser structure.**

## 2.3 High-power laser systems and beam combination techniques

The output power of the state-of-the-art high power laser diodes has reached significant levels. The highest power level obtained from a single emitter, reported in the literature, is 29 W from a broad area laser and a reliable operating power level at 21 W[18]. Nevertheless, the beam quality of broad area lasers is poor, and while other laser structures can provide a good beam quality, such as tapered lasers ($M^2_{2nd\ moment} = 1.9$ at P = 1 W [5]), their beam quality degrades at higher power ($M^2_{2nd\ moment} = 14.5$ at P = 10 W [5]). Moreover, there are constraints to increasing the power from a single emitter such as COMD. However, with recent advances in high power laser diode technologies, highly efficient laser diodes (> 70%[20]) with excellent beam quality at low power are becoming available. Thus, an alternative approach to building high-brightness lasers is to use arrays of these relatively lower power laser diodes, in which, the beams from the array elements are combined while maintaining the propagation characteristics of a single beam. The brightness of the combined beams (units = $Wcm^{-2}sr^{-1}$) depends on the brightness of the individual diode sources.

There are many beam-combining techniques, but they mostly fall within three broad categories: incoherent beam combining (IBC), coherent beam combining (CBC) and wavelength beam combining (WBC). In principle, using these techniques it is possible to scale up the brightness by large amounts by increasing the number emitters. The external optics found in IBC systems are mainly to collimate, shape and focus the output beams of the individual elements to fill the delivery fibre aperture. In WBC and

CBC systems, however, the external cavity optics serve two goals. The first goal is to combine the output beams of the individual laser sources. The second goal is to overcome the deficiencies of the individual sources, so that the brightness of their combined output beam is conserved while output power is scaled up, i.e. laser diodes need spectral control and/or mutual coherence preservation.

In IBC, multiple lasers are placed side by side and their output beams are spatially arranged so that they all couple into a multimode fibre. Figure 2.9 shows an example of an IBC for combining the beams of 4 laser diodes.

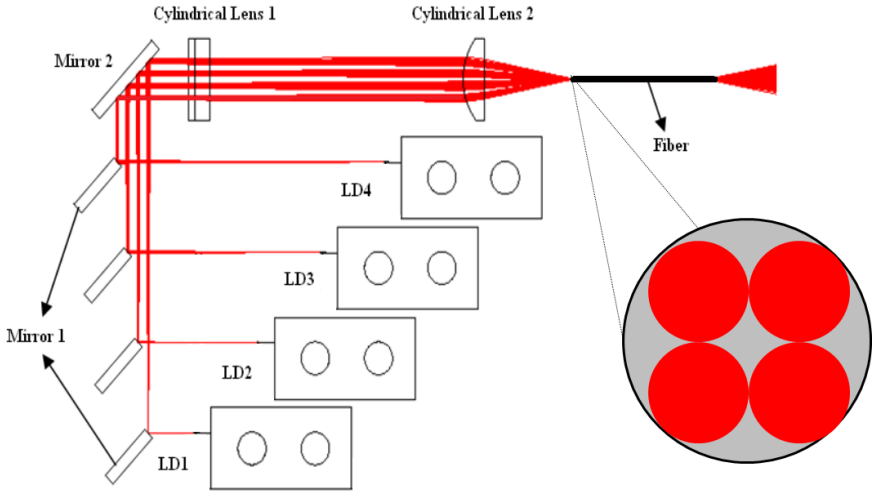



**Figure (2.9): Typical setup of incoherent beam combining system for 4 laser diodes, adapted from [45].**

The simplicity of this technique comes from the fact that the laser elements do not require any control of their spectra or phases. The total output power can be simply increased by increasing the number of elements, however, the total brightness decreases as the number of emitters increases. This is because adding more elements will increase the aperture size without a corresponding decrease in the total beam divergence angle. In other words, the brightness of the IBC system cannot be greater than that of the individual elements. For this reason, studying the impact of

unintentional feedback is important, as will be seen in this work; this feedback degrades the beam quality of individual laser diodes and hence their brightness, leading to decreased brightness of the whole system.

In WBC, the array elements operate at different wavelengths and a dispersive optical system is used to overlap the different wavelengths spatially. Typical dispersive optical systems use gratings, prisms, or wavelength-selective reflectors. This is equivalent to what is done in wavelength division multiplexing for optical communications. The differences here are that the goal is higher power, and, therefore, the efficiency is more important. For example, TeraDiode succeeded in producing a 2 kW laser system with beam quality, from the delivery fibre, of Q = 3.75 mm.mrad, using wavelength beam combining (WBC) technique [46]. These ultra-high brightness laser systems would not be possible without the use of external cavity optics. Figure 2.10 shows an example of WBC module.

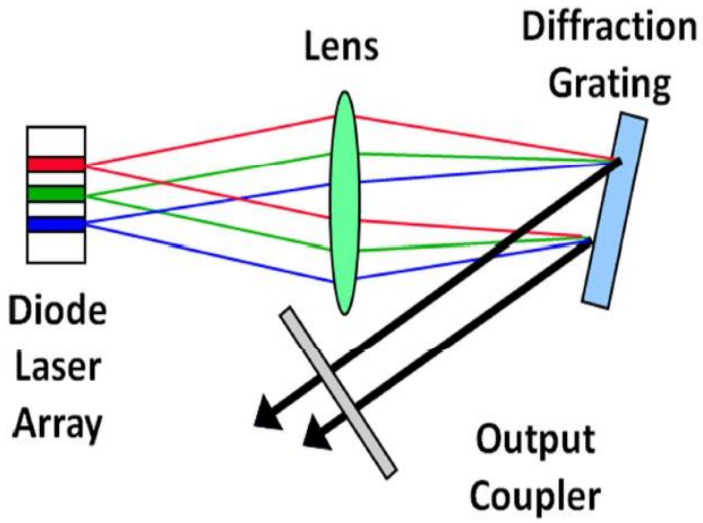



**Figure (2.10): Schematic of a typical WBC module [46].**

In CBC, the output beams of the different elements are forced to operate with same frequency and the same phase. In this case, when the beams are spatially overlapped the respective electric fields add up coherently to provide constructive

interference. In these systems, in order to coherently add the input beam powers of the emitters to produce the output beam of the system, the input beams need to have the same phase, the same polarisation and their powers must be identical in order to achieve constructive interference. Moreover, the beams must overlap in the near-field and the far-field planes. Different implementations of CBC systems have been reported in the literature: active feedback, leaky-wave coupling, self-organising (the super mode approach) and common resonator[47].

In the common resonator approach, the different elements are placed inside the common resonator and the feedback from the resonator is used to force all of the elements to the lowest-order transverse mode operation. This mode selection using feedback from a resonator has been done using the Talbot effect, which is explained in the next section.

In the self-organising approach, the elements within the array have different optical path lengths and the optical spectrum adjusts itself to minimise the loss of the array. This approach is essentially the Michelson interferometric resonator generalised for multiple emitters rather than just two. The use of a Michelson interferometer to phase-lock and coherently combine the beams of two tapered lasers has been reported in the literature[48]. The obtained output power was 4.2 W.

## 2.4 Role of intentional feedback in external cavity lasers and systems

High-power broad area laser diodes are multi-mode lasers, which oscillate in a multiple mode, lateral and longitudinal. The multiple lateral mode operation leads to

poor beam quality, and hence, poor spatial brightness. The multiple longitudinal modes, spanning a wide range of frequencies, lead to poor spectral brightness. These poor output characteristics limit the performance of these devices. For example, with poor beam quality, these devices cannot be used in high-brightness systems used in applications such as metal cutting and additive manufacturing. Also, the spectra of these devices are typically 3-6 nm wide, at full-width half-maximum (FWHM) and vary with temperature (at a rate of 0.3 nm/°C[1]) and driving current. This makes these devices not suitable for wavelength sensitive applications, such as pumping solid-state lasers, like alkali vapour lasers (e.g. rubidium and cesium) which require pumping line width of 10 GHz[49]. Their poor spectral brightness also make these devices unusable for dense wavelength beam combining, in which the spectral spacing between individual beams is in the order of 3nm[50]. Several techniques, such as the use of asymmetric and symmetric feedback utilising mirrors, have been developed to enhance the beam quality of broad area lasers[51]–[55]. Wavelength locking techniques were developed to enhance the spectral line width using the feedback from external diffraction gratings[56], [57].

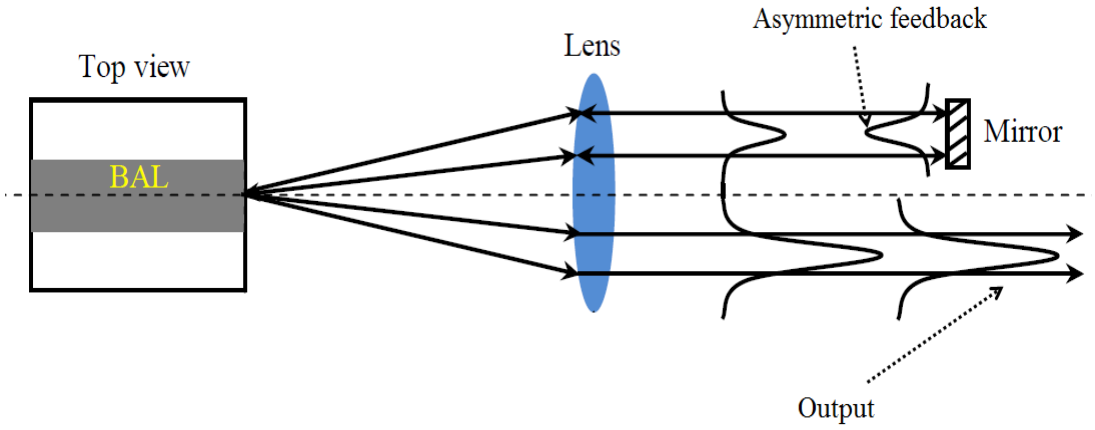



**Figure (2.11): Schematic of broad-area laser with asymmetric feedback**

Figure 2.11 shows the schematic diagram of a broad-area laser with asymmetric

feedback.

Broad area lasers produce a multi-lobed far-field pattern, which is attributed to the multi-lateral mode operation. The asymmetric feedback method relies on reflecting part of the output beam back into the laser so that only one lateral mode is selected. Higher-order lateral modes produce double lobed far-field profiles, which is in agreement with Fourier transform of these higher-order modes. By carefully selecting the position and the width of the mirror a single lobe, belonging to a specific lateral mode, is reflected. This leads to reinforcement of that lateral mode and hence, increasing the modal discrimination relative to other lateral modes. The result is a single lobed output beam with an enhanced beam quality. Lang *et al.* [52] used this asymmetric feedback method to enhance the beam quality of a 100 µm wide broad area laser emitting at 975 nm and reduce the beam propagating factor $M^2$ from $M^2$ = 30 (for a free running laser) to $M^2 = 2.69$. Other techniques involve the use of two mirrors, with reflectivity of 80%, to provide a symmetric feedback. This way, the obtained output beam is symmetric and the reported enhancement of beam, quality is from $M^2$ = 42 to $M^2$ = 3.3[51]. Also, Thestrup *et. al.* demonstrated the use of asymmetric feedback to enhance the beam quality of two polarisation coupled broad area lasers (with $M^2$ values of 29 and 34) to obtain a single beam with a beam quality of $M^2 = 1.6$[54].

Another example of the use of intentional feedback to improve the laser performance is wavelength locking using feedback from a diffraction grating to reduce the output bandwidth of a diode laser. Wavelength locking (or wavelength stabilisation) of laser diodes can be done either internally, using a DBR integrated into the laser chip, or externally using a volume Bragg grating (VBG). External wavelength locking can be achieved by placing the grating at an angle and utilising the first order

diffracted beam as feedback to the laser while using the zeroth order diffracted beam as the output. The tuning is achieved by rotating the grating, i.e. changing the angle. This setup is called the Littrow cavity. Figure 2.12 shows a typical schematic diagram of a Littrow cavity.

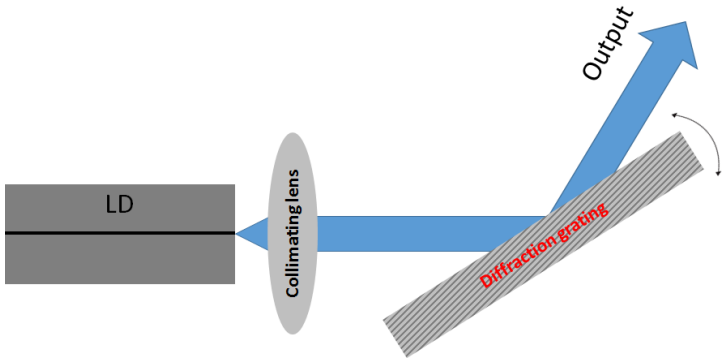



**Figure (2.12): A schematic diagram of the Littrow cavity configuration**

The Littrow cavity configuration has been used to narrow the output bandwidth and lock the laser into a specific wavelength from a wide tunable range of wavelengths. For example, Chann *et al.* succeeded in narrowing the bandwidth of a laser array of broad area lasers, from 670 GHz (1.4 nm) down to 120 GHz (0.3 nm) [58]. Arnold *et al.* on the other hand, developed a Littrow cavity that provides 20 nm of tuning range for a diode laser[59]. Other Littrow configurations succeeded in narrowing the bandwidth of broad area lasers from 2 nm to 0.03 nm[60].

The Littrow cavity configuration can also be used for wavelength beam combining applications. In this case, the grating is used to lock the different emitters in a bar to different wavelengths simultaneously. Figure 2.10, in the previous section, shows a typical configuration of a WBC module using Littrow cavity configuration.

There is another external cavity configuration that utilises the diffraction grating to enhance the spectral properties of lasers. In this configuration the zeroth order reflection, from a mirror, is used as an output. This configuration is called the

Littman cavity which is depicted in figure 2.13. In this configuration, tuning is achieved by rotating the mirror. With this configuration, the bandwidth of laser diodes can be narrowed to 0.07 nm[56] and achieve a tuning range greater than 20 nm[61].

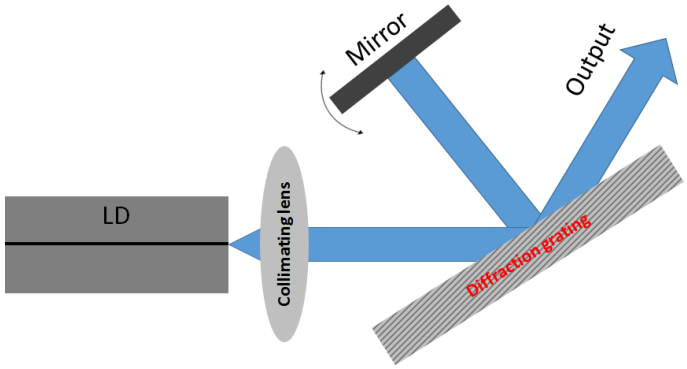



**Figure (2.13): A schematic diagram of the Littman cavity configuration**

Intentional feedback is not always used to enhance laser diodes properties. In specific applications, intentional feedback is used to change the properties of multiple lasers and make them all synchronise. In CBC applications, the beam of individual laser emitters in a laser bar are added coherently, requiring all the emitters to be phase-locked to achieve constructive interference. A popular phase locking technique is the use of a Talbot cavity[62], which relies on external cavity optics to provide intentional feedback so that all emitters in the laser bar are in phase. A typical phase locking of a laser array configuration, based on a Talbot cavity, is shown in figure 2.14.

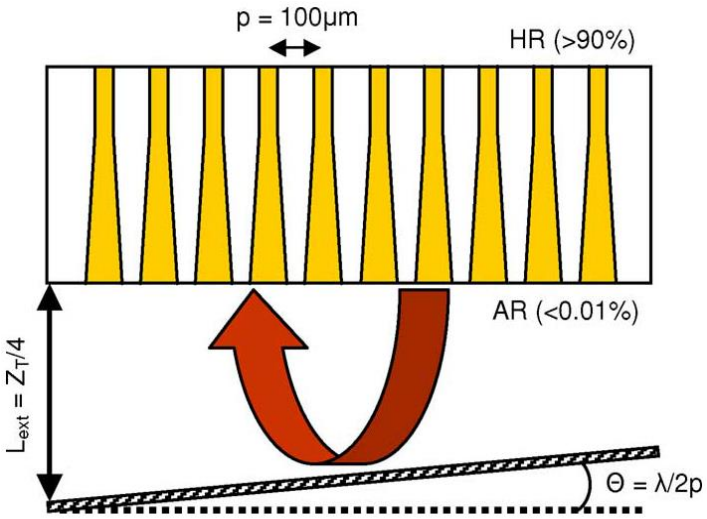



**Figure (2.14): Schematic diagram of a Talbot cavity.**

In this case, phase-locking is achieved using the Talbot effect, where the out-of-phase mode is self-imaged and the in-phase mode is imaged with a lateral shift of p/2 (where p is the emitter pitch) after traveling half the Talbot distance (ZT = 2p2/λ). By placing a mirror in an external cavity at a distance ZT /4 with a tilt of λ/2p, the in-phase mode is self-imaged while the out-of-phase mode is laterally displaced by p/2. This increases the modal discrimination between the in-phase and out-of-phase modes, thus phase-locking the emitters in the in-phase mode. The challenge is to lock as many emitters in phase to produce a coherently combined beam with significant power. Different groups have reported different output power levels achieved by CBC using the Talbot cavity. Waarts *et. al.* showed that, using a Talbot cavity, the coherently combined beams of 20 laser diodes reached a power level of 900mW[63]. Paboeuf *et al.* on the other hand, achieved a power of 1.7 W through coherently combining the beams of 10 tapered lasers using the Talbot cavity, where a diffraction grating was used as a wavelength stabiliser, a mirror and an output coupler[64].

## 2.5 Impact of unintentional feedback on laser performance

The initial performance evaluation of high-brightness laser diodes is usually carried out without considering the feedback from an external optical system. In practice, as seen from the previous section, they are almost always part of a larger optical system. Whether the external cavity optics provide intentional feedback or are just used to collimate, shape and focus the output beam, they all can introduce unintentional optical feedback, in the form of parasitic reflections off the optics. As the output power of laser diodes continues to increase, even small amounts of unintentional feedback can affect the performance and even the degradation/failure of the laser. Furthermore, large optical cavity (LOC) structures are commonly used in high-power laser diodes to reduce the vertical far-field divergence and simplify optical coupling. These LOC structures support multiple vertical modes, but (in the absence of external feedback) lasing is limited to the mode which reaches threshold first (usually the fundamental mode). When operated in a system with external feedback, however, back coupling to higher-order modes can cause them to lase. Even if the external feedback does not allow these modes to reach threshold, the additional simulated emission, free-carrier absorption processes can reduce the laser's efficiency and cause self-heating.

Unintentional feedback was first studied by Lang and Kobayashi in 1980[65]. They showed that external feedback has an impact on the emission properties of the laser making it multi-stable causing the gain spectrum peak to blue or red shift, depending on the length of the laser cavity, the injection current and the feedback strength. Recently, unintentional feedback has become an important issue, as even small levels of feedback can change the laser performance in different ways such as

reduction of threshold current, reduction of optical output power and emission kinetics, not to mention irreversible effects such as COMD. Different studies have investigated the impact of unintentional feedback on high-power lasers[66]–[70].

Hempel *et al.*[68] studied and quantified the impact of external feedback on the gradual degradation of 808 nm AlGaAs broad area lasers. They showed that with 25% external optical feedback, the output power degradation rate is double that of stand-alone devices after 200 hours of operation. This degradation was due to point defects, observed in the cladding layers 5-20 nm from the facet along the longitudinal axis. These point defects were caused by the absorption of external optical feedback in high Al-content ($Al_{0.45}$ $Ga_{0.55}$ As) at 808 nm. Leonhäuser *et al.*[67] did a similar study, but on 976 nm GaAs-based broad area lasers. Their results showed no point defects in any of the laser structure layers. This reveals different absorption behaviour in broad area lasers operated under feedback, emitting at 808 nm and 976 nm. At 976 nm, the reflected optical power absorbed in the substrate was spread along the cavity length, since the absorption coefficient for the GaAs material is ~ 5 $cm^{-1}$[71]. The situation is different for 808 nm lasers where the substrate absorption is 10,000 $cm^{-1}$. This spread absorption of external feedback leads to gradual degradation of the device.

External optical feedback in high-power lasers can also be responsible for complete device failure by COMD. The constructive interference between the internally reflected and the externally coupled optical fields accounts for high density peaks at the front facet. For modelling purposes, this shows the importance of tracking the phases of the fields propagating in the external system in order to ensure the coherent addition of externally coupled and internally reflected fields, as discussed in chapter 3. If these high energy peaks exceed the COMD threshold even for few

nanoseconds, this will lead to facet damage[66]. These high intensity peaks are caused by the filaments in the near-field developed in high-power lasers exposed to external feedback. High intensity filaments observed in the near-field come as a result of the non-uniform index distribution due to nonlinear effects such as Kerr effect and Joule heating[72]. When the intensity of the fields propagating through the active medium is perturbed, the parts of the wave front with high intensity will cause a higher stimulated emission rate, leading to a localised reduction in the carrier density in these areas and hence, higher refractive index. Optical fields passing through a non-uniform index will experience a different phase velocity in different regions leading to the formation of the filaments in the near field profile. The intensity of these filaments was found to increase with external feedback[66]. Figure 2.9 shows a comparison between two near-field profiles for two broad-area lasers, emitting at 976 nm and with a front facet reflectivity 1%, one with external feedback (exposed to optical feedback strength of 4%) and the other without.

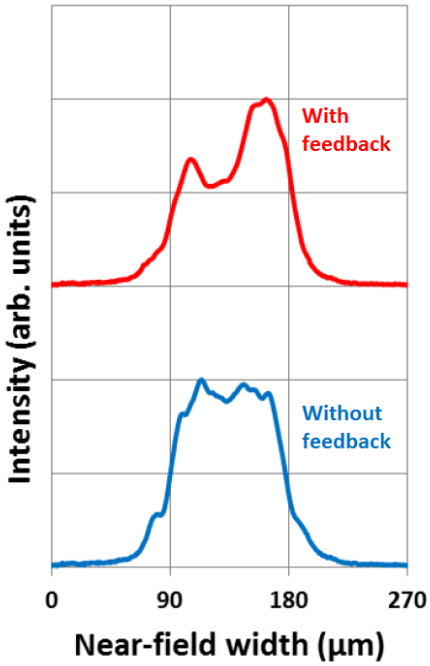



**Figure (2.15): Near-field profiles of broad-area laser with and without feedback [66].**

Figure 2.15 shows the presence of two filaments in the case of external feedback, while the in the stand-alone case, the near-field profile has a top-hat shape. A comparison of simulated near-field profiles is also presented in chapter 5 for two cases with and without feedback. The simulated results agree with the experimental results in figure 2.9. These filaments are responsible for local high intensity peaks at the facet. When these local high intensity peaks are present in the near field, they act as a precursor to COMD and thus, the failure of the device[66], [69].

Unintentional feedback can also lead to reduction of threshold current and power conversion efficiency [73] which agrees with the results presented in chapter 5. The reduction of PCE and threshold current is can be attributed to the increased effective front facet reflectivity. However, in chapter 5, the simulated results confirm that the excitation/lasing of higher-order modes contribute significantly to PCE reduction.

## 2.6 References

[1] H. I. and G. D. Goodno, *High Power Laser Handbook*. McGraw-Hill Professional, 2011.

[2] D. F. Welch, "A brief history of high-power semiconductor lasers," *Selected Topics in Quantum Electronics, IEEE Journal of*, vol. 6, no. 6. pp. 1470–1477, 2000.

[3] F. Abe, K. Osakada, M. Shiomi, K. Uematsu, and M. Matsumoto, "The manufacturing of hard tools from metallic powders by selective laser melting," *J. Mater. Process. Technol.*, vol. 111, no. 1–3, pp. 210–213, 2001.

[4] R. J. Lang, K. Dzurko, A. A. Hardy, S. Demars, A. Schoenfelder, and D. F. Welch, "Theory of grating-confined broad-area lasers," *Quantum Electronics, IEEE Journal of*, vol. 34, no. 11. pp. 2196–2210, 1998.

[5] C. Fiebig, G. Blume, C. Kaspari, D. Feise, J. Fricke, M. Matalla, W. John, H. Wenzel, K. Paschke, and G. Erbert, "12W high-brightness single-frequency DBR tapered diode laser," *Electronics Letters*, vol. 44, no. 21. pp. 1253–1255, 2008.

[6] R. K. Huang, B. Chann, and J. D. Glenn, "Extremely high-brightness kW-class fiber coupled diode lasers with wavelength stabilization," *Proc. SPIE*, vol. 8039, p. 80390N–80390N–10, 2011.

[7] M. Hempel, M. Chi, P. M. Petersen, U. Zeimer, and J. W. Tomm, "How does external feedback cause AlGaAs-based diode lasers to degrade?," *Applied Physics Letters*, vol. 102, no. 2. pp. 23502–23504, 2013.

[8] K. Shigihara, K. Kawasaki, Y. Yoshida, S. Yamamura, T. Yagi, and E. Omura, "High-power 980-nm ridge waveguide laser diodes including an

asymmetrically expanded optical field normal to the active layer," *IEEE J. Quantum Electron.*, vol. 38, no. 8, pp. 1081–1088, 2002.

[9] H.-U. Pfeiffer, S. Arlt, M. Jacob, C. S. Harder, I. D. Jung, F. Wilson, T. Oldroyd, and T. E. D.-S. Hext A., "Reliability of 980 nm pump lasers for submarine, long-haul terrestrial, and low-cost metro applications," in *Optical Fiber Communications Conference*, 2002, vol. 70, p. ThN4.

[10] D. Crawford, M. McElhinney, R. McGowan, P. Thiagarajan, J. Cahill, S. Nelson, S. Olson, P. Pedersen, and C. Lennon, "Design and performance of 980 nm pump laser modules exhibiting greater than 400 mW kink-free fiber-coupled power," *Optical Fiber Communication Conference and Exhibit*. pp. 482–483, 2002.

[11] G. Yang, G. M. Smith, M. K. Davis, D. A. S. Loeber, M. Hu, C. Zah, and R. Bhat, "Highly reliable high-power 980-nm pump laser," *IEEE Photonics Technology Letters*, vol. 16, no. 11. pp. 2403–2405, 2004.

[12] H. Wenzel, K. Häusler, G. Blume, J. Fricke, M. Spreemann, M. Zorn, and G. Erbert, "High-power 808 nm ridge-waveguide diode lasers with very small divergence, wavelength-stabilized by an external volume Bragg grating," *Opt. Lett.*, vol. 34, no. 11, pp. 1627–1629, 2009.

[13] H. Wenzel, F. Bugge, M. Dallmer, F. Dittmar, J. Fricke, K. H. Hasler, and G. Erbert, "Fundamental-Lateral Mode Stabilized High-Power Ridge-Waveguide Lasers With a Low Beam Divergence," *IEEE Photonics Technology Letters*, vol. 20, no. 3. pp. 214–216, 2008.

[14] B. Sverdlov, H.-U. Pfeiffer, E. Zibik, S. Mohrdiek, T. Pliska, M. Agresti, and N. Lichtenstein, "Optimization of fiber coupling in ultra-high power pump modules at λ = 980 nm," vol. 8605, p. 860508, 2013.

[15] J. P. Donnelly, R. K. Huang, J. N. Walpole, L. J. Missaggia, C. T. Harris, J. J. Plant, R. J. Bailey, D. E. Mull, W. D. Goodhue, and G. W. Turner, "AlGaAs-InGaAs slab-coupled optical waveguide lasers," *IEEE J. Quantum Electron.*, vol. 39, no. 2, pp. 289–298, 2003.

[16] R. K. Huang, B. Chann, L. J. Missaggia, S. J. Augst, M. K. Connors, G. W. Turner, A. Sanchez-Rubio, J. P. Donnelly, J. L. Hostetler, C. Miester, and F. Dorsch, "Coherent Combination of Slab-Coupled Optical Waveguide Lasers Robin," *Proc. SPIE*, vol. 7230, p. 72301G–72301G–12, 2009.

[17] R. K. Huang, J. P. Donnelly, L. J. Missaggia, C. T. Harris, B. Chann, A. K. Goyal, A. Sanchez-Rubio, T. Y. Fan, and G. W. Turner, "High-brightness slab-coupled optical waveguide lasers," 2007, vol. 6485, p. 64850F–64850F–9.

[18] P. Crump, G. Blume, K. Paschke, R. Staske, A. Pietrzak, U. Zeimer, S. Einfeldt, A. Ginolas, F. Bugge, K. Häusler, P. Ressel, H. Wenzel, and G. Erbert, "20W continuous wave reliable operation of 980nm broad-area single emitter diode lasers with an aperture of 96µm," *Proc. SPIE*, vol. 7198, no. 719814, pp. 1–9, 2009.

[19] R. Diehl, Ed., *High-Power Diode Lasers: Fundamentals, Technology, Applications*. Springer Science & Business Media, 2003.

[20] P. Crump, G. Erbert, H. Wenzel, C. Frevert, C. M. Schultz, K.-H. Hasler, R. Staske, B. Sumpf, A. Maaßdorf, F. Bugge, S. Knigge, and G. Tränkle, "Efficient High-Power Laser Diodes," *IEEE J. Sel. Top. Quantum Electron.*, vol. 19, no. 4, pp. 1–11, 2013.

[21] O. Hess, S. W. Koch, and J. V Moloney, "Filamentation and beam propagation in broad-area semiconductor lasers," *Quantum Electronics, IEEE Journal of*, vol. 31, no. 1. pp. 35–43, 1995.

[22] J. R. Marciante and G. P. Agrawal, “Spatio-temporal characteristics of filamentation in broad-area semiconductor lasers: experimental results,” *Photonics Technology Letters, IEEE*, vol. 10, no. 1. pp. 54–56, 1998.

[23] A. Knigge, G. Erbert, J. Jonsson, W. Pittroff, R. Staske, B. Sumpf, M. Weyers, and G. Trankle, “Passively cooled 940 nm laser bars with 73% wall-plug efficiency at 70 W and 25/spl deg/C,” *Electronics Letters*, vol. 41, no. 5. pp. 250–251, 2005.

[24] J. J. Lim, T. M. Benson, and E. C. Larkins, “Design of wide-emitter single-mode laser diodes,” *Quantum Electronics, IEEE Journal of*, vol. 41, no. 4. pp. 506–516, 2005.

[25] J. Decker, P. Crump, J. Fricke, A. Maaßdorf, G. Erbert, and G. Tränkle, “Narrow Stripe Broad Area Lasers With High Order Distributed Feedback Surface Gratings,” *IEEE Photonics Technology Letters*, vol. 26, no. 8. pp. 829–832, 2014.

[26] P. Crump, K. H. Hasler, H. Wenzel, S. Knigge, F. Bugge, and G. Erbert, “High efficiency, 8W narrow-stripe broad-area lasers with in-plane beam-parameter-product below 2 mm mrad,” *2013 Conf. Lasers Electro-Optics Eur. Int. Quantum Electron. Conf. CLEO/Europe-IQEC 2013*, vol. 20, no. 314719, p. 824111, 2013.

[27] J. Skidmore, M. Peters, V. Rossin, J. Guo, Y. Xiao, J. Cheng, A. Shieh, R. Srinivasan, J. Singh, C. Wei, R. Duesterberg, J. J. Morehead, and E. Zucker, “ Advances in high-power 9XXnm laser diodes for pumping fiber lasers ,” 2016, vol. 9733, p. 97330B–97330B–7.

[28] R. J. Lang, K. Dzurko, A. A. Hardy, S. Demars, A. Schoenfelder, and D. F. Welch, “Theory of grating-confined broad-area lasers,” *IEEE J. Quantum*

*Electron.*, vol. 34, no. 11, pp. 2196–2210, 1998.

[29] K. Paschke, R. Giither, J. Fricke, E. Bugge, G. Erbert, and G. Trankle, "High power and high spectral brightness in 1060 nm a-DFB lasers with long resonators," *Electron. Lett.*, vol. 39, no. 4, pp. 369–370, 2003.

[30] C. Fiebig, G. Blume, M. Uebernickel, D. Feise, C. Kaspari, K. Paschke, J. Fricke, H. Wenzel, and G. Erbert, "High-power DBR-tapered laser at 980 nm for single-path second harmonic generation," *IEEE J. Sel. Top. Quantum Electron.*, vol. 15, no. 3, pp. 978–983, 2009.

[31] B. Sumpf, P. Adamiec, J. Fricke, P. Ressel, H. Wenzel, G. Erbert, and G. Tränkle, "Comparison of 650 nm tapered lasers with different lateral geometries at output powers up to 1 W," 2010, vol. 7616, p. 76161H–76161H–8.

[32] M. T. Kelemen, J. Weber, G. Kaufel, G. Bihlmann, R. Moritz, M. Mikulla, and G. Weimann, "Tapered diode lasers at 976 nm with 8 W nearly diffraction limited output power," *Electronics Letters*, vol. 41, no. 18. pp. 1011–1013, 2005.

[33] J. N. Walpole, E. S. Kintzer, S. R. Chinn, C. A. Wang, and L. J. Missaggia, "High-power strained-layer InGaAs/AlGaAs tapered traveling wave amplifier," *Appl. Phys. Lett.*, vol. 61, no. 7, pp. 740–742, 1992.

[34] B. Chann, A. K. Goyal, T. Y. Fan, A. Sanchez-Rubio, B. L. Volodin, and V. S. Ban, "Efficient, high-brightness wavelength-beam-combined commercial off-the-shelf diode stacks achieved by use of a wavelength-chirped volume Bragg grating," *Opt. Lett.*, vol. 31, no. 9, pp. 1253–1255, 2006.

[35] P. Crump, M. Grimshaw, J. Wang, W. Dong, S. Zhang, S. Das, J. Farmer, and M. Devito, "85 % Power Conversion Efficiency 975-nm Broad Area Diode

Lasers at – 50 ° C , 76 % at 10 ° C," vol. 1, pp. 6–7, 2006.

[36] F. Dittmar, B. Sumpf, J. Fricke, G. Erbert, and G. Tränkle, "High-power 808-nm tapered diode lasers with nearly diffraction-limited beam quality of M2 = 1.9 at P = 4.4 W," *IEEE Photonics Technol. Lett.*, vol. 18, no. 4, pp. 601–603, 2006.

[37] S. Sujecki, L. Borruel, J. Wykes, P. Moreno, B. Sumpf, P. Sewell, H. Wenzel, T. M. Benson, G. Erbert, I. Esquivias, and E. C. Larkins, "Nonlinear Properties of Tapered Laser Cavities," *IEEE J. Sel. Top. Quantum Electron.*, vol. 9, no. 3, pp. 823–834, 2003.

[38] J. J. Lim *et al.*, "Design and Simulation of Next-Generation High-Power, High-Brightness Laser Diodes," *Selected Topics in Quantum Electronics, IEEE Journal of*, vol. 15, no. 3. pp. 993–1008, 2009.

[39] S. N. Kaunga-Nyirenda, S. Bull, J. J. Lim, K. h. Hasler, J. Fricke, and E. C. Larkins, "Factors influencing brightness and beam quality of conventional and distributed Bragg reflector tapered laser diodes in absence of self-heating," *IET Optoelectronics*, vol. 8, no. 2. pp. 99–107, 2014.

[40] E. C. Larkins, S. Bull, S. Kaunga-Nyirenda, M. A. Helal, V. Vilokkinen, P. Uusimaa, P. Crump, and G. Erbert, "Design optimisation of high-brightness laser diodes for external cavity operation in the BRIDLE project," in *Conference Digest - IEEE International Semiconductor Laser Conference*, 2014.

[41] X. Wang, G. Erbert, H. Wenzel, P. Crump, B. Eppich, S. Knigge, P. Ressel, A. Ginolas, A. Maaßdorf, and G. Tränkle, " High power, high beam quality laser source with narrow, stable spectra based on truncated-tapered semiconductor amplifier ," 2013, vol. 8605, p. 86050G–86050G–11.

[42] M. Buda, W. C. van der Vleuten, G. Iordache, G. A. Acket, T. G. van de Roer, C. M. van Es, B. H. van Roy, and E. Smalbrugge, "Low-loss low-confinement GaAs-AlGaAs DQW laser diode with optical trap layer for high-power operation," *IEEE Photonics Technology Letters*, vol. 11, no. 2. pp. 161–163, 1999.

[43] J. W. Tomm, M. Ziegler, M. Hempel, and T. Elsaesser, "Mechanisms and fast kinetics of the catastrophic optical damage (COD) in GaAs-based diode lasers," *Laser Photon. Rev.*, vol. 5, no. 3, pp. 422–441, 2011.

[44] P. Crump, S. Knigge, A. Maaßdorf, F. Bugge, S. Hengesbach, U. Witte, H.-D. Hoffmann, B. Köhler, R. Hubrich, H. Kissel, J. Biesenbach, G. Erbert, and G. Traenkle, "Low-loss smile-insensitive external frequency-stabilization of high power diode lasers enabled by vertical designs with extremely low divergence angle and high efficiency," *SPIE Vol 8605 High-power Diode Laser Technol. Appl. XI*, vol. 8605, p. 86050T, 2013.

[45] Y. Jin, Y. Zou, X. Ma, J. Li, Y. Li, L. Jin, L. Xu, W. Zhao, Q. Sui, and Z. Zhang, "Study on Laser Diode Incoherent Beam Combining Technology Based on Tracepro," in *International Conference on Optoelectronics and Microelectronics (ICOM)*, 2012, pp. 23–25.

[46] R. K. Huang, B. Chann, J. Burgess, M. Kaiman, R. Overman, J. D. Glenn, and P. Tayebati, "Direct diode lasers with comparable beam quality to fiber, CO2, and solid state lasers," *Proc. SPIE*, vol. 8241, no. 824102, pp. 1–6, 2012.

[47] T. Y. Fan, "Laser beam combining for high-power, high-radiance sources," *IEEE J. Sel. Top. Quantum Electron.*, vol. 11, no. 3, pp. 567–577, 2005.

[48] G. Schimmel, I. Doyen, S. Janicot, L. P. Ramirez, M. Hanna, P. Georges, G. Lucas-Leclin, V. Vilokkinen, P. Melanen, P. Uusimaa, J. Decker, P. Crump, G.

Erbert, S. Bull, S. N. Kaunga-Nyirenda, and E. C. Larkins, “Separate phase-locking and coherent combining of two laser diodes in a Michelson cavity,” in *High-Power Diode Laser Technology and Applications XII, SPIE Photonics West*, 2015.

[49] B. Köhler, T. Brand, M. Haag, and J. Biesenbach, “Wavelength stabilized high-power diode laser modules,” 2009, vol. 7198, pp. 719810–719812.

[50] C. Wessling, M. Traub, D. Hoffmann, and R. Poprawe, “Dense wavelength multiplexing for a high power diode laser,” 2006, vol. 6104, p. 61040O–61040O–8.

[51] M. Chi, N. S. Bøgh, B. Thestrup, and P. M. Petersen, “Improvement of the beam quality of a broad-area diode laser using double feedback from two external mirrors,” *Appl. Phys. Lett.*, vol. 85, no. 7, pp. 1107–1109, 2004.

[52] L. Lang, J. J. Lim, S. Sujecki, and E. C. Larkins, “Improvement of the beam quality of a broad-area diode laser using asymmetric feedback from an external cavity,” *Opt. Quantum Electron.*, vol. 40, no. 14–15 SPEC. ISS., pp. 1097–1102, 2008.

[53] M. Løbel, P. M. Petersen, and P. M. Johansen, “Single-mode operation of a laser-diode array with frequency-selective phase-conjugate feedback.,” *Opt. Lett.*, vol. 23, no. 11, pp. 825–7, 1998.

[54] B. Thestrup, M. Chi, B. Sass, and P. M. Petersen, “High brightness laser source based on polarization coupling of two diode lasers with asymmetric feedback,” *Appl. Phys. Lett.*, vol. 82, no. 5, pp. 680–682, 2003.

[55] C. Liu, J. Ge, and J. Chen, “Study on a broad-area laser diode with external cavity feedback,” *Opt. Laser Technol.*, vol. 39, no. 1, pp. 169–173, 2007.

[56] E. Samsøe, P. Andersen, S. Andersson-Engels, and P. Petersen, “Improvement

of spatial and temporal coherence of a broad area laser diode using an external-cavity design with double grating feedback.," *Opt. Express*, vol. 12, no. 4, pp. 609–16, 2004.

[57] M. Løbel, P. M. Petersen, and P. M. Johansen, "Single-mode operation of a laser-diode array with frequency-selective phase-conjugate feedback," *Opt. Lett.*, vol. 23, no. 11, pp. 825–827, 1998.

[58] B. Chann, I. Nelson, and T. G. Walker, "Frequency-narrowed external-cavity diode-laser-array bar," *Opt. Lett.*, vol. 25, no. 18, pp. 1352–1354, 2000.

[59] A. S. Arnold, J. S. Wilson, and M. G. Boshier, "A simple extended-cavity diode laser," *Rev. Sci. Instrum.*, vol. 69, no. 1998, p. 1236, 1998.

[60] F. Wang, A. Hermerschmidt, and H. J. Eichler, "Narrow-bandwidth high-power output of a laser diode array with a simple external cavity," *Opt. Commun.*, vol. 218, no. 1–3, pp. 135–139, 2003.

[61] K. C. Harvey and C. J. Myatt, "External-cavity diode laser using a grazing-incidence diffraction grating," *Opt. Lett.*, vol. 16, no. 12, pp. 910–912, 1991.

[62] J. R. Leger, "Lateral mode control of an AlGaAs laser array in a Talbot cavity," *Appl. Phys. Lett.*, vol. 55, no. 4, pp. 334–336, 1989.

[63] R. Waarts, D. Mehuys, D. Nam, D. Welch, W. Streifer, and D. Scifres, "High-power, cw, diffraction-limited, GaAlAs laser diode array in an external Talbot cavity," *Appl. Phys. Lett.*, vol. 58, no. 23, pp. 2586–2588, 1991.

[64] D. Paboeuf, G. Lucas-Leclin, P. Georges, N. Michel, M. Krakowski, J. Lim, S. Sujecki, and E. Larkins, "Narrow-line coherently combined tapered laser diodes in a Talbot external cavity with a volume Bragg grating," *Appl. Phys. Lett.*, vol. 93, no. 21, 2008.

[65] R. Lang and K. Kobayashi, "External optical feedback effects on

semiconductor injection laser properties," *Quantum Electronics, IEEE Journal of,* vol. 16, no. 3. pp. 347–355, 1980.

[66] B. Leonhäuser, H. Kissel, A. Unger, B. Köhler, and J. Biesenbach, " Feedback-induced catastrophic optical mirror damage (COMD) on 976nm broad area single emitters with different AR reflectivity ," 2014, vol. 8965, pp. 896506–896510.

[67] B. Leonhäuser, H. Kissel, J. W. Tomm, M. Hempel, A. Unger, and J. Biesenbach, "High-power diode lasers under external optical feedback," *High-Power Diode Laser Technol. Appl. XIII*, vol. 9348, no. M, p. 93480M, 2015.

[68] M. Hempel, M. Chi, P. M. Petersen, U. Zeimer, and J. W. Tomm, "How does external feedback cause AlGaAs-based diode lasers to degrade?," *Appl. Phys. Lett.*, vol. 102, no. 2, 2013.

[69] Y. Takiguchi, T. Asatsuma, and S. Hirata, "Effect of the threshold reduction on a catastrophic optical mirror damage in broad-area semiconductor lasers with optical feedback," 2006, vol. 6104, p. 61040X–61040X–7.

[70] S. K. Mandre, I. Fischer, and W. Elsässer, "Control of the spatiotemporal emission of a broad-area semiconductor laser by spatially filtered feedback," vol. 28, no. 13, pp. 1135–1137, 2003.

[71] W. G. Spitzer and J. M. Whelan, "Infrared absorption and electron effective mass in n-type gallium arsenide," *Phys. Rev.*, vol. 114, no. 1, pp. 59–63, 1959.

[72] Amrita and A. K. Sharma, "Filamentation instability in a semiconductor laser," *J. Appl. Phys.*, vol. 94, no. 1, pp. 19–22, 2003.

[73] H. Kissel, B. Leonhäuser, J. W. Tomm, M. Hempel, A. Unger, and J. Biesenbach, "Fiber coupled laser diode reliability : Impact of feedback on diode lifetime and failure modes," in *High Power Diode Lasers and Systems*

*Conference (HPD)*, 2015, pp. 41–42.

Chapter 3

# 3 Modelling of external cavity high-brightness laser diodes

Predictive modelling tools are needed to address the problems posed by high-brightness diode lasers operating in systems with external optical feedback. These tools have important applications in the design and simulation of high-brightness laser systems that meet the targets imposed by various high-brightness laser applications. The laser diode and the external optical system pose different modelling challenges and require the use of different modelling approaches and software tools. These approaches and tools must be brought together to model the laser diode and the external optical system self-consistently. The next few sections will describe the laser modelling tool used to run the simulations from which the results were used to investigate the cause behind beam quality degradation at high bias current in DBR tapered lasers, analyse the impact of external optical feedback on the high-brightness lasers and analyse how spectral feedback in a Littrow cavity locks the laser onto a specific wavelength.

The external cavity modelling tool is comprised of 3 pieces of software: *Speclase,* an in-house laser simulation tool that has been developed by multiple researchers within the university of Nottingham; *OpticStudio*, a commercial coherent-ray tracing software capable of simulating and modelling optical systems; and an automated software, developed by the author using *Matlab*, to bidirectionally couple *Speclase* and *OpticStudio*. A concise description of *Speclase* and how it was developed is included in this work to build a complete picture of how the optical fields

were treated and how the results were obtained, processed and analysed. For full description of the laser modelling tool, the reader is referred to the references used and listed at the end of the chapter. A detailed description of the interface software and how it was created is also included. This should give the reader an insight on how the optical fields were extracted from *Speclase*, converted into rays and configured within *OpticStudio* as well as how the reflected rays, impinging in the facet, were converted to fields propagating within the laser cavity.

## 3.1 Laser diode simulation tool *"Speclase"*

The simulation of high-brightness laser diodes is a challenging task, which requires self-consistent modelling of the electrical, thermal and optical processes throughout the device [1]–[4]. At high-power, additional challenges are imposed on the simulation tools to model phenomena associated with high-power lasers, such as spectral hole burning and carrier/thermal lensing. Moreover, large optical cavity (LOC) devices with external feedback bring another layer of complexity- the challenge of simulating fields with different vertical mode profiles and their competition for the available gain. Other challenges can be the ability to model the spectral performance of the laser, especially in cases where modelling laser diodes with wavelength locking is required.

For this work, the simulation of the laser diode was performed with an in-house laser simulation tool, *Speclase* [4]. Although *Speclase* is capable of performing a self-consistent quasi-3D electrical, thermal and optical simulation of high-brightness laser diodes, throughout this work, however, the thermal solver was turned off, i.e. the simulations were isothermal. Isothermal simulations were used because we were

interested in analysing how the external feedback is coupled to the higher-order modes and how this affects the performance of the high-brightness laser. By eliminating temperature effects, we could understand how excitation and lasing of higher-order modes alone can lead to lower power-conversion efficiency and allows the impact of feedback coupled to the higher-order modes and the feedback coupled to the fundamental mode to be differentiated, as will be seen in chapter 5. Another reason for neglecting the thermal effects was constraints on simulation time. Turning on the thermal solver not only complicates the problem of the external feedback but increases simulation time significantly, delaying the development of the model and complicating the debugging process.

### 3.1.1 Electrical model

*Speclase* calculates the bipolar carrier density profiles for a series of 2-D planes (x-y) orthogonal to the optical axis along the longitudinal dimension of the device, while neglecting heat and carrier flow in the z-direction. The electrical model is comprised of 5 basic semiconductor equations:

- The Poisson's equation:

$$\nabla.(-\varepsilon_r \varepsilon_0 \nabla\phi) - q(p - n + p_w - n_w + N_D^+ - N_A^-) = 0 \tag{3.1}$$

- The continuity equations for both confined and unconfined carriers:

$$\nabla.J_n - q\left(R_{non-rad} + R_{spont} + R_{cap}^n\right) = 0 \tag{3.2}$$

$$\nabla.J_p + q\left(R_{non-rad} + R_{spont} + +R_{cap}^p\right) = 0 \tag{3.3}$$

$$\nabla . J_{nw} - q\left(R_{non-rad}^{qw} + R_{spont}^{qw} + R_{stim}^{qw} - R_{cap}^{n}\right) = 0 \quad (3.4)$$

$$\nabla . J_{pw} + q\left(R_{non-rad}^{qw} + R_{spont}^{qw} + R_{stim}^{qw} - R_{cap}^{p}\right) = 0 \quad (3.5)$$

Table 3.1 lists the definitions of the symbols used in those equations:

| Symbol/s | Description | Unit |
|---|---|---|
| $J_n$ | current density of electrons (bulk) | $[Acm^{-2}]$ |
| $J_p$ | current density of holes (bulk) | $[Acm^{-2}]$ |
| $J_{nw}$ | current density of electrons (QW) | $[Acm^{-2}]$ |
| $J_{pw}$ | current density of holes (QW) | $[Acm^{-2}]$ |
| $R_{non-rad}$, $R_{non-rad}^{qw}$ | the total non-radiative recombination rate (including Shockley-Read-Hall and Auger) for bulk and QW | $[cm^{-3}s^{-1}]$ |
| $R_{spont}$ ,$R_{spont}^{qw}$ | the spontaneous recombination rate for bulk and QW | $[cm^{-3}s^{-1}]$ |
| $R_{cap}^{n}$, $R_{cap}^{p}$ | the net carrier capture recombination rate for electrons and holes | $[cm^{-3}s^{-1}]$ |
| $R_{spont}^{qw}$ | the stimulated recombination rate for QW | $[cm^{-3}s^{-1}]$ |
| $q$ | the electron charge | $[1.6\ 10^{-19}\ C]$ |
| $p_w$ | confined hole density of holes | $[cm^{-3}]$ |
| $p$ | unconfined hole density of holes | $[cm^{-3}]$ |
| $n_w$ | confined electron density of holes | $[cm^{-3}]$ |
| $n$ | unconfined electron density of holes | $[cm^{-3}]$ |

| | | |
|---|---|---|
| $\Phi$ | electrostatic potential | $[V]$ |
| $\varepsilon_0$ | free-space permittivity | $[8.85\ 10^{-14}\ F/cm]$ |
| $\varepsilon_r$ | relative permittivity | - |
| $N_A^-$ | ionized acceptor concentration | $[cm^{-3}]$ |
| $N_D^+$ | ionized donor concentration | $[cm^{-3}]$ |

**Table (3.1): Definitions and units of terms used in Poisson's and continuity equations.**

The electrical solver works through numerically solving the five coupled nonlinear partial differential equations (3.1-3.5), using Newton's method [5] .

### 3.1.2 Optical model

The optical model relies on the effective index approximation [6] to reduce the dimensionality of the wave equation from full 3-D (x,y,z) into a 2-D (x,z). While a full 3-D simulation of the electric field is more accurate, the computational penalty is significant. Comparison with other models, employing 3D electro-thermal solvers, has shown that the effective index approximation is valid for laser structures that are slowly varying in the longitudinal direction [4]. The effective index method is based on the assumption that the electric field $E(x, y, z)$ within the device can be separated into two components: a component in the junction plane $\psi(x, z)$ and a component perpendicular to the junction plane $\phi(y)$. This leads to the following definition of the electric field in the cavity

$$E(x, y, z) = \phi(y; x, z).\psi(x, z) \tag{3.6}$$

Writing the 3-D Helmholtz equation in terms of $E(x, y, z)$ will give:

$$\frac{\partial^2 E}{\partial x^2} + \frac{\partial^2 E}{\partial y^2} + \frac{\partial^2 E}{\partial z^2} - 2j\beta \frac{\partial E}{\partial z} + E[k^2(x, y, z) - \beta^2] = 0 \tag{3.7}$$

Substituting (3.6) into (3.7), and using separation of variables, will give two wave equations, one for the field perpendicular to the junction plane, equation (3.8), and another in the junction plane, equation (3.9), as shown below:

$$\frac{\partial^2 \emptyset}{\partial y^2} + \emptyset\left[k_0^2\, n^2(x, y, z) - \beta_{eff}^2(x, z)\right] = 0 \tag{3.8}$$

$$\frac{\partial^2 \psi}{\partial x^2} + \frac{\partial^2 \psi}{\partial z^2} - 2j\beta \frac{\partial \psi}{\partial z} + \psi\left[\beta_{eff}^2(x, z) - \beta^2)\right] = 0 \tag{3.9}$$

Equation (3.8) is an eigenvalue equation and can be solved, using the transfer matrix method, to obtain the effective propagation constant $\beta_{eff}$, which is substituted in (3.9). Equation (3.9) is then solved using FD-BPM. From equations (3.8) and (3.9), both field components can be obtained across the device. The refractive index $n(x, y, z)$ is complex and perturbations to the refractive index are caused by different phenomena such as temperature change and carrier density change. Every time the refractive index changes, equation (3.8) can be solved to obtain the new $\beta_{eff}$. However, a more efficient approach is to consider the refractive index changes as small perturbations to the eigenvalue problem. This is justified as the vertical structure can support a finite number of vertical modes, giving $\beta_{eff}$ specific values corresponding to the different vertical mode profiles supported by the structure.

Using the variational principle, the eigenvalue $\beta_{eff}^2$ can be calculated from the Rayleigh quotient [2]:

$$\beta_{eff}^2(x,z) = \frac{\int_{-\infty}^{\infty} \emptyset^* \left[\frac{\partial^2}{\partial y^2} + k_0^2 n^2(x,y,z)\right] \emptyset \, dy}{\int_{-\infty}^{\infty} |\emptyset|^2 \, dy} \tag{3.10}$$

The perturbation to both the refractive index and the effective refractive index is generally expressed as:

$$n_{eff} = n_{eff,0} + \Delta \, n_{eff} \tag{3.11}$$

$$n = \ n_0 + \ \Delta n \tag{3.12}$$

where $n_0$ is the unperturbed refractive index and $\Delta n$ represents the refractive index perturbation. The effective propagation constant is related to the effective index through the following expression:

$$\beta_{eff} = n_{eff} k_0 \tag{3.13}$$

Using equations (3.11), (3.12) and (3.13) along with (3.10) we can reach an expression for the effective index perturbation:

$$\Delta \, n_{eff}(x,z) = \ \frac{1}{n_{eff,0}} \frac{\int_{-\infty}^{\infty} \emptyset^* \, [n_0(x,y,z) \Delta n(x,y,z)] \emptyset \, dy}{\int_{-\infty}^{\infty} |\emptyset|^2 \, dy} \tag{3.14}$$

For this work, we used a version of *Speclase* that only considers carrier induced changes to the refractive index. This was done to be able to study the impact of feedback and the problem of exciting higher-order modes and how this affects the beam quality without involving the additional complexity of self-heating. In other

words, the laser simulations performed were isothermal. The change in refractive index can be separated into different components as expressed below:

$$\Delta n = \Delta n_r + \frac{j(g - \alpha_{fca} - \alpha_{scat})}{2k_0}, \tag{3.15}$$

where $\Delta n_r$ represents the carrier-induced reduction in the refractive index, $g$ is the gain or loss caused by stimulated emission or recombination, $\alpha_{fca}$ is the loss caused by free-carrier absorption (intra-band and inter-valence absorption) and $\alpha_{scat}$ is the scattering loss. The scattering loss is carrier–density independent and is taken as constant, determined by the experimental results. The change in the refractive index due to gain/loss and free-carrier loss corresponds to a change in the effective refractive index, gain/loss and free-carrier absorption respectively:

$$\Delta n_{eff} = \Delta n_{r,eff} + \frac{j(g_{eff} - \alpha_{eff,fca} - \alpha_{scat})}{2k_0} \tag{3.16}$$

The contribution of both the effective gain/loss and effective free-carrier absorption can be calculated by substituting those two contributions, from equation (3.15), into equation (3.14). The resulting expressions are:

$$g_{eff}(x,z) = \frac{1}{n_{eff,0}} \frac{\int_{-\infty}^{\infty} \emptyset^* [n_0(x,y,z)\, g)] \emptyset \, dy}{\int_{-\infty}^{\infty} |\emptyset|^2 \, dy} \tag{3.17}$$

$$\alpha_{eff,fca}(x,z) = \frac{1}{n_{eff,0}} \frac{\int_{-\infty}^{\infty} \emptyset^* \left[n_0(x,y,z)\alpha_{fca}\right] \emptyset \, dy}{\int_{-\infty}^{\infty} |\emptyset|^2 \, dy} \tag{3.18}$$

The free-carrier absorption $\alpha_{fca}$ can be calculated by [7] :

$$\alpha_{fca} = \sigma_{fc,n} n + \sigma_{fc,p} p \tag{3.19}$$

where $\sigma_{fc,n}$ and $\sigma_{fc,p}$ are the free-carrier capture cross-section for electrons and holes, respectively.

### 3.1.3 Coupling between models

*Speclase* is used to simulate semiconductor laser diodes of stripe geometry as illustrated in figure 3.1.

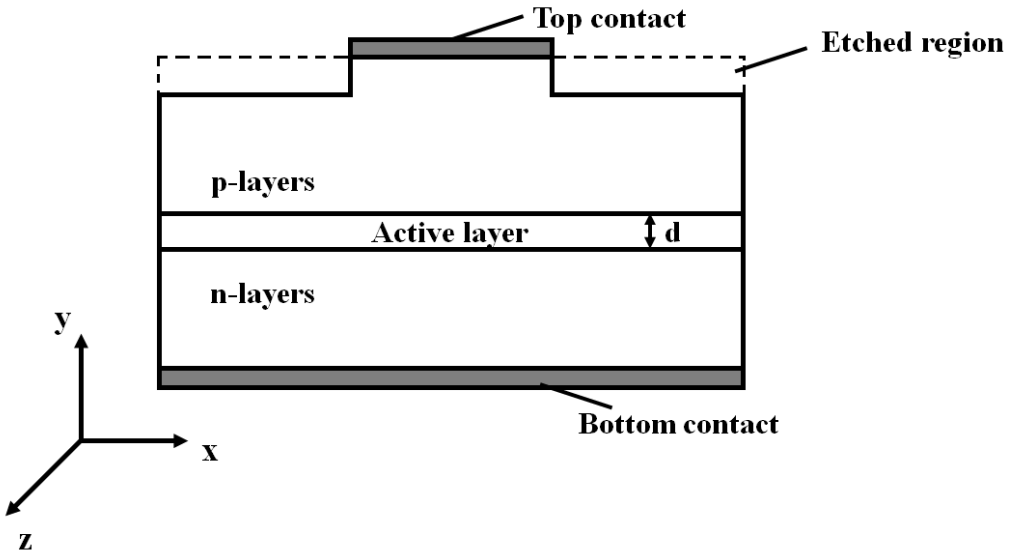



**Figure (3.1): Cross-section of a typical laser structure simulated by *Speclase*.**

The electrical model is represented by equations (3.1 to 3.5) while the optical model is represented by equation (3.9). In order to perform a semiconductor laser simulation, both models, electrical and optical, need to be solved self-consistently. The electrical and optical models are coupled through the stimulated emission/absorption and ASE processes and refractive index perturbations. These index perturbations are calculated from perturbations of the gain/absorption spectra using the Kramers-Kronig relations [8]. Figure 3.2 shows slices of electrical and optical models.

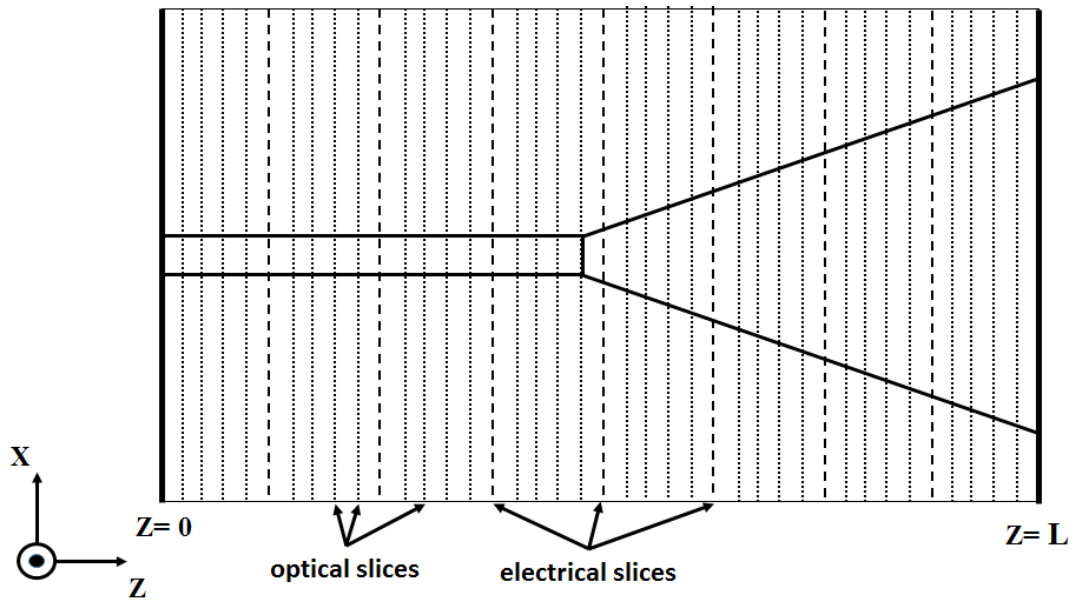



**Figure (3.2): Top view (x-z) of discretised tapered laser structure into electrical and optical slices**

The carrier distribution profiles are calculated at every (x-y) slice, and the changes in carrier densities, gain/absorption and FCA absorption are coupled into the 2D WA FD-BPM (x-z) through the change in index, equations (3-15) and (3-16), which leads to updating the refractive index and the effective propagation constant in equation (3.10), which accounts for the longitudinal variation in the optical field. The optical field is propagated to the next electrical slice where the carrier distribution profiles are updated through stimulated emission/absorption and spontaneous emission. The optical field is propagated forward and backward, whilst updating the carrier density profiles. This process is repeated using an accelerated Fox–Li iterative approach [9] until a self-consistent solution of both optical field and carriers profile is found. Once the optical field profile remains constant over two successive iterations, then the laser resonator condition is satisfied and the simulation is considered to be converged. The convergence of the simulation is reached when the shape and power of the optical field shape remain invariant.

The optical solver can also model the spectral behaviour of the device by propagating multiple wavelengths and their competition through the spectral-spatial gain distribution. Figure 3.3 shows the flow diagram of *Speclase*.

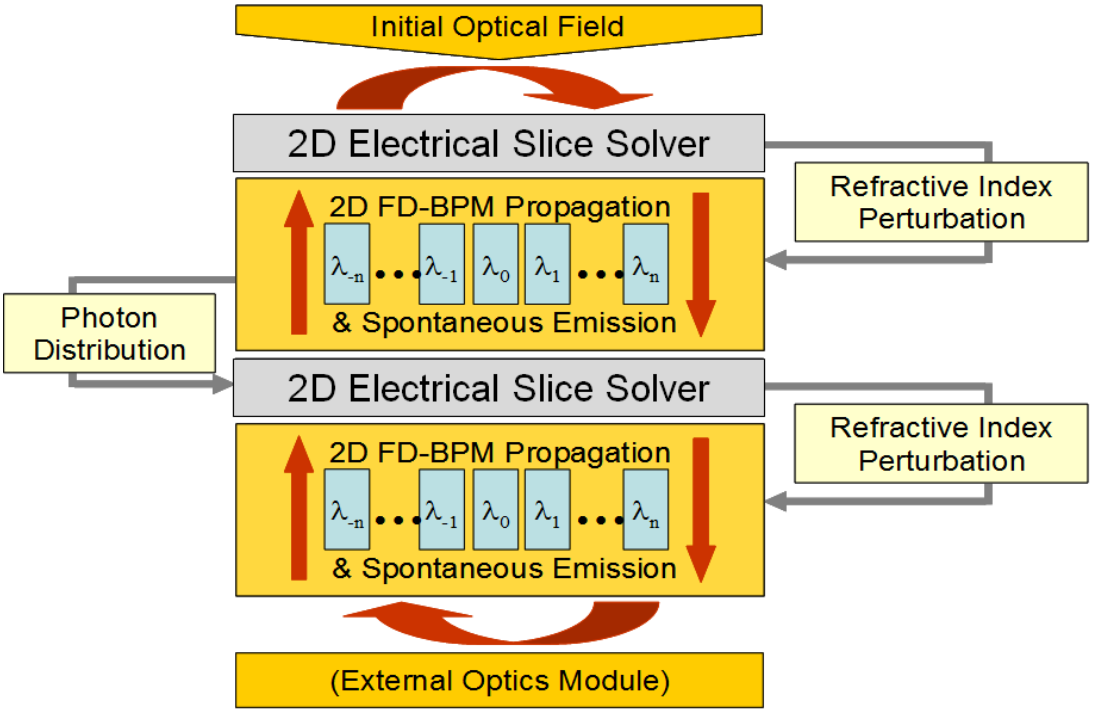



**Figure (3.3): Flow diagram of stand-alone *Speclase* with multiple wavelengths [4].**

In order to model the excitation and competition of fields with different vertical mode profiles, *Speclase* was modified to calculate each of the vertical field distributions and their vertical confinement factors. This allows *Speclase* to calculate the effective index and free-carrier absorption distributions needed for the 2D propagation of the fields with each of the allowed vertical mode profiles. Figure 3.4 describes the flow diagram of *Speclase* for the simulation of a high-brightness LOC laser diode, with multiple vertical modes, coupled to an external cavity. The vertical modes, containing the amount of power coherently-coupled from the external cavity and the internally reflected fields, are propagated by Speclase inside the laser cavity using a Fox-Li approach. This whole process is repeated until convergence.

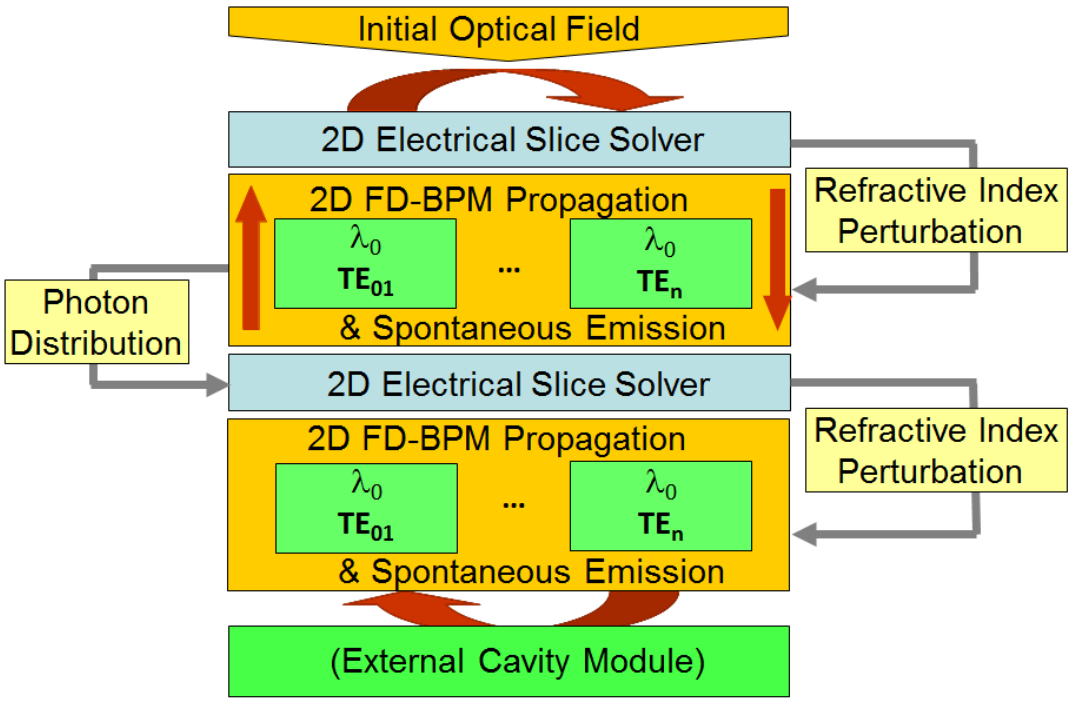



**Figure (3.4): Flow diagram of *Speclase* with multiple vertical modes with external cavity feedback.**

### 3.1.4 *Speclase* output variables

To study the impact of external feedback, we need to plot different characteristics of the laser. External feedback leads to drop in both power and efficiency. It also affects the NF/FF shape and this in turn has an impact on the beam quality.

The L-I curve is obtained when *Speclase* is run for multiple currents and the output power is plotted as a function of current. The output power, $P_{out}$, is taken to be the power emitted from the front facet. This is equivalent to the energy flux, integrated in the transverse plane, multiplied by the front facet transmission coefficient:

$$P_{out} = (1 - R_0) \iint S(x, y, L) dx\, dy \tag{3.20}$$

where $S(x, y, L)$ is the energy flux at the front facet, $z = L$ and $R_0$ is the power reflectivity of the front facet. The energy flux is expressed as:

$$S = \frac{h}{2\pi}\ \omega\ v_g N_{ph} \tag{3.21}$$

where $h$ is Planck's constant, $\omega$ is the angular frequency, $v_g$ is the group velocity and $N_{ph}$is the photon density. The photon density can be calculated from the 2D field intensity at the front facet:

$$N_{ph}(x, y, L) = N_s\ \psi_f^2(x, L)\ \phi^2(y; x, L) \tag{3.22}$$

Substituting (3.21) and (3.22) into (3.20), and integrating the field intensity at the facet, the total output power can be expressed as:

$$P_{out} = (1 - R_0)\frac{h}{2\pi}\ \omega\ v_g\ N_s \int_{-\infty}^{\infty} \psi_f^2(x, L)dx \int_{-\infty}^{\infty} \phi^2(y; x, L)dy \tag{3.22}$$

Based on equation (3.25), we can write the expression for the output near-field as:

$$E(x) = \sqrt{(1 - R_0)\frac{h}{2\pi}\ \omega\ v_g\ N_s \int_{-\infty}^{\infty} \phi^2(y; x, L)dy}\ \ \psi_f(x, L) \tag{3.24}$$

while the near-field intensity distribution is given by:

$$I(x) = \left[(1 - R_0)\frac{h}{2\pi}\ \omega\ v_g\ N_s \int_{-\infty}^{\infty} \phi^2(y; x, L)dy\right]\ \psi_f^2(x, L) \tag{3.25}$$

The total current injected into the device is calculated by integrating the current density over the total area of the contact layer:

$$I = \iint_{contact\ area} (J_n + J_p)dxdz \tag{3.26}$$

The total photon density can be calculated using forward and backward propagating optical fields:

$$N_{ph}(x, z) = N_s\ \left(\psi_f^2(x, z)\ \psi_b^2(x, z)\right) \tag{3.27}$$

## 3.2 External cavity simulation tool

The modelling of the external cavity requires modelling of 3-D free-space optical propagation, including transmission, reflection and scattering effects. The optical models used inside the laser diode are not well suited to free-space optical propagation, where Fourier optics and coherent ray tracing methods are more appropriate. Fourier optics models preserve the wave nature of the optical propagation, but the underlying paraxial approximation is best suited to low divergence beams. Coherent ray tracing is better suited for external cavity laser diodes with large beam divergence. Coherent ray tracing methods are also fast and flexible, making them attractive for modelling complex optical systems. We describe an external cavity modelling tool (*OpticStudio*) based on coherent ray-tracing.

### 3.2.1 Coupling of the laser diode simulation tool and coherent ray tracing tools

The coupling of the laser simulator and the coherent ray tracing tool for the external cavity is not straightforward, since the light is treated as a wave inside the laser diode, but as rays in the external cavity. Careful analysis of the output beam of the laser diode is needed to produce the input rays for the external cavity model, while maintaining all of the properties of the beam emitted from the laser diode (e.g. near- and far-field patterns, astigmatism). Bi-directional coupling is even more challenging, requiring conversion of the rays back into an optical field distribution containing both intensity and phase information.

Firstly, the field data produced by *Speclase* (near-field, far-field and wavelength) must be converted into rays, which represent the laser source in *OpticStudio*. The rays are defined by three attributes: launching coordinates, direction cosines and intensity. The intensity and launching coordinates are obtained from the near-field data, while the direction cosines are calculated from the far-field data.
*Speclase* calculates the profiles of the vertical modes supported by the cavity, and propagates their associated lateral field distributions using 2D WA FD-BPM. An example of a vertical mode profile and the associated lateral field distribution, produced by *Speclase*, is shown in fig 3.5. Figure 3.5 (left) shows the vertical profile of the fundamental mode while figure 3.5 (right) shows the associated lateral field distribution.

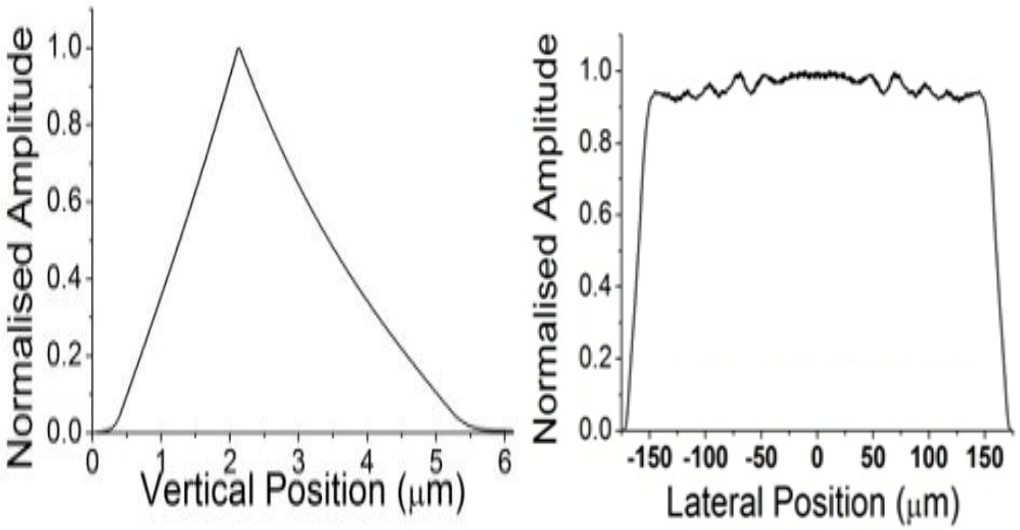



**Figure (3.5): 1-D output fields of the fundamental mode. Vertical mode profile (left). Slow-axis near-field (right)**

In order to calculate the 2D-near-field distribution at the facet, the lateral near field pattern is multiplied by the associated vertical field profile, as shown in figure 3.6 (left). This is done based on the previous assumption that vertical and lateral fields within the laser cavity are separable. Figure 3.6 (left) shows the 2D near-field of the fundamental mode while figure 3.6 (right) shows the associated 2D far-field.

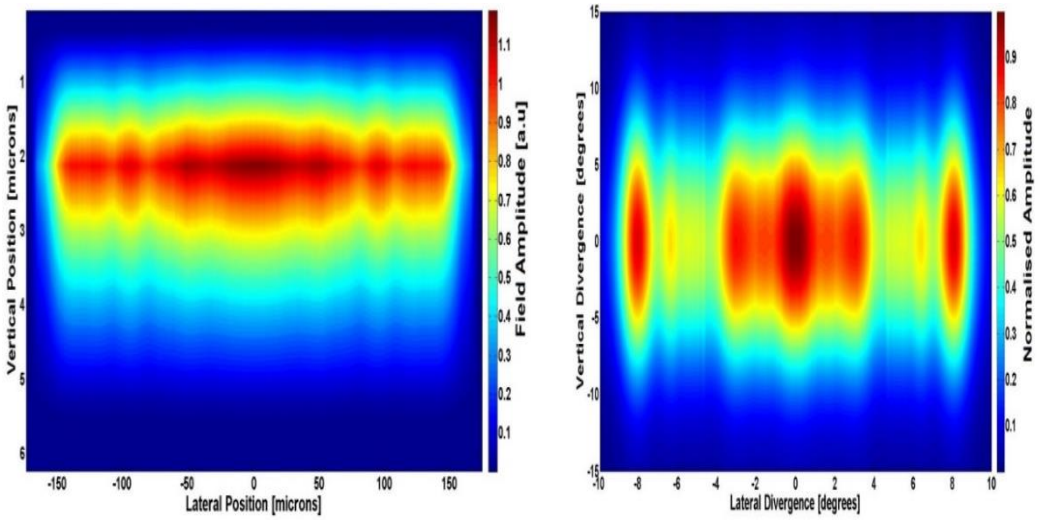



**Figure (3.6): 2D near- and far- field of the fundamental mode. 2D near-field (left). 2D far-field (right).**

# Chapter 3

The horizontal and vertical far-field patterns are calculated using the Fraunhofer diffraction relation describing the diffraction from a rectangular aperture. Due to the diffraction, the waves leaving the laser diode can be traced back to a single point within the cavity. That point is called the virtual line source (or virtual point source in the case of non-astigmatic beams). Placing a screen at the facet we will see an image on the screen that will resemble the aperture image. This image is called the near-field pattern or the Fresnel Diffraction [10]. Plotting the intensity of this image against the vertical spatial dimensions of the aperture will give us the vertical near-field pattern. If we plot it against the horizontal dimensions we get the horizontal near-field pattern. If the screen was moved far away from the facet until the image on the screen ceases to resemble the image of the aperture, the resulting pattern is called the Fraunhofer Diffraction. The Fresnel pattern and the Fraunhofer pattern are related mathematically by the Fourier transform, which is derived in Appendix I. The Fraunhofer diffraction (or the Fourier transform) gives the field in terms of spatial frequencies. In order to calculate the direction cosines, we need to calculate the far-field pattern in terms of angles of diffraction:

$$\psi(\theta_H) = (\cos\theta_H)^2 \left| \int_{-\infty}^{+\infty} \mathrm{E}(x) e^{j(\sin\theta_H k_0 x)}\, dx \right|^2 \tag{3.28}$$

$$\psi(\theta_V) = (\cos\theta_V)^2 \left| \int_{-\infty}^{+\infty} \mathrm{E}(y) e^{j(\sin\theta_V k_0 y)} dy \right|^2 \tag{3.29}$$

where $\psi$ is far-field profile, $\theta$ is the divergence angle, $\mathrm{E}$ is the electric field, $k_0$ is the wavenumber. Appendix I also shows how to convert the spatial frequencies to angles of divergence from the beam propagation axis.

Due to the astigmatic nature of the laser beam, the output rays will appear to originate from two virtual line sources (non-astigmatic sources have a virtual point source), a horizontal line source (HLS) and a vertical line source (VLS) as shown in figure (3.7), where $\theta_V$ and $\theta_H$ are the vertical and horizontal divergence angles, respectively.

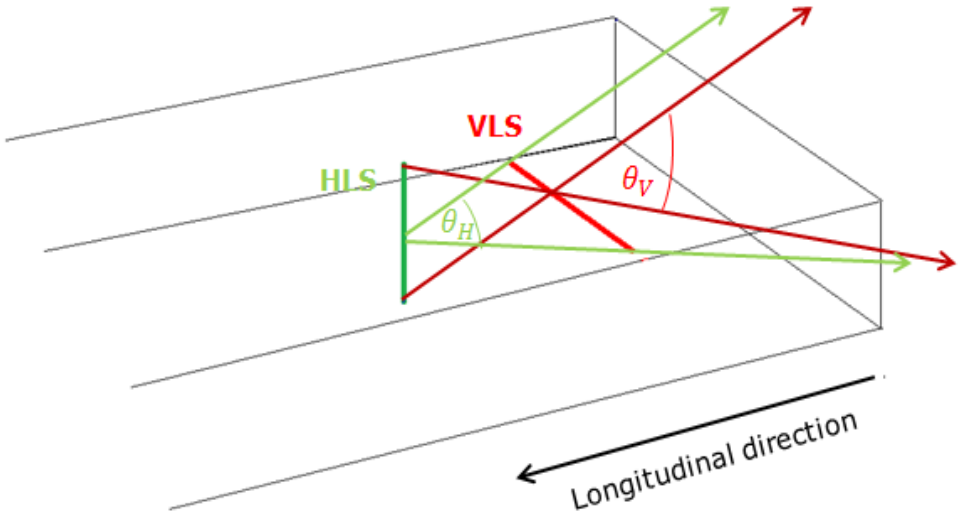



**Figure (3.7): Schematic of vertical and horizontal lines sources of a typical laser beam.**

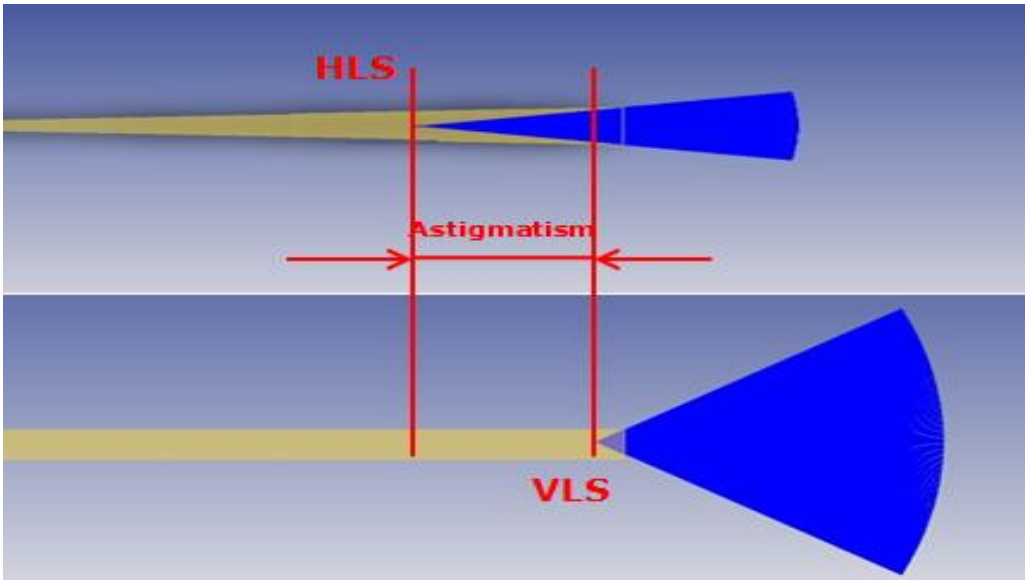



**Figure (3.8): Top and side view of laser modelled in *OpticStudio*, showing vertical and horizontal lines sources and the astigmatism**

The output rays must intersect both of these line sources - one for the vertical beam divergence and the other for the horizontal beam divergence. In this thesis, we are dealing with a tapered laser. The lateral beam at the facet is the adiabatic expansion of the beam diffracted from the ridge-waveguide section aperture, as shown in figure 3.9.

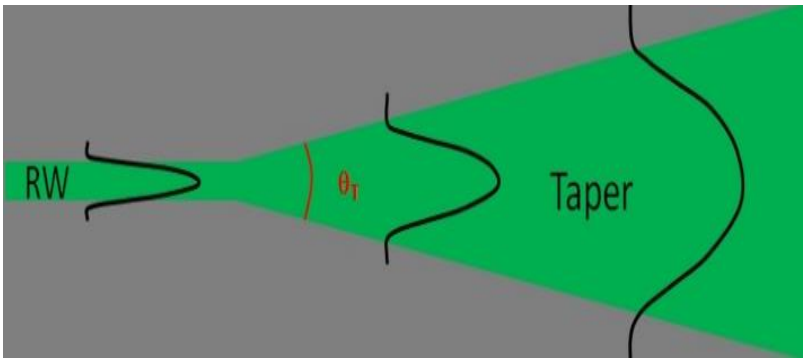



**Figure (3.9): Schematic diagram of a tapered laser, showing the adiabatic expansion of the beam in the taper.**

One of the properties of the tapered laser is that the taper angle is chosen to match the beam divergence angle from the ridge-waveguide aperture. This ensures adiabatic expansion of the single-mode lateral beam, diffracted from the RW aperture as shown in figure 3.9. Therefore, to obtain the longitudinal position of the horizontal line source, FO backpropagation is used. The longitudinal position is found using the following equation:

$$E(x;z_1) = \mathrm{F}^{-1}\left\{A(f_x;z_2)\exp\left[-j\left(\frac{2\pi}{\lambda}\sqrt{1-(\lambda f_x)^2}\right)(z_2 - z_1)\right]\right\} \tag{3.30}$$

where $E(x;z_1)$ is the lateral spatial field distribution of the electric field at point $z_1$, $\mathrm{F}^{-1}$ is the inverse Fourier transform operator, $A(f_x;z_2)$ is the angular distribution at point $z_2$, $\lambda$ and $f_x$ are the wavelength and the lateral spatial frequency, respectively.

This equation is derived in Appendix II. What the above equation does is finding the lateral field distribution at point $z_1$ from the angular distribution of the field at point $z_2$ [11]. In essence, if we know that a field has propagated from $z_1$ to $z_2$, then by knowing the field distribution at $z_2$ we can calculate the field distribution at $z_1$. Considering that the origin of the Z axis is at the facet, and the positive direction of Z axis is pointing away from the facet towards the external cavity, then $z_2 = 0$ and equation (3.30) becomes:

$$E(x; z_1) = \mathcal{F}^{-1}\left\{A(f_x; 0)\exp\left[-j\left(\frac{2\pi}{\lambda}\sqrt{1-(\lambda f_x)^2}\right)(-z_1)\right]\right\} \tag{3.31}$$

$z_1$ is arbitrary, as we still need to know where the line source is located. The location of the line source corresponds to the beam waist, the point at which the width of the beam is the narrowest, as shown in figure 3.10.

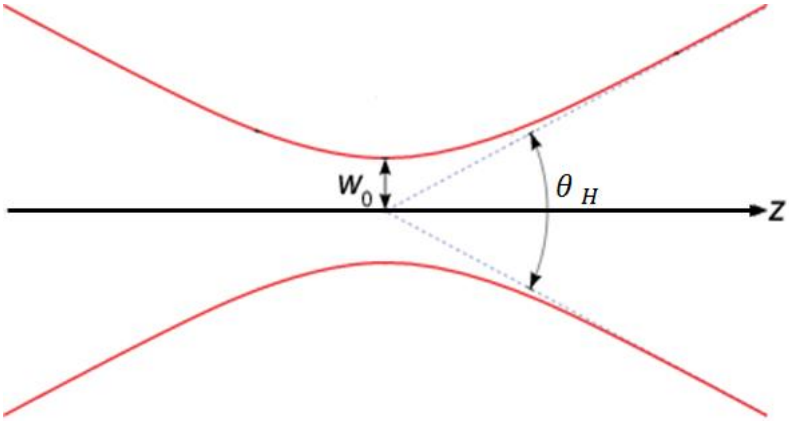



**Figure (3.10): Beam expansion as a function of Z.**

$w_0$ is the beam waist, $\theta_H$ is the horizontal divergence angle. The way of finding the beam waist is by calculating the width of the field intensity at different points along the axis Z. The position of the line source is where the minimum $w_0$ is found along the axis Z. Now that we have both the positions of VLS and HLS and the divergence

angles in both directions, and the fact that each and every ray will have to pass through a point on the output facet, then with simple trigonometry we can calculate the direction cosines of the ray. Once we have the launch coordinates, direction cosines and intensity for each ray, we can configure the laser as a source in *OpticStudio* through "Source File". "Source File" is a binary file used by OpticStudio to configure the laser source in the external cavity.

Once the source is configured for the external cavity, *OpticStudio* can launch the rays the of the source and trace them through the optical elements within the external cavity.

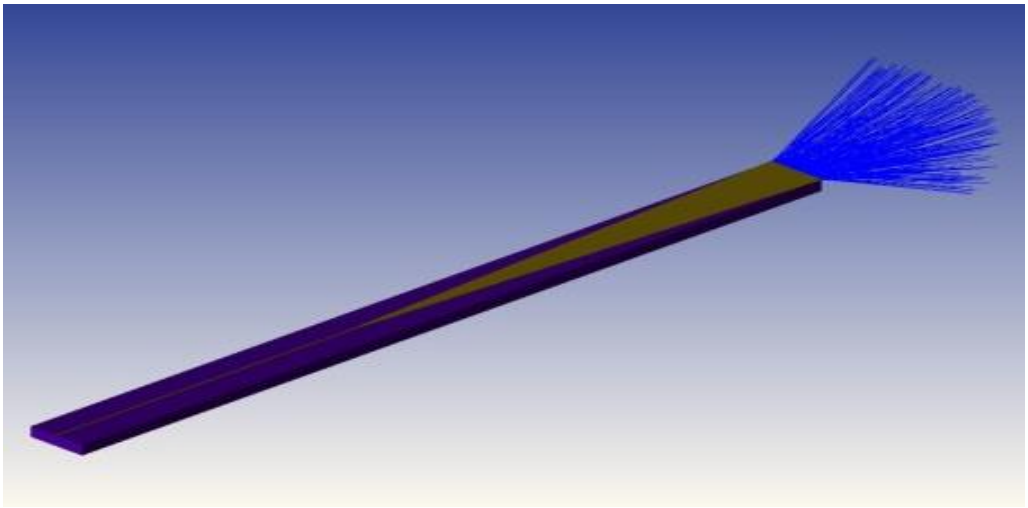


**Figure (3.11): Modelling laser output beam in *OpticStudio***

At the surface of each element in the external cavity, rays will split, transmit, scatter, refract or reflect. We are interested in rays that scatter and reflect off the optics elements and come back impinging on the laser facet. The next challenge is to convert the rays returning to the laser facet back into complex field distributions, taking the ray phases into account.

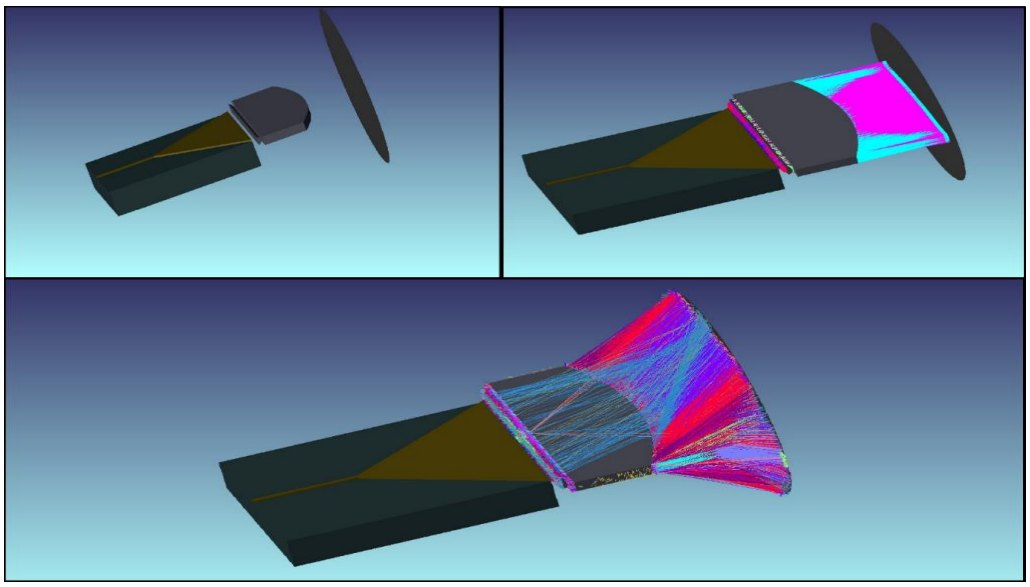


**Figure (3.12): Propagating laser output beam in an external cavity using *OpticStudio*. External cavity of two collimating lenses and a mirror (top left). Rays scattering and splitting turned off (top right). Rays scattering and splitting turned on (bottom)**

The 2D electric field distribution of those rays, can be calculated through a rectangular "Detector" placed at the facet with dimensions matching the facet dimensions. The "Detector" is defined within *OpticStudio* as a surface element that measures the rays' coherent intensity and coherent phase spatial distributions. The rays' intensity distribution is measured in W/area, while the phase is measured in degrees. Figure 3.13 shows an example of both the coherent intensity and phase distributions measured by *OpticStudio.*

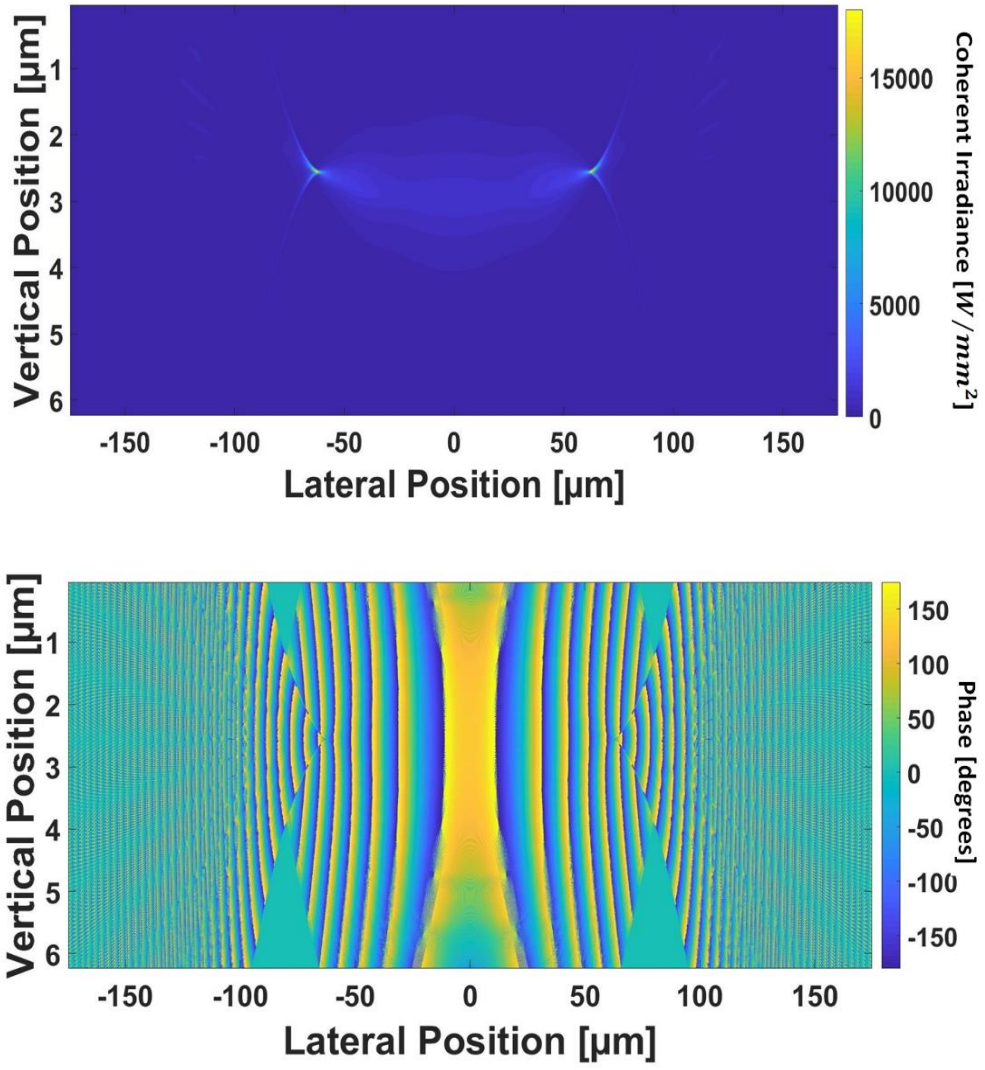



**Figure (3.13): 2D spatial distribution of reflected rays (impinging on the facet). 2D Reflected rays coherent irradiance (top). 2D reflected rays coherent phase (bottom)**

The complex electric field of the rays impinging on the facet can re-constructed from the coherent intensity and phase distributions. A fraction of the optical energy returned to the laser facet at each lateral position (x) is coupled into the laser for each of the vertical modes supported by the LOC structure. The amount of energy coupled to each vertical mode is calculated using the overlap integral at each lateral position (x):

$$\eta_n(x) = \frac{\left|\int_{-\infty}^{+\infty}\{E_{ext}(y;x)\ TE_n(y)^*\}\,dy\right|^2}{\int_{-\infty}^{+\infty}|E_{ext}(y;x)|^2\,dy\ \ \int_{-\infty}^{+\infty}|TE_n(y)|^2\,dy} \tag{3.32}$$

where $E_{ext}(y;x)$ is the vertical distribution of the external field incident on the facet at this lateral position $(x)$, $TE_n$ is the n[th] vertical field profile, $TE_n(y)^*$ is the complex conjugate of the n[th] vertical field profile and $\eta_n(x)$ is the percentage of the reflected power coupled into cavity mode n at position $(x)$. Figure 3.14 shows an example of the vertical distribution of the externally reflected field at one lateral position $E_{ext}(y; x = 0\ \mu m)$.

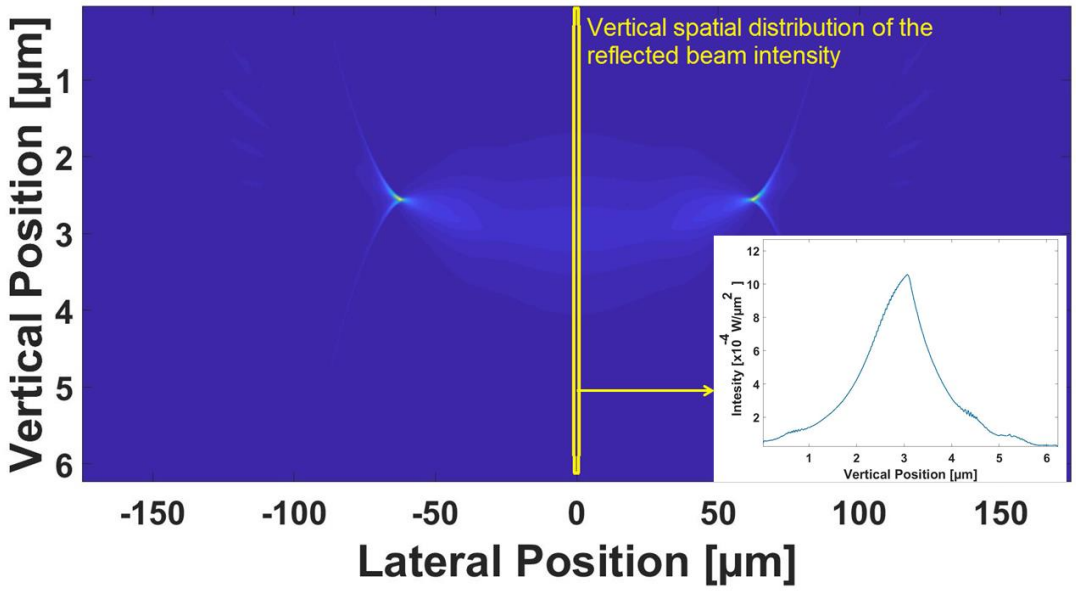



**Figure (3.14): 2D spatial distribution of reflected beam intensity (main). Vertical spatial distribution of reflected beam intensity at lateral position $x = 0\ \mu m$ (inlay).**

$\eta_n(x)$ is called the coupling coefficient distribution for mode $n$. To obtain the amount of power coupled into the cavity, the lateral intensity distribution of the reflected beam at the facet needs to be calculated. This is done by integrating the 2D coherent intensity in the vertical direction at each lateral position (x), and then

multiplying the resultant lateral intensity by the coupling coefficient distribution.

$$\left|E_{n,\ ext,coupled}(x)\right|^2 = \eta_n(x) \int |E_{ext}(x,y)|^2\ dy \tag{3.33}$$

As for the phase of each coupled field at each lateral position (x), it can be calculated by

$$\varphi_n(x) = \tan^{-1}\left[\frac{Im\{\int_{-\infty}^{+\infty}\{E_{ext}(y;x)\ TE_n(y)^*\}\,dy\}}{Re\{\int_{-\infty}^{+\infty}\{E_{ext}(y;x)\ TE_n(y)^*\}\,dy\}}\right] \tag{3.34}$$

Figure 3.15 shows the profiles of vertical modes supported by the vertical structure.

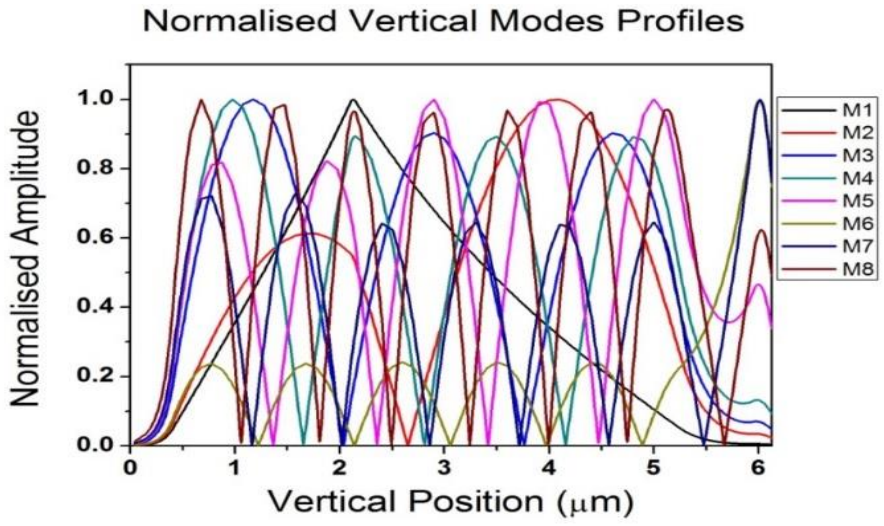



**Figure (3.15): Vertical modes profiles supported by the laser cavity**

Using the phase distribution calculated by equation (3.34) and the coupled field distribution calculated by equation (3.33), the complex fields coupled into the laser cavity are obtained:

$$E_{n,\ ext,coupled}(x) = E_{n,\ ext,coupled}(x)\ [\cos(\varphi_n(x)) + j\ \sin(\varphi_n(x))\ ] \tag{3.35}$$

Figure 3.16 shows the lateral distribution of the coupled fields.

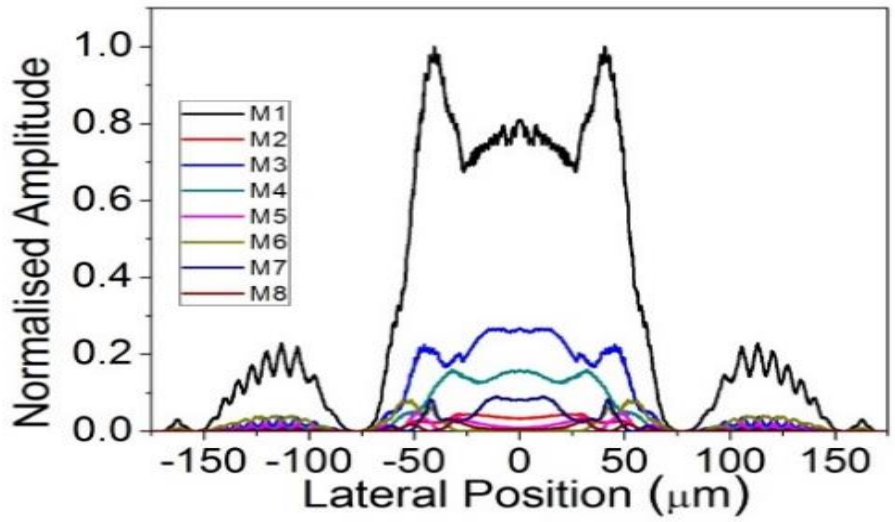



**Figure (3.16): Spatial lateral distributions of fields coupled into the laser cavity**

The resulting 1D field distributions are coherently added to the internally reflected fields. The internally reflected field at the front facet is given by:

$$\psi_b(x, L) = \psi_f(x, L)\sqrt{R_0} \tag{3.36}$$

while the composite field is given by:

$$\psi_{b,comp}(x, L) = \psi_b(x, L) + E_{n,\ ext,coupled}(x) \tag{3.37}$$

where $\psi_{b,comp}(x, L)$ is the composite field at the facet that is propagated backwards inside the laser diode by *Speclase* using 2D WA FD-BPM.

The entire external cavity simulation is repeated using Fox-Li iterations until it converges. Figure 3.17 shows a schematic diagram of the coupling of *Speclase* and *OpticStudio*.

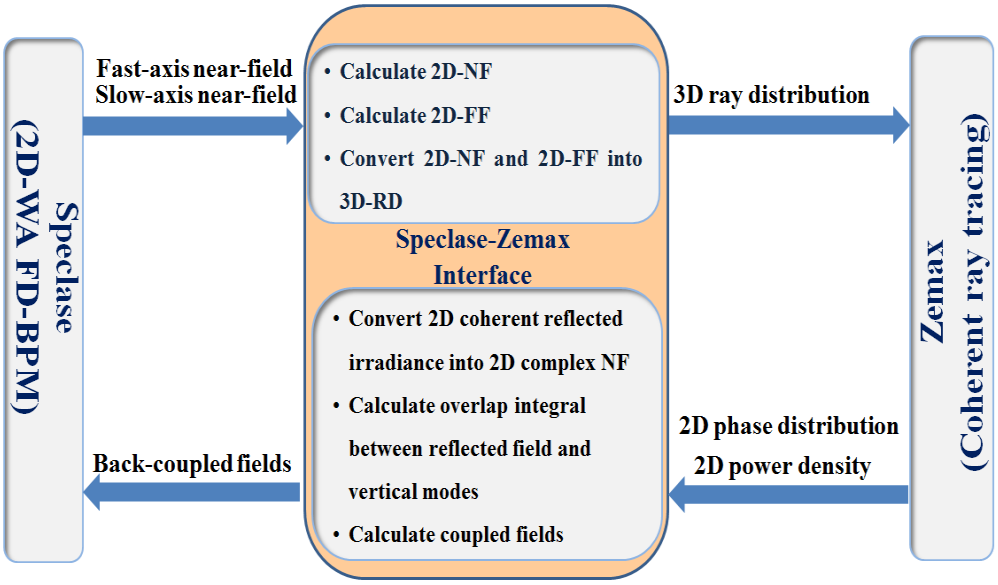



**Figure (3.17): Schematic of coupling *Speclase* to *OpticStudio*.**

## 3.3 Post simulation results processing

Different processes take place within the laser: stimulated recombination, non-radiative recombination and absorption. These processes lead to the flow of carriers across the junction, which contributes to the total current flowing through the device. The flow of current across the device will also contribute to Joule heating. The external optical feedback leads to the excitation/lasing of higher order modes. When these excited modes propagate and instigate absorption- exciting carriers to higher energy levels, the subsequent energy relaxation of these excited carriers generate heat in the form of phonons released to the structure. There are two types of heating mechanism resulting from absorption: optical bleaching heat, free-carrier absorption heating.

The calculation of heat, despite the use of the isothermal laser modelling tool, is done to emphasise the mechanisms through which the efficiency is degraded. When external optical feedback is coupled into the laser and into higher-order modes, that power will either cause these higher-order modes to lase or the power is lost. Heat

calculations, therefore, aim at showing where the coupled power that does not lead to lasing is lost.

### 3.3.1 Heat calculations

Joule heating is the heat generated in the device due to stimulated current flowing through the junction and incurring resistance. Also, the carrier energy loss is incurred due to the bending of both the conduction and valence bands by the applied electric field. Joule heating can be calculated based on the stimulated current flowing through the device. The stimulated current is the current drawn from the source to support the process of stimulated emission. Thus, the Joule heating rate can be calculated as the difference between the stimulated electrical power injected into the device and optical power generated by the stimulated current and hence, the following expression is used:

$$H_{Joule} = \left[\iint J_{stm}(x,z)\, dx\, dz\right]\left(V - \eta\, h\, \frac{c}{\lambda q}\right) \tag{3.38}$$

where $J_{stm}$ is the stimulated current density, $V$ is the applied voltage, $\eta$ is the internal quantum efficiency of the laser, $h$ is Planck's constant, $c$ is the speed of light, $\lambda$ is the wavelength and $q$ is the electron charge. The integration above is performed only in areas where net gain takes place. These areas would include the contact area and extend to where injected carriers defuse.

As the fields back-propagate, they leave the contact area and enter the absorber area, mostly due to diffraction at the aperture between the taper and RW section. Stimulated emission does not take place in these areas, as they are not forward biased, and optical pumping by absorption of the laser beam cannot cause population

inversion at the lasing energy- instead, the absorption saturates the material until it reaches transparency. The absorption of photons leads to generation of carriers, and when they relax to the lower energy state, energy is released in the form of heat. When the absorber regions become transparent (bleached from carriers), this leads to subsequent fields propagating and reaching the back facet. This process is called absorption bleaching. The associated heat is calculated by the following expression:

$$H_{abs} = \left[ \iint J_{stm}(x,z)\, dx\, dz \right] \; h\, \frac{c}{\lambda q} \tag{3.39}$$

In this case, the integration is performed over the regions where net absorption takes place.

The last type of heat we are investigating is the heat generated due to free-carrier absorption, which is the process at which inter-valence band absorption takes place. The heat generated due to free carrier absorption is calculated by [12]:

$$H_{FCA} = h\, \frac{C}{\lambda}\, v_g \iint_{xz} \alpha_{fca}(x,z) dx dz \int_{-\infty}^{\infty} N_{ph}(x,y,z) \phi^2(y;x,z) dy \tag{3.40}$$

Equations (3.38), (3.39) and (3.40) will be used to plot and calculate the heat generated in the device in chapter 5.

## 3.4 References

[1] K. A. Williams, R. V Penty, I. H. White, D. J. Robbins, F. J. Wilson, J. J. Lewandowski, and B. K. Nayar, “Design of high-brightness tapered laser

arrays," *Selected Topics in Quantum Electronics, IEEE Journal of*, vol. 5, no. 3. pp. 822–831, 1999.

[2] J. J. Lim, "Investigation of factors influencing the brightness of high-power laser diodes," University of Nottingham, 2003.

[3] S. Sujecki, L. Borruel, J. Wykes, P. Moreno, B. Sumpf, P. Sewell, H. Wenzel, T. M. Benson, G. Erbert, I. Esquivias, and E. C. Larkins, "Nonlinear Properties of Tapered Laser Cavities," *IEEE J. Sel. Top. Quantum Electron.*, vol. 9, no. 3, pp. 823–834, 2003.

[4] J. J. Lim, S. Sujeck, L. Lang, Z. Zhang, D. Paboeuf, Pauliat, G. Gilles Lucas-Leclin, P. Georges, R. C. I. MacKenzie, P. Bream, S. Bull, K. H. Hasler, B. Sumpf, H. Wenzel, G. Erbert, B. Thestrup, P. M. Petersen, N. Michel, M. Krakowski, E. C. Larkins, "Design and Simulation of Next-Generation High-Power, High-Brightness Laser Diodes," *Selected Topics in Quantum Electronics, IEEE Journal of*, vol. 15, no. 3. pp. 993–1008, 2009.

[5] E. M. Buturla and P. E. Cottrell, "Simulation of semiconductor transport using coupled and decoupled solution techniques," *Solid. State. Electron.*, vol. 23, no. 4, pp. 331–334, 1980.

[6] J. Buus, "The effective index method and its application to semiconductor lasers," *IEEE Journal of Quantum Electronics*, vol. 18, no. 7. pp. 1083–1089, 1982.

[7] H. C. Casey Jr. and M. B. Panish, *Heterostructure Lasers Part A: Fundamental Principles*. Academic Press, 1978.

[8] S. Ramo, J. R. Whinnery, and T. Van Duzer, *Fields and Waves in Communication Electronics*, 3rd ed. John Wiley & Sons, 1994.

[9] G. P. Agrawal, "Fast-Fourier-transform based beam-propagation model for

stripe-geometry semiconductor lasers: Inclusion of axial effects," *J. Appl. Phys.*, vol. 56, no. 11, pp. 3100–3109, 1984.

[10] E. Hecht, *"Optics"*, 4th ed. Pearson, 2014.

[11] J. W. Goodman and R. Gustafson Steven C., "Introduction to Fourier Optics, Second Edition," *Opt. Eng.*, vol. 35, no. 5, p. 1513, 1996.

[12] R. MacKenzie, "Thermal Simulation and Temperature Dependent Measurement of Quantum Well Laser Diodes," University of Nottingham, 2008.

Chapter 4

# 4 Analysis of beam quality degradation in high-brightness tapered lasers at high output power

Tapered laser diodes have been receiving great attention as they combine the high beam quality of ridge-waveguide lasers with the high output power of broad area lasers. The tapered laser diode comprises ridge waveguide (RW) and tapered amplifier (TA) sections. The ridge waveguide supports a single lateral mode. Hence, the output beam is diffraction-limited which is injected into the tapered amplifier. The ridge also serves as a spatial filter (to filter out higher-order lateral modes) for the back-propagating beam, allowing only the fundamental mode to couple into the ridge waveguide. The taper angle is chosen to match the diffraction angle from the ridge waveguide [1], [2], allowing the beam to expand adiabatically in the taper producing a smooth output field profile, as illustrated in Figure 4.1. The tapered amplifier, also, provides a large gain volume with a large output aperture.

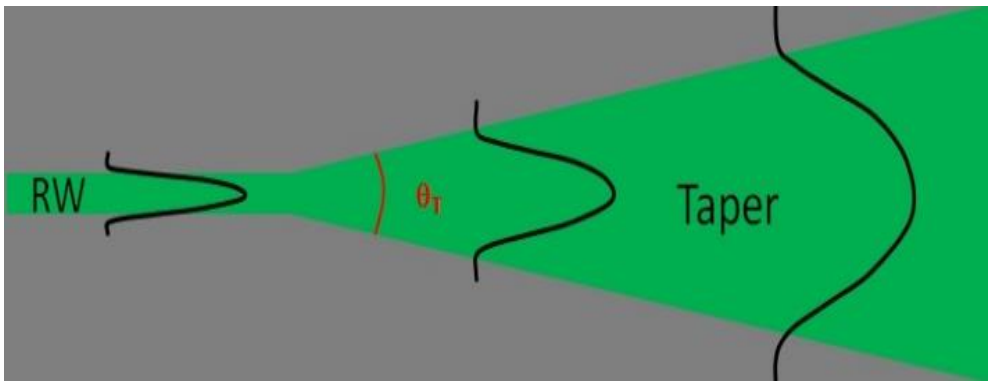



**Figure (4.1): Generic schematic diagram of a tapered laser, showing the adiabatic expansion of the beam in the taper.**

# Chapter 4

A nearly diffraction limited lateral beam is obtained from conventional tapered lasers at low to moderate power, but the beam quality degrades rapidly at high power.

This chapter aims to investigate and analyse the reasons behind the beam quality degradation in tapered lasers at high power. It is beneficial to differentiate the factors intrinsic to tapered lasers from the effect of external feedback on the beam quality, which will be studied in the next chapter.

The main purpose of this chapter is to present an analysis of how beam quality of tapered lasers degrades. It starts by explaining the phenomena responsible for the degradation of beam quality of conventional tapered laser. Previous attempts for improving the beam quality of conventional tapered lasers are also presented and explained. Implementing a patterned rear-facet reflectivity and a DBR was one of successful solutions to the beam degradation problem in conventional tapered laser. However, even DBR tapered lasers suffer from degraded beam quality at currents >2.5 times the threshold bias current. For completeness, the work by Dr. Kaunga-Nyirenda on the impact of RW width and etch depth on beam quality is included. Nevertheless, it is shown that both RW width and etch depth did not improve the beam quality. This motivated the author to investigate the real reason behind this beam quality degradation. The laser simulation tool was used to further investigate why DBR tapered lasers still suffer from poor beam quality at high power.

## 4.1 Beam quality degradation mechanisms in conventional tapered lasers

This beam quality degradation for conventional high-power tapered lasers can

be attributed to multiple factors such as: excess gain at the edges of the taper, leading to index guiding and what is called "Batman ears" in the output near-field [3]; gain saturation inside the ridge waveguide and absorption bleaching in regions adjacent to the RW, by the backward travelling fields outside of it [3]–[5]. Both of these factors lead to reduced RW spatial filtering performance. The absorption bleaching (due to band filling by the generated carriers) renders the material transparent and allows the backward travelling fields outside the RW to reach the rear facet, where they are reflected and re-enter the tapered amplifier, as shown in Figure 4.2. These unfiltered fields create high spatial frequency features in the near field pattern [5], [6].

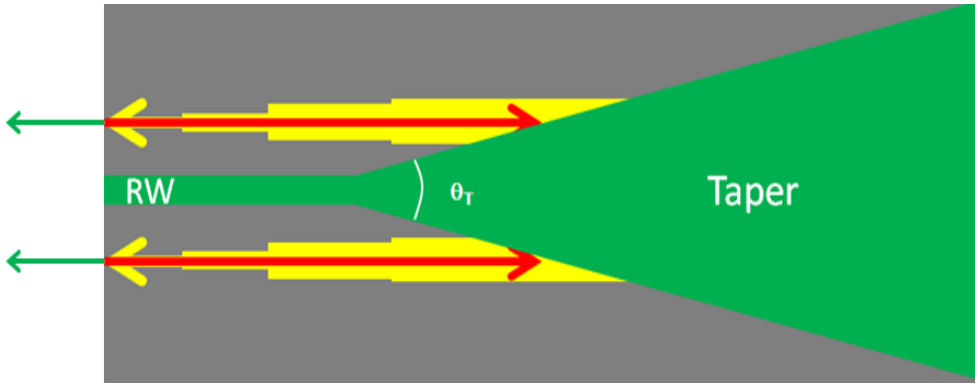
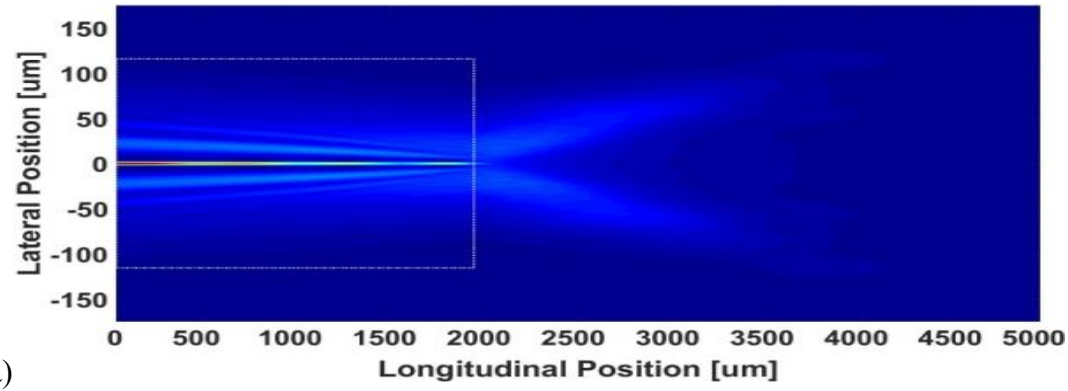


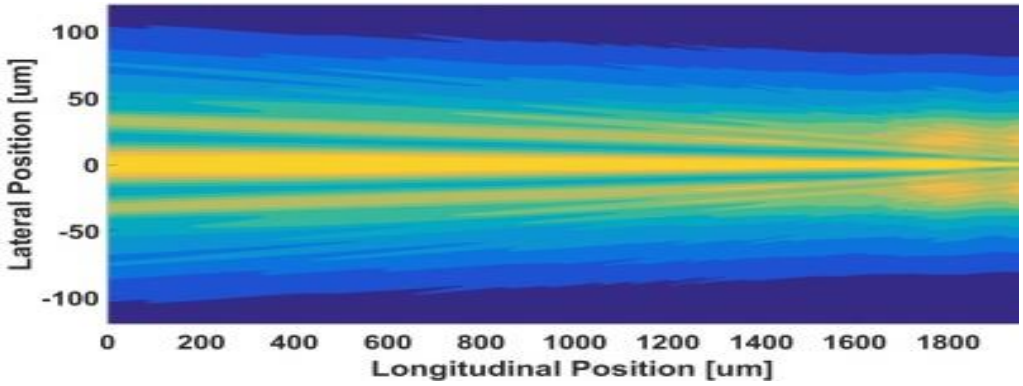

**Figure (4.2): Generic schematic of a conventional tapered laser showing how beam outside the ridge waveguide bleaches the absorption in these regions, allowing the reflected beam from the back fact to travel back and couple into the tapered amplifier.**

Those backward travelling fields in regions adjacent to RW are caused by diffraction of the fields that do not couple into the RW. Figure 4.3 (a) shows the back propagating field in the 975nm DBR tapered laser, described in chapter 3, at I=15A. The backward travelling fields are amplified in the taper and gain-guided at the edges of the taper to form a high- intensity field distribution at the interface where the RW joins the TA. The fields diffracting from this interface are clearly visible alongside the RW. To understand whether the diffraction is due to the high-intensity side lobes or

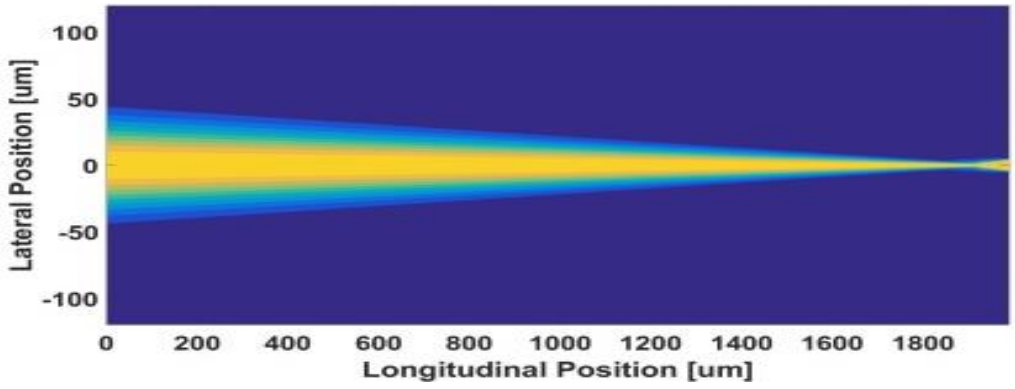
the main lobe, the field at the RW-TA was propagated in the absence of index and gain-guiding effects, as shown in figure 4.3 (b). Figures 4-3 (b-d) correspond to the region inside the white box in figure 4.3 (a). It can be observed that the centre lobe in figure 4.3 (b) expands due to the absence of index guiding effects of the RW. In Figure 4.3 (c), only the central field lobe (the lobe that couples into the RW) was back-propagated, while in Figure 4.3 (d) only the outer lobes of the field, at the RW-TA, were propagated. Figures 4-3 (c-d) show that only the fields that did not couple into the RW give rise to the diffraction pattern - and thus, are responsible for the absorption bleaching and beam quality degradation.



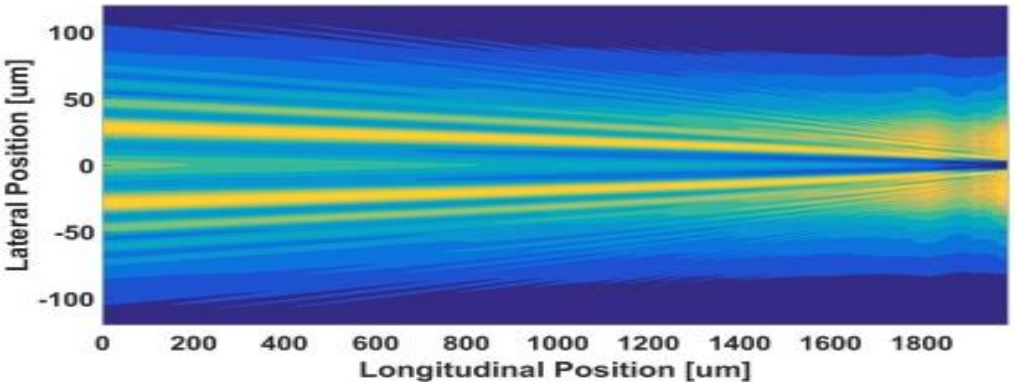

(a)




(b)




(c)




(d)

**Figure (4.3): (a) Backward propagating field in 975nm tapered laser (I = 15A) for converged simulation. Backward-propagated photon distribution in the RW section for transparent, uniform index material for: (b) the total field; (c) the central lobe coupled into the ridge waveguide; and (d) the fields *not* coupled into the ridge waveguide.**

Finally, spatial hole burning at the centre of the taper and electrical over-pumping at the edges creates high carrier densities and gain at the edges of the taper as seen in quantitative intra-cavity spontaneous emission imaging measurements [7], [8]. Amplification and carrier-induced waveguiding in these regions cause the "batman" ears in the near field pattern and amplify / guide the backward fields that degrade the RW filter performance [3], [9].

## 4.2 Attempts to improve beam quality of tapered lasers

Different techniques have been suggested to overcome the degradation of beam

quality, such as reducing the front facet reflectivity, using beam spoilers or using a longer RW section. These techniques were proposed to supress the propagation of fields in the regions adjacent to RW.

Reducing the front facet reflectivity will reduce the intensity of the backward travelling fields. The goal is to eliminate the absorption bleaching in the regions adjacent to the RW, hence, making those regions act as absorbers preventing the reflected fields from the rear facet coupling into the taper. Sujecki *et. al* [3] investigated the impact of reducing the front facet reflectivity, for a 732 nm conventional tapered laser, on the total photon density distribution. Figure 4.4 shows how reducing the front facet reflectivity leads to decreased absorption bleaching by reducing the intensity of the back-propagating waves and hence resulting in a square shaped near-field [3]. At the emitter powers sought for high-brightness direct diode lasers (> 10 W), however, these techniques are insufficient.

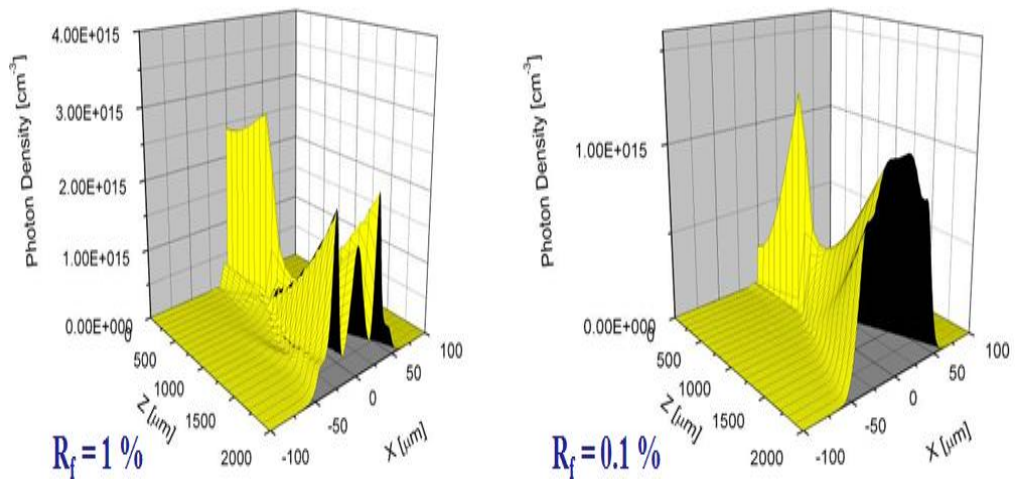



**Figure (4.4): Impact of front facet reflectivity on the shape of forward and backward travelling waves. Both figures (left and right) show the total photon density distribution (forward +backward) [3].**

A profiled rear facet reflectivity, involving an integrated DBR (distributed Bragg reflector) mirror at the end of the RW and AR coated regions, outside the RW,

provides a solution with better high-power performance. The DBR (and AR-coated facet) act a spatial filter, allowing the backward travelling fields in the regions outside the RW to exit the rear facet, as illustrated in figure 4.5.

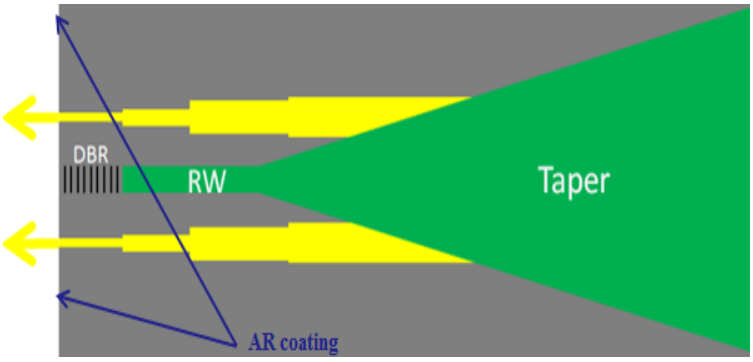



**Figure (4.5): Generic schematic diagram of a DBR tapered laser, showing how the back-propagating beams outside of the ridge waveguide are allowed to leave the structure, instead of coupling back into the tapered amplifier.**

In order to compare the spatial filtering performance of the RW between a conventional tapered laser (with constant rear facet reflectivity) and a DBR tapered laser (with DBR mirror and AR coated rear facet), a RW filter response is used. The RW filter response is defined as the ratio of the forward and backward propagating field distributions at the interface between RW and TA sections [6]:

$$H_{RW} = log_{10}\left[\frac{P_{forward}}{P_{backward}}\right] \quad (4.1)$$

The higher the response in the RW region and the lower the response elsewhere, the better the structure at absorbing fields propagating in the regions outside the RW. Kaunga-Nyirenda *et. al* [4] compared the performance of a DBR tapered laser to a conventional tapered laser both emitting at 1060nm. The two lasers are identical in terms of RW width and length and taper angle, as shown in figure 4.6.

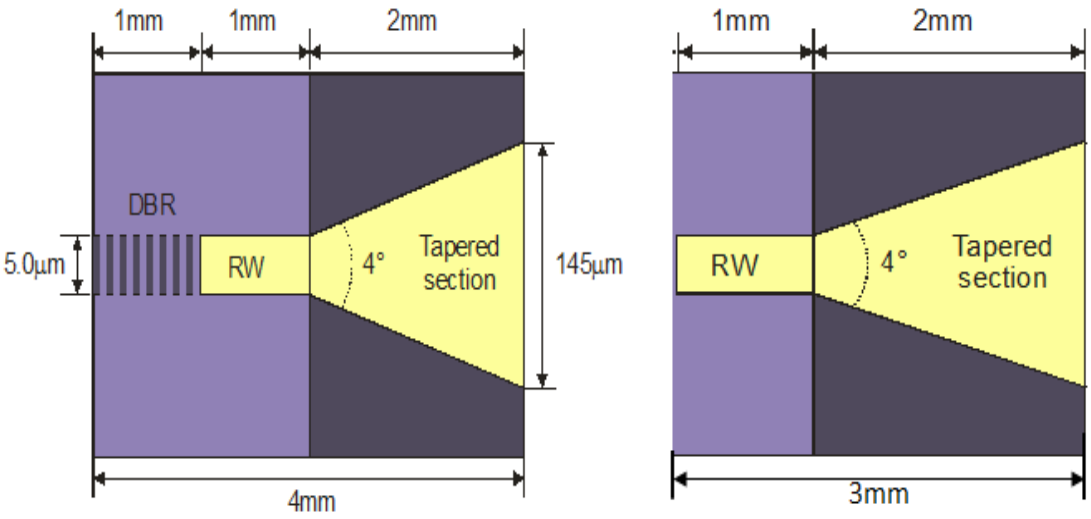



**Figure (4.6): Geometrical structure of the 1060 nm tapered laser [4].**

Figure 4.7 compares the RW filter responses of both the DBR and conventional tapered lasers [6]. The plotted filter responses are for constant taper current and a variable RW current. For the conventional tapered laser, and at $I_{RW} = 0$, it can be observed that the field within the RW is not amplified as well as the fields outside the RW, which are propagating to the rear facet and being reflected. The resultant RW filter performance is significantly poor.

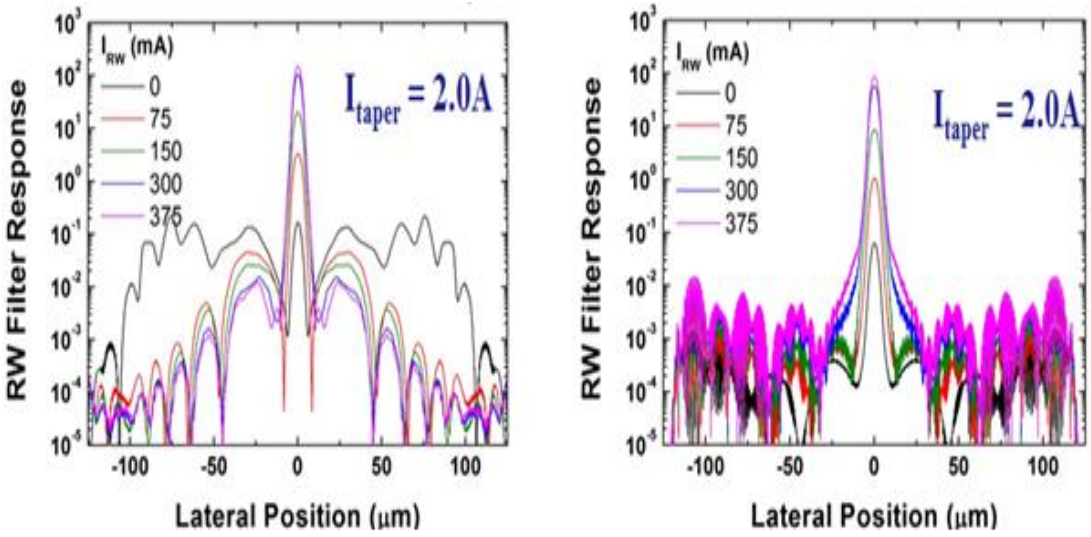



**Figure (4.7): RW filter performance comparison of conventional (left) and DBR (right) tapered lasers [6].**

In the DBR tapered laser, however, due to the AR coated facet (outside RW), the fields outside the RW are lower than that of RW, even at $I_{RW} = 0$. In the DBR tapered laser, fields (outside RW) are not reflected, so the filter performance remains good.

DBR tapered lasers provide a very good beam quality at high power. Beam propagation of $M^2_{e^{-2}} < 1.2$ at powers over 10W were achieved [10]. Nevertheless, $M^2_{2nd\ moment}$ for DBR tapered laser at high powers still increases with power. To understand this, the author presents the work of Dr Kaunga-Nyirenda for BRIDLE, who studied the evolution of the near- and far- field patterns and the RW response with current for asymmetric large optical cavity (ASLOC) DBR tapered laser based on the same lateral design and vertical ELoD2 epitaxy as the DBR tapered laser described in chapter 3, however, with thinner waveguide. The impact of RW width and etch depth is shown in figure 4.8. As the current increases, high spatial frequency features appear in the near field pattern and they grow in strength (figure 4.8 (left)). The high spatial frequencies in the near-field causes the far-field to depart from Gaussian shape and these high-spatial frequencies can be seen to grow in strength with increasing current (figure 4.8 (middle)). As a result, the RW filter performance is degraded; the degradation can reach up to 15 dB as shown in figure 4.8 (right).

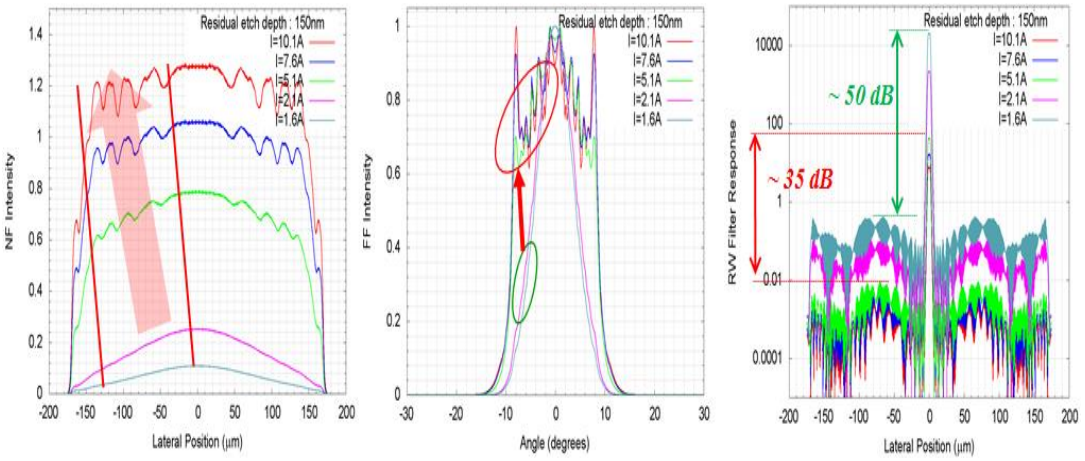



**Figure (4.8): Evolution of near-field (left), far-field (middle) and RW filter response (right) with current (courtesy of Dr Simeon Kaunga-Nyirenda).**

Furthermore, the RW width and etch depth have little impact on beam quality, as seen in figure 4.9. Figure 4.9 also shows that $M^2_{e^{-2}}$ is independent of current, while $M^2_{2nd\ moment}$ increases rapidly with current. For this reason, $M^2_{2nd\ moment}$ provides a more sensitive measure of the changes in the near and far field patterns.

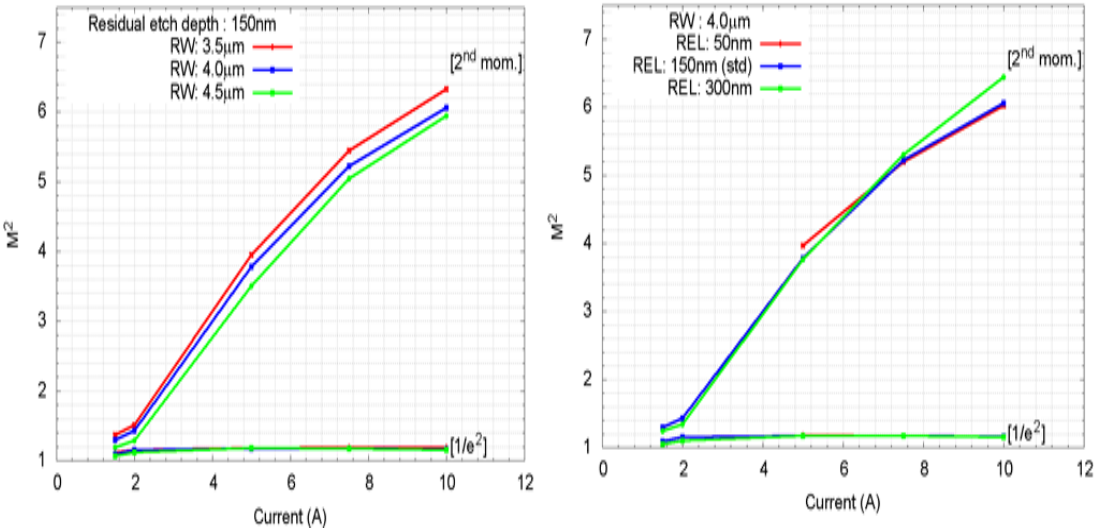



**Figure (4.9): Impact of ridge waveguide width (left) and ridge waveguide etch depth (right) on beam quality, (courtesy of Dr Simeon Kaunga-Nyirenda).**

The high spatial frequency features in the near-field are a clear indication of high-order lateral modes. This motivated the author to investigate the origins of these

higher-order lateral modes by checking nature of the fields in the RW before the RW-TA interface. Figure 4.10 shows the log scale of the forward propagating photon density in the middle of the RW. It is clear that there are fields propagating outside the RW, which will couple into the taper and excite higher-order lateral modes.The question here is: *where do these fields come from?*

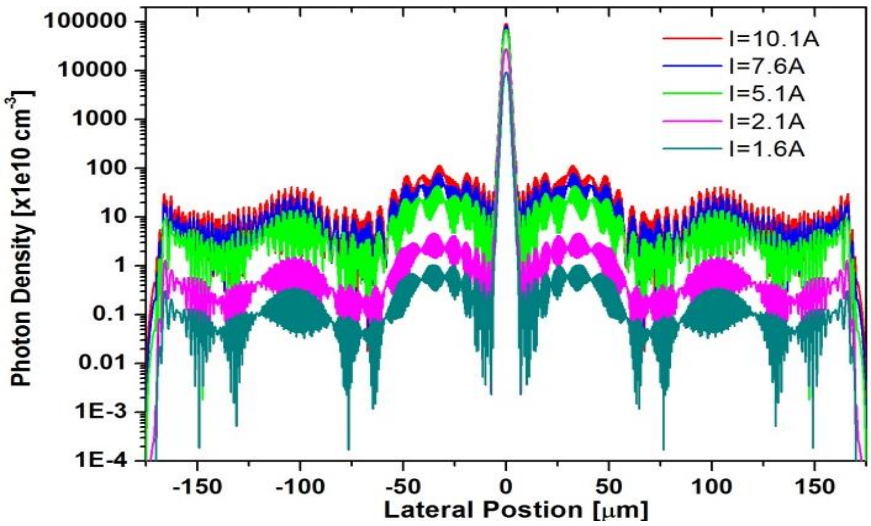



**Figure (4.10): Forward propagating photon density in the middle of the RW section**

There are four possibilities to explain where those fields are coming from: amplified spontaneous emission in the regions outside RW, residual reflections from the AR coating at the back facet (outside RW), lateral mode coupling from the RW to the adjacent carrier-induced parasitic waveguides or leaky mode coupling from RW to the outside regions. Figure 4.10 shows representations of these four possibilities.

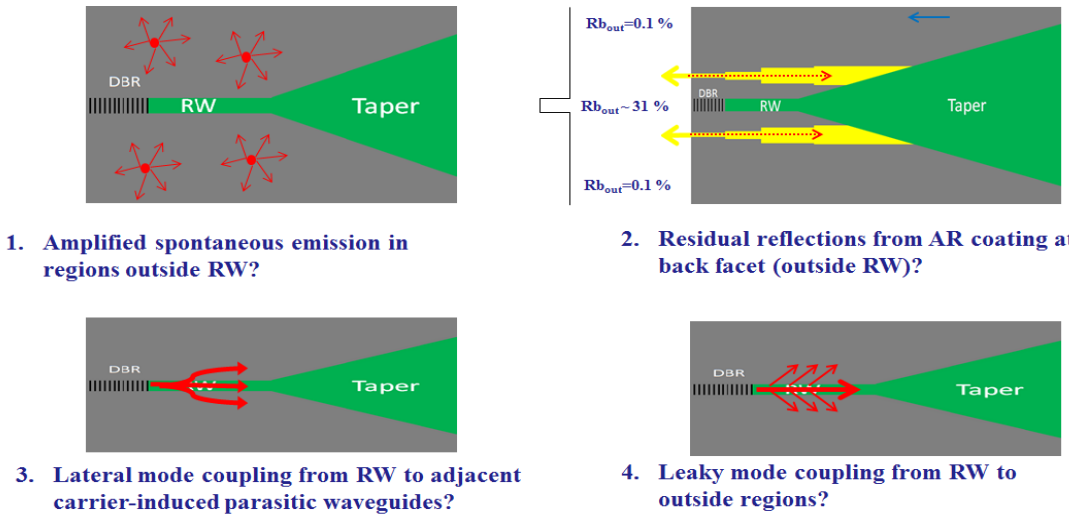
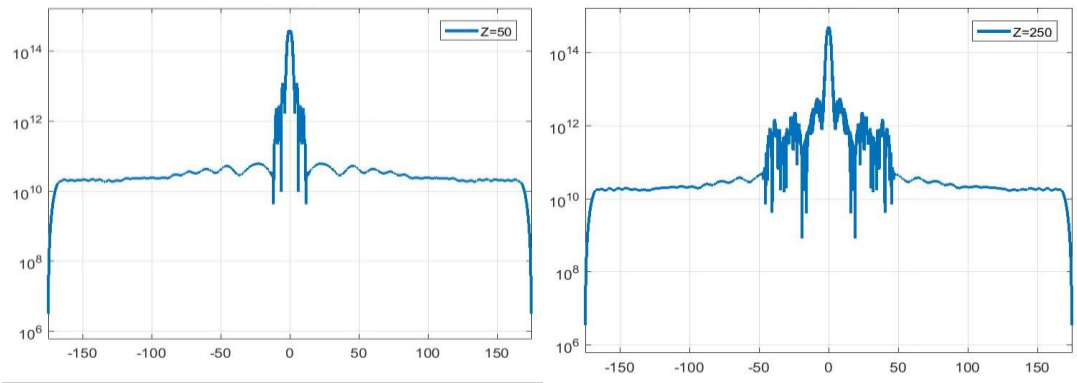



**Figure (4.10): Four possibilities to explain fields forward propagating in the regions outside RW. ASE outside RW (top left). Residual reflections back facet (top right). mode coupling from RW to adjacent parasitic waveguides (bottom left). Leaky mode coupling from RW to outside regions (bottom right).**

The first possibility cannot actually explain the existence of fields outside RW; the amplified spontaneous emission was turned off and the AR coated back facet was given a reflectivity of 0.1%. In order to further investigate this problem, the forward propagating photon density was plotted at different intervals, starting from the back facet until the RW-TA interface, as shown in figure 4.11.



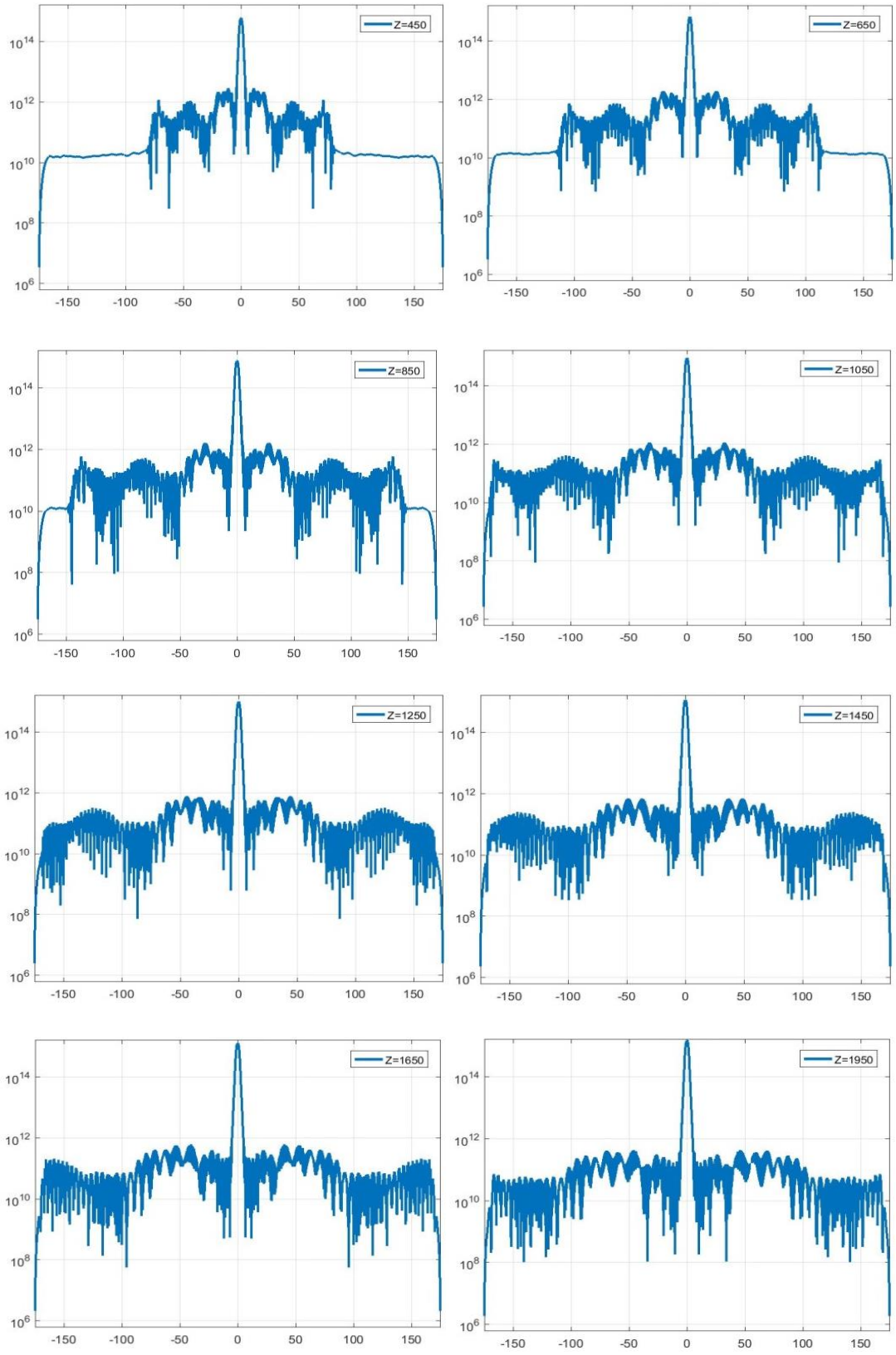



**Figure (4.11): Forward propagating photon distribution between rear facet and the RW/TA interface of a DBR tapered laser.**

Although the fields outside the RW are small, they will be strongly amplified. At the back facet, the ratio between the fields outside RW and inside RW is more than $10^4$. At the RW-TA interface this difference becomes $< 10^3$. The behaviour at which those outside fields grow does not match leaky mode coupling from the RW to the outside regions. Moreover, by plotting the index distribution in the RW section, as shown in figure 4.12, it is clear that the index contrast is $< 10^{-5}$ which is less than needed for significant waveguiding.

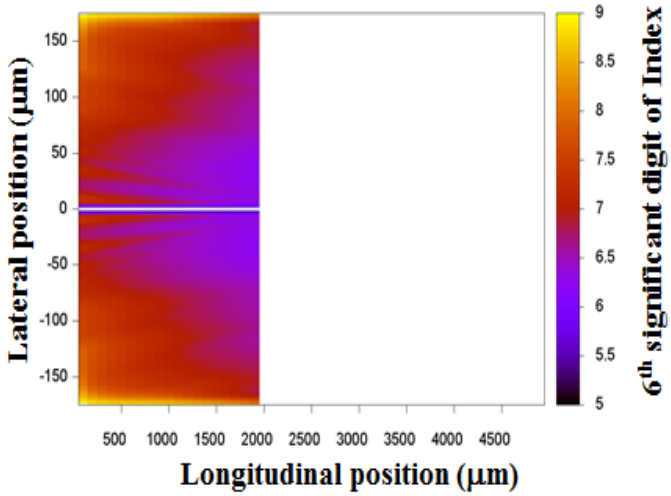



**Figure (4.12): Carrier-induced index distribution in the RW section**

The fields outside the RW section explain the degradation of the filter function, and the changes in the near- and far- field patterns, but there is a problem: *If the backward propagating fields outside the RW all escape through the AR-coated rear facet, then where do these forward propagating fields come from?* The answer lies in the forward propagating photon distribution plotted in figure 4.13.

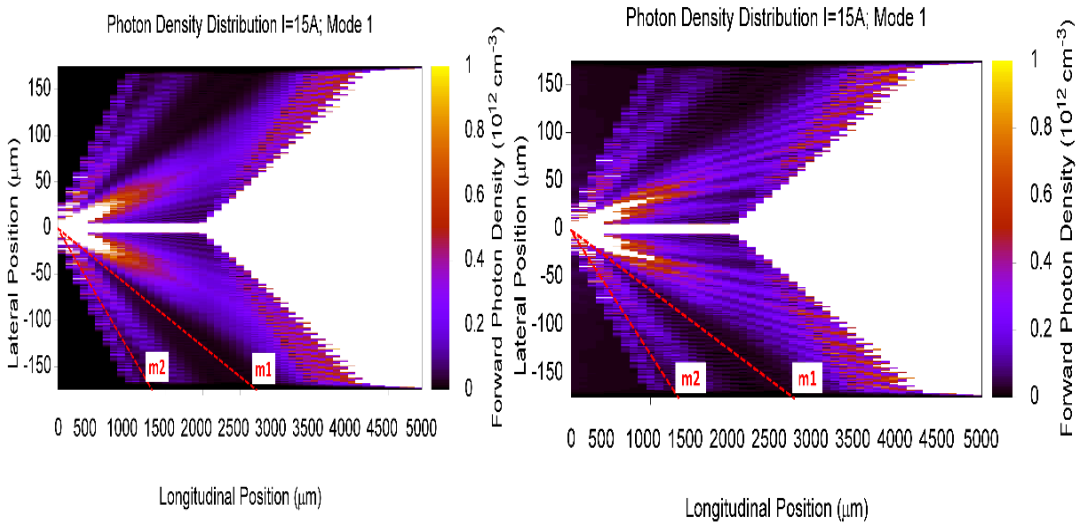



**Figure (4.13): 2D forward propagating photon density with a perfect AR-coating on the rear facet (left) and with an AR-coating with a power reflectivity of 0.1% (right).**

The observed pattern matches the single aperture diffraction pattern as confirmed by the positions of the nodes in the pattern. To validate this analytically, two phenomena need to be considered: the single-slit diffraction at the rear facet and the refraction at the interface between two dielectric regions, namely the RW and the outside region. In other words, the dark fringe angles are shifted by the refraction taking place between the RW and the outside region.

The general expression for dark fringes caused by single-slit diffraction is given by:

$$b \sin \theta_m = m \frac{\lambda}{n} \qquad (4.2)$$

where $b$ is the width of slit, $\theta_m$ is the angle of diffraction, $m$ is the diffraction order of the dark fringe, $\lambda$ is the free-space wavelength and $n$ is the index of medium. In this case, $b$ is the width of the RW and $\frac{\lambda}{n}$ is the wavelength of the diffracted beam inside the RW.

To test whether the dark fringes are caused by diffraction, the measured angles of the dark fringes can be compared to the predicted values. Equation (4.2) calculates the angles of the diffracted beam inside the RW but the observations of the dark fringes in figure 4.13 is in the outside region. Therefore, the refraction of the beam between the RW and the outside region needs to be considered by applying Snell's law (equation 4.3)

$$n_1 \sin \theta_1 = n_2 \sin \theta_2 \qquad (4.3)$$

The theoretical diffraction and refraction of the dark beams from the rear facet is shown in figure 4.14. In calculating these angles, the refractive index of the RW and outer region are assumed to be 3.36566 and 3.36027[1]. The first order dark fringe should occur, assuming the hypothesis, at 4.2° and the second order at 8.32°, as shown in figure 4.14.[2]

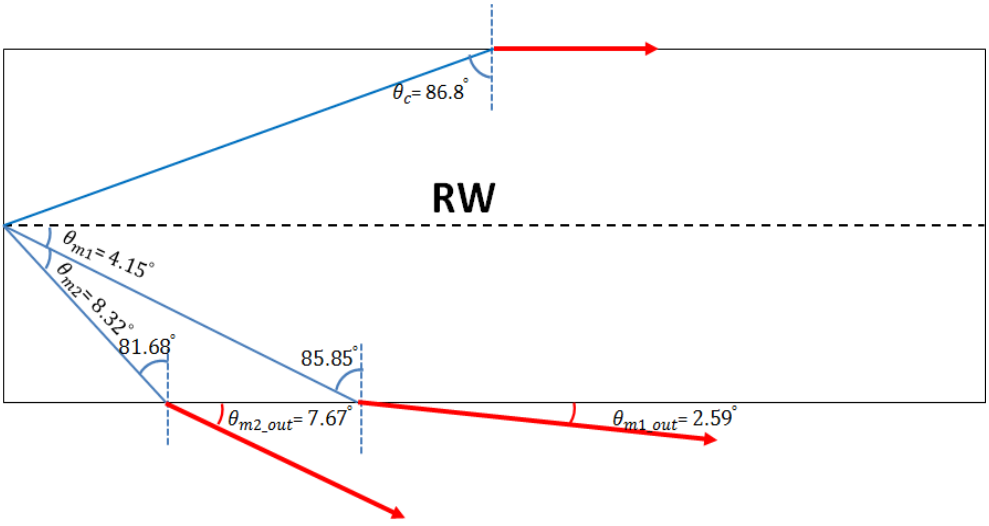



**Figure (4.14): Representation of two "dark" rays going under a slit-diffraction and refraction.**

[1] These refractive index values were provided by Ferdinand Braun Institute, the manufacturer of the simulated tapered laser. Accordingly, these values were used in the calibrated simulation tool.
[2] The x and y scales in figure 4.13 are different which accentuates the dark fringe angles.

The measured dark fringe angles were $4^{\circ}$ and $7.9^{\circ}$ are very close to the predicted values indicating the cause of the dark fringes is diffraction from the back facet.

The discovery of the rear-facet diffraction and that it is the cause behind beam quality degradation is important, especially for photonic circuits engineers where multiple elements are put on one chip and such phenomenon could cause the diffraction beam to couple to other neighbouring elements. Moreover, with these findings, laser engineers can enhance the beam quality by engineering the lateral structure in a way to minimise the intensity of the diffracted beam coupling to the regions outside of the RW.

## 4.3 References

[1] J. N. Walpole, E. S. Kintzer, S. R. Chinn, C. A. Wang, and L. J. Missaggia, "High-power strained-layer InGaAs/AlGaAs tapered traveling wave amplifier," *Appl. Phys. Lett.*, vol. 61, no. 7, pp. 740–742, 1992.

[2] J. E. Pearson, T. C. McGill, S. Kurtin, and A. Yariv, "Diffraction of Gaussian Laser Beams by a Semi-Infinite Plane," *J. Opt. Soc. Am.*, vol. 59, no. 11, pp. 1440–1445, 1969.

[3] S. Sujecki, L. Borruel, J. Wykes, P. Moreno, B. Sumpf, P. Sewell, H. Wenzel, T. M. Benson, G. Erbert, I. Esquivias, and E. C. Larkins, "Nonlinear Properties of Tapered Laser Cavities," *IEEE J. Sel. Top. Quantum Electron.*, vol. 9, no. 3, pp. 823–834, 2003.

[4] S. N. Kaunga-Nyirenda, S. Bull, J. J. Lim, K. h. Hasler, J. Fricke, and E. C.

Larkins, “Factors influencing brightness and beam quality of conventional and distributed Bragg reflector tapered laser diodes in absence of self-heating,” *IET Optoelectronics*, vol. 8, no. 2. pp. 99–107, 2014.

[5] E. C. Larkins, S. Bull, S. Kaunga-Nyirenda, M. A. Helal, V. Vilokkinen, P. Uusimaa, P. Crump, and G. Erbert, “Design Optimisation of High-Brightness Laser Diodes for External Cavity Operation in the BRIDLE Project,” *Semiconductor Laser Conference (ISLC), 2014 International*. pp. 21–22, 2014.

[6] J. J. Lim, S. Bull, S. Kaunga-Nyirenda, S. Sujecki, E. C. Larkins, K. H. Hasler, and J. Fricke, “Factors influencing the brightness and beam quality of tapered laser diodes and bars,” *2012 IEEE Photonics Soc. Summer Top. Meet. Ser. PSST 2012*, vol. 1, pp. 35–36, 2012.

[7] S. Bull, J. Wykes, A. V. Andrianov, J. J. Lim, L. Borruel, S. Sujecki, S. C. Auzanneau, M. Calligaro, M. Krakowski, I. Esquivias, and E. C. Larkins, “Imaging of spontaneous emission from 980 nm tapered lasers with windowed N-contacts,” *Eur. Phys. J. Appl. Phys.*, vol. 27, pp. 455–459, 2004.

[8] S. Bull, A. Andrianov, J. G. Wykes, J. J. Lim, S. Sujecki, S. C. Auzanneau, M. Calligaro, M. Lecomte, O. Parillaud, M. Krakowski, and E. C. Larkins, “Quantitative imaging of intracavity spontaneous emission distributions using tapered lasers fabricated with windowed n-contacts,” *IEE Proceedings - Optoelectronics*, vol. 153, no. 1. pp. 2–7, 2006.

[9] K. A. Williams, R. V Penty, I. H. White, D. J. Robbins, F. J. Wilson, J. J. Lewandowski, and B. K. Nayar, “Design of high-brightness tapered laser arrays,” *Selected Topics in Quantum Electronics, IEEE Journal of*, vol. 5, no.

3. pp. 822–831, 1999.

[10] C. Fiebig, G. Blume, C. Kaspari, D. Feise, J. Fricke, M. Matalla, W. John, H. Wenzel, K. Paschke, and G. Erbert, “12W high-brightness single-frequency DBR tapered diode laser,” *Electronics Letters*, vol. 44, no. 21. pp. 1253–1255, 2008.

Chapter 5

# 5 Investigation of the role of parasitic feedback on DBR tapered laser

High-brightness tapered lasers are usually characterised and simulated as stand-alone devices. Nevertheless, when utilised in an external cavity, these devices are exposed to back reflections. These back reflections result in external feedback that can couple into the laser cavity and lead to performance degradation. Therefore, simulation of large optical cavity (LOC) high-power and high-brightness laser diodes operating in external optical systems is required to model how these devices will perform once operated in external optical systems. The coupling of external feedback into the laser cavity is responsible for degradation of the slow-axis beam quality and can excite higher order vertical modes, leading to current leakage and a corresponding drop in output power and efficiency. The propagation of these higher order modes will also generate different types of heat such as Joule heating, free-carrier absorption heat and absorption bleaching heat. Moreover, in real systems, where tens of Watts are required, multiple laser diodes are fabricated in a laser bar. Laser bars often bend slightly when they are soldered to a heatsink, so that the emitter near field patterns deviate from a straight line – an effect referred to as "smile"[1]. Figure 5.1 shows how “smile” of packaged laser bars displaces the emitters vertically ($\pm$ 0.5 $\mu m$) from the axis. This leads to pointing errors and different external optical feedback levels coupled to different emitters within the bar, leading to different performances by different emitters, eventually leading to performance degradation of the whole laser bar.

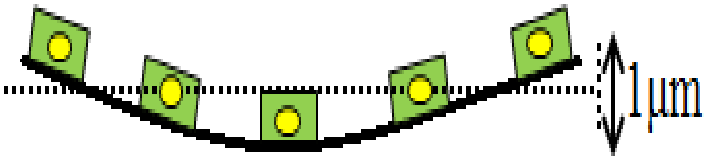



**Figure (5.1): "Smile" of a linear laser array or bar, which is caused by bending as the bar is soldered to a heatsink.**

In this chapter, the simulation of a LOC tapered laser operating in a simple optical system, comprised of fast- and slow-axis beam collimation lenses and an uncoated optical fibre, is presented. The output light from the laser is collimated in both directions and is incident on the end of an uncoated fibre, with a reflectivity of $R = 5\%$, as illustrated in Figure 5.2.

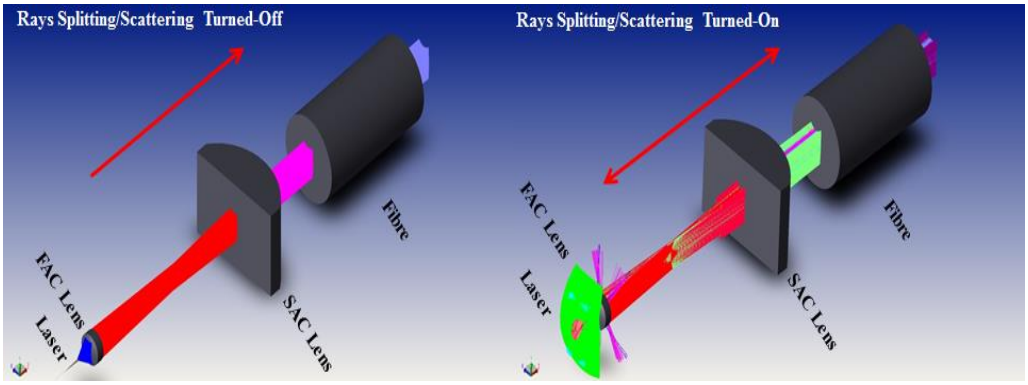



**Figure (5.2): External cavity setup used in the simulation consists of a FAC (fast-axis collimation) lens, an SAC (slow-axis collimation) lens and a fibre. Rays splitting and scattering turned off (left). Rays splitting and scattering turned on (right).**

This described setup is used to simulate the high-brightness tapered laser with two feedback conditions: with feedback and without feedback. By vertically displacing the laser, in *OpticSudio*, in the range ($\pm 0.5\mu m$), different levels of feedback are coupled at different displacements. This was done to emulate external feedback coupling to different laser diodes in a laser bar with a “smile”.

The purpose of this study is to analyse how the feedback from the external optical system, whether it is to all vertical modes or some, affects the performance the laser, and also to observe the impact of external optical feedback on the excitation of

higher-order vertical modes. The laser performance is characterised by optical and electro-optical metrics such as: output power, power conversion efficiency and lateral beam quality and, therefore, these metrics will be observed and compared in various feedback cases. This study will also reveal how the excitation of higher-order vertical modes gives rise to additional self-heating mechanisms. The significance of investigating additional heat mechanisms comes from the fact that they represent a new path of power loss and hence directly affect the PCE. Finally, this study will explore approaches for supressing the impact of exciting higher-order vertical modes.

This chapter starts by describing the laser diode simulated and the parameters used to simulate it, then 3 external cavity simulations are performed, corresponding to 3 different vertical displacements. The laser performance in these 3 cases is compared to the performance of the stand-alone laser. Finally, the results are discussed and analysed.

## 5.1 Description of the laser and simulation parameters

The laser diode in this study is a 975 nm LOC distributed Bragg reflector (DBR) tapered laser based on the extremely low vertical divergence (ELoD2) structure [2]. The ELoD2 structure is based on a 4.8 μm thick $Al_{0.15}Ga_{0.85}As$ vertical waveguide, with three InGaAs quantum wells, separated by $GaAs_{0.66}P_{0.34}$ barriers. This laser diode has a 4 μm wide and 2 mm long ridge waveguide and a 3mm long gain-guided amplifier with a 6° taper. The DBR is represented by a patterned reflectivity (R = 31% inside the ridge waveguide, R = 0.1% adjacent to it). The front facet reflectivity is 1%. A schematic diagram of the laser diode is shown in figure 5.3. Simulations were performed at bias currents of 2.5, 5.0, 10, 15 and 20 A. The discussion will focus on

the performance of the laser at a bias current of 15 A, since this produces an output power in the range of interest (10-12 W).

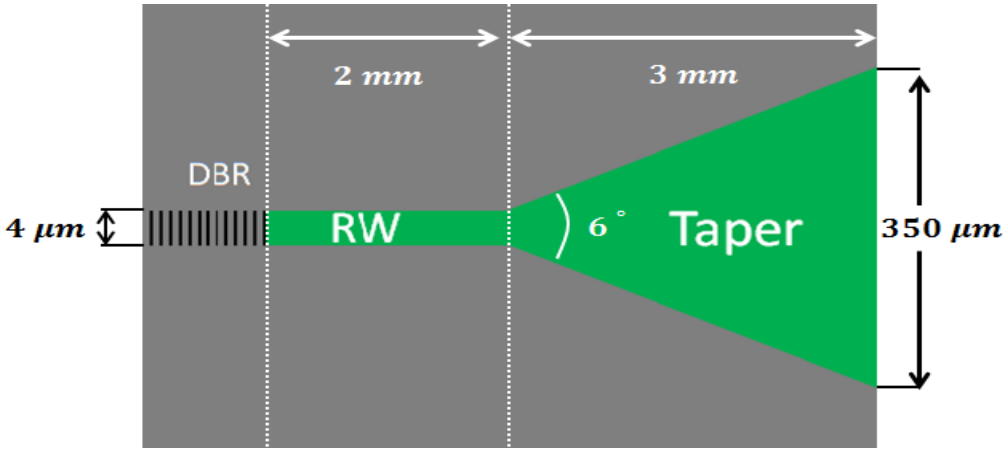



**Figure (5.3): Schematic of ELoD2 tapered laser.**

Figure 5.4 shows the simulated and experimental power and PCE –vs– current behaviour of an ELoD2 broad area (BA) laser.

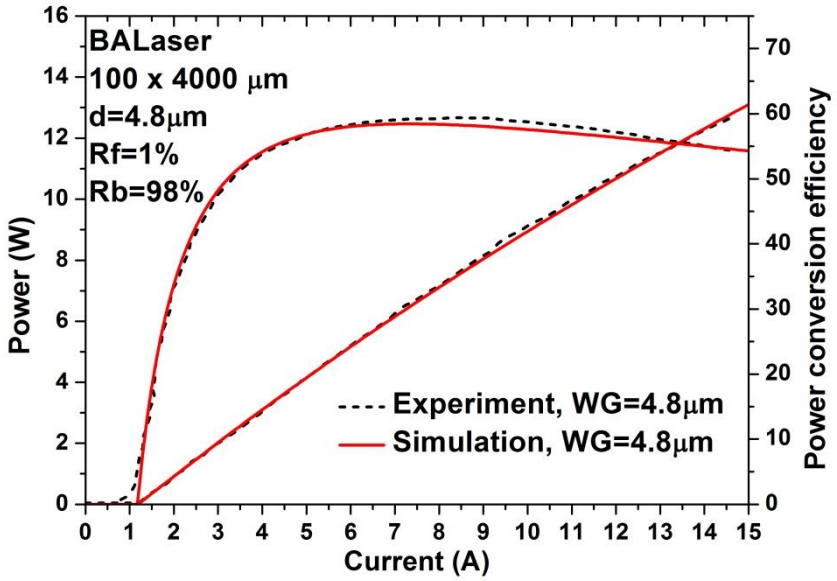



**Figure (5.4): Simulation vs. experiment for ELoD2 structure.**

Stray external cavity reflections are included by enabling ray splitting and scattering in *OpticStudio*.

Two types of external cavity simulations were performed; on- and off-axis, and both were compared to a stand-alone simulation, i.e. no external feedback. The

overlap integrals of the externally reflected field of the fundamental mode (from the stand-alone simulation) and each of the vertical cavity modes were calculated in order to estimate the coupling coefficients of laser output beam to each of the vertical modes. The coupling coefficients were calculated for different vertical displacements, as shown in Figure 5.5, to show how these coupling coefficients change with vertical displacement (VD). To investigate the impact of different values of feedback to different vertical modes, two off-axis points were chosen: one at a displacement of $+\ 0.5\ \mu m$, where the fundamental mode coupling coefficient (29.5%) approaches that of a higher-order mode (19%, mode 2) and another at $-\ 0.25\ \mu m$, where the coupling coefficient of mode 4 (the mode with lowest modal discrimination) approaches its highest value: 10%.

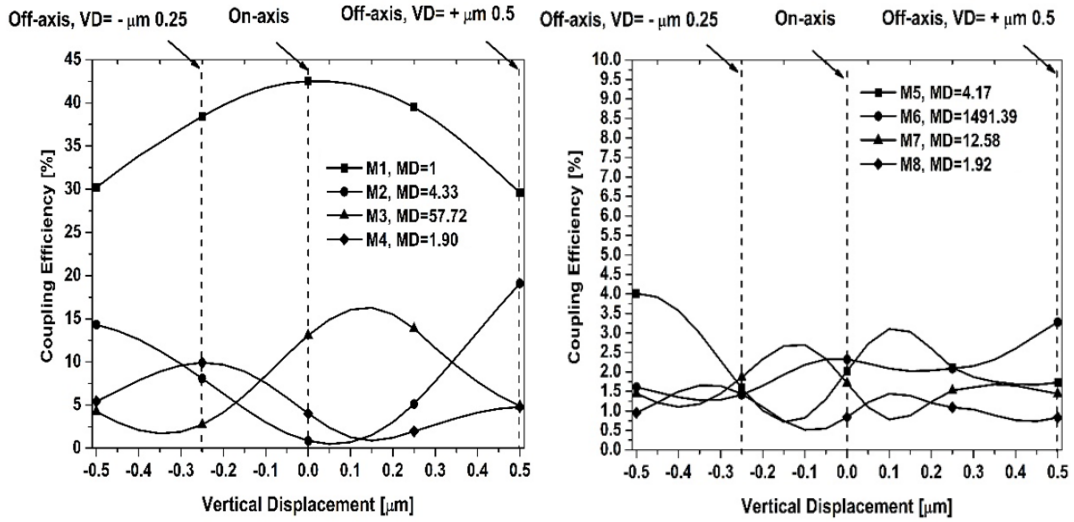



**Figure (5.5): Impact of smile on external cavity coupling coefficients. Modes M1-M4 (left) have coupling > 10%, while modes M5-M8 (right) have coupling < 5% (right). Two off-axis points of interest are: displacement= +0.5 μm and displacement= -0.25 μm**

## 5.2 Parasitic reflections with on-axis alignment

Figures 5.6 and 5.7 show the power –vs– current and PCE –vs– current characteristics, respectively, to compare the performance of the laser with and without

feedback. Both figures show that the optical feedback reduces the output power and the power conversion efficiency. At I = 15 A, the on-axis feedback caused the fundamental mode power, mode 1, to drop from 11.67 W to 9.49 W, while the PCE fell from 47.1% to 38.4%. Figures 5.6 and 5.7 also show that the higher the output power, the higher the feedback and the more power and PCE drop.

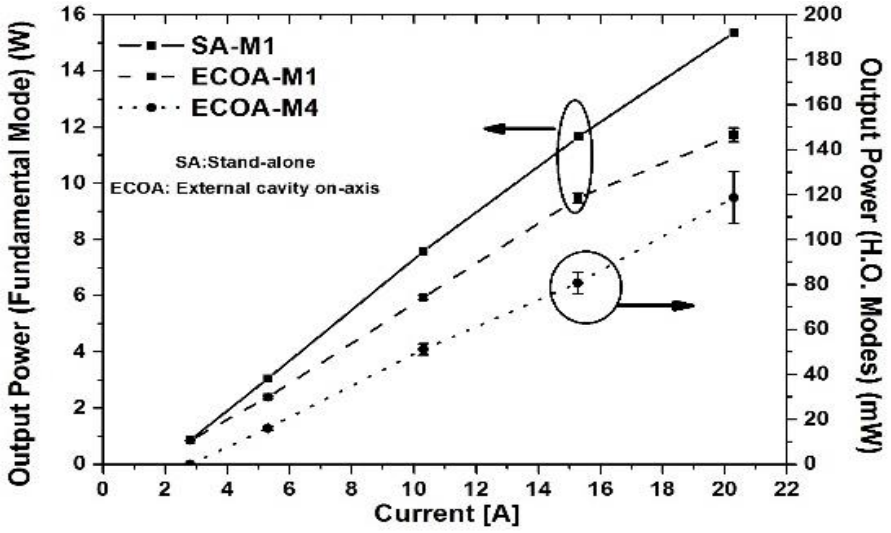



**Figure (5.6): Comparison of L-I curves of lasing modes (M1 and M4) for stand-alone (SA) and external cavity with on-axis (ECOA) feedback configurations.**

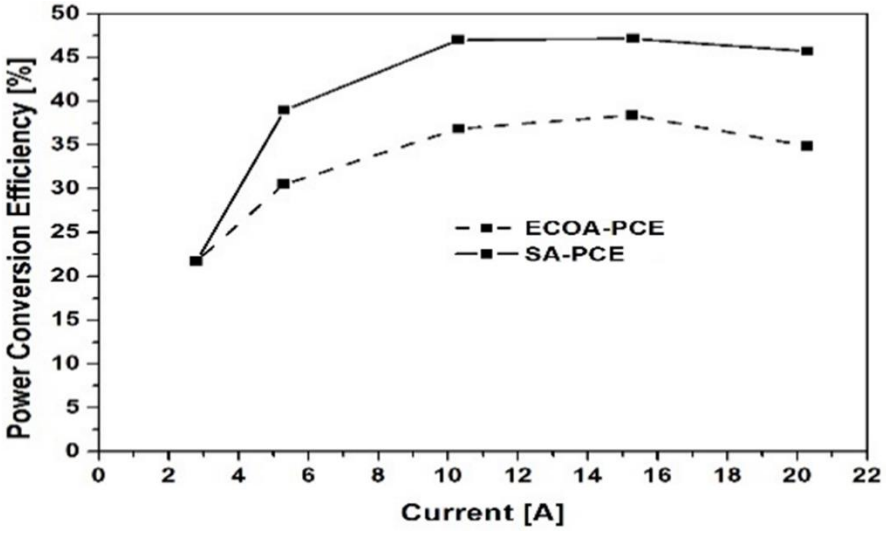



**Figure (5.7): Simulated power conversion efficiency (PCE) of the tapered laser with external cavity on-axis feedback (ECOA) and without feedback, i.e. stand-alone (SA).**

Figures 5.8 and 5-9 compare the lateral near field and far-field patterns,

respectively, of the on-axis laser simulation with and without feedback. The feedback also increases the modulation depth of the high spatial frequency components in the near-field pattern, as observed experimentally by Leonhäuser *et. al.* and Hempel *et. al.*[3], [4]. The feedback may also lead to excitation and lasing of higher order modes. In this case mode 4 also lases.

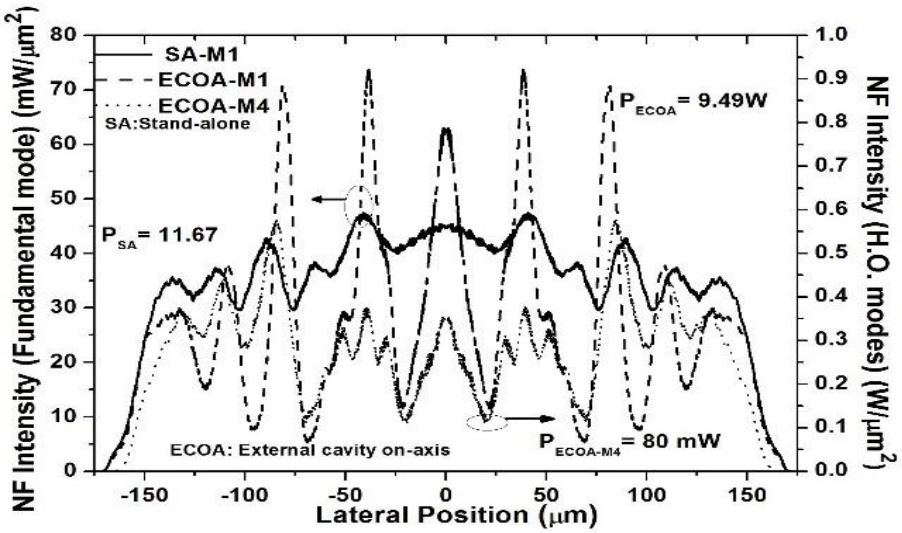



**Figure (5.8): Lateral near field profiles of lasing vertical modes (M1 and M4) for external cavity with on-axis (ECOA) feedback stand-alone (SA) simulations.**

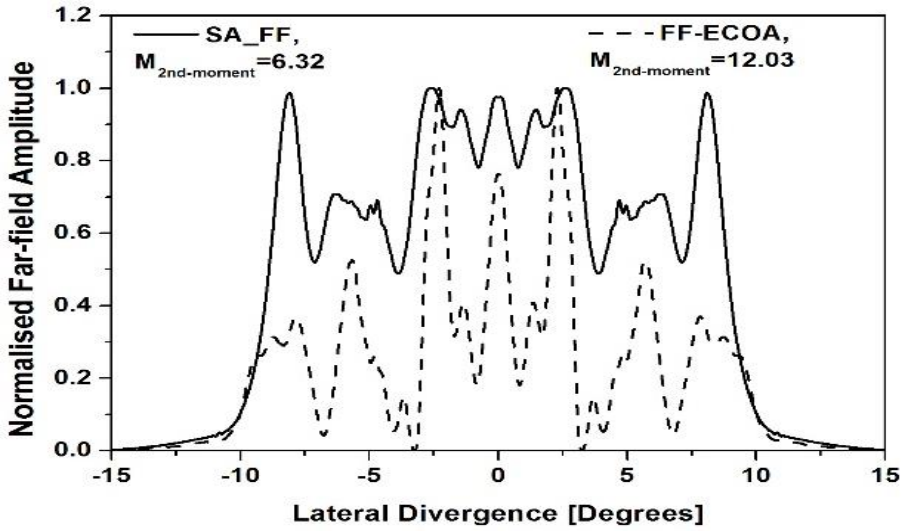



**Figure (5.9): lateral far-field profiles of the fundamental vertical mode for external cavity with on-axis feedback (ECOA) feedback and stand-alone (SA) simulations.**

Figure 5.10 shows the current dependence of the beam propagation factor $M_x^2$ (both the $e^{-2}$ and $2^{nd}$ moment definitions) for the on-axis external cavity feedback and stand-alone simulations.

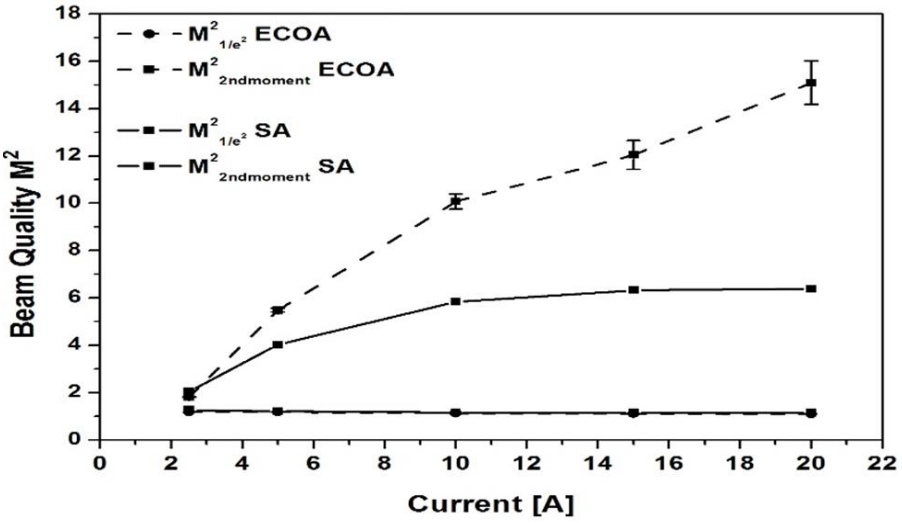



**Figure (5.10): Dependence of $M_x^2$ on bias current for stand-alone (SA) and external cavity with on-axis (ECOA) feedback simulations.**

At I=15A, the feedback had little effect on $M_{x,e^{-2}}^2$, but $M_{x,2ndmoment}^2$ increased from 6.32 to 12.03. This illustrates very clearly the importance of using the 2nd moment definition.

The total photon distributions (the sum of forward and backward propagating photon densities) for the laser of on-axis feedback are shown in Figure 5.11 for the first four vertical modes. Only modes 1 and 4 are lasing. Nevertheless, light is also coupled into the other modes. Although they do not lase or produce an output beam (and are difficult to characterise and easy to overlook) they affect the laser through optical pumping (absorption bleaching), parasitic current leakage and parasitic power-loss/heat generation.

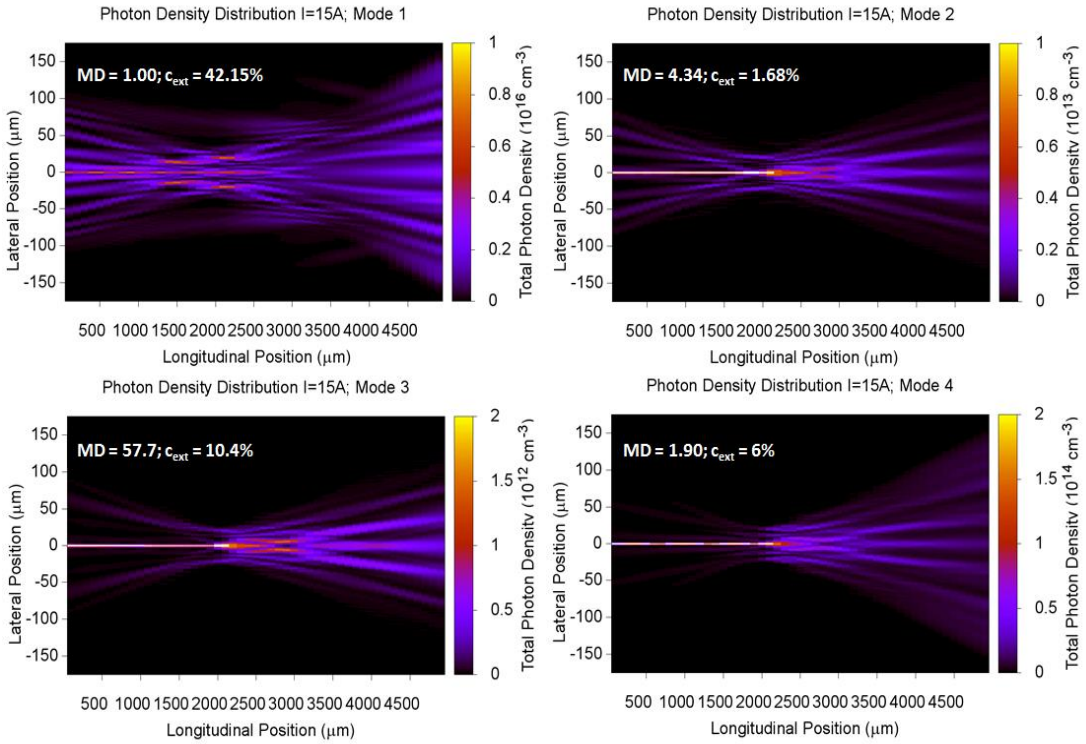



**Figure (5.11): Total photon density for mode 1 (top left) mode 2 (top right) mode 3 (bottom left) mode 4 (bottom right). Modal discrimination (MD) and coupling coefficient ($C_{ext}$) are quoted for each mode.**

For comparison, figure 5.12 shows the total photon density distribution of the fundamental mode from the stand-alone simulation. Figure 5-11 shows clearly how the external feedback leads to high density photon distributions in the areas adjacent to the RW, leading to increased absorption bleaching.

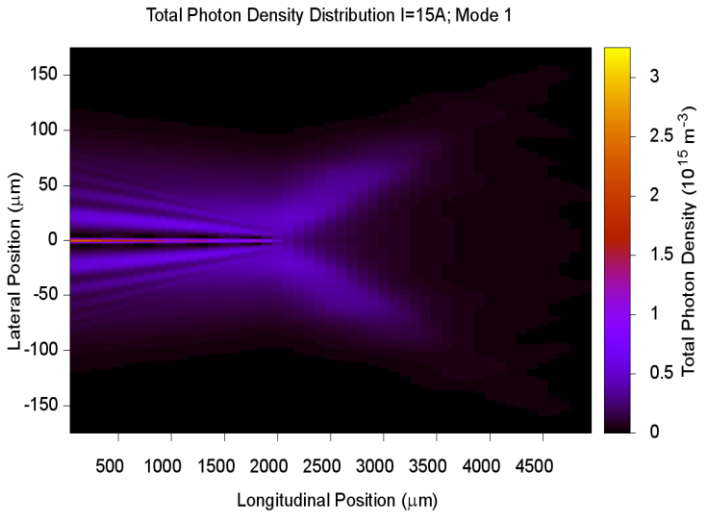



**Figure (5.12): Total photon density of mode 1 for stand-alone simulation.**

Figure 5.13 shows the Joule heating distributions caused by the currents supporting stimulated emission of the different modes at I=15A – as well as how the different vertical modes share/compete for the available gain.

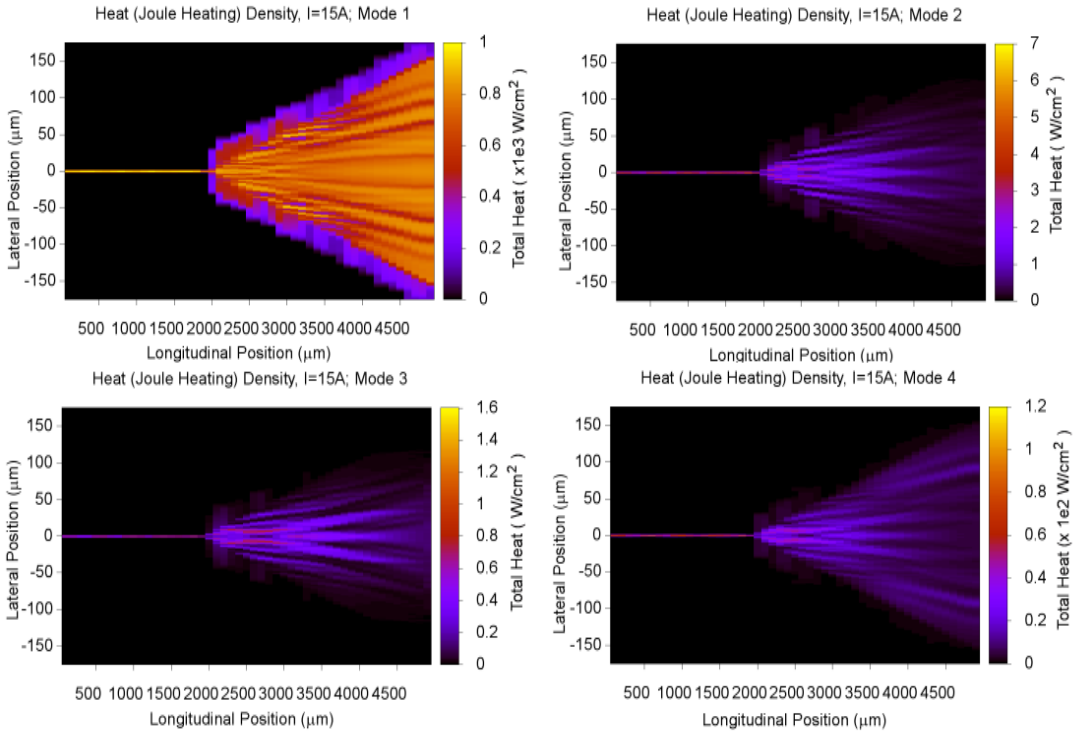



**Figure (5.13): Self-heating due to Joule heating by mode 1 (top left), mode2 (top right), mode 3 (bottom left) and mode 4 (bottom right) at a bias current of I=15A and with on-axis external feedback.**

These distributions show where the stimulated emission occurs within the device for each of the vertical modes. For the higher order modes, this occurs solely because of the power fed back into them from the external cavity. Figure 5.14 shows the self-heating distributions due to optical pumping (absorption) at I=15A.

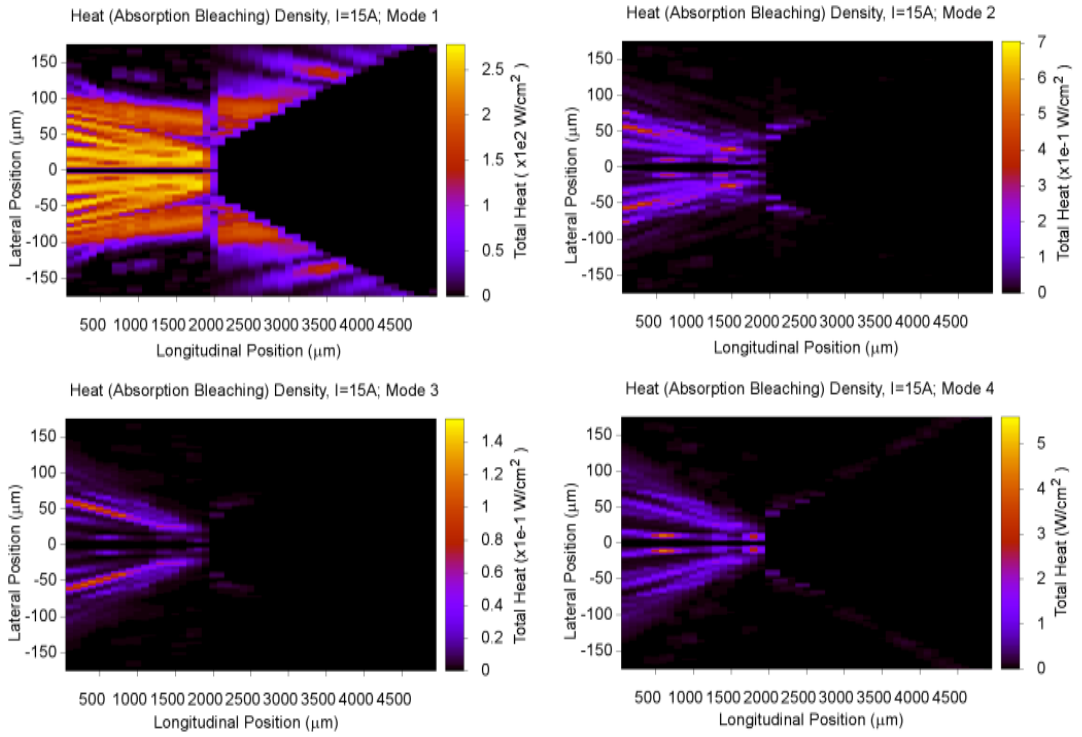



**Figure 5.14: Distribution of self-heating due to optical pumping for mode 1 (top left), mode2 (top right), mode 3 (bottom left) and mode 4 (bottom right) at a bias current of I=15A and with on-axis external feedback.**

This pumping causes the absorption bleaching which plays a critical part in the degradation of the RW spatial filter performance. These distributions show the spatial distribution and the relative contributions of the vertical modes to the absorption bleaching. The fundamental mode clearly plays a dominant role in the optical pumping, but the other modes also contribute. For comparison, figure 5.15 shows the optical bleaching heat distribution for the fundamental mode in a stand-alone simulation.

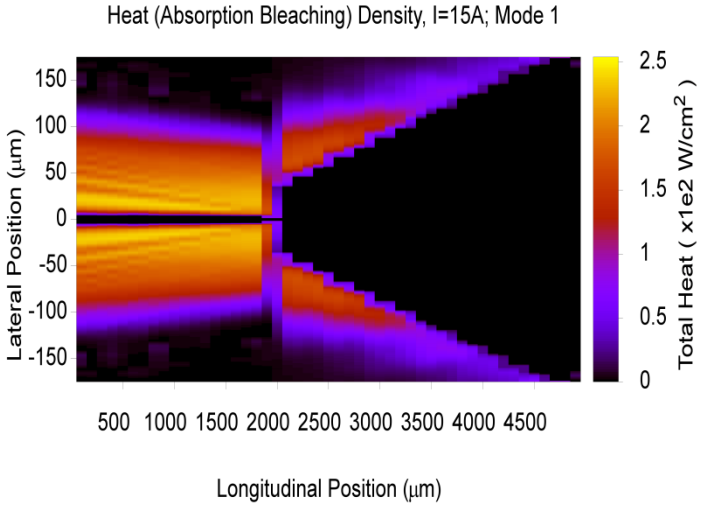



**Figure 5.15: Distribution of self-heating due to optical pumping by mode 1 at a bias current of I=15A without external feedback.**

Figure 5.16 shows the spatial distributions of self-heating due to free carrier absorption (FCA).

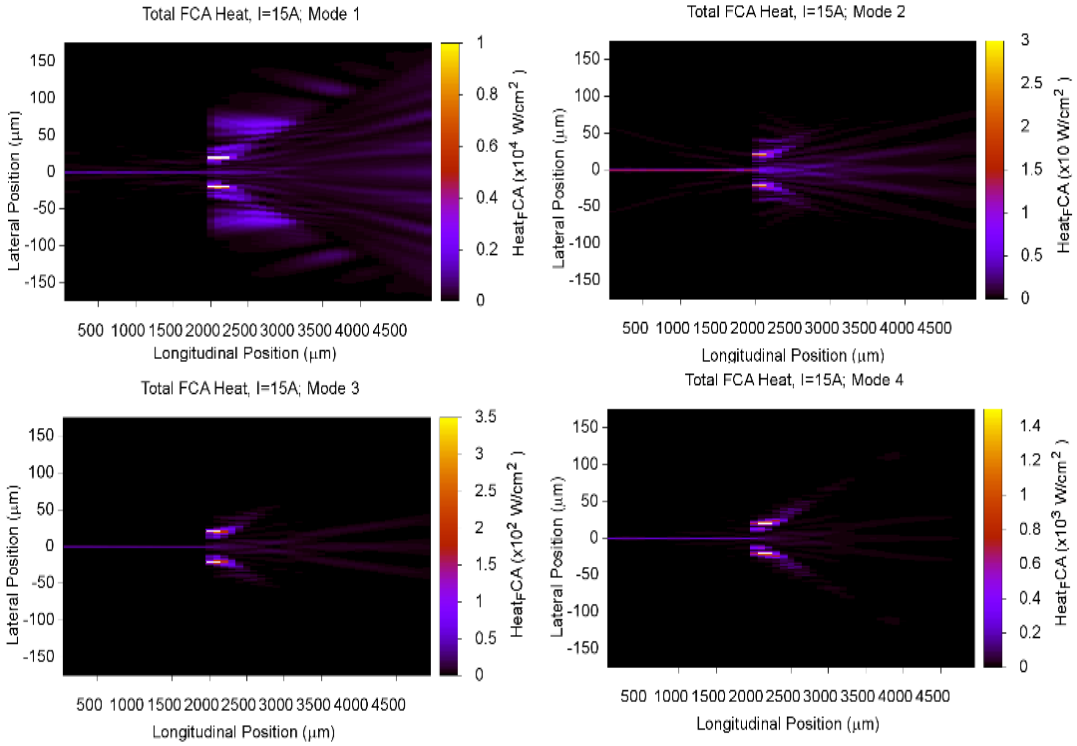



**Figure (5.16): Distribution of self-heating due to free carrier absorption by mode 1 (top left), mode 2 (top right), mode 3 (bottom left) and mode 4(bottom left) at a bias current of I=15A with on-axis external feedback.**

The drop in FCA to the left of the RW-TA interface is due to the RW etch. The higher

order modes lose much more power due to free-carrier absorption than to optical pumping.

The excited higher order modes clearly play a role in the operation of the device, but their overall power is small compared to that of the fundamental mode (which also receives the greatest feedback power). The question is, whether the degradation in PCE and beam quality is primarily caused by the feedback to the higher order vertical modes or to the fundamental vertical mode. Table 5.1 compares the output power, power conversion efficiency and $M^2{}_{2ndmoment}$ for the laser in isolation (stand-alone), with on-axis feedback to all vertical modes, with on-axis feedback only to the fundamental mode and with on-axis feedback only to the higher-order modes.

| **Simulation** | **Output Power (W)** | **PCE (%)** | $\boldsymbol{M^2{}_{2nd\ moment}}$ |
|---|---|---|---|
| Stand-alone | 11.67 | 47.13 | 6.32 |
| External Cavity (all modes) | 9.49 | 38.39 | 12.04 |
| External Cavity (mode1 only) | 9.46 | 38.13 | 12.3 |
| External Cavity (H.O. modes only) | 8.52 | 35.7 | 6.431 |

**Table (5.1): Impact of external cavity feedback on the laser performance (power, efficiency and beam quality) for coupling to all modes and for coupling just to the fundamental mode.**

It is clear that the feedback to the higher-order modes has the greatest effect on PCE while their impact on beam quality is minimal. This is understood as the feedback to the fundamental mode leads to degraded beam quality while feedback to higher order vertical modes plays a smaller role. The significant drop in PCE can be explained in the context of increased stimulated current going to the higher-order modes to support the stimulated emission caused by the external feedback. On the

other hand, the beam quality was not affected by external feedback to these modes as the intensity of the lateral field of the fundamental mode decreased and hence, the diffracted field from the DBR (explained in chapter 4) had less intensity as it couples into the taper. Figure 5.17 shows the comparison of the near-field intensity profile of the fundamental mode for the three cases of stand-alone and external feedback coupled to only higher-order modes and external feedback coupled only to the fundamental mode. The near-field pattern in the case of coupling to higher-order modes has a good degree of resemblance to the near-field pattern in the stand-alone case. The difference comes from the carrier-lensing effect created by the feedback. On the other hand, the near-field pattern in the case of feedback coupling to the fundamental mode shows high intensity filaments compared with the near-field in the stand-alone case. When external feedback couples to the fundamental mode, it increases the intensity of the back-propagated beam, and hence, the absorption bleaching adjacent to the RW and it also increases the power incident on the DBR reflector inside the RW, as discussed in section chapter 4. All of these will contribute to the beam quality degradation in two ways first: by reducing the spatial filtering of the RW and second by increasing the power in the side-lobes of the diffraction from the DBR reflector.

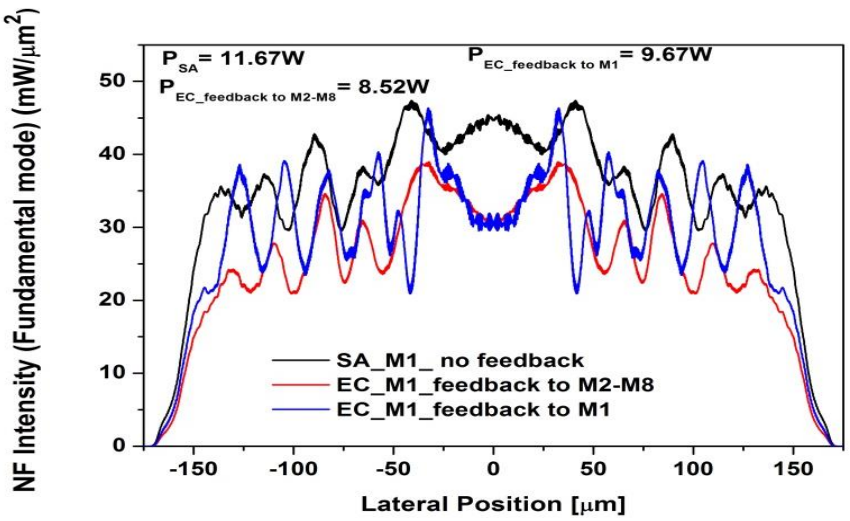



**Figure (5.17): Lateral near field profiles of fundamental mode for on-axis external cavity (EC) feedback (coupling only to higher-order modes M2-M8), on-axis external cavity (EC) feedback (coupling only to the fundamental mode), and stand-alone (SA) simulations.**

Figure 5.18 shows the feedback coupling to only higher-order modes leads to larger output power drop almost at all currents.

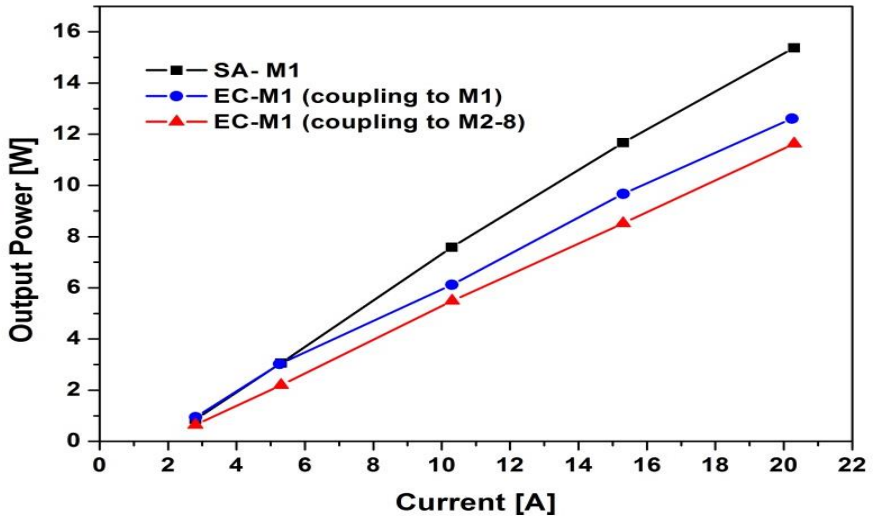



**Figure (5.18): L-I curves for the three cases of on-axis external cavity (EC) feedback coupled to the higher-order modes M2-M8, on-axis external cavity (EC) feedback coupled to the fundamental mode and stand-alone (SA) simulations.**

## 5.3 Parasitic reflections with off-axis alignment, at $+0.5\ \mu m$

The level of external optical feedback, coupling to different vertical modes, changes when the alignment to the waveguide changes. Here, we explore the impact of a vertical emitter shift of +0.5μm due to "smile." Table 4.1 shows that modes 2 and 4 have moderate ($MD_2 = 4.33$) and low ($MD_4 = 1.90$) values of modal discrimination. Figure 5.5 shows that, at a displacement of +0.5μm, they have large (19%) and moderate (4.8%) coupling coefficients. Thus, the performances of these two modes should reveal the relative importance of the modal discrimination and the coupling coefficient. The coupling to the fundamental mode also decreases from 42.15% (on-axis) to 29.5% (off-axis).

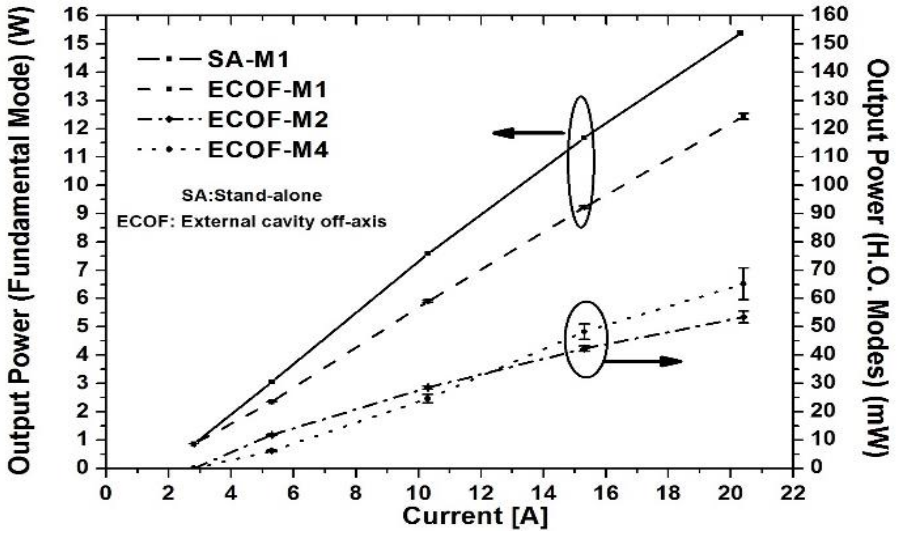



**Figure (5.19): L-I curves of all lasing modes (M1, M2 and M4) for the tapered laser in the stand-alone (SA) and external cavity with off-axis (ECOF) feedback configurations. The external-cavity off-axis (ECOF) simulation was performed with a vertical emitter displacement= +0.5 μm.**

Figures 5.19 and 5.20 show the power –vs– current and power conversion

efficiency –vs– current characteristics, respectively, of the LOC tapered laser.

With the off-axis optical feedback, the output power and PCE at I=15A dropped from 11.67 W to 9.22 W, while the PCE fell from 47.1% to 37.3%. These results support the findings of the last section; as the level of feedback coupled to the higher-order modes increases, the more the PCE and output power drop. The coupling into mode 2 increased by a factor of ~11, allowing both modes 2 and 4 to lase.

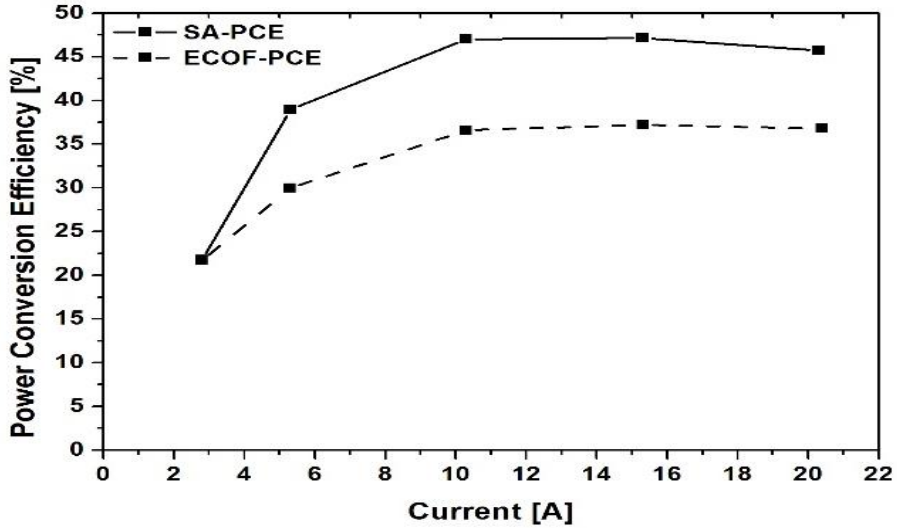



**Figure (5.20): Power conversion efficiency (PCE) curves for the tapered laser in the stand-alone (SA) and external cavity with off-axis (ECOF) feedback configurations. The external-cavity off-axis (ECOF) simulation was performed with a vertical emitter displacement= +0.5 µm.**

Figure 5.21 shows the lateral near field patterns of the lasing vertical modes with and without off-axis feedback while figure 5.22 shows the corresponding far-field patterns of the fundamental mode.

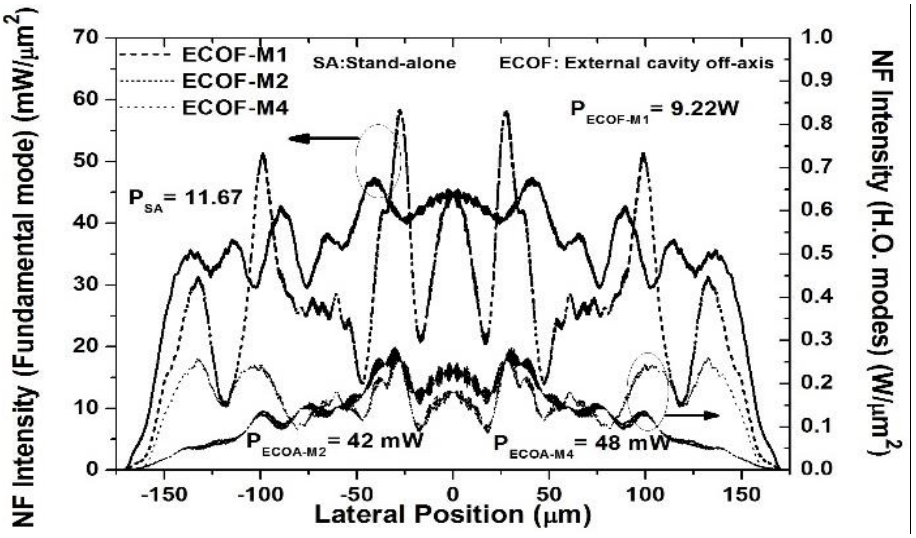



**Figure (5.21): Comparison of lateral intensity profiles of vertical modes M1, M2 and M4 for stand-alone (SA) and with external cavity with off-axis (ECOF) feedback configurations. The external-cavity off-axis (ECOF) simulation was performed with a vertical emitter displacement= +0.5 μm.**

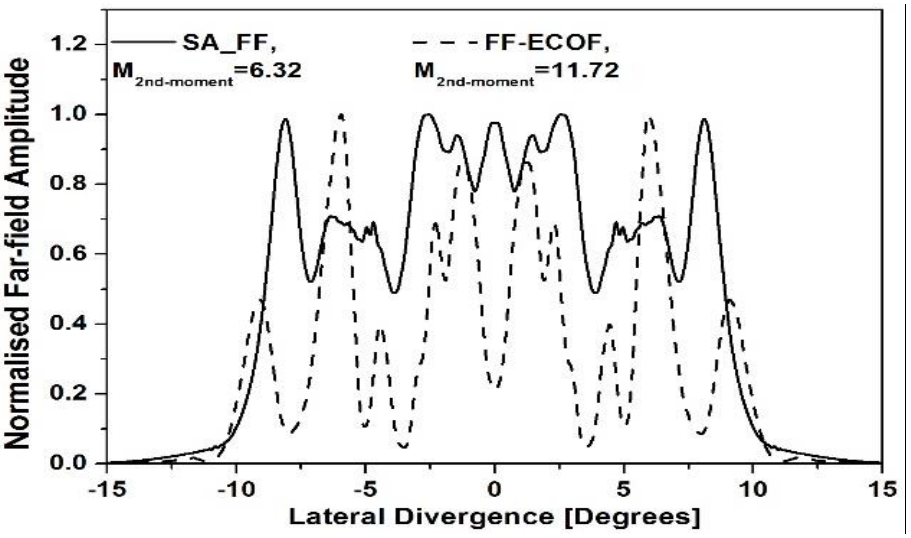



**Figure (5.22): Comparison of Far-field profiles of the fundamental mode for stand-alone (SA) and external cavity with off-axis (ECOF) feedback simulations. The off-axis external-cavity simulation was performed with a vertical emitter displacement= +0.5 μm.**

Figure 5.23 shows the current dependence of the beam propagation parameter $M_x^2$ (both the $e^{-2}$ and 2nd moment definitions) for the off-axis external cavity feedback condition. At I=15A, the off-axis feedback did not change$M_{x,e^{-2}}^2$, but $M_{x,2ndmoment}^2$ increased from 6.32 to 11.72, which is lower than the case of on-axis feedback. Again,

this can be explained by the lower feedback level coupled into the fundamental mode, leading to less absorption bleaching and hence, less intensity of the field diffracted from the DBR.

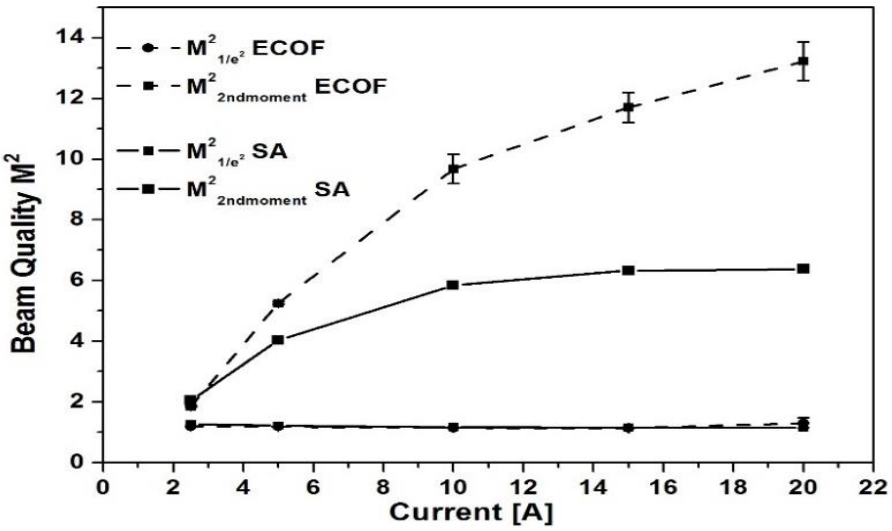



**Figure 5.23: Dependence of $M_x^2$ on bias current for both stand-alone (SA) and external cavity with off-axis (ECOF) feedback simulations. The external-cavity with off-axis (ECOF) feedback simulation was performed with a vertical emitter displacement = + 0.5 µm.**

Figure 5.24 shows the total photon density distributions of modes 1-4. Modes 1, 2 and 4 are lasing and have significant photon densities in the ridge waveguide.

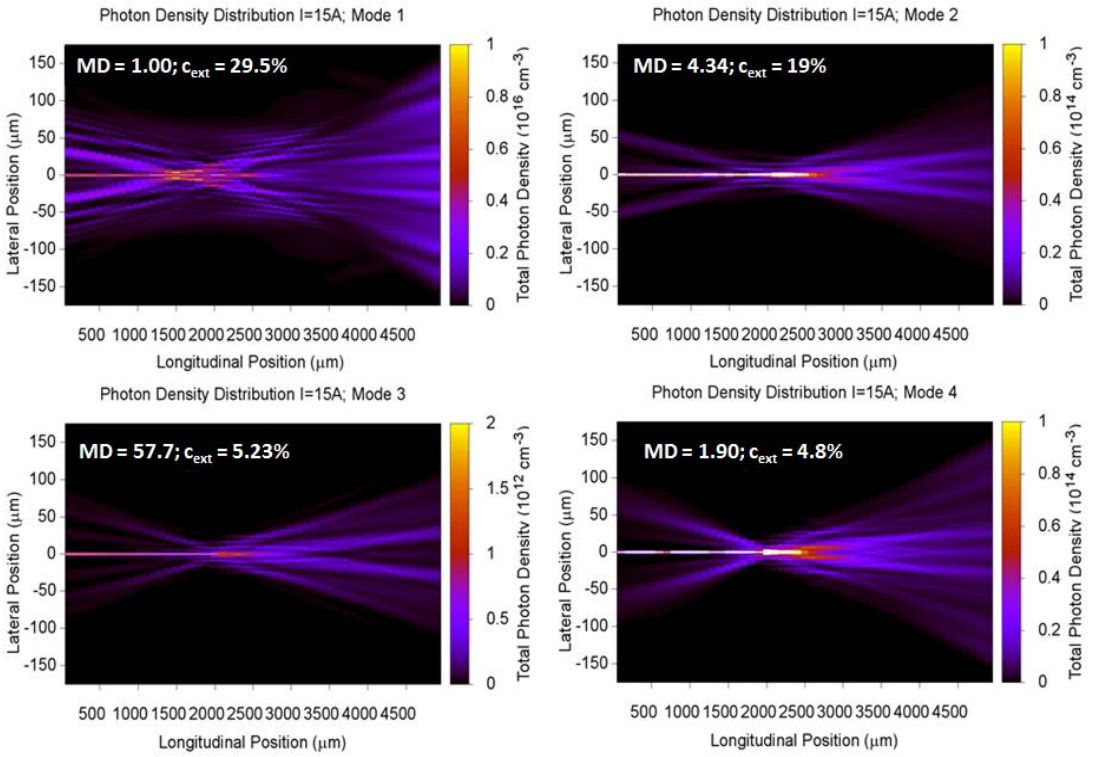



**Figure (5.24): Total photon density distributions for mode 1 (top left), mode 2 (top right), mode 3 (bottom left), and mode 4 (bottom right) at a bias current of I=15A and off-axis external cavity feedback. The external-cavity simulation was performed with a vertical emitter displacement= +0.5 μm.**

Another thing that can be noticed is the diffraction of the back-propagating beams at the RW-TA interface. The intensity of the diffracted beam increases when the internally reflected and externally coupled beams are coherently added, resulting in the fields not entirely converging at the RW aperture.

Figure 5.25 shows the heat power distributions caused by Joule heating of the stimulated emission currents for modes 1-4. The amount of Joule heating generated by mode 4 is almost similar to that in the on-axis case (figure 5.13), while the heat generated for mode 2 is ~11 times that of the on-axis case. This is due the fact that the feedback level for this off-axis case is 11 times that of the on-axis case.

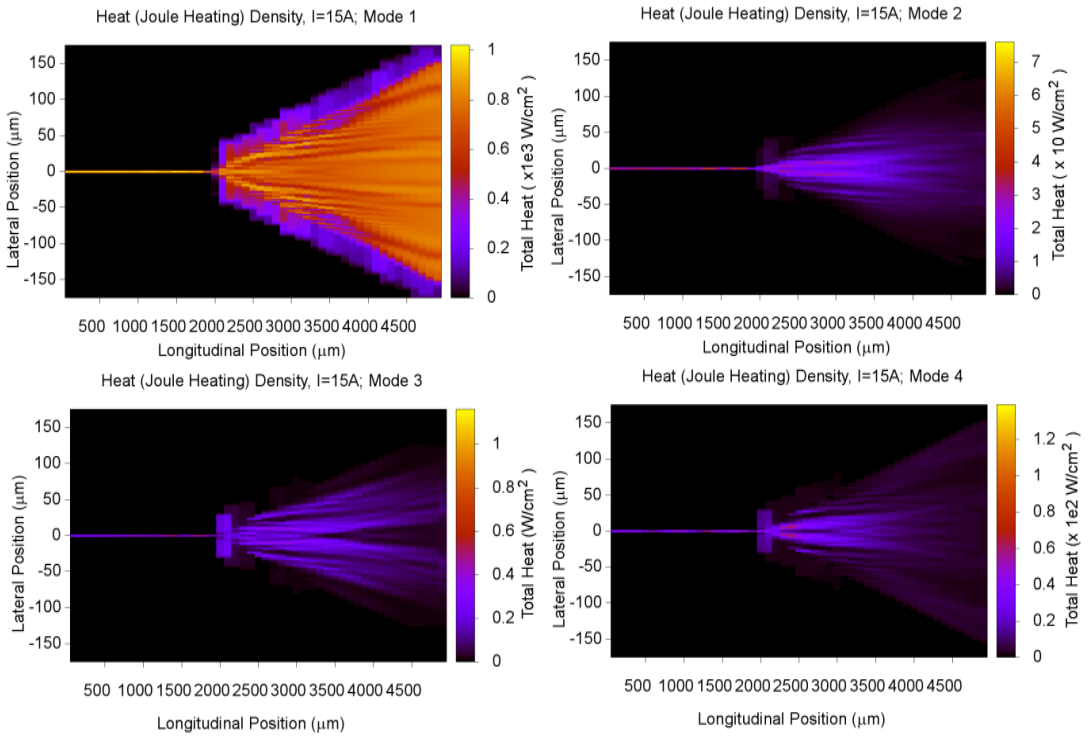



**Figure (5.25): Distribution of self-heating due to Joule heating for mode 1 (top left), mode 2 (top right), mode 3 (bottom left) and mode 4 (bottom right) at a bias current of I=15A with off-axis external cavity feedback. The external-cavity simulation was performed with a vertical emitter displacement= +0.5 μm.**

Figures 5.26 show the heat power distributions caused by absorption bleaching. Again, the optical bleaching for mode 2 increased by a factor of ~11 as the feedback level to it increased by the same amount. Also, comparing figure 5.26 to figure 5.14, the spatial distribution of the externally coupled fields changes the spatial distribution of the back-propagating fields and hence, the bleaching spatial distribution. This is predominantly observed in the case of mode 2.

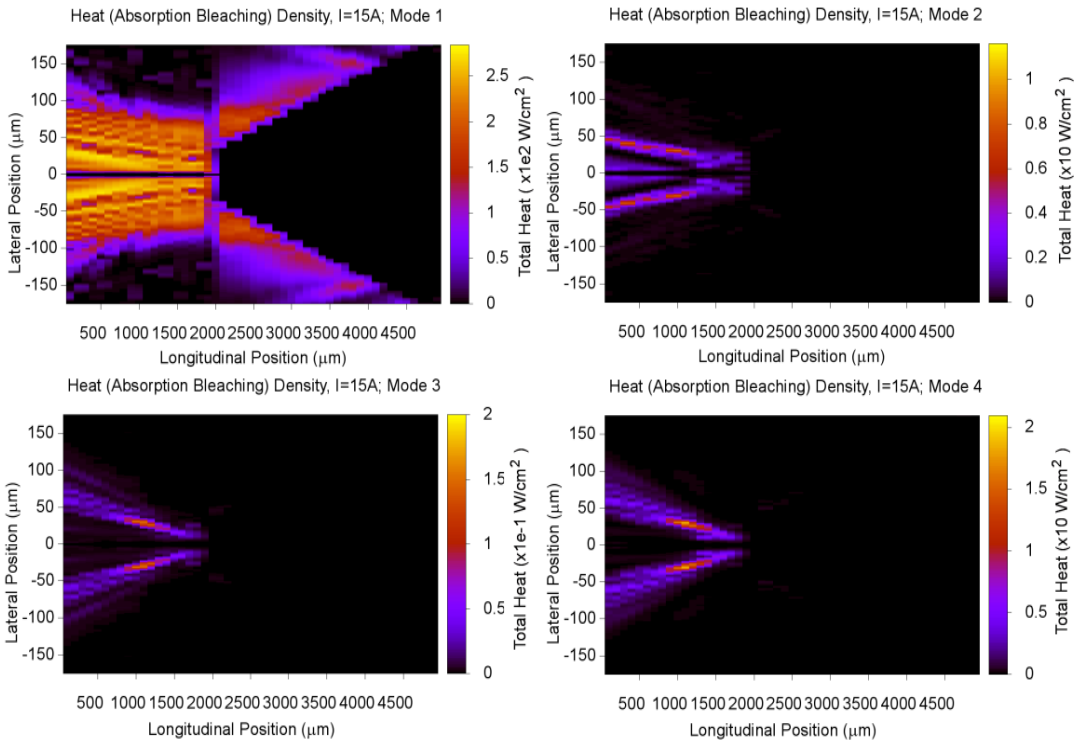



**Figure (5.26): Distribution of self-heating due to absorption bleaching by mode 1 (top left), mode 2 (top right), mode 3 (bottom left) and mode 4 (bottom right) at a bias current of I=15A with off-axis external cavity feedback. The external-cavity simulation was performed with a vertical emitter displacement= +0.5 μm.**

Figure 5.27 shows the heat distribution caused by FCA absorption. The overall increase in FCA absorption heat for mode 2 is only a factor of ~9. This is caused by the moderate modal discrimination (MD) value of mode 2, i.e. MD=4.34. Mode 3, on the other hand, has an MD of 57.7, and thus, when the coupling coefficient decreased from 10.4 to 5.23, the FCA heat reduced by half.

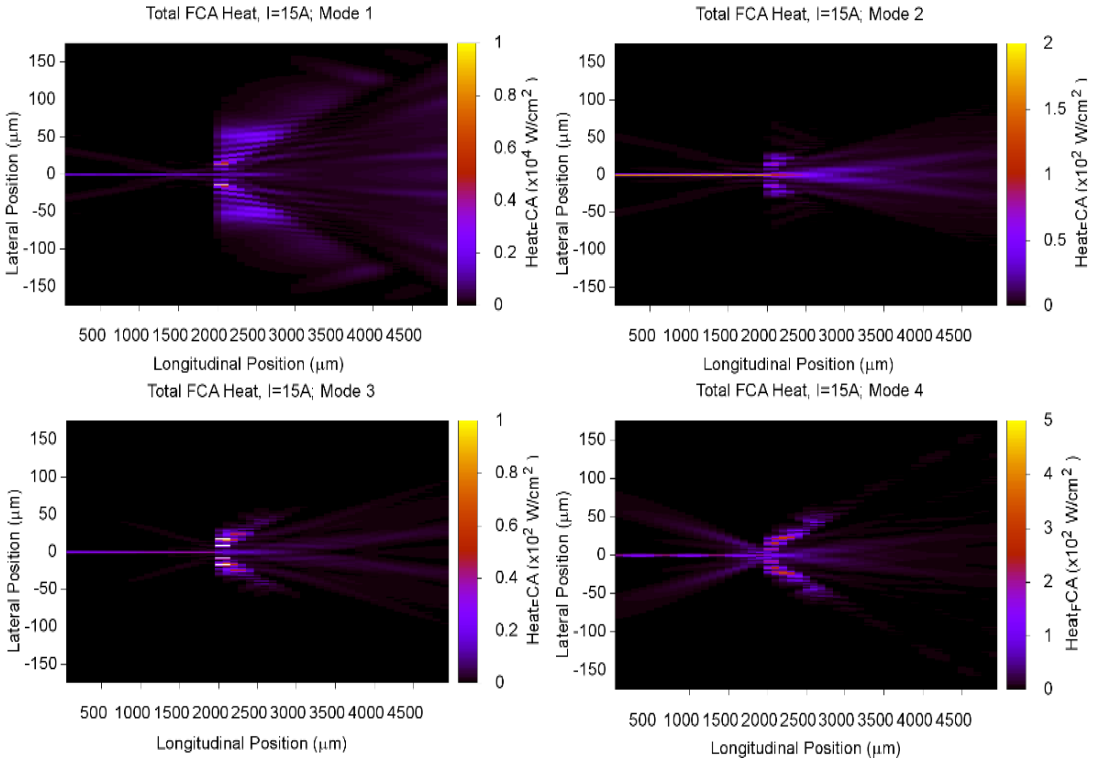



**Figure (5.27): Distribution of self-heating due to free-carrier absorption by mode 1 (top left), mode 2 (top right), mode 3 (bottom left) and mode 4 (bottom right) at a bias current of I=15A with external cavity off-axis feedback. The external-cavity simulation was performed with a vertical emitter displacement= +0.5 μm.**

## 5.4 Parasitic reflections with off-axis alignment, at $-0.25$ μm

This section discusses the results of external feedback at a vertical displacement of $-0.25$ μm. We have seen until now how mode 4, the one with the lowest modal discrimination, can be excited even though the feedback coupled into it is significantly lower than that of other modes, i.e. mode 3 for on-axis simulation and modes 2 and 3 for the off-axis case, at $+0.5$ μm. At this displacement, the coupling coefficient of mode 4 is the highest, 9.7%, of all the higher-order vertical modes, while the fundamental mode has a coupling coefficient of 36.5%.

Figures 5.28 and 5.29 show the power –vs– current and power conversion

efficiency –vs– current characteristics, respectively, of the LOC tapered laser.

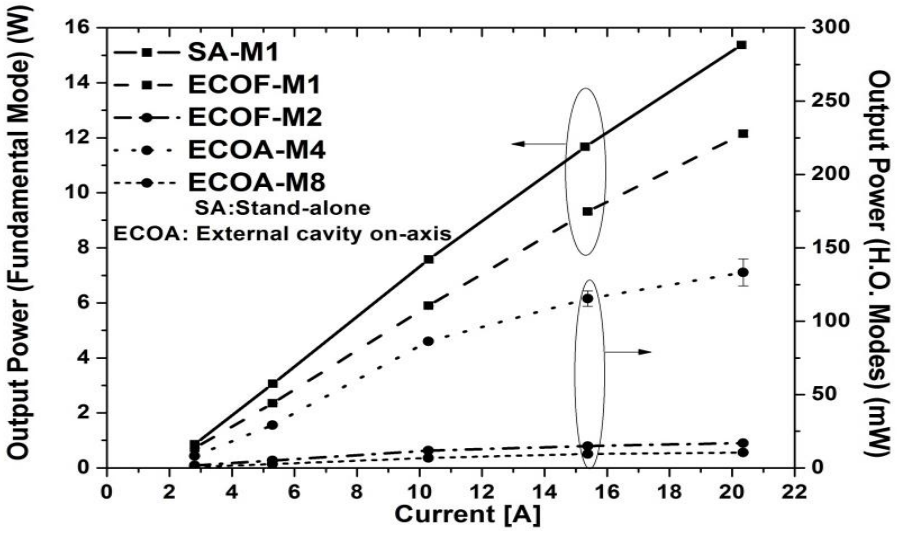



**Figure (5.28): Comparison of L-I curves of all lasing modes (M1, M2, M4 and M8) for the tapered laser in the stand-alone (SA) and external cavity with off-axis feedback (ECOF) configurations, at a bias current of I = 15 A. The external-cavity simulation was performed with a vertical emitter displacement= - 0.25 µm.**

With the off-axis feedback, the output power at I=15A dropped from 11.67 W to 9.32 W, while the PCE dropped from 47.1% to 36.6%.

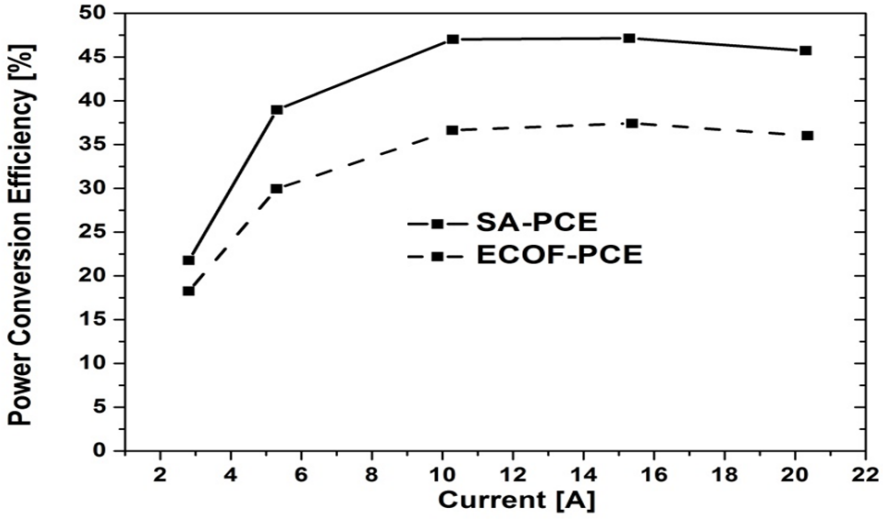



**Figure (5.29): Power conversion efficiency (PCE) curves for the tapered laser in the stand-alone (SA) and external cavity with off-axis (ECOF) feedback configurations, at a bias current of I = 15 A. The external-cavity simulation was performed with a vertical emitter displacement = - 0.25 µm.**

The percentage drop in PCE in this case is the highest, compared to the

previous two cases. This is due to the fact that in this case, the coupling coefficient to mode 4 (the higher-order mode with lowest modal discrimination) is the highest, i.e. 9.4%. This leads to increased stimulated current going to support stimulated emission caused by external optical feedback coupled to mode 4.

Figure 5.30 compares the near-field intensity profiles of lasing modes in the cases of stand-alone and external cavity simulations. Higher-order modes 2, 4 and 8 are lasing. At this displacement mode 2 has 9.1% coupling efficiency and mode 8 has 1.8%.

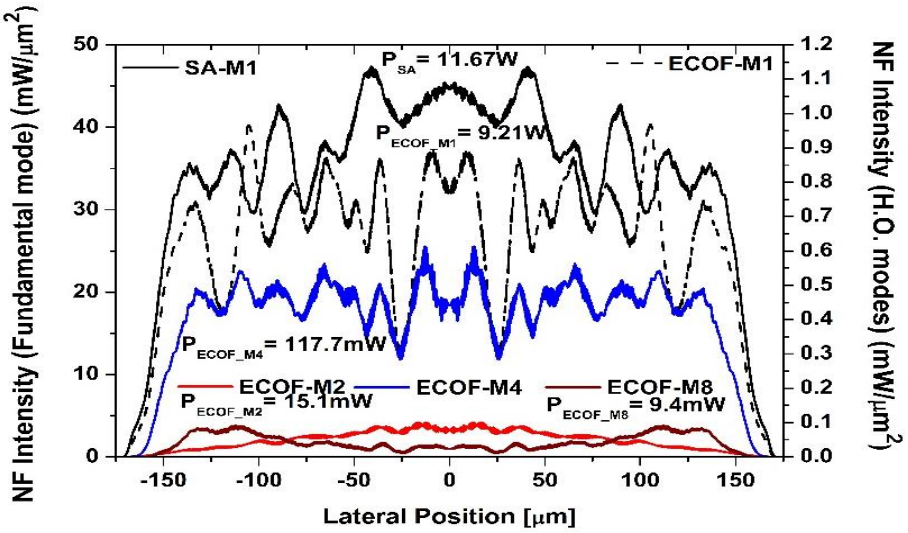



**Figure (5.30): Comparison of lateral intensity profiles of vertical modes M1, M2, M4 and M8 for stand-alone (SA) and with external cavity with off-axis (ECOF) feedback configurations, at a bias current of I = 15 A. The external-cavity simulation was performed with a vertical emitter displacement = - 0.25 μm.**

Figure 5.31 compares the far-field profiles of the fundamental mode with and without feedback.

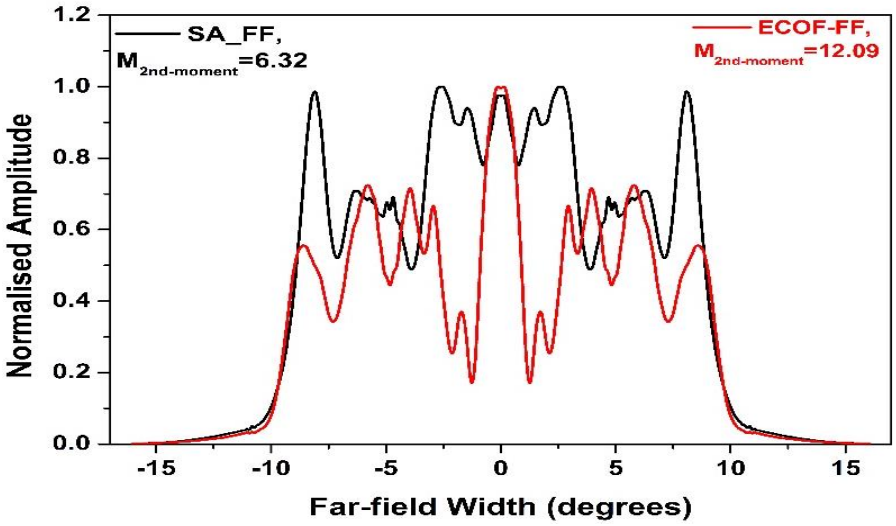



**Figure (5.31): Comparison of far-field profiles of the fundamental mode for stand-alone (SA) and external cavity with off-axis (ECOF) feedback configurations. The external-cavity simulation was performed with a vertical emitter displacement= -0.25 µm.**

Figure 5.32 shows the current dependence of the beam propagation parameter $M_x^2$ (both the $e^{-2}$ and 2nd moment definitions) for the off-axis external cavity feedback condition. At I=15A, the off-axis feedback did not change $M_{x,e^{-2}}^2$ but $M_{x,2ndmoment}^2$ increased from 6.32 to 12.16.

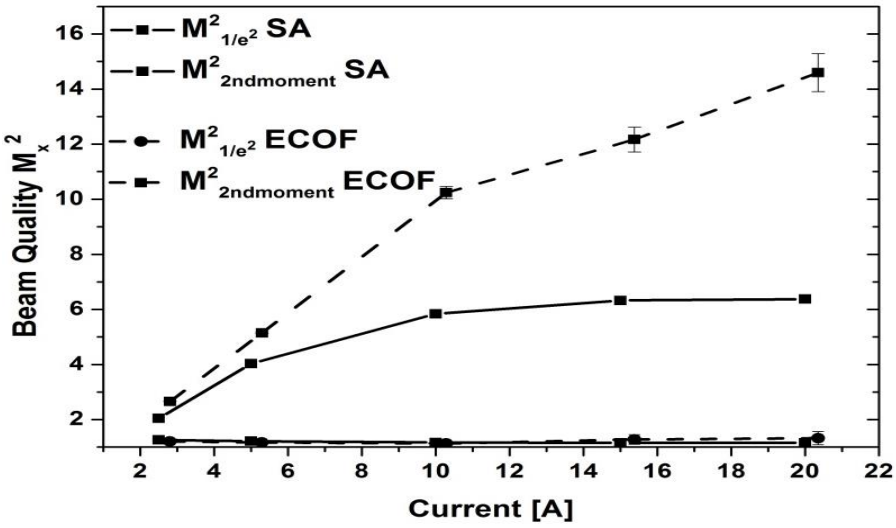



**Figure 5.32: Dependence of $M_x^2$ on bias current for both stand-alone (SA) and external cavity with off-axis (ECOF) feedback simulations. The external-cavity with off-axis (ECOF) feedback simulation was performed with a vertical emitter displacement = - 0.25 µm.**

At +0.5 µm displacement, the coupling coefficient to the fundamental mode was only 29.5% compared to -0.25 µm displacement. This is why in the previous case of misalignment the $M^2_{x,2ndmoment}$ was increased to only 11.72 as compared to 12.16 in this case.

Figures 5.33 to 5-36 show the photon density distributions, Joule heating, absorption bleaching heat and FCA heat of lasing modes: 1, 2, 4 and 8.

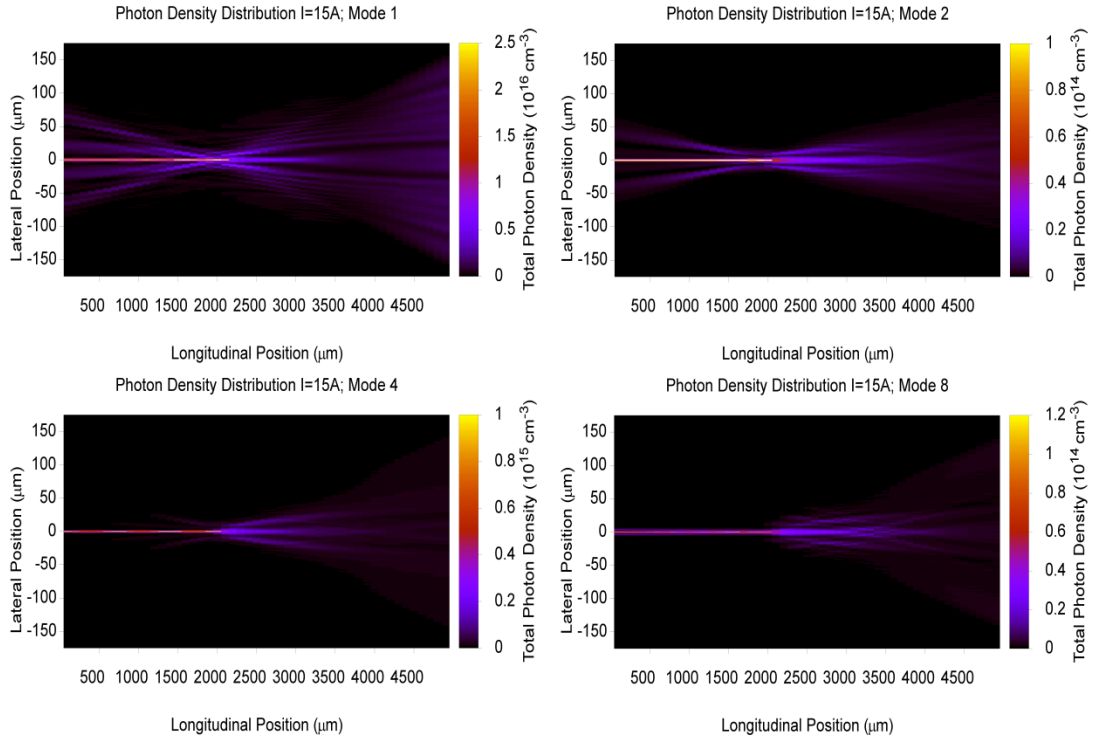



**Figure (5.33): Total photon density distributions for mode 1 (top left), mode 2 (top right), mode 4 (bottom left), and mode 8 (bottom right) at a bias current of I=15A and off-axis external cavity feedback. External cavity simulation was performed with vertical displacement = - 0.25 µm.**

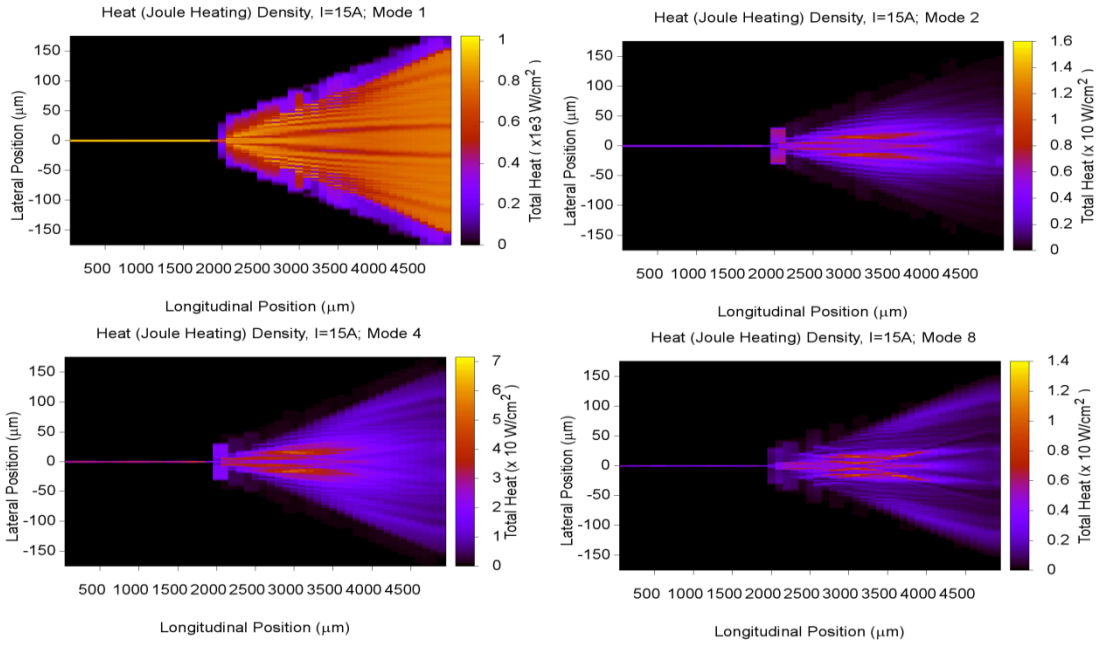



**Figure (5.34): showing self-heating due to Joule heating for mode 1(top left), mode 2 (top right), mode 3 (bottom left), and mode 4 (bottom right) at a bias current of I=15A and off-axis external cavity feedback. External cavity simulation was performed with vertical displacement = - 0.25 μm.**

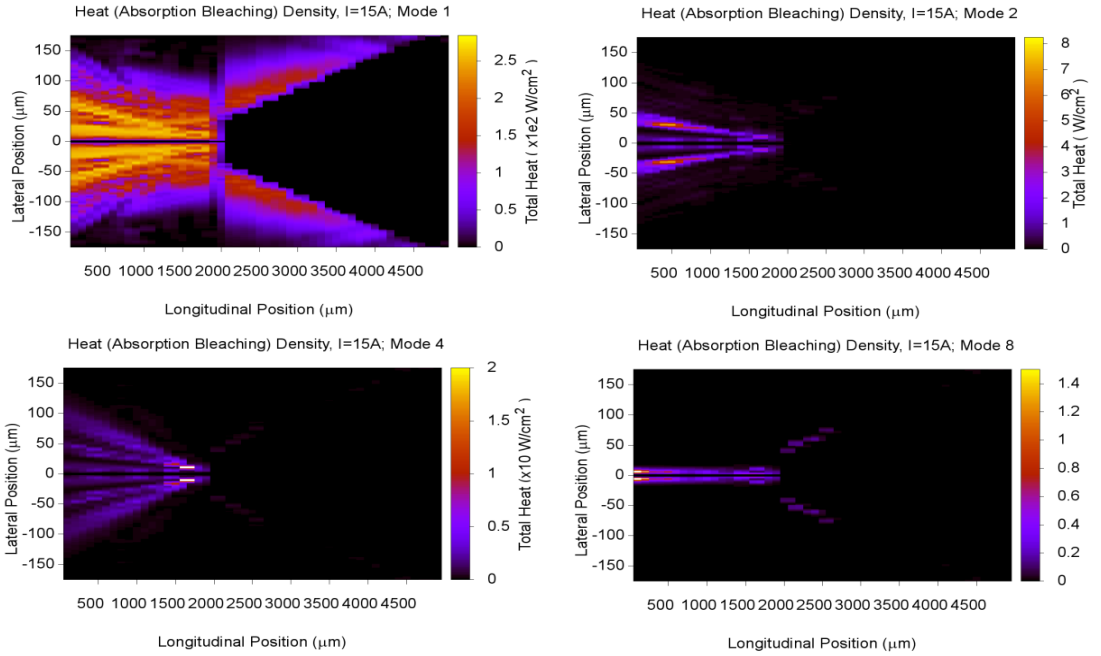



**Figure (5.35): Distribution of self-heating due to absorption bleaching by mode 1 (top left), mode 2 (top right), mode 4 (bottom left) and mode 8 (bottom right) at a bias current of I=15A. External cavity simulation was performed with vertical displacement = - 0.25 μm.**

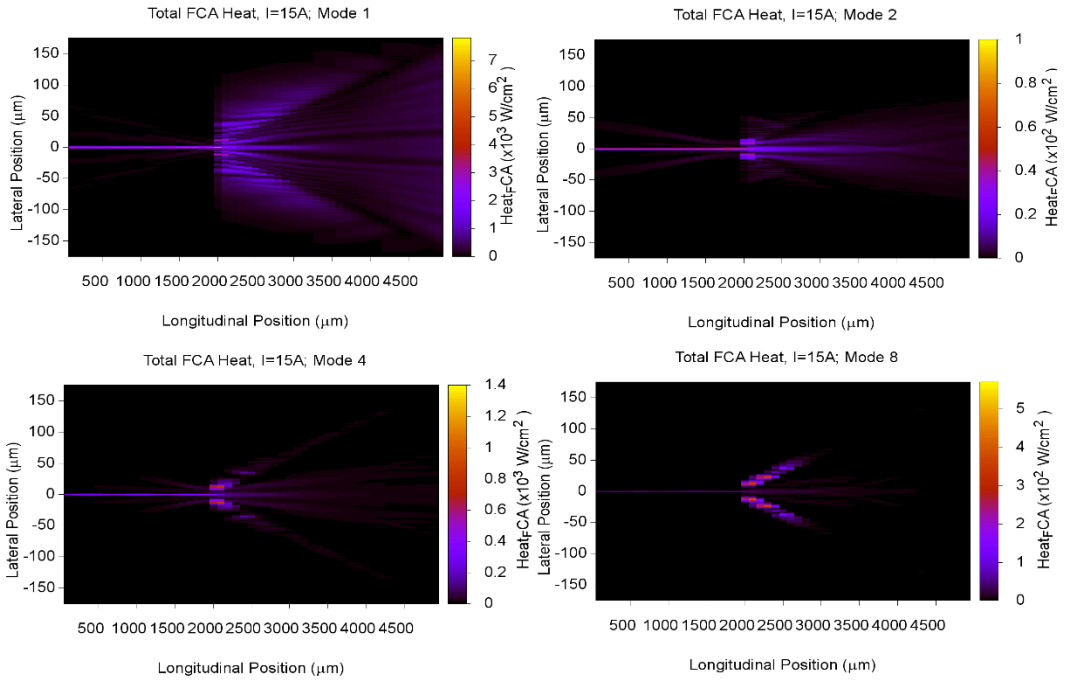



**Figure (5.36): Distribution of self-heating due to free carrier absorption by by mode 1 (top left), mode 2 (top right), mode 4 (bottom left) and mode 8 (bottom right) at a bias current of I=15A. External cavity simulation was performed with vertical displacement = - 0.25 μm.**

## 5.5 Analysis and discussion

This section analyses and discusses what happens to the power fed back into the vertical modes and how it affects the performance of the laser. It is particularly interesting to understand how the feedback effects depend on parameters that can be influenced during the design of the laser: modal discrimination, coupling coefficient, free-carrier absorption. It is also interesting to understand how the external cavity optics can be designed to minimise feedback effects.

Below are tables summarising the impact of optical feedback on optical and electrical metrics for four cases of high-brightness tapered laser simulations: stand-alone, external cavity (on-axis), external cavity (off-axis, at +0.5 μm) and external

cavity (off-axis, -0.25 μm). These tables will help to understand how different conditions of feedback affect the performance of the laser. This is very helpful for the design stage, as the impact of feedback is governed by the magnitude of feedback, coupling coefficients, modal discrimination and free-carrier absorption.

| **Mode** | **MD** | **Coupling Coefficient (%)** | **Coupled External Power (mW)** | **Output Power (W)** | **$H_{stm}$ (W)** | **$H_{abs}$ (W)** | **$H_{FCA}$ (W)** | **$I_{stm}$ (A)** |
|---|---|---|---|---|---|---|---|---|
| **1** | **1.00** | **-** | **0** | **11.67** | **4.0** | **0.88** | **2.485** | **11.71** |
| **Total for higher order** | | | 0 | 0 | 0 | 0 | 0 | 0 |
| **Total for all modes** | | | 0 | 11.67 | 4.0 | 0.88 | 2.485 | 11.71 |

**Table (5.2): Summary of impact of MD on optical metrics of all modes for on-axis simulation for a current of 15A.**

| **Mode** | **MD** | **Coupling Coefficient (%)** | **Coupled External Power (mW)** | **Output Power (W)** | **$H_{stm}$ (W)** | **$H_{abs}$ (W)** | **$H_{FCA}$ (W)** | **$I_{stm}$ (A)** |
|---|---|---|---|---|---|---|---|---|
| **1** | **1.00** | **42.15** | **155.3** | **9.5** | **3.86** | **0.95** | **3.2** | **11.2** |
| 2 | 4.34 | 1.68 | 6.2 | 3.1e-3 | 2.4e-3 | 3.14e-4 | 4.2e-3 | 7.1e-3 |
| 3 | 57.7 | 10.4 | 38.6 | 2.6e-3 | 5.8e-4 | 4.43e-5 | 27.7e-3 | 1.7e-3 |
| **4** | **1.90** | **6** | **22.2** | **80.1e-3** | **47.7e-3** | **1.7e-3** | **124.6e-3** | **138.1e-3** |
| 5 | 4.17 | 1.2 | 4.6 | 1e-3 | 1.5e-3 | 9.48e-5 | 10.9e-3 | 4.5e-3 |
| 6 | 1491. | 2.2 | 8.4 | 4e-6 | 3.6e-6 | 4.83e-8 | 8e-3 | 7.6e-6 |
| 7 | 12.58 | 2.2 | 8.3 | 1.6e-4 | 4.6e-4 | 3.94e-6 | 11e-3 | 1.3e-3 |
| 8 | 1.92 | 0.65 | 2.4 | 5.9e-3 | 4.6e-3 | 2.43e-5 | 22.2e-3 | 13.4e-3 |
| **Total for higher order** | | | 90.7 | 92.9e-3 | 57.2e-3 | 3e-3 | 208.6e-3 | 166.1e-3 |
| **Total for all modes** | | | 246.0 | 9.59 | 3.92 | 0.953 | 3.41 | 11.37 |

**Table (5.3): Summary of impact of MD on optical metrics of all modes for on-axis simulation for a current of 15A.**

| Mode | MD | Coupling Coefficient (%) | Coupled External Power (mW) | Output Power (W) | $H_{stm}$ (W) | $H_{abs}$ (W) | $H_{FCA}$ (W) | $I_{stm}$ (A) |
|---|---|---|---|---|---|---|---|---|
| **1** | **1.00** | **29.5** | **142.6** | **9.22** | **3.71** | **0.96** | **3.03** | **10.96** |
| **2** | **4.34** | **19** | **92** | **42.3e-3** | **26.5e-3** | **2.7e-3** | **38.5e-3** | **76.6e-3** |
| 3 | 57.7 | 5.23 | 25.28 | 1.5e-3 | 4.13e-4 | 3.81e-5 | 13.3e-3 | 1.2e-3 |
| **4** | **1.90** | **4.8** | **23.2** | **48.2e-3** | **38.4e-3** | **4.7e-3** | **81.4e-3** | **111.2e-3** |
| 5 | 4.17 | 1.73 | 8.4 | 1.4e-4 | 2.5e-3 | 2.62e-4 | 17.1e-3 | 7.1e-3 |
| 6 | 1491 | 3.28 | 15.88 | 1.94e-6 | 4.12e-6 | 1.08e-7 | 13.3e-3 | 1.2e-5 |
| 7 | 12.58 | 1.44 | 6.97 | 5e-5 | 4.58e-4 | 1.08e-5 | 8.8e-3 | 1.3e-3 |
| **8** | 1.92 | 0.83 | 4 | 1.8e-3 | 4.6e-3 | 4.35e-4 | 31.8e-3 | 13.4e-3 |
| **Total for higher order** | | | 175.7 | 94.0e-3 | 72.9e-3 | 8.1e-3 | 204.2e-3 | 210.8e-3 |
| **Total for all modes** | | | 318.3 | 9.31 | 3.78 | 0.9681 | 3.23 | 11.17 |

**Table (5.4): Summary of impact of MD on optical metrics of all modes for off-axis (VD=$+0.5\mu m$) simulation for a current of 15A.**

| Mode | MD | Coupling Coefficient (%) | Coupled External Power (mW) | Output Power (W) | $H_{stm}$ (W) | $H_{abs}$ (W) | $H_{FCA}$ (W) | $I_{stm}$ (A) |
|---|---|---|---|---|---|---|---|---|
| **1** | **1.00** | **36.5** | **121.7** | **9.33** | **3.87** | **0.92** | **2.797** | **10.467** |
| **2** | **4.34** | **9.1** | **30.3** | **15e-3** | **11.4e-3** | **1.7e-3** | **16.5e-3** | **31.7e-3** |
| 3 | 57.7 | 2.0 | 6.93 | 3e-4 | 1.32e-4 | 1.27e-5 | 3.8e-3 | 3.7e-4 |
| **4** | **1.90** | **9.7** | **32.4** | **117.7e-3** | **70.9e-3** | **4.1e-3** | **131.7e-4** | **201.9e-3** |
| 5 | 4.17 | 2.40 | 8 | 15.6e-3 | 2.3e-3 | 1.46e-4 | 12.8e-3 | 6.7e-3 |
| 6 | 1491 | 1.41 | 4.73 | 5.07e-7 | 1.92e-6 | 5.8e-8 | 6.4e-3 | 5.5e-6 |
| 7 | 12.58 | 1.38 | 4.61 | 1e-4 | 2.9e-4 | 6.26e-6 | 5.7e-3 | 8.35e-4 |
| **8** | **1.92** | **1.8** | **6** | **9.4e-3** | **9.1e-3** | **1.35e-4** | **38.3e-3** | **26.2e-3** |
| **Total for higher order** | | | 92.97 | 158.1e-3 | 94.1e-3 | 6.1e-3 | 215.2e-3 | 267.7e-3 |
| **Total for all modes** | | | 214.67 | 9.3711 | 3.9641 | 0.9261 | 3.012 | 10.7347 |

**Table (5.5): Summary of impact of MD on optical metrics of all modes for off-axis (VD=$-0.25\mu m$) simulation for a current of 15A.**

Tables 5.2 to 5.5 summarise a range of power-related performance metrics for each of the vertical modes at a bias current of 15A. This bias was selected, as it

produces an output power of 11.7 W in the absence of external feedback and is within our targeted power range of 10-12 W. Table 5.2 is for a stand-alone simulation, while table 5.3 is for the simulation with on-axis feedback. Table 5.4 is for the off-axis simulation when the emitter is vertically displaced by 0.5μm and table 5.5 is for the off-axis simulation when the emitter is vertically displaced by -0.25μm. Modes in boldface font are lasing. $H_{stm}$ is the Joule heating power of the current needed to support the stimulated emission of the mode, $I_{stm}$. $H_{abs}$ is the total heat power due to band to band absorption outside the gain regions and is responsible for absorption bleaching. $H_{FCA}$ is the total heat power due to free carrier absorption.

For the case of on-axis feedback, 91 mW of light is coupled into the higher order modes, which consume 166 mA of current and produce 93 mW of light and 269 mW of heat. For the case of off-axis feedback (VD=+0.5μm), 176 mW of light is coupled into the higher order modes, which consume 211 mA of current and produce 94 mW of light and 290 mW of heat. In the other case of off-axis feedback (VD=−0.25μm), 93mW of external feedback is coupled into the higher-order modes, which consume 268mW of current and produce 158mW of light and 315mW of heat.

The previous 3 sections showed that external feedback can cause higher order vertical modes to lase. For the laser diode and external cavity simulated here, only the fundamental mode lases without feedback, while mode 4 also lases in the case with on-axis feedback. For the cases of off-axis feedback, three higher order vertical modes also lase (modes 2 and 4 at VD=+0.5 and 2, 4 and 8 at VD=−0.25). For the device and cavity investigated here, tables 5.3 to 5.5 suggest that modes with modal discrimination of MD < 2 are able to start lasing with comparatively small external cavity coupling coefficients of < 5%, while modes with MD ~ 4 require larger coupling

coefficients (e.g. 10-20 %). Additional simulations showed that the feedback required for higher order mode lasing also depends on the coupling of the reflected beam into the ridge waveguide (i.e. into the RW aperture at the RW-TA interface). This is also apparent from the photon distributions in Figures 5.11, 5.24 and 5.33.

The feedback reduces the power and PCE of the fundamental mode, which can be attributed partly to lasing of higher order modes and partly to an increase in the effective facet reflectivity as light is fed back to the fundamental mode. As the higher order modes began to lase more strongly, they began to compete with the fundamental mode for the spatial gain distribution and modal power oscillations consistent with mode partition noise were observed in the simulations. Although the higher order mode powers were small, they appear to affect the power conversion efficiency by competing for gain and current. Feedback to the fundamental mode however, contributes to spatial oscillation in near- and far-field patterns of the fundamental mode – consistent with experimental observations[3], [4]. For stable operation, $M^2{}_{e^{-2}}$ remains below 1.5 and is insensitive to feedback, while $M^2{}_{2nd\ moment}$ ~ 6 for stand-alone operation and nearly doubles with feedback. Increased feedback to the fundamental mode has the greatest impact on beam quality.

The optical power back-coupled into the higher order vertical modes also creates heat. This occurs even if the modes are not lasing, but increases dramatically if they are. The heat power of the higher order modes is dominated by free carrier absorption, followed by Joule heating associated with the current supporting stimulated emission into these modes. The heat generated per feedback photon decreases with modal discrimination. This shows the importance of both modal discrimination and free carrier absorption for suppressing feedback amplification and thus, heating by the higher order modes. At this bias level (15A), the total heat

generation in the higher order modes is 0.269-0.315 W (depending on the alignment of the laser diode), corresponding to a 3.2-4% increase in heat power. The heat generated by the excitation of these higher order vertical modes is distributed along the entire cavity – irrespective of the modal discrimination. Thus, although the excitation and lasing of higher order modes affects the PCE, it is probably not responsible for observed increases in device degradation. Instead, as shown by Leonhäuser and Kissel *et. al*. [5], [6], the observed increase in degradation is probably due to feedback that is *not* coupled into the waveguide (i.e. into the substrate) – particularly when the substrate is strongly absorbing (i.e. $E_{g_substrate} < E_{photon}$).

This chapter has shown that external feedback can cause lasing of higher order vertical modes, resulting in self-heating, and mode partition instabilities. It also has shown that feedback to the fundamental mode is responsible for beam quality degradation. The question is: *How can we design the laser diode and optical system to reduce the impact of optical feedback?* For the design of the laser diode, modal discrimination and free-carrier absorption are key parameters for suppressing the impact of higher-order modes. The external cavity coupling coefficients play a smaller role, but are still important. For the design of the external cavity, the reflected power must be minimised – for example, by using good antireflection coatings and, perhaps, tilted facets to eliminate specular reflections. For high powers, however, other approaches may also be required, such as off-axis optical alignment to prevent reflected beams from coupling into the RW filter. Finally, care must also be taken to minimise the power coupled into the substrate – particularly if the substrate is absorbing.

## 5.6 References

[1] J. F. Monjardin, K. M. Nowak, H. J. Baker, and D. R. Hall, “Correction of beam errors in high power laser diode bars and stacks.,” *Opt. Express*, vol. 14, no. 18, pp. 8178–83, 2006.

[2] P. Crump, S. Knigge, A. Maaßdorf, F. Bugge, S. Hengesbach, U. Witte, H.-D. Hoffmann, B. Köhler, R. Hubrich, H. Kissel, J. Biesenbach, G. Erbert, and G. Traenkle, “Low-loss smile-insensitive external frequency-stabilization of high power diode lasers enabled by vertical designs with extremely low divergence angle and high efficiency,” *SPIE Vol 8605 High-power Diode Laser Technol. Appl. XI*, vol. 8605, p. 86050T, 2013.

[3] B. Leonhäuser, H. Kissel, A. Unger, B. Köhler, and J. Biesenbach, “ Feedback-induced catastrophic optical mirror damage (COMD) on 976nm broad area single emitters with different AR reflectivity ,” 2014, vol. 8965, pp. 896506–896510.

[4] M. Hempel, M. Chi, P. M. Petersen, U. Zeimer, and J. W. Tomm, “How does external feedback cause AlGaAs-based diode lasers to degrade?,” *Appl. Phys. Lett.*, vol. 102, no. 2, 2013.

[5] B. Leonhäuser, H. Kissel, J. W. Tomm, M. Hempel, A. Unger, and J. Biesenbach, “High-power diode lasers under external optical feedback,” *High-Power Diode Laser Technol. Appl. XIII*, vol. 9348, no. M, p. 93480M, 2015.

[6] H. Kissel, B. Leonhäuser, J. W. Tomm, M. Hempel, A. Unger, and J. Biesenbach, “Fiber coupled laser diode reliability : Impact of feedback on diode lifetime and failure modes,” in *High Power Diode Lasers and Systems Conference (HPD)*, 2015, pp. 41–42.

Chapter 6

# 6 Tapered laser diode operating in a Littrow cavity: Impact of asymmetric spectral feedback

Diode lasers are compact and simple to fabricate, but they have shortcomings such their frequency sensitivity to temperature and injection current [1]. In some applications such as atomic cooling and spectroscopy, a tunable single-wavelength laser diode with moderate output power is required [2]. In other applications, where the required total output power is higher than what a single laser diode can provide, arranging those laser diodes in a laser bar where the beams of the individual lasers are combined becomes a necessity, such as spectral beam combining (SBC). In SBC applications, the individual laser diodes are required to operate at different wavelengths and with narrow linewidths. Wavelength locking is an effective method to narrow the laser diode bandwidth and to stabilise the emission wavelength. Wavelength locking can be either internal or external. Internal wavelength locking is achieved through the use of a diffraction grating etched in the structure of the active region of the semiconductor laser [3]. External wavelength locking is achieved through the use of an external diffraction grating producing wavelength selective feedback to the laser diode [2].

In some SBC techniques, laser diodes with different operating wavelengths are arranged in an external cavity that provides selective spectral feedback to each of the laser diodes. The external cavity ensures that each laser diode tunes to a specific wavelength and with a narrow linewidth. There are two examples of these external

cavities, namely: Littrow cavity and Littman-Metcalf cavity configurations [2]. Both of these external cavity configurations utilise a diffractive wavelength selective element, such as diffraction grating, to provide the selective spectral feedback. In the more popular configuration, the Littrow cavity, the diffraction grating is tilted at a specific angle where the first-order diffracted beam is coupled back into the laser while the zeroth-order is considered as the system output. Figure 6.1 shows the schematic of the Littrow cavity configuration.

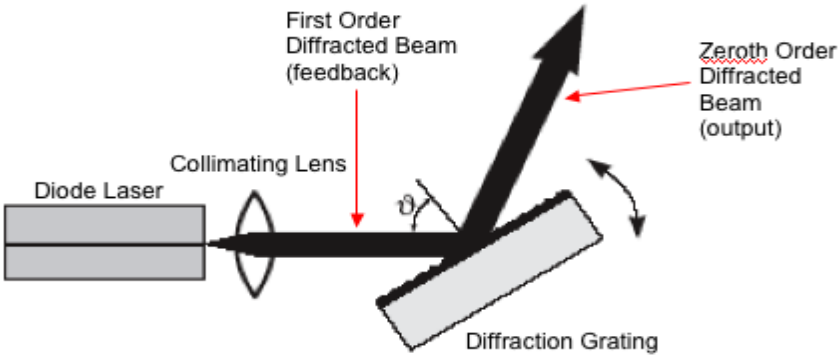



**Figure (6.1): A schematic of the Littrow cavity configuration**

The angle at which the grating is tilted depends on the period of the grating and on which order of diffraction is utilised as spectral feedback to the laser. In the case of the Littrow cavity example shown in figure 6.1, which will be the same setup investigated in this chapter, the first-order diffracted beam is the spectral feedback. Therefore, the correct angle is obtained from the following expression:

$$n_2 \sin\theta_2 - n_1 \sin\theta_1 = \frac{M\,\lambda}{d} \tag{6.1}$$

where subscripts 1 and 2 denote the incident and reflected beams, $n$ is the refractive index, $\theta$ is the angle measured from the normal to the grating surface, $M$ is the diffraction order, $\lambda$ is wavelength, $d$ is the grating spacing.

# Chapter 6

In the case of spectral beam combining, the feedback from the Littrow cavity is designed to force laser diodes fabricated in a linear bar array to operate at different, evenly spaced wavelengths. This is achieved by varying the grating angle to give different spectral feedback to different lasers within the bar, causing each diode to operate at a specified wavelength.

The purpose of this study is to analyse how feedback from a tilted diffraction grating is coupled into a single tapered laser. It also shows how reflected fields with different wavelengths couple and propagate with the laser cavity which leads the laser to favour a specific wavelength over the others. Finally, the role of the RW section is given special attention- this case study will demonstrate how the ridge waveguide acts as a filter and how this will affect the laser linewidth. This will also show how intentional spectral feedback injection locks the laser to a specific wavelength. The RW acts as an aperture or spatial filter, which only allows the re-focused external cavity fields at the centre wavelength to couple into the RW.

This chapter starts by describing the laser diode simulated and the parameters used to simulate it. Next, the Littrow cavity used is described. This is followed by the simulation of a tapered laser placed in Littrow cavity. Finally, the results are discussed and analysed.

## 6.1 Description of the laser, external cavity and simulation parameters

This case study uses the same 975nm large optical cavity (LOC) tapered laser based on the ELoD2 epitaxy used in chapter 5. In this case, the simulation of multiple wavelengths is enabled, while the number of simulated vertical modes is restricted to

only the fundamental mode.

The Littrow cavity, shown in figure 6.2, begins with two lenses to collimate beam along the slow- and fast- optical axes. These are followed by a concave and convex lens pair to act as a telescopic beam expander, which expands the beam in the lateral direction (optical slow axis) to cover the entire width of the grating. The collimated beam is incident on the grating at the first-order diffraction of the centre wavelength, so that the first order diffraction forms the feedback to the laser. Wavelengths on either side of the centre wavelength are reflected back at angles on either side of the optical axis.

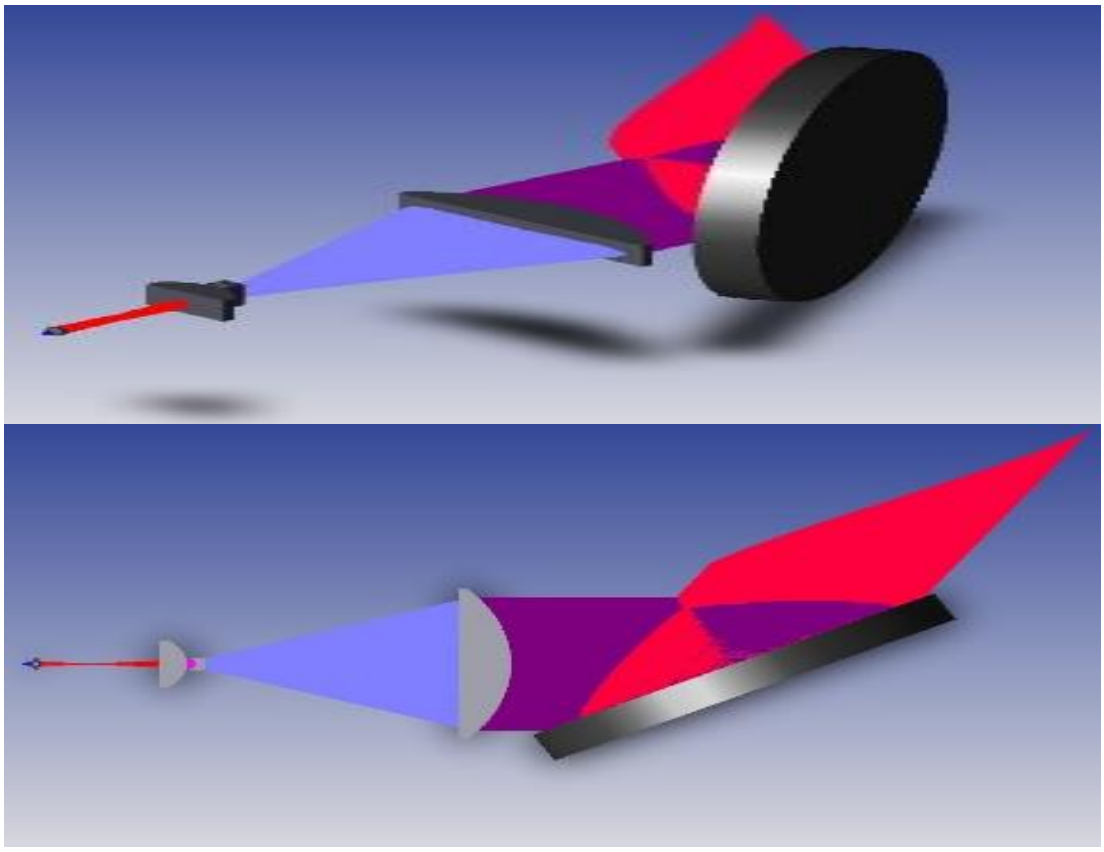


**Figure (6.2): External cavity setup used in the simulation consists of a FAC lens, two SAC lenses and a beam expander lens and a diffraction lens. Isometric view (top). Top view (bottom).**

For clarity and simplicity, the plots and figures will show 7 wavelengths with a spectral spacing of 1 nm and the centre wavelength is at 971.9 nm. The total number

of wavelengths configured in the simulation is 61 with a spacing of 0.1 nm. The choice of the centre wavelength is based on the gain spectrum and the experimental results provided by *Ferdinand Braun Institute* for the ELoD2 structure [4]. Therefore, with a bias of 15 A, the centre wavelength should have enough gain to produce an output power > 10 W. Figure 6.3 (left) shows the evolution of power as a function of Fox-Li iteration number. Figure 6.3 (right) shows the power spectrum of the chosen 7 wavelengths for a converged stand-alone simulation.

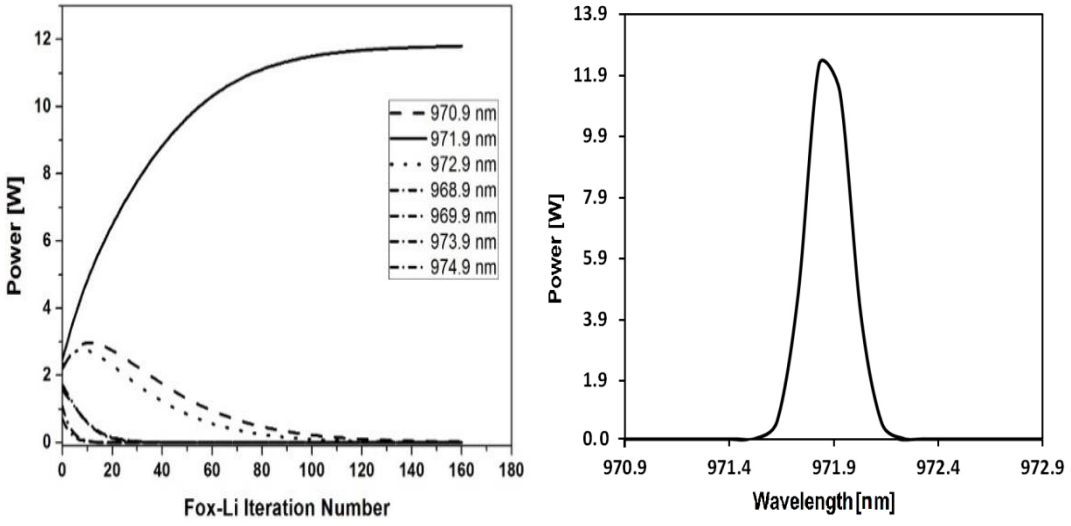



**Figure (6.3): Converged stand-alone results. Convergence of different wavelengths (left). Power spectrum (right). The laser linewidth is clearly narrower than the chosen wavelength spacing.**

The external feedback from the Littrow cavity is modelled using coherent ray tracing in *OpticStudio*. Ray-splitting is turned on to model the diffraction from the grating. The diffraction grating used in this simulation has T = 1.8 lines/μm (1800 lines/mm) and can be described by equation (6.1). The grating angle is chosen so that the centre wavelength (971.9nm) is reflected at the first order of the grating. Equation (6.1) gives this grating angle as 61.01°, so that the centre wavelength propagates from the grating back to the laser parallel to the optical axis. Figure 6.4 shows a simplified schematic diagram of the external cavity and how different beams (with different

wavelengths) are diffracted. Black arrows represent the multiple wavelength output. The blue dotted arrows represent the optical feedback (first-order of diffraction at the centre wavelength), while green and red dotted arrows represent the diffracted beams at wavelengths longer and shorter than the centre wavelength.

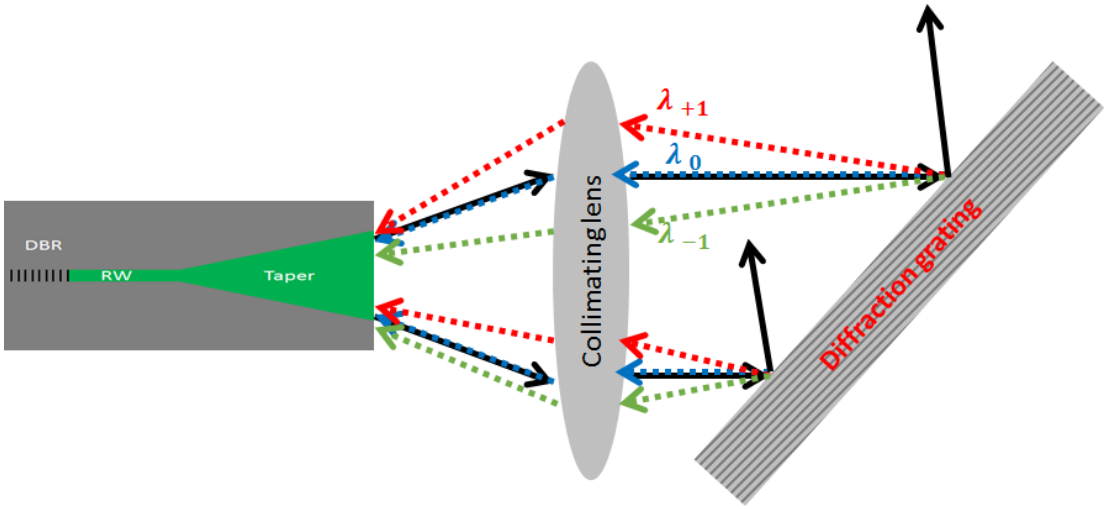



**Figure (6.4): Littrow schematic diagram. Output beam (black arrows) is diffracted into three beams at three different wavelengths.**

## 6.2 External cavity with asymmetric spectral feedback

In the case of stand-alone simulations, the simulated wavelengths all start with the same initial power. After many Fox-Li iterations, and specifically at convergence, the wavelength with highest gain will have more power, while the power at other wavelengths will diminish, as was shown in figure 6.3. In order to study how the asymmetric feedback, containing all wavelengths, is coupled into the laser cavity, the back reflected fields within the first few Fox-Li iterations need to be plotted. Figure 6.5 shows the lateral field intensity distributions of the feedback beams incident on the laser facet for the first Fox-Li iteration. The large aperture of the lens before the grating is able to collect the diffracted beams of all 7 wavelengths in this simulation, so that

they all reach the laser facet.

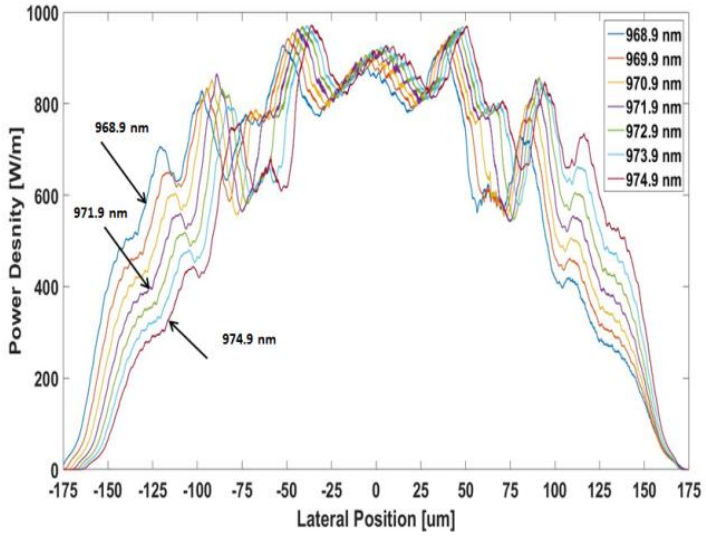



**Figure (6.5): Reflected intensity profiles of all wavelengths calculated at the facet for the first Fox-Li iteration**

Figure 6.5 shows that the power distribution of the centre wavelength is symmetric and aligned with the laser aperture, while the longer and shorter wavelengths stretch or shrink laterally and become asymmetric. However, it is the shape and spectral dependence of the phase distribution which is the most important. Figure 6.6 shows the lateral spatial phase distributions of the back reflected fields. The centre wavelength has a parabolic profile, consistent with the re-focusing of the beam back at the virtual point source at the beginning of the taper (i.e. the RW aperture). Wavelengths adjacent to the centre wavelength show tilted phase profiles, in which a positively (shorter wavelength) or negatively (longer wavelength) linearly sloped phase distribution is added to the parabolic phase of the converging beam. This linear phase profile describes the propagation of the collimated beams at an angle to the optical axis and is a direct consequence of the spectral dependence of the diffraction from the grating.

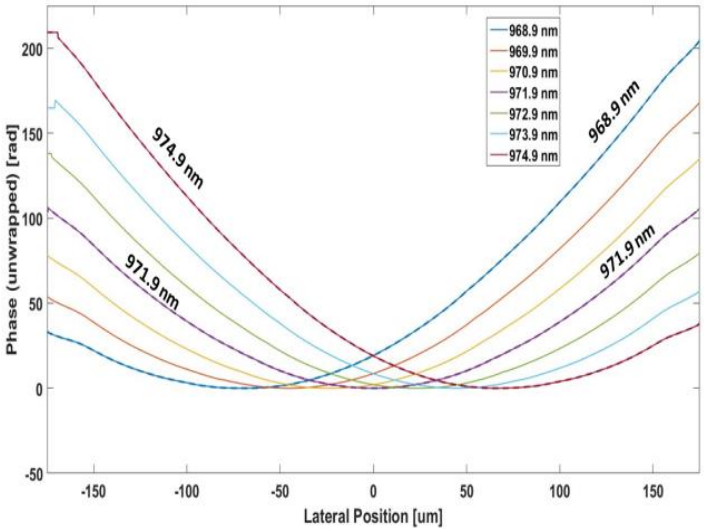



**Figure (6.6): Lateral phase distribution of different reflected beams for the first Fox-Li iteration.**

Figure 6.7 shows the impact of the tilted parabolic phase distributions of the feedback beams. The backward propagating beam of the centre wavelength (971.9 nm) refocuses at the input of the RW and couples into it. The beams at shorter and longer wavelengths also re-focus, but to points on either side of the RW aperture – so they do not couple into the RW. Nevertheless, some light at other wavelengths does refocus at the entrance to the RW. These "ghost" beams are due to residual facet reflections from the output facet of the laser diode and are caused by the coherent addition of the internally and externally reflected beams.

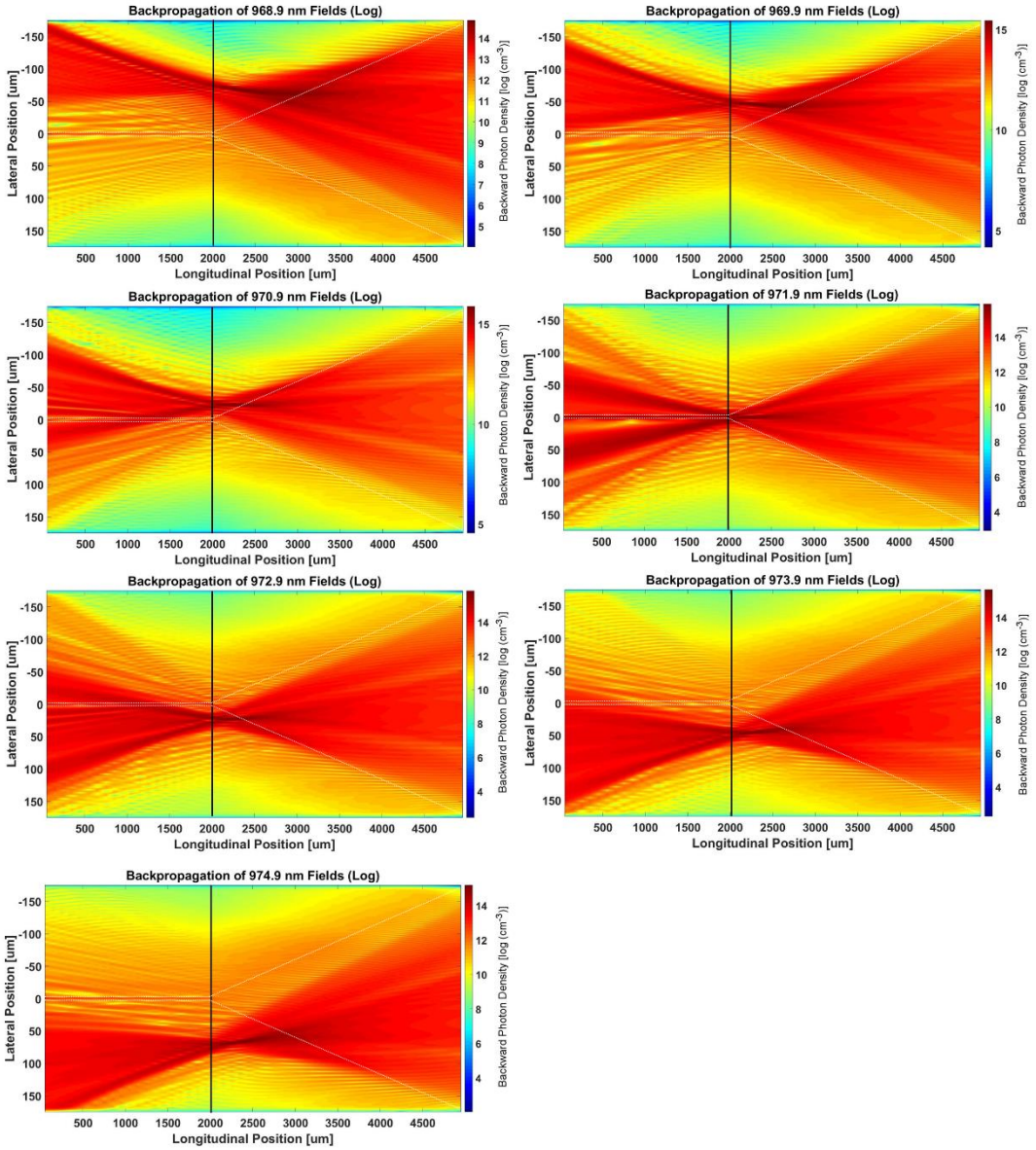



**Figure (6.7): 2D distribution of back-propagated fields within the laser. The black line is drawn at the RW-L interface. The white dashed-line outlines the taper and RW sections.**

These results show that the RW acts like the slit of a spectrometer and rejects the "out of band" wavelengths. Once again, the RW acts as a spatial filter - but this time for wavelengths and not just for the lateral spatial modes. By comparison, if a broad area (BA) laser were used, the spectral selection would be poor and multimode lasing could occur. However, external cavity wavelength stabilisation of "stacked" BA laser bars has been performed using spectral dispersion along the fast axis, where the narrow vertical cavity acts as the spatial filter [5], [6].

Figure 6.8 shows the normalised spatial intensity distributions of the beam spots of the back propagating beams as they are re-focused at the RW-taper interface. It also shows how the width and position of these beam spots depend on wavelength.

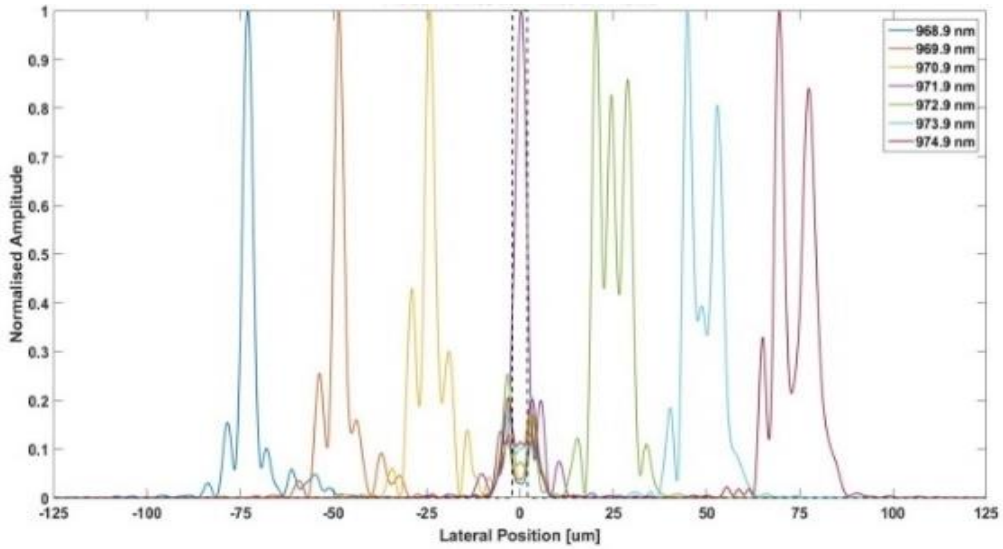



**Figure (6.8): Normalised spatial intensity distributions of focused back-propagating beams at the RW-taper interface.**

The spatial intensity field of the focused beam of the centre wavelength has the narrowest width, which can couple into the RW with high efficiency. The coupling efficiency can be calculated using the overlap integral between the field of each wavelength and the lateral fundamental mode of the RW. The overlap integrals of the beam spots of all simulated wavelengths with the RW mode profile give the spectral coupling efficiency into the RW. By plotting the coupling efficiency as a function of wavelength we can get the spectral response of the RW, as shown in figure 6.9.

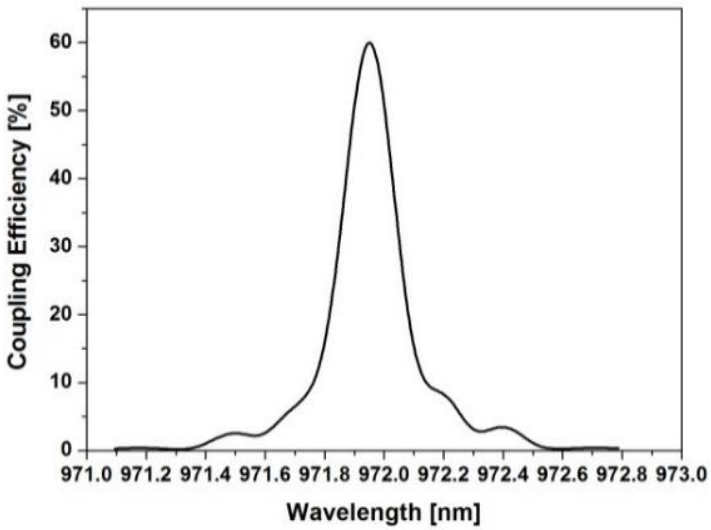



**Figure (6.9): Estimated spectral dependence of the coupling of the optical feedback into RW**

Figure 6.9 indicates that the centre wavelength (971.9 nm) has the highest coupling efficiency, while the efficiency for the rest of the wavelengths is lower. This result also shows that the spectral width at threshold should be ~ 0.25 nm. As this result is from the first Fox-Li iteration, spatial gain and lensing effects have not been properly included and the actual linewidth will change. For pumping levels above threshold, gain competition is also expected to affect the spectral width (e.g. linewidth narrowing).

The simulation was supposed to be run until the solution converged, however, due to a bug in the software, the simulation crashed. After investigation, we found out that the reason behind crashing was due to a bug in the software that was only discovered after enabling the WA-2D FD-BPM algorithm to simulate full space fields while interfaced to the external cavity module. For the previous two chapters, the half-space algorithm was sufficient as the beams (forward and backward) were all symmetric, and hence, the half-space algorithm was sufficient. However, the spectral fields, coupled from the external cavity, were asymmetric and hence, the use of full-space algorithm is required. Due to the short time and the fact that the author did not

have any access to *Speclase* source code, he was unable to fix the problem. Nevertheless, even with the results obtained from the first Fox-Li iteration we can still draw solid conclusions about how the Littrow cavity works. By plotting the back-propagating fields of the first Fox-Li iteration we can see clearly, from figures 6.5, 6.6, 6.7 and 6.8, that only the centre wavelength is able to couple into the RW and hence, obtaining more gain compared to the other wavelengths, locking the laser to that wavelength.

## 6.3 References

[1] A. S. Arnold, J. S. Wilson, and M. G. Boshier, "A simple extended-cavity diode laser," *Rev. Sci. Instrum.*, vol. 69, no. 1998, p. 1236, 1998.

[2] K. C. Harvey and C. J. Myatt, "External-cavity diode laser using a grazing-incidence diffraction grating," *Opt. Lett.*, vol. 16, no. 12, pp. 910–912, 1991.

[3] J. Fricke, F. Bugge, A. Ginolas, W. John, A. Klehr, M. Matalla, P. Ressel, H. Wenzel, and G. Erbert, "High-power 980-nm broad-area lasers spectrally stabilized by surface bragg gratings," *IEEE Photonics Technol. Lett.*, vol. 22, no. 5, pp. 284–286, 2010.

[4] P. Crump, S. Knigge, A. Maaßdorf, F. Bugge, S. Hengesbach, U. Witte β, H. Hoffmann β, B. Köhler, R. Hubrich, H. Kissel, J. Biesenbach, G. Erbert, and G. Tränkle Ferdinand, "Low-loss, smile-insensitive external frequency-stabilization of high power diode lasers enabled by vertical designs with extremely low divergence angle and high efficiency."

[5] B. Chann, A. K. Goyal, T. Y. Fan, A. Sanchez-Rubio, B. L. Volodin, and V. S. Ban, "Efficient, high-brightness wavelength-beam-combined commercial off-

the-shelf diode stacks achieved by use of a wavelength-chirped volume Bragg grating," *Opt. Lett.*, vol. 31, no. 9, pp. 1253–1255, 2006.

[6] B. L. Volodin, S. V Dolgy, E. D. Melnik, J. Harrison, T. Crum, and Y. Hu, "Wavelength-tunable narrowband high-power diode laser stacks based on volume Bragg grating technology," 2007, vol. 6456, pp. 645614–645616.

Chapter 7

# 7 Conclusions and future work

For many applications that employ high-brightness diode lasers, it is necessary to scale the output power through beam combination techniques, whilst maintaining an excellent beam quality. All beam combination techniques cause light to be fed back into the laser cavity. In some instances, this feedback can be exploited, such as in the wavelength stabilisation of diode lasers and arrays. However, any laser placed in an external system will be exposed to unintentional feedback (parasitic reflections). The work in this thesis involved a detailed description of how the external cavity laser simulation tool was developed, an investigation of the cause behind beam quality degradation in DBR tapered lasers at high powers, an investigation of the impact of unintentional feedback on a DBR tapered laser, and an analysis of how intentional feedback, provided by a diffraction grating – in a Littrow cavity configuration, improves the laser spectral performance.

The external cavity modelling tool consists of a laser simulation tool, *Speclase*, a commercial optics modelling software, *OpticStudio,* and an interface software the bidirectionally couples both *Speclase* and *OpticStudio*. The external cavity modelling tool was used to investigate the impact of the unintentional feedback on the DBR tapered laser, as well as to analyse how the intentional feedback in Littrow cavity can enhance the DBR tapered laser spectral performance. *Speclase*, was used to investigate the cause behind beam quality degradation in DBR tapered lasers at high powers.

# Chapter 7

## 7.1 Conclusions

The lateral cavity design of high-power laser diodes has a significant impact on brightness and the tapered laser is a strong contender for high-brightness laser systems. Tapered lasers offer, to a certain extent, the beam quality advantages of a RW laser and the high-power advantages of a BA laser. However, despite this and even without external parasitic feedback, conventional tapered lasers suffer from beam quality degradation at high bias currents due to the diffraction and scattering of backpropagated beam at the RW-taper interface [1]. Reducing the front facet reflectivity as well as incorporating beam spoilers in the tapered laser helped reduce the intensity of the backporpagatd beams, which lead to less absorption bleaching in the regions adjacent to RW. Nevertheless, the incorporation of a DBR at the back facet provided a better RW filter response[2]. Nevertheless, the results in chapter 4 showed that DBR tapered lasers still suffer from degraded beam quality at bias currents > 2.5 times which also in line with the experimental results given by Fiebig *et al.* [3]. Investigations of the cause of this beam quality degradation, in chapter 4, revealed that diffraction of light at the back aperture leads to light leaving the RW, propagating in the adjacent regions rendering them transparent, due to absorption bleaching. As those regions become bleached from carriers, i.e. non-absorbing, this allows the beam propagating in those regions to couple into the taper section, exciting higher-order degrading the beam quality [1]–[3].

In large optical cavity lasers, as required to reach the highest output powers, the vertical design of the cavity must be carefully considered. The structure must be designed to minimise the coupling of parasitic feedback to the fundamental mode as well as the higher order modes. The effects of parasitic feedback on the performance

(output power, power conversion efficiency and beam quality) of a DBR tapered laser in a simple optical system were studied. The excitation and propagation of higher-order modes increases the free-carrier absorption causing self-heating, eventually causing degradation of the output power and efficiency. Moreover, the parasitic feedback coupled to the higher-order vertical modes contributes slightly to the absorption bleaching, leading also to degradation of the lateral beam quality. However, the feedback to the fundamental mode is the major contributor to absorption bleaching and hence, degraded beam quality. Therefore, the inclusion of external parasitic feedback in the design process is highly significant. Coupling coefficients and modal discrimination (MD) values can be used to engineer a laser structure that is less affected by feedback. This can be accomplished by ensuring that modes with low to moderate MD values have the lowest coupling coefficients, thereby minimising the light coupled into them.

The RW section in a tapered laser is proven to be highly significant as a spatial filter. This is true for the filtering out of spatial modes, but also for filtering spatio-spectral fields coupled into the cavity, for example, through a diffraction grating in a spectral beam combining (SBC) system. In such a system with a diffraction grating, different fields converging at the RW-taper interface are filtered out and only the field designed to converge at the centre is coupled to the RW. Thus, tapered lasers are not only strong candidates for high-brightness emitters, but are also well placed to be used in an array format in SBC applications, where spectral cross-talk must be minimised.

This work contributed to the field of high-power and high-brightness diode lasers in different ways. The developed external cavity modelling tool is capable of modelling both unintentional and intentional optical feedback. The developed tool can be and should be incorporated in the design stages. This tool can predict how the diode

laser will perform when placed in an external cavity. Moreover, this tool can be used to mitigate the effects of unintentional feedback by engineering the laser diode structure to provide less confinement of higher-order modes which are subject to large amounts of optical feedback. This can be done by reducing the MD of higher-order modes with high external cavity coupling coefficients. Also, the ability to calculate the amount of coupled light dissipation within the structure, either through FCA or absorption bleaching, to understand how the unintentional feedback affect the power conversion efficiency and hence, the total output power. The developed external cavity modelling tool also gives an insight on how the intentional feedback enhances the laser diode performance. This is useful in the optimisation stage where it will be important to optimise the performance of the laser diode through making sure that the intentional feedback is efficiently coupled into the laser cavity while the coupling of unintentional feedback is minimised. Finally, the investigation carried out in chapter 4 showed the exact reason why the beam quality is degraded, at currents > 2.5 times the threshold current, which the diffraction of the backpropagated beam at the back facet. This discovery answered a significant question: If the back facet is AR coated at regions outside the RW, which allows the backpropagating beam in regions adjacent to RW to escape the structure, then where is forward propagating in those regions coming from? Knowing that the diffraction is cause behind beam degradation, this gives an insight to laser engineers on how to minimise the intensity of this diffracted beam, leading to a better beam quality at high powers.

## 7.2 Suggestions for future work

The results presented in this work have qualitative agreement with experiments. The external optical feedback leads to increased modulation depth and filaments within the output near-field [4]–[6]. Nevertheless, quantitative agreement is yet to be investigated. To achieve this, an ELoD2 structure [7] DBR tapered laser must be put in external optical system matching the one simulated in chapter 5.

The modelling tool has the potential to be upgraded from modelling single laser emitter to modelling laser bars. To achieve this, multiple instances of *Speclase* can be run, while the external optical system can be modelled in *OpticStudio* in the form of multiple beams propagating through the optical system.

Another area where the model can be upgraded is to include thermal simulations. The inclusions of thermal simulations will contribute to the understanding how external optical feedback can contribute to thermal lensing and hence, the contribution to the formation of filaments in the near-field.

Finally, the model can be used to investigate other intentional feedback mechanisms such as the use of asymmetric feedback to enhance the beam quality of broad-area lasers. The results in literature [8] show the enhancement of beam quality but at low power. It will be interesting to use the model and investigate whether the beam quality degrades at high power.

## 7.3 References

[1] S. Sujecki, L. Borruel, J. Wykes, P. Moreno, B. Sumpf, P. Sewell, H. Wenzel, T. M. Benson, G. Erbert, I. Esquivias, and E. C. Larkins, “Nonlinear Properties

of Tapered Laser Cavities," *IEEE J. Sel. Top. Quantum Electron.*, vol. 9, no. 3, pp. 823–834, 2003.

[2] S. N. Kaunga-nyirenda, S. Bull, J. J. Lim, K. h. Hasler, J. Fricke, and E. C. Larkins, "Factors influencing brightness and beam quality of conventional and distributed Bragg reflector tapered laser diodes in absence of self-heating," *IET Optoelectronics*, vol. 8, no. 2. pp. 99–107, 2014.

[3] C. Fiebig, G. Blume, C. Kaspari, D. Feise, J. Fricke, M. Matalla, W. John, H. Wenzel, K. Paschke, and G. Erbert, "12W high-brightness single-frequency DBR tapered diode laser," *Electronics Letters*, vol. 44, no. 21. pp. 1253–1255, 2008.

[4] B. Leonhäuser, H. Kissel, A. Unger, B. Köhler, and J. Biesenbach, " Feedback-induced catastrophic optical mirror damage (COMD) on 976nm broad area single emitters with different AR reflectivity ," 2014, vol. 8965, pp. 896506–896510.

[5] B. Leonhäuser, H. Kissel, J. W. Tomm, M. Hempel, A. Unger, and J. Biesenbach, "High-power diode lasers under external optical feedback," *High-Power Diode Laser Technol. Appl. XIII*, vol. 9348, no. M, p. 93480M, 2015.

[6] H. Kissel, B. Leonhäuser, J. W. Tomm, M. Hempel, A. Unger, and J. Biesenbach, "Fiber coupled laser diode reliability : Impact of feedback on diode lifetime and failure modes," in *High Power Diode Lasers and Systems Conference (HPD)*, 2015, pp. 41–42.

[7] P. Crump, S. Knigge, A. Maaßdorf, F. Bugge, S. Hengesbach, U. Witte, H.-D. Hoffmann, B. Köhler, R. Hubrich, H. Kissel, J. Biesenbach, G. Erbert, and G. Traenkle, " Low-loss smile-insensitive external frequency-stabilization of high power diode lasers enabled by vertical designs with extremely low divergence

angle and high efficiency ," 2013, vol. 8605, p. 86050T–86050T–13.

[8] L. Lang, J. J. Lim, S. Sujecki, and E. C. Larkins, "Improvement of the beam quality of a broad-area diode laser using asymmetric feedback from an external cavity," *Opt. Quantum Electron.*, vol. 40, no. 14–15 SPEC. ISS., pp. 1097–1102, 2008.

# Appendix I

In this appendix, the derivation of Fourier transform for spatial frequencies is given and how it can be used to obtain the Fraunhofer distribution, used to calculate the far-field pattern.

Assuming that the laser diode is producing a single mode, i.e. the laser source is diffraction limited. Due to the diffraction, the waves leaving the laser diode will diverge in an angle determined by the wavelength, the aperture dimensions, and the spatial frequency components in the near-field patter. Placing a screen very close to the facet will show an image on the screen that will resemble the aperture image. This 2D image is called the near-field pattern or the Fresnel Diffraction. Plotting the intensity of this image against the vertical spatial dimensions of the aperture will give us the vertical near-field pattern, and plotting it with the horizontal dimensions we get the horizontal near-field pattern. If the screen was moved far away from the facet until the image on the screen ceases to resemble the image of the aperture and the result pattern is the Fraunhofer pattern. The Fresnel pattern and the Fraunhofer pattern are related mathematically by Fourier transform. Which is going to be proved through a derivation that follows. Figure I-1 shows two arbitrary points in the near-field and far-field.

# Appendix

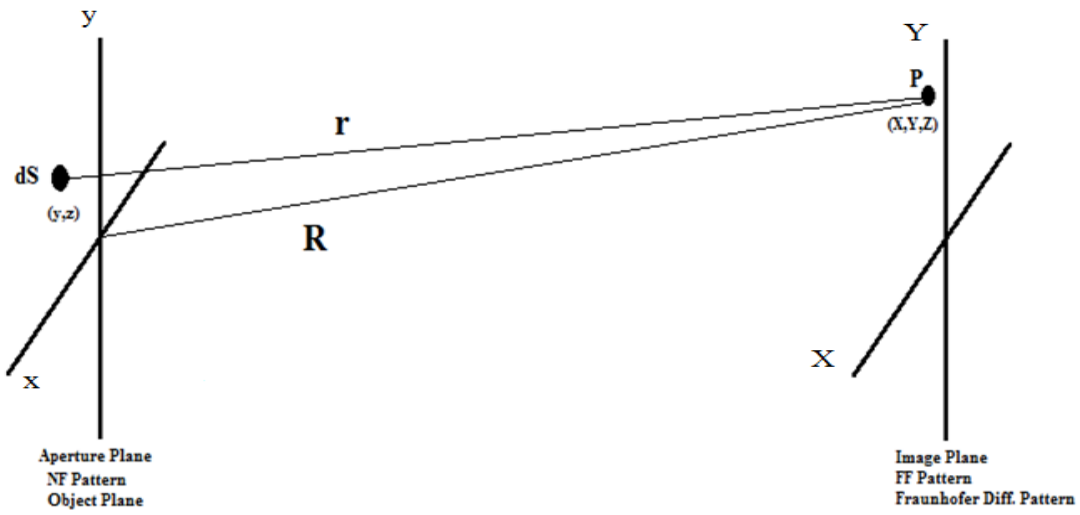



**Figure (I-1): Showing relationship between points on the near-field and the far-field**

For the sake of simplicity, let's assume that the laser cavity outputs only the fundamental vertical mode. The electric field disturbance at the far-field pattern or the Fraunhofer diffraction is given by the expression:

$$dE = \left(\frac{\mathcal{E}_A}{r}\right) e^{i(\omega t - \kappa r)} dS \qquad \text{(I.1)}$$

where $dE$ is the electric field disturbance, $\frac{\mathcal{E}_A}{r}$ : the amount by which the aperture field power is attenuated due to the travelled distance $r$ , $\mathcal{E}_A$ represents the field strength per unit area across the aperture which is assumed to be constant over dS, $e^{i(\omega t - \mathrm{R}r)}$ is the fast varying component of the electric field with phase change of $\kappa r$, $\kappa$ is the angular frequency which is given by $\kappa = {}^{2\pi}/_{\lambda}$.

Figure (I-1) shows that an infinitesimal area within the aperture plane travelled, with an angle (due to diffraction) a distance $\boldsymbol{r}$ and formed an image on the image plane (far-field plane). The coordinates of the infinitesimal area is (x,y) while the coordinates of the diffracted image is (X,Y,Z). The distance between the centre of the aperture plane and the diffracted point is $R$. Using geometry, the following expressions for $R$ & $r$ can be written as:

# Appendix

$$R = \sqrt{X^2 + Y^2 + Z^2} \tag{I.2}$$

$$r = \sqrt{X^2 + (X - x)^2 + (Y - y)^2} \tag{I.3}$$

Expanding the last two terms in (I.3) and substituting (I.2) in (I.3) we get:

$$r = [R^2 - 2Xx + x^2 - 2Yy + y^2]^{1/2}$$

$$r = R\left[1 - \frac{(2Xx + 2Yy)}{R} + \frac{(x^2 + y^2)}{R}\right]^{1/2} \tag{I.4}$$

In order for the Fraunhofer diffraction to occur, distance $R$ has to be considerably large compared with the aperture dimensions. Using this condition, the last term in (I.4) can be neglected:

$$r = R\left[1 - \frac{(2Xx + 2Yy)}{R}\right]^{1/2} \tag{I.5}$$

Using the polynomial expansion to expand (I.5) and keeping the first two terms while neglecting the rest, as they involve higher orders of $R$ in the denominator, we get:

$$r = R\left[1 - \frac{(Xx + Yy)}{R^2}\right] \tag{I.6}$$

Substituting (I.6) in (I.1) we get:

$$dE = \left(\frac{\mathcal{E}_A}{R}\right) e^{i\left\{\omega t - \kappa R\left[1 - \frac{(Xx+Yy)}{R^2}\right]\right\}} dS \tag{I.7}$$

Essentially, at a plane far enough for the Fraunhofer pattern to occur $R$ and $r$ are very close, given the small aperture. But since the phase change is much more

sensitive to variations than amplitude, the second term of (I.6) was neglected only when substituting in $\left(\frac{\varepsilon_A}{r}\right)$.

$$dE = \left(\frac{\mathcal{E}_A}{R}\right) e^{i\{\omega t - \kappa R\}} e^{i\kappa\left[\frac{(Xx+Yy)}{R}\right]} dS \tag{I.8}$$

To get the electrical field distribution at the far-field we integrate over the aperture area to get:

$$E_P = \left(\frac{\mathcal{E}_A}{R}\right) e^{i\{\omega t - \kappa R\}} \iint_{apperture} e^{i\kappa\left(\frac{Xx+Yy}{R}\right)} dS \tag{I.9}$$

(I.9) gives the total electric field disturbance at point P far away from the aperture.

The 2-D spatial Fourier transform is given by[1]:

$$F(K_X, K_Y) = \int_{-\infty}^{+\infty}\int f(x,y) e^{i(K_X x + K_Y y)}\, dxdy \tag{I.10}$$

where $K_X, K_Y$ are the spatial frequencies. Assuming that the flux density at the aperture can be described by a function $f(x,y)$ then $F\left(K_x, K_y\right)$ would be the Fourier transform of that function. Going back to relation (I.7), if the field across the aperture can be described by a complex function in terms of spatial dimensions and phase:

$$A(x,y) = A_0(x,y) e^{i\phi(x,y)} \tag{I.11}$$

where $A_0(x,y)$ the amplitude over the aperture and $e^{i\phi(x,y)}$ is the point-to-point phase variation. Replacing the constant amplitude-phase infinitesimal area $dS$ by a varying amplitude-phase element source $dxdy$ in (I.9) :

# Appendix

$$E(X,Y) = \iint_{-\infty}^{+\infty} A(y,z) e^{i\kappa\left(\frac{Xx+Yy}{R}\right)} dxdy \tag{I.12}$$

The integral limits were extended to infinity knowing that beyond the aperture: $A(x,y) = 0$ . Using Euler's relation, the term $e^{i\kappa\left(\frac{Xx+Yy}{R}\right)}$ can be expanded to:

$$e^{i\kappa\left(\frac{Xx+Yy}{R}\right)} = \cos\kappa\frac{Xx+Yy}{R} + \mathrm{i}\sin\kappa\frac{Xx+Yy}{R} \tag{I.13}$$

Using a trigonometric identity, (I.13) can be further expanded to:

$$\cos\kappa\frac{Xx+Yy}{R} + \mathrm{i}\sin\kappa\frac{Xx+Yy}{R}$$

$$= \cos\left(\kappa\frac{Xx}{R}\right)\cos\left(\kappa\frac{Yy}{R}\right) - \sin\left(\kappa\frac{Xx}{R}\right)\sin\left(\kappa\frac{Yy}{R}\right) +$$

$$i\left\{\cos\left(\kappa\frac{Xx}{R}\right)\cos\left(\kappa\frac{Yy}{R}\right) + \sin\left(\kappa\frac{Xx}{R}\right)\sin\left(\kappa\frac{Yy}{R}\right)\right\}$$

The spatial terms $\cos\left(\kappa\frac{Yy}{R}\right)$ & $\sin\left(\kappa\frac{Yy}{R}\right)$ are similar to the temporal $\cos(\omega t)$ & $sin(\omega t)$ terms. So we can say that the spatial frequencies $K_Y, K_Z$ can be defined as:

$$K_X = \kappa\frac{X}{R} \tag{I.14}$$

$$K_Y = \kappa\frac{X}{R} \tag{I.15}$$

Substituting (I.14) and (1.15) in (I.10) we get:

$$E(K_X,K_Y) = \iint_{-\infty}^{+\infty} A(x,y) e^{i(K_X x + K_Y y)} dxdy \tag{I.16}$$

Comparing (I.16) with (I.8) shows that the 2D Fraunhofer diffraction can be described by the two dimensional Fourier transform of the aperture function. In other words, the spatial Fourier transform of the near-field pattern will give the far-field

pattern. And this is the technique that will be used within the external cavity model to obtain the far-field pattern.

The far-field pattern can also be expressed in terms of divergence angles rather spatial frequencies. Figure I.2 shows the 2 divergence angles of one point at the near-field.

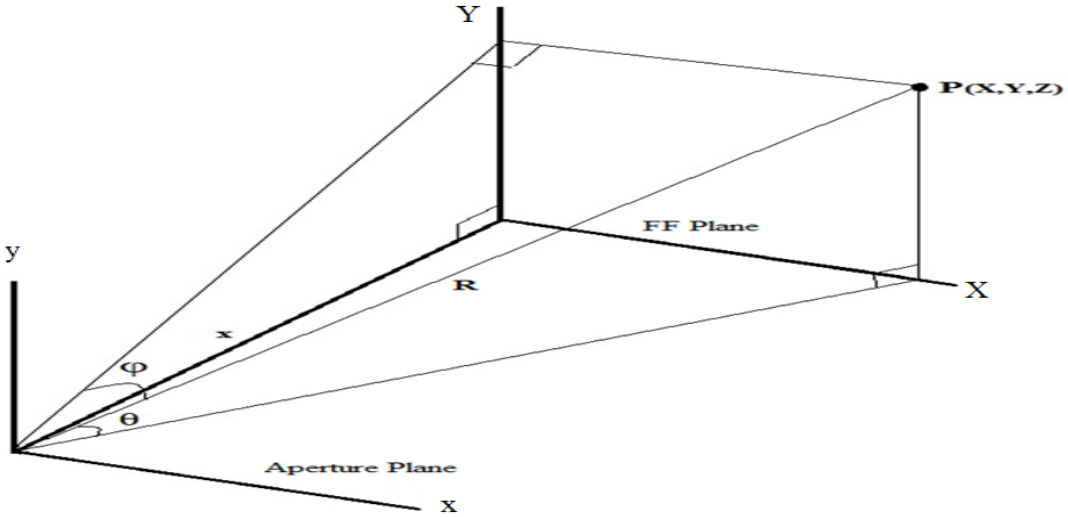



**Figure (I.2): Showing the relation between spatial dimensions between the near-field and the far-field and the angles of diffraction**

From figure I.2, the angle θ is the angle of vertical diffraction while φ is the angle of horizontal diffraction and they can be expressed as the following:

$$\sin\theta = \frac{X}{R} \tag{I.17}$$

$$\sin\varphi = \frac{Y}{R} \tag{I.18}$$

Substituting this in (I.17) and (I.18) in (I.14) and (I.15) we get a new definition of the spatial frequencies $K_X$ & $K_Y$:

$$K_X = \kappa \sin\theta \tag{I.19}$$

$$K_Y = \kappa \sin\varphi \tag{I.20}$$

and therefore we can get the angles of divergence from:

$$\theta = \sin^{-1}\left({}^{K_X}/_{\kappa}\right) \tag{I.21}$$

$$\varphi = \sin^{-1}\left({}^{K_Y}/_{\kappa}\right) \tag{I.22}$$

## References

[1] E. Hecht, *Optics*, 4th ed. Pearson, 2014.

# Appendix II

The general concept of back propagation is find out the field distribution at $z = z_0$ from the knowledge of field distribution $z = z_1$, where $z_1 > z_0$ . We will start by deriving the forward propagation formulism, $z_0\ to\ z_1$, then using the fact that the propagation formulism is linear, we can deduce the inverse solution to our problem.

Many imaging systems, involving signals with spatial nature, share common properties with communications systems, involving signals with temporal nature, namely: invariance and linearity. Therefore, the mathematics used to describe communications systems can be used to describe imaging systems; Fourier analysis and systems theory.

Just like the case with temporal signal, the spatial signals can be synthesised with much more basic signals obtained from Fourier decomposition. The complex spatial distribution across any plane can be written in terms of it spatial Fourier components, which are simple plane waves travelling in different directions. In other words, the field at any point can be calculated by adding the different contributions of these Fourier components.

Let's assume that at $z = z_0$ an optical field $U(x, y)$ exists across a plane $(x, y)$. Attempting to write this field in terms of it Fourier components we find:

$$U(x, y; z_0) = \iint_{-\infty}^{\infty} A(f_x, f_y; z_0) \exp\left[j2\pi \left(f_x x + f_y y\right)\right] \, df_x df_y \qquad \text{(II.1)}$$

where $A(f_x, f_y)$ is the spatial frequency spectrum given by:

# Appendix

$$A(f_x, f_y; z_0) = \iint_{-\infty}^{\infty} U(x, y; z_0) \exp\left[-j2\pi \left(f_x x + f_y y\right)\right] \, dxdy \tag{II.2}$$

$f_x, f_y$ are the spatial frequencies in the x and y directions. The following notation is considered: $U(x, y; z_0) = U(x, y)|_{z=z_0}$ and $A\left(f_x, f_y; z_0\right) = A\left(f_x, f_y\right)\big|_{z=z_0}$.

To interpret (II.1) physically, we consider $U(x, y; z_0)$ to be comprised of plane waves at each spatial frequency pair:$f_x, f_y$ with relevant amplitude: $A\left(f_x, f_y\right) df_x df_y$, travelling in different directions away from plane $z = z_0$ making angles $(-\pi \leftrightarrow \pi)$ with $z$. The relation between the spatial frequencies and the directions at which these plane waves are traveling can be obtained. The expression for a simple plane wave, propagating with wave vector $\vec{k}$ making and direction cosines $(\alpha, \beta, \gamma)$, can be written as:

$$p(x, y, z) = \exp\left(j\vec{k}\vec{r}\right) \tag{II.3}$$

where $\vec{r}$ is the position vector given by: $r = x\vec{x} + y\vec{y} + z\vec{z}$ and the propagation vector $\vec{k}$ is given by:

$$\vec{k} = \frac{2\pi}{\lambda}(\alpha\vec{x} + \beta\vec{y} + \gamma\vec{z}) = k_x\vec{x} + k_y\vec{y} + k_z\vec{z} \tag{II.4}$$

where $\alpha, \beta, \gamma$ are the direction cosines. Substituting in (II.4) in (II.3) we get:

$$p(x, y, z) = \exp\left[j2\pi\left(\frac{\alpha}{\lambda} + \frac{\beta}{\lambda} + \frac{\gamma}{\lambda}\right)\right] \tag{II.5}$$

The exponential term can be separated in to two:

$$p(x, y, z) = \exp\left[j2\pi\left(\frac{\alpha}{\lambda} + \frac{\beta}{\lambda}\right)\right] \exp\left[j2\pi\left(\frac{\gamma}{\lambda}\right)\right] \tag{II.6}$$

Direction cosines are related through the following expressions:

# Appendix

$$\alpha^2 + \beta^2 + \gamma^2 = 1 \tag{II.7}$$

Comparing the expression for a simple unity plane wave, in (II.6), and the one in (II.1) we find:

$$\exp\left[j2\pi\left(f_x X + f_y Y\right)\right] = \exp\left[j2\pi\left(\frac{\alpha}{\lambda} + \frac{\beta}{\lambda}\right)\right] \tag{II.8}$$

And thus we realise that the direction cosines can be written in terms of the spatial frequencies:

$$\alpha = \lambda f_x \, , \beta = \lambda f_y$$

and utilising (II.7) we get and expression for $\gamma$:

$$\gamma = \sqrt{1 - \alpha^2 - \beta^2} = \sqrt{1 - (\lambda f_x)^2 - \left(\lambda f_y\right)^2}$$

Now we can re-write (II.1) in terms of direction cosines:

$$U(x, y; z_0) = \iint_{-\infty}^{\infty} A(\frac{\alpha}{\lambda}, \frac{\beta}{\lambda}; z_0) \exp\left[j2\pi\left(\frac{\alpha}{\lambda}x + \frac{\beta}{\lambda}y\right)\right] d\frac{\alpha}{\lambda} d\frac{\beta}{\lambda} \tag{II.9}$$

where $A(\frac{\alpha}{\lambda} + \frac{\beta}{\lambda})$ is called the angular spectrum given by:

$$A(\frac{\alpha}{\lambda}, \frac{\beta}{\lambda}; z_0) = \iint_{-\infty}^{\infty} U(x, y; z_0) \exp\left[-j2\pi\left(\frac{\alpha}{\lambda}x + \frac{\beta}{\lambda}y\right)\right] dxdy \tag{II.10}$$

The goal is to find out the field distribution $U(x, y; z_1)$ from the knowledge of $U(x, y; z_0)$. If $U(x, y; z_0)$ and $U(x, y; z_1)$ are related then their respective angular spectra are also related.

Using equation (II.9), we can write the field distribution at any plane along the axis z.

# Appendix

$$U(x,y;z) = \iint_{-\infty}^{\infty} A(\frac{\alpha}{\lambda},\frac{\beta}{\lambda};z)\exp\left[j2\pi\left(\frac{\alpha}{\lambda}x+\frac{\beta}{\lambda}y\right)\right] d\frac{\alpha}{\lambda}d\frac{\beta}{\lambda} \quad \text{(II.11)}$$

Since $U(x,y)$propagated from $z = z_0\ to\ z = z_1$ then it must satisfy the Helmholtz equation: $\nabla^2 U + k^2 U = 0$ and since $A(\frac{\alpha}{\lambda},\frac{\beta}{\lambda};z)$ is one the components of $U(x,y;z)$, then it must satisfy the differential equation:

$$\frac{d^2}{dz^2}\left[A\left(\frac{\alpha}{\lambda},\frac{\beta}{\lambda};z\right)\right] + (k_z)^2 A\left(\frac{\alpha}{\lambda},\frac{\beta}{\lambda};z\right) = 0$$

$$\frac{d^2}{dz^2}\left[A\left(\frac{\alpha}{\lambda},\frac{\beta}{\lambda};z\right)\right] + \left(\frac{2\pi}{\lambda}\right)^2 \gamma^2\, A\left(\frac{\alpha}{\lambda},\frac{\beta}{\lambda};z\right) = 0$$

$$\frac{d^2}{dz^2}\left[A\left(\frac{\alpha}{\lambda},\frac{\beta}{\lambda};z\right)\right] + \left(\frac{2\pi}{\lambda}\right)^2 (1-(\alpha)^2-(\beta)^2)\, A\left(\frac{\alpha}{\lambda},\frac{\beta}{\lambda};z\right) = 0 \quad \text{(II.12)}$$

(II.12) is a homogeneous 2nd order differential equation which has a solution of the form:

$$A\left(\frac{\alpha}{\lambda},\frac{\beta}{\lambda};z\right) = A\left(\frac{\alpha}{\lambda},\frac{\beta}{\lambda};0\right)\exp\left[j\left(\frac{2\pi}{\lambda}\sqrt{1-(\alpha)^2-(\beta)^2}\right)z\right] \quad \text{(II.13)}$$

Substituting (II.13) in (II.11):

$$U(x,y;z)$$

$$= \iint_{-\infty}^{\infty} A\left(\frac{\alpha}{\lambda},\frac{\beta}{\lambda};0\right)\exp\left[j\left(\frac{2\pi}{\lambda}\sqrt{1-(\alpha)^2-(\beta)^2}\right)z\right]\exp\left[j2\pi\left(\frac{\alpha}{\lambda}x+\frac{\beta}{\lambda}y\right)\right] d\frac{\alpha}{\lambda}d\frac{\beta}{\lambda} \quad \text{(II.14)}$$

Using the relationships between the direction cosines and the spatial frequencies we can write:

$$U(x,y;z)$$

$$= \iint_{-\infty}^{\infty} A(f_x,f_y;0)\exp\left[j\left(\frac{2\pi}{\lambda}\sqrt{1-(\lambda f_x)^2-(\lambda f_y)^2}\right)z\right]\exp[j2\pi\,(f_x x+f_y y)]\, df_x df_y \quad \text{(II.15)}$$

# Appendix

To symbolise Fourier transform we use the symbol "ℱ". Therefore, we can write:

$$A(f_x, f_y; 0) = \mathcal{F}[U(x, y; 0)]$$

$$A(f_x, f_y; z) = \mathcal{F}[U(x, y; z)]$$

$$U(x, y; z) = \mathcal{F}^{-1}[A(f_x, f_y; z)]$$

$$U(x, y; 0) = \mathcal{F}^{-1}[A(f_x, f_y; 0)]$$

Re-writing (II.15) using the above notations we get:

$$U(x, y; z) = \iint_{-\infty}^{\infty} \mathcal{F}[U(x, y; 0)] \exp\left[j\left(\frac{2\pi}{\lambda}\sqrt{1 - (\lambda f_x)^2 - (\lambda f_y)^2}\right)z\right] \exp[j2\pi(f_x x + f_y y)]\, df_x df_y$$

$$U(x, y; z) = \mathcal{F}^{-1}\left\{\mathcal{F}[U(x, y; 0)] \exp\left[j\left(\frac{2\pi}{\lambda}\sqrt{1 - (\lambda f_x)^2 - (\lambda f_y)^2}\right)z\right]\right\}$$

$$\mathcal{F}[U(x, y; 0)] \exp\left[j\left(\frac{2\pi}{\lambda}\sqrt{1 - (\lambda f_x)^2 - (\lambda f_y)^2}\right)z\right] = \mathcal{F}[U(x, y; z)]$$

$$\mathcal{F}[U(x, y; 0)] = \mathcal{F}[U(x, y; z)] \exp\left[-j\left(\frac{2\pi}{\lambda}\sqrt{1 - (\lambda f_x)^2 - (\lambda f_y)^2}\right)z\right]$$

$$A(f_x, f_y; 0) = A(f_x, f_y; z) \exp\left[-j\left(\frac{2\pi}{\lambda}\sqrt{1 - (\lambda f_X)^2 - (\lambda f_y)^2}\right)z\right] \qquad \text{(II.16)}$$

Equation (II.6) shows that we can find the angular spectrum at $z = 0$ in terms of the angular spectrum at $z = z$. It is worth noting that $z = 0$ is a point which can be chosen arbitrarily along the z axis. Thus in order to make (II.16) more general, we write:

$$A(f_x, f_y; z_1)$$

$$= A(f_x, f_y; z_2) \exp\left[-j\left(\frac{2\pi}{\lambda}\sqrt{1-(\lambda f_x)^2-\left(\lambda f_y\right)^2}\right)(z_2 - z_1)\right] \quad \text{(II.17)}$$

where $z_2 > z_1$. We can also write (II.17) in terms of $U(x, y; z_1)$ & $U(x, y; z_2)$:

$$U(x, y; z_1)$$

$$= \mathbb{F}^{-1}\left\{A(f_x, f_y; z_2) \exp\left[-j\left(\frac{2\pi}{\lambda}\sqrt{1-(\lambda f_x)^2-\left(\lambda f_y\right)^2}\right)(z_2 - z_1)\right]\right\} \quad \text{(II.18)}$$